From Ocean Floor to Stratosphere: Investigating Astrobiologically Relevant Processes and Molecules on Solar System Bodies

Thesis by
Theresa Marlin

In Partial Fulfillment of the Requirements for the
Degree of
Doctor of Philosophy



CALIFORNIA INSTITUTE OF TECHNOLOGY
Pasadena, California

2026
Defended August 18, 2025

© 2026

Theresa Marlin
ORCID: 0009-0003-0670-5474

All rights reserved

"All we have to decide is what to do with the time that is given us."
~J. R. R. Tolkien

ACKNOWLEDGEMENTS

My acknowledgements go first and foremost to my advisors, Katherine de Kleer and Morgan Cable. The advice I got over and over again when starting grad school was "choose your advisor wisely," advice that I was only able to fully appreciate over the course of my Ph.D. as I lived through my experiences and observed those of fellow grad students around me. Astrobiology was a random idea that slowly grew in my mind during many nights staring at starry skies in the Australian Outback and the Atacama Desert in the months prior to starting grad school. Both Katherine and Morgan took a chance on me, facilitating my grad school traverse from RNA biology to planetary astronomy and giving me research experiences that I could truly never have imagined a decade ago. Katherine, thank you for having time for me every week, for a stream of ideas and suggestions and insights, for teaching me planetary astronomy from square one. I am an astronomer because of you. Morgan, thank you for the unconditional positivity and support, the hours in lab, the many lunch chats, and for inspiring me to go deeper into a field far from anything I had studied before. Thank you both for being strong examples of scientists with integrity, honesty, and balance throughout a Ph.D. book-ended with unprecedented events. Doing this degree with you two and diving headlong into Solar System science has been one of the greatest privileges of my life.

Thank you also to my committee chair, Dianne Newman, and my additional committee member, Heather Knutson. Dianne for guiding me through the transition from Biology to Planetary Science and Heather for her excellent classroom instruction and research insights.

Over the course of my Ph.D., I was lucky to have extended collaborations with several other people. With Jessica Weber and Laurie Barge, I have many good memories in the Origins and Habitability Lab. Thanks for advising me for so many years and for all the good science chats. A special acknowledgement to JPL postdocs Rachel Sheppard and Bonnie Teece for their friendship and advice for the future, and the OHL interns for fun times in and out of lab. Probably the most Zoom hours of my Ph.D. were with Eliot Young. Thank you for many good science discussions, life chats, the pedagogical moments, ukulele demonstrations, and humor. I learned so much from you.

One of the highlights of grad school has been observing nights. My thanks to Sherry Yeh, Carlos Alvarez, and Percy Gomez at Keck, and Carolyn Heffner, Kathleen Koviak, Paul Nied, Isaac Wilson, and Diana Roderick at Palomar, for making my Titan observational dreams a reality.

My thanks to the NIH Intramural Research program, the NSF Graduate Research Fellowship Program, the NASA *Cassini* Data Analysis Program, and the NASA Solar System Observations program — for financial contributions that enabled me to become a researcher.

Grad school would never have happened without the support from professors and scientists in my undergrad and postbac years. Thank you Julie Himmelberger and Judy Rance-Roney for motivating me, Joe Leese, Kathleen Ryan, and Nick Guydosh for providing research opportunities and mentorship, and Grant Jones, David Young, and John Taylor Hosmer-Quint for being such supportive labmates during my NIH days.

Last but not least, my thanks to option managers Liz Ayala (BBE) and Julie Lee (GPS), who both went above and beyond with administrative help and real kindness in my Ph.D.

Beyond academic acknowledgements, I am deeply grateful for the personal relationships that have carried me through grad school.

My family. My siblings — Joseph, for joining me on the career pivot to space and the perfect balance of teasing and supportive big brother energy; Maria, for showing me what it means to have a passion; Cat, for always being ready for an adventure, the road trips, and being the one I can call when a fat centipede as long as my hand appears in the shower; Dit, for musical embroidery sessions, puzzles together, and being my forever #1 dance partner. My parents, the first scientists I ever met, who made sure science and math were a normal part of life. My Grandma, the sharpest, busiest 94-year-old I ever met. I hope I grow up to be just like you. Aunt Martha, I hope you're stocking up on Beanie Babies in heaven — I miss you. My extended family, for being the network I know has my back from all over the country.

My partner, Zsófi Nagy. Dating a grad student is hard, dating across 9 time zones is hard; you navigated both with grace, endless patience, and perpetual cheerfulness. Köszönöm szépen, it means the world.

The friendships I made in grad school will be one of the things I hold closest in the years and decades to come. To my bio friends, the first squad I found at Caltech —

Matteo Guareschi and Victoria Jorgensen for the cooking nights, opera adventures, and Settebello excursions, Kevin Le for endless CAR cafe work sessions, and the rest of the boot camp squad for being a consistent fun time during sporadic hangouts through the years.

To the second division I found a home in — GPS. Julie, for a friendship forged in the depths of the KarGenie office over nachos and a dubious salesman. My group mates for the laughs and learning throughout the weeks and years — Maria Camarca, Zac Milby, Tina Seeger, Yu Yu Phua, Xander Thelen especially — I feel so lucky to have shared so many years in this group exploring the outer Solar System together. To Elin Marken and Amanda Bednarick, for breakfast dates and explorations and a shining example of the longevity of good friendship.

To my non-Caltech friends who keep me grounded and made grad school breeze by. Colleen Prince, for being a bonus sister across decades and countries, always making me think critically and examine my own beliefs, and being at my side through it all. Nalin Mehta, for your kindness and humor, the depth to which you care about my well-being, the conversations about science and the world and everything in between. Jenn Yaeger, for being a true friend through eventful years. Prachi Vakharia, for challenging me to be my best self personally and professionally. Robert Seidl, for your curiosity and friendship and humor and the immediate willingness for spontaneous adventures. Hannah Stockdale, for a friendship born on stage as kids that stood the test of time as life took us in different directions. Uroš Stojadinvic, for showing me Serbia and Berlin and inspiring me with your enthusiasm for knowledge. Milutin Manojlovic, for being rad. Diana Avila, for your generosity and fun. Emese Papp and Anna Fóti, for introducing me to a culture I grew to love more than my own. The GRBA astro team — for making me discover astronomy all over again, this time without a computer screen.

I am grateful to all the roommates over the years who have made my house a home and joined me on adventures large and small. My DC/NIH roommates, who set the standard high. Masami Hazu, the first Caltech friend I ever made, for showing the value of dedication and loyalty. Maria Derda, where to start? My memories of my time at Caltech will forever be intertwined with fikas and Broadway parties in the Cats, Sunday porch lunches, the sound of your camera shutter across the western US, Spy x Family, but above all — the gift of six years of living with you. Francesca Li, for your cheerfulness and smiles, the laughs and long chats. Wai Wai Htay, for bringing the heart of your country and culture straight to North Michigan and

sharing it with us all. Masoma Naseri, for the fierceness and loyalty with which you hold onto the people you love — you inspire me. Each of you made these years some of the best of my life.

To the circus/flying trapeze family I found while searching for an outlet from research — the early days at TSNY-DC and then the SoCal days at Trapeze High. The coaches that pushed me to new limits and helped me to see life differently while flipping off of a trapeze bar several dozen feet up in the air.

To those above — and to the people I met around the world along the way — my deepest gratitude to you all.

ABSTRACT

In astrobiology, the quest to understand the origin of life on Earth is often paired with an outward focus on whether life can be found elsewhere in the universe. The most accessible corner of the universe in which to search for extraterrestrial life is our own Solar System — the planets, their satellites, and the minor bodies present throughout. An examination of the essential elements for life on Earth returns three critical factors: liquid water, complex chemistry, and a source of energy. Searching for these three elements in bodies beyond Earth returns a suite of candidates: the ocean worlds of the outer Solar System. These moons, while too cold to harbor liquid water on their surfaces, are thought to have subsurface liquid water reservoirs which could potentially harbor life. Of particular note are two Saturnian satellites: Enceladus, with predicted hydrothermal activity and water-rock interactions, and Titan, with a dense atmosphere filled with complex organics with potential prebiotic significance. This thesis broadly addresses astrobiological questions on Earth, Enceladus, and Titan via laboratory chemistry and observational astronomy.

(I): Chemical gardens as analogs for hydrothermal vents on ocean worlds. This chapter probes laboratory-synthesized analogs of hydrothermal vents as reaction catalysts with alpha keto acids as reactants under various conditions. NMR spectroscopy results support the formation of prebiotically-relevant molecules including glycine (an amino acid) and maloyl formate (a precursor to alpha keto glutarate (AKG)).

(II): Propyne: determination of physical properties and unit cell parameters under Titan-relevant conditions. Many questions remain about the organic species that are photochemically produced in Titan's atmosphere. Propyne (CH_3CCH) has been detected in gas phase and is a candidate for Titan's mixed-species ice clouds. This work presents a characterization of solid propyne using Raman spectroscopy, infrared spectroscopy, and X-ray diffraction.

(III): Zonal winds in Titan's middle atmosphere from a stellar occultation observed with Keck adaptive optics. Winds in Titan's atmosphere vary seasonally, and stellar occultations present a unique chance to probe them. This work presents spatially-resolved images of the refracted "lightspots" visible around Titan's limb during an occultation, and discusses the zonal wind profile which best matches the observed data.

PUBLISHED CONTENT AND CONTRIBUTIONS

Marlin, Theresa C., Eliot F. Young, Katherine de Kleer, Martin Cordiner, Nicholas A. Lombardo, Imke de Pater, Juan M. Lora, Paul Corlies, Richard Cosentino, Conor Nixon, Sébastien Rodriguez, Alexander Thelen (Dec. 2025a). "Zonal Winds in Titan's Middle Atmosphere from a Stellar Occultation Observed with Keck Adaptive Optics". In: *The Planetary Science Journal* 6.12, p. 286. DOI: 10.3847/PSJ/ae03a6. URL: https://doi.org/10.3847/PSJ/ae03a6.

T. C. M. collected, reduced, and analyzed the data, ran the forward model with input from E. F. Y., and wrote the manuscript with input from other authors.

Marlin, Theresa C., Jessica M. Weber, Rachel Y. Sheppard, Scott Perl, Derek Diener, Marc M. Baum, Laura M. Barge (Jan. 2025b). "Chemical gardens as analogs for prebiotic chemistry on ocean worlds". English. In: *Chem* 11.1. Publisher: Elsevier. ISSN: 2451-9294, 2451-9308. DOI: 10.1016/j.chempr.2024.08.012. URL: https://www.cell.com/chem/abstract/S2451-9294(24)00427-3.

T. C. M. conducted all experiments, analyzed all NMR data, and wrote the manuscript with input from other authors.

Marlin, Theresa C., Morgan L. Cable, Tuan Vu, Helen E. Maynard-Casely, Melissa Ugelow, Carrie Anderson, Robert Hodyss (May 2024). "Propyne: Determination of Physical Properties and Unit Cell Parameters under Titan-Relevant Conditions". In: *ACS Earth and Space Chemistry* 8.5. Publisher: American Chemical Society, pp. 957–964. DOI: 10.1021/acsearthspacechem.3c00303.

T. C. M. conducted the Raman spectroscopy experiments, analyzed the Raman and infrared data, and wrote all sections of the manuscript besides the XRD analysis section, with input from other authors.

TABLE OF CONTENTS

Acknowledgements iv
Abstract viii
Published Content and Contributions ix
Table of Contents x
List of Illustrations xii
List of Tables xxix
Chapter I: Introduction 1
1.1 The origin of life on Earth 1
1.2 From deep sea hydrothermal vent to benchtop chemical garden . . . 2
1.3 The search for life beyond Earth: ocean worlds of the Solar System . 4
1.4 Titan: Before the *Cassini-Huygens* mission 6
1.5 The *Cassini-Huygens* mission 7
1.6 Propyne: building on the findings of *Cassini* 9
1.7 Ground-based observations of Titan with adaptive optics 10
1.8 Stellar occultations: zonal wind snapshots 11
1.9 Thesis overview 12
Chapter II: Chemical gardens as analogs for prebiotic chemistry on ocean worlds 21
2.1 Introduction 22
2.2 Results 25
2.3 Discussion 38
2.4 Experimental Procedures 42
2.5 Acknowledgements 42
2.6 Author Contributions 42
Chapter III: Propyne: Determination of physical properties and unit cell parameters under Titan-relevant conditions 50
3.1 Introduction 51
3.2 Experimental Methods 53
3.3 Results 56
3.4 Discussion 62
3.5 Conclusions 64
3.6 Author Information 65
3.7 Acknowledgements 66
3.8 Abbreviations 66
Chapter IV: Zonal winds in Titan's middle atmosphere from a stellar occultation observed with Keck adaptive optics 71
4.1 Introduction 72
4.2 Data collection, reduction, and processing 78
4.3 Forward modeling 87

4.4 Results 99
4.5 Discussion 105
4.6 Conclusions 109
4.7 Acknowledgements 111
Chapter V: Conclusion and Future Directions 116
5.1 Chemical gardens as analogs for prebiotic chemistry on ocean worlds: 118
5.2 Propyne: Determination of Physical Properties and Unit Cell Parameters under Titan-Relevant Conditions 120
5.3 Zonal winds in Titan's middle atmosphere from a stellar occultation observed with Keck adaptive optics 123
Appendix A: Chemical Gardens Supplemental Information 128
A.1 Figures and Tables 128
A.2 Experimental Procedures 241
Appendix B: Propyne Supplemental Information 248
Appendix C: Occultation Supplemental Information 253

LIST OF ILLUSTRATIONS

Number *Page*

1.1 A selection of the ocean worlds in the Solar System; not to scale. Image credit: Woods Hole Oceanographic Institute 5

1.2 A cross section of Jupiter's moon Europa, displaying the rock-water interface posited to exist below the surface ice layer. Image credit: NASA/JPL 5

1.3 Titan as captured from 3.6 million kilometers away by *Pioneer 11* on September 3, 1979. Image credit: NASA. 7

1.4 Photolysis of molecular nitrogen and methane leads to recombination and formation of complex organic molecules. Figure from Nixon, 2024. 9

2.1 *CG growth with time*. Iron silicate CG in sodium silicate solution after (A) 5 min and (B) 1 week of growth. 26

2.2 *Organic analysis demonstrates limited formation of glycine and maloyl formate, broad formation of acetate, formate, and glycolate*. Products formed from pyruvate and/or glyoxylate under prebiotic and/or Enceladus conditions. Reaction conditions leading to product formation include the following: (A) glyoxylate, NH_3, and CG (pH 7.25); (B) glyoxylate, NH_3, and CG (pH 10); (C) glyoxylate, pyruvate, NH_3, and CG (pH 10); and (D) glyoxylate, pyruvate, NH_3, and CG (pH 7.25).
***: product was observed in all reactions.
X: product was not observed in any reactions.
*: Product observed under benchtop, anaerobic, and heated conditions.
§: Product observed under benchtop and anaerobic conditions only.
AKG: alpha-ketoglutarate. Blue reactions: decomposition; gray reactions: reduction; green reactions: reductive amination; orange reaction: aldol addition. 33

2.3 *Formate yields varied depending on the conditions and components of the reactions.*. In all instances, the presence of a CG increased formate production. Formate production was inhibited under anaerobic conditions. GA, glyoxylate; PA, pyruvate. The presence of ammonia led to decreased formate production in instances when Enceladus-like salts were not present. 34

2.4 *Product formation observed in reactions containing pyruvate, glyoxylate, and ammonia*. NMR spectrum of a chemical garden, glyoxylate, pyruvate, and NH_3 at pH 10. Benchtop conditions, t = 2 weeks. . . . 35

2.5 *VNIR reflectance spectroscopy indicates diverse solid formation in CG reactions*. VNIR reflectance spectra of various CG precipitates following 3 weeks of reactions. Blue: pH 7.25, no NH_4Cl; orange: pH 7.25, added NH_4Cl; green: pH 10, no NH_4Cl; red: pH 10, added NH_4Cl.
(A) Glyoxylate and benchtop.
(B) Glyoxylate and heated.
(C) Glyoxylate and anaerobic.
(D) Pyruvate and benchtop.
(E) Pyruvate and heated.
(F) Pyruvate and anaerobic. 37

3.1 Pawley fit of the 90 K synchrotron diffraction data to the *Pbca* unit cell, a = 15.89410(11) Å, b = 13.2987(1) Å, and c = 5.7070(6) Å. Tick marks below the data indicate the expected positions of Bragg peaks from this unit cell. The fit of these data yielded R_{wp} = 8.46%, R_p = 6.21% with peaks described by a Thomson-Cox Hastings model and background by a 7-order Chebyshev polynomial (additional large-width peak included in the background to describe amorphous scattering from the silicate capillary). 57

3.2 Diffraction patterns of propyne obtained on the laboratory X-ray source (λ = 1.5406 Å) as a function of temperatures. The sample was first frozen at 85 K, followed by an incremental temperature increase every 5 K. 58

3.3 Thermal expansion of propyne as derived from Pawley refinements (Table 3.1). Lattice constants and unit cell volumes are normalized to those at the coldest temperature under study (85 K). 59

3.4 Thermal expansion of propyne as derived from Pawley refinements (Table 3.1). Lattice constants and unit cell volumes are normalized to those at the coldest temperature under study (85 K). 60

3.5 Infrared spectra of the amorphous phase (red trace; bottom) and crystalline (blue trace; top) phase propyne ice. Expanded views of characteristic spectral regions are highlighted in the bottom panels. . 62

4.1 The top panels show the diamond-shaped caustic (concentration of light rays) that results from a planet with a uniformly rotating, oblate atmosphere (depicted as a black oval, top left panel). The black lines represent refracted starlight, and the caustic is highlighted in red. The top right panel depicts a magnified version of the caustic for the atmosphere on the left, showing the abrupt variations in flux that are present. Observation chords intersecting the caustic show rapid changes in flux at the center of an occultation event, allowing observers to determine the shape of the caustic. The bottom panels show the caustic that is formed in an alternative case: when the atmosphere is not uniformly rotating, but rather has a strong zonal wind in the north causing atmospheric distortion (highlighted by the red flattened circle outline). The distorted atmosphere produces a triangle-shaped caustic (the red triangle in the middle of the bottom left panel); the caustic and its flux variations are depicted in the bottom right panel. As in the case of the oblate atmosphere, observation chords that intersect the caustic capture variations in flux that allow mapping of the caustic. As caustics are highly sensitive to nonspherical distortions, observations of the central flash allow observers to determine the shape of Titan's atmosphere and therefore the zonal wind profile at the time of the occultation. (From Figs. 9 and 10 of Sicardy, 2022). 75

4.2 Main figure: Path of the star (from the vantage point of Maunakea) as it is occulted by Titan. Red plus signs represent 1-minute increments. The center of the occultation shadow path passes within 50 km of Maunakea, making this site ideal for perceiving the “central flash" (rapidly changing stellar refraction patterns) that occurs near the center of the occultation shadow path. Inset: full shadow path of star 2MASS 21312124-1602427, K_{mag} = 12.9. The hatched line represents the center of the shadow path; solid lines are the outer edges. 79

4.3 Left: reduced data from pre-event. Scattered light around both Titan and the star are caused by Earth’s atmosphere. Right: the same frame following Richardson-Lucy deconvolution. Circle center and radius determined by fitting a circle to radial gradient minima around the limb. 80

4.4 Isolated refracted lightspots during the occultation event. Titan’s solid body radius is marked with a white circle; the star’s interpolated offset relative to Titan’s disk is marked in each frame with a white plus sign. Panels A-C are from near the midpoint of the occultation, with Panel B being the most central frame of the occultation that we captured. In the middle panels, multiple refracted lightspots are visible that change position rapidly with the cadence of the images. Panel D is from shortly before egress. The position of the refracted lightspot is aligned with the chord of the occultation. 82

4.5 Top: linear fits (green and pink lines) to calculate x- and y-offsets between the centers of Titan and the occulted star. Bottom: residuals in the x- (left) and y-directions (right) following the subtraction of the fit. 83

4.6 Continuum-subtracted ALMA observations of Titan on 2022-09-06, showing the spectrally integrated line flux maps for the CH_3CN J = 35 – 34 and J = 36 – 35 bands (left panels) and corresponding spectra (right panels), integrated within a 1″.2-diameter circular aperture centered on Titan. The FWHM of the spatial resolution element (ellipse) is shown in the lower left of the maps. 84

4.7 Peak-normalized wind contribution function for the observed CH_3CN J = 35 – 34 transitions at 643 GHz. 87

4.8 A: The atmospheric temperature profile derived by the HASI instrument on board the Huygens probe. B: Pressure is calculated from the temperature profile by leveraging the law of hydrostatic equilibrium and approximating Titan's atmosphere as 100% nitrogen. C: The integrated line-of-sight refractivity is found by stepping across 8000 km chords with step size = 1 km. At each step, refractivity ν is calculated, and the integrated line-of-sight refractivity is the sum of $\nu \cdot ds$ across the chord. D: Bending angles are calculated from the gradient of the phase delay screen. The orange vertical line in Panels B-D denotes Titan's surface. 91

4.9 Quantitative comparison of data and model can be achieved by treating Titan's disk as a circle and expressing the sum of the distribution of light around its limb as a function of angle θ. This figure demonstrates this for a model frame near the center of the occultation. Both near- and far-limb spots are visible (inset), and when the sum of the light distribution around the limb is plotted, the peaks of the lightspots are found to be at $\theta = 156°$ and $\theta = -11°$. 95

4.10 Snapshots of simulated zonal wind profiles from TAM at an altitude z = 307 km. L_s values of 0°, 90°, 180°, and 270° correspond to northern vernal equinox, summer solstice, autumnal equinox, and winter solstice, respectively. Wind trends are most dynamic around the two equinoxes. The orange line represents the latitude of ingress (−9°) and the green line represents latitude of egress (31°). 97

4.11 The radial distortions (contours of level pressure) corresponding to the 36 zonal wind snapshots in Figure 4.10. The orange line represents the latitude of ingress (−9°) and the green line represents latitude of egress (31°). 98

4.12 Left: the color map shows line-of-sight CH_3CN Doppler shifts, averaged across all observed transitions, overlaid on a Titan wireframe grid at the epoch of our ALMA observations. Velocity contours (labeled in units of m s^{-1}) are also overlaid. Right: error map showing 1σ statistical uncertainties on the Doppler shift for each pixel. The spatial resolution (elliptical beam FWHM) is indicated in the lower left corner. 99

4.13 Zonal wind velocity profile ($v(l)$) and 1σ error envelope retrieved from our ALMA CH_3CN observations on 2022-09-06, using a continuously variable parameterization with latitudinal sampling of 30°. 100
4.14 Best-match distributions of the angles of the refracted lightspots visible during occultation on the ingress and egress sides of Titan's disk. Data are depicted in blue and the model simulations with a starting atmosphere from the TAM simulation at $L_s = 120°$ are depicted in red. 101
4.15 Distributions of the angles of the refracted lightspots visible during occultation on the ingress and egress side of Titan's disk. Data are depicted in blue and the model simulations (with an atmosphere corresponding to double the GCM wind speeds) at $L_s = 30°$ are depicted in red. 102
4.16 Distributions of the angles of the refracted lightspots visible during occultation on the ingress and egress side of Titan's disk. Data are depicted in blue, and the model simulations (with an atmosphere corresponding to half the GCM wind speeds) at $L_s = 120°$ are depicted in red. 103
4.17 Distributions of the angles of the refracted lightspots visible during occultation on the ingress and egress sides of Titan's disk. Data are depicted in blue, and the model simulations are depicted in red. Model simulations correspond to a starting zonal wind profile derived from the ALMA data. 104
4.18 Limb light distributions for a circular Titan. Case A (left panel) shows Titan as seen by an observer at mid-event with the star directly behind Titan's disk. If Titan's atmosphere is circularly symmetric, there will be a ring of light around the entire limb because the projected lines from the star to the limb are perpendicular to the isopycnal lines all around the disk. In Case B, the star is offset from the center, and there are only two regions where the projected lines from the star are perpendicular to the isopycnal lines. 107
4.19 The left panel shows the resolved image of Titan taken closest to mid-event, when the star is nearly directly behind Titan's disk. The right panel is a diagram to show regions where the Δr level surface is perpendicular to the radial lines from star. 107

5.1 The many flavors of the H-C≡C region of propyne under ambient pressure. 121
A.1 Photos of chemical gardens in various stages. (A): filtering after growth. (B): stirred into a reaction. (C): in a reaction without being stirred (heated condition). (D): freeze-dried mineral remaining after the reaction used for VNIR analysis. 128
A.2 Control ^{1}H nuclear magnetic resonance (NMR) spectra; glyoxylate (GA) reaction under benchtop/aerobic conditions, pH 7.25. A: t = 0 weeks, B: t = 1 week, C: t = 2 weeks. 131
A.3 NMR spectra; glyoxylate and chemical garden reaction under benchtop/aerobic conditions, pH 7.25. A: t = 0 weeks, B: t = 1 week, C: t = 2 weeks, D: t = 3 weeks. 132
A.4 Control NMR spectra; glyoxylate and ammonium chloride reaction under benchtop/aerobic conditions, pH 7.25. A: t = 0 weeks, B: t = 1 week, C: t = 2 weeks. 133
A.5 NMR spectra; glyoxylate, ammonium chloride, and chemical garden reaction under benchtop/aerobic conditions, pH 7.25. A: t = 0 weeks, B: t = 1 week, C: t = 2 weeks, D: t = 3 weeks. 134
A.6 Control NMR spectra; pyruvate reaction under benchtop/aerobic conditions, pH 7.25. A: t = 0 weeks, B: t = 1 week, C: t = 2 weeks. . . . 135
A.7 NMR spectra; pyruvate and chemical garden reaction under benchtop/aerobic conditions, pH 7.25. A: t = 0 weeks, B: t = 1 week, C: t = 2 weeks, D: t = 3 weeks. 136
A.8 Control NMR spectra; pyruvate and ammonium chloride reaction under benchtop/aerobic conditions, pH 7.25. A: t = 0 weeks, B: t = 1 week, C: t = 2 weeks. 137
A.9 NMR spectra; pyruvate, ammonium chloride and chemical garden reaction under benchtop/aerobic conditions, pH 7.25. A: t = 0 weeks, B: t = 1 week, C: t = 2 weeks, D: t = 3 weeks. 138
A.10 Control NMR spectra; glyoxylate reaction under benchtop/aerobic conditions, pH 10. A: t = 0 weeks, B: t = 1 week, C: t = 2 weeks. . . . 139
A.11 NMR spectra; glyoxylate and chemical garden reaction under benchtop/aerobic conditions, pH 10. A: t = 0 weeks, B: t = 1 week, C: t = 2 weeks, D: t = 3 weeks. 140

A.12 Control NMR spectra; glyoxylate and ammonium chloride reaction under benchtop/aerobic conditions, pH 10. A: t = 0 weeks, B: t = 1 week, C: t = 2 weeks. 141
A.13 NMR spectra; glyoxylate, ammonium chloride, and chemical garden reaction under benchtop/aerobic conditions, pH 10. A: t = 0 weeks, B: t = 1 week, C: t = 2 weeks, D: t = 3 weeks. 142
A.14 Control NMR spectra; pyruvate reaction under benchtop/aerobic conditions, pH 10. A: t = 0 weeks, B: t = 1 week, C: t = 2 weeks. 143
A.15 NMR spectra; pyruvate and chemical garden reaction under benchtop/aerobic conditions, pH 10. A: t = 0 weeks, B: t = 1 week, C: t = 2 weeks, D: t = 3 weeks. 144
A.16 Control NMR spectra; pyruvate and ammonium chloride reaction under benchtop/aerobic conditions, pH 10. A: t = 0 weeks, B: t = 1 week, C: t = 2 weeks. 145
A.17 NMR spectra; pyruvate, ammonium chloride, and chemical garden reaction under benchtop/aerobic conditions, pH 10. A: t = 0 weeks, B: t = 1 week, C: t = 2 weeks, D: t = 3 weeks. 146
A.18 Control NMR spectra; pyruvate, glyoxylate, and ammonium chloride reaction under benchtop/aerobic conditions, pH 10. A: t = 0 weeks, B: t = 1 week, C: t = 2 weeks, D: t = 3 weeks. 147
A.19 NMR spectra; pyruvate, glyoxylate, ammonium chloride, and chemical garden reaction under benchtop/aerobic conditions, pH 10. A: t = 0 weeks, B: t = 1 week, C: t = 2 weeks, D: t = 3 weeks. 148
A.20 Control NMR spectra; pyruvate, glyoxylate, and ammonium chloride reaction under benchtop/aerobic conditions, pH 7.25. A: t = 0 weeks, B: t = 1 week, C: t = 2 weeks, D: t = 3 weeks. 149
A.21 NMR spectra; pyruvate, glyoxylate, ammonium chloride, and chemical garden reaction under benchtop/aerobic conditions, pH 7.25. A: t = 0 weeks, B: t = 1 week, C: t = 2 weeks, D: t = 3 weeks. 150
A.22 Control NMR spectra; glyoxylate, sodium chloride, and sodium carbonate reaction under benchtop/aerobic conditions. A: t = 0 weeks, B: t = 1 week, C: t = 2 weeks, D: t = 3 weeks. 151
A.23 NMR spectra; glyoxylate, sodium chloride, sodium carbonate, and chemical garden reaction under benchtop/aerobic conditions. A: t = 0 weeks, B: t = 1 week, C: t = 2 weeks, D: t = 3 weeks. 152

A.24 Control NMR spectra; glyoxylate, sodium chloride, sodium carbonate, and ammonium chloride reaction under benchtop/aerobic conditions. A: t = 0 weeks, B: t = 1 week, C: t = 2 weeks, D: t = 3 weeks. 153
A.25 NMR spectra; glyoxylate, sodium chloride, sodium carbonate, ammonium chloride, and chemical garden reaction under benchtop/aerobic conditions. A: t = 0 weeks, B: t = 1 week, C: t = 2 weeks, D: t = 3 weeks. 154
A.26 Control NMR spectra; pyruvate, sodium chloride, and sodium carbonate reaction under benchtop/aerobic conditions. A: t = 0 weeks, B: t = 1 week, C: t = 2 weeks, D: t = 3 weeks. 155
A.27 NMR spectra; pyruvate, sodium chloride, sodium carbonate, and chemical garden reaction under benchtop/aerobic conditions. A: t = 0 weeks, B: t = 1 week, C: t = 2 weeks, D: t = 3 weeks. 156
A.28 Control NMR spectra; pyruvate, sodium chloride, sodium carbonate, and ammonium chloride reaction under benchtop/aerobic conditions. A: t = 0 weeks, B: t = 1 week, C: t = 2 weeks, D: t = 3 weeks. 157
A.29 NMR spectra; pyruvate, sodium chloride, sodium carbonate, ammonium chloride, and chemical garden reaction under benchtop/aerobic conditions. A: t = 0 weeks, B: t = 1 week, C: t = 2 weeks, D: t = 3 weeks. 158
A.30 Control NMR spectra; glyoxylate, sodium chloride, increased sodium carbonate, and ammonium chloride reaction under benchtop/aerobic conditions. A: t = 0 weeks, B: t = 1 week, C: t = 2 weeks, D: t = 3 weeks. 159
A.31 NMR spectra; glyoxylate, sodium chloride, increased sodium carbonate, ammonium chloride, and chemical garden reaction under benchtop/aerobic conditions. A: t = 0 weeks, B: t = 1 week, C: t = 2 weeks, D: t = 3 weeks. 160
A.32 Control NMR spectra; pyruvate, sodium chloride, increased sodium carbonate, and ammonium chloride reaction under benchtop/aerobic conditions. A: t = 0 weeks, B: t = 1 week, C: t = 2 weeks, D: t = 3 weeks. 161

A.33 NMR spectra; pyruvate, sodium chloride, increased sodium carbonate, ammonium chloride, and chemical garden reaction under benchtop/aerobic conditions. A: t = 0 weeks, B: t = 1 week, C: t = 2 weeks, D: t = 3 weeks. 162
A.34 Control NMR spectra; glyoxylate reaction under heated conditions, pH 7.25. A: t = 0 weeks, B: t = 1 week, C: t = 2 weeks, D: t = 3 weeks. 163
A.35 NMR spectra; glyoxylate and chemical garden reaction under heated conditions, pH 7.25. A: t = 0 weeks, B: t = 1 week, C: t = 2 weeks, D: t = 3 weeks. 164
A.36 Control NMR spectra; glyoxylate and ammonium chloride reaction under heated conditions, pH 7.25. A: t = 0 weeks, B: t = 1 week, C: t = 2 weeks, D: t = 3 weeks. 165
A.37 NMR spectra; glyoxylate, ammonium chloride, and chemical garden reaction under heated conditions, pH 7.25. A: t = 0 weeks, B: t = 1 week, C: t = 2 weeks, D: t = 3 weeks. 166
A.38 Control NMR spectra; pyruvate reaction under heated conditions, pH 7.25. A: t = 0 weeks, B: t = 1 week, C: t = 2 weeks, D: t = 3 weeks. . 167
A.39 NMR spectra; pyruvate and chemical garden reaction under heated conditions, pH 7.25. A: t = 0 weeks, B: t = 1 week, C: t = 2 weeks, D: t = 3 weeks. 168
A.40 Control NMR spectra; pyruvate and ammonium chloride reaction under heated conditions, pH 7.25. A: t = 0 weeks, B: t = 1 week, C: t = 2 weeks, D: t = 3 weeks. 169
A.41 NMR spectra; pyruvate, ammonium chloride and chemical garden reaction under heated conditions, pH 7.25. A: t = 0 weeks, B: t = 1 week, C: t = 2 weeks, D: t = 3 weeks. 170
A.42 Control NMR spectra; glyoxylate reaction under heated conditions, pH 10. A: t = 0 weeks, B: t = 1 week, C: t = 2 weeks, D: t = 3 weeks. 171
A.43 NMR spectra; glyoxylate and chemical garden reaction under heated conditions, pH 10. A: t = 0 weeks, B: t = 1 week, C: t = 2 weeks, D: t = 3 weeks. 172
A.44 Control NMR spectra; glyoxylate and ammonium chloride reaction under heated conditions, pH 10. A: t = 0 weeks, B: t = 1 week, C: t = 2 weeks, D: t = 3 weeks. 173

A.45 NMR spectra; glyoxylate, ammonium chloride, and chemical garden reaction under heated conditions, pH 10. A: t = 0 weeks, B: t = 1 week, C: t = 2 weeks, D: t = 3 weeks. 174
A.46 Control NMR spectra; pyruvate reaction under heated conditions, pH 10. A: t = 0 weeks, B: t = 1 week, C: t = 2 weeks, D: t = 3 weeks. . . 175
A.47 NMR spectra; pyruvate and chemical garden reaction under heated conditions, pH 10. A: t = 0 weeks, B: t = 1 week, C: t = 2 weeks, D: t = 3 weeks. 176
A.48 Control NMR spectra; pyruvate and ammonium chloride reaction under heated conditions, pH 10. A: t = 0 weeks, B: t = 1 week, C: t = 2 weeks, D: t = 3 weeks. 177
A.49 NMR spectra; pyruvate, ammonium chloride, and chemical garden reaction under heated conditions, pH 10. A: t = 0 weeks, B: t = 1 week, C: t = 2 weeks, D: t = 3 weeks. 178
A.50 Control NMR spectra; pyruvate, glyoxylate, and ammonium chloride reaction under heated conditions, pH 10. A: t = 0 weeks, B: t = 1 week, C: t = 2 weeks, D: t = 3 weeks. 179
A.51 NMR spectra; pyruvate, glyoxylate, ammonium chloride, and chemical garden reaction under heated conditions, pH 10. A: t = 0 weeks, B: t = 1 week, C: t = 2 weeks, D: t = 3 weeks. 180
A.52 Control NMR spectra; pyruvate, glyoxylate, and ammonium chloride reaction under heated conditions, pH 7.25. A: t = 0 weeks, B: t = 1 week, C: t = 2 weeks, D: t = 3 weeks. 181
A.53 NMR spectra; pyruvate, glyoxylate, ammonium chloride, and chemical garden reaction under heated conditions, pH 7.25. A: t = 0 weeks, B: t = 1 week, C: t = 2 weeks, D: t = 3 weeks. 182
A.54 Control NMR spectra; glyoxylate, sodium chloride, and sodium carbonate reaction under heated conditions. A: t = 0 weeks, B: t = 1 week, C: t = 2 weeks, D: t = 3 weeks. 183
A.55 NMR spectra; glyoxylate, sodium chloride, sodium carbonate, and chemical garden reaction under heated conditions. A: t = 0 weeks, B: t = 1 week, C: t = 2 weeks, D: t = 3 weeks. 184
A.56 Control NMR spectra; glyoxylate, sodium chloride, sodium carbonate, and ammonium chloride reaction under heated conditions. A: t = 0 weeks, B: t = 1 week, C: t = 2 weeks, D: t = 3 weeks. 185

A.57 NMR spectra; glyoxylate, sodium chloride, sodium carbonate, ammonium chloride, and chemical garden reaction under heated conditions. A: t = 0 weeks, B: t = 1 week, C: t = 2 weeks, D: t = 3 weeks. 186
A.58 Control NMR spectra; pyruvate, sodium chloride, and sodium carbonate reaction under heated conditions. A: t = 0 weeks, B: t = 1 week, C: t = 2 weeks, D: t = 3 weeks. 187
A.59 NMR spectra; pyruvate, sodium chloride, sodium carbonate, and chemical garden reaction under heated conditions. A: t = 0 weeks, B: t = 1 week, C: t = 2 weeks, D: t = 3 weeks. 188
A.60 Control NMR spectra, pyruvate, sodium chloride, sodium carbonate, and ammonium chloride reaction under heated conditions. A: t = 0 weeks, B: t = 1 week, C: t = 2 weeks, D: t = 3 weeks. 189
A.61 NMR spectra; pyruvate, sodium chloride, sodium carbonate, ammonium chloride, and chemical garden reaction under heated conditions. A: t = 0 weeks, B: t = 1 week, C: t = 2 weeks, D: t = 3 weeks. 190
A.62 Control NMR spectra; glyoxylate, sodium chloride, increased sodium carbonate, and ammonium chloride reaction under heated conditions. A: t = 0 weeks, B: t = 1 week, C: t = 2 weeks, D: t = 3 weeks. 191
A.63 NMR spectra; glyoxylate, sodium chloride, increased sodium carbonate, ammonium chloride, and chemical garden reaction under heated conditions. A: t = 0 weeks, B: t = 1 week, C: t = 2 weeks, D: t = 3 weeks. 192
A.64 Control NMR spectra; pyruvate, sodium chloride, increased sodium carbonate, and ammonium chloride reaction under heated conditions. A: t = 0 weeks, B: t = 1 week, C: t = 2 weeks, D: t = 3 weeks. 193
A.65 NMR spectra; pyruvate, sodium chloride, increased sodium carbonate, ammonium chloride, and chemical garden reaction under heated conditions. A: t = 0 weeks, B: t = 1 week, C: t = 2 weeks, D: t = 3 weeks. 194
A.66 Control NMR spectra; glyoxylate reaction under anaerobic conditions, pH 7.25. A: t = 0 weeks, B: t = 1 week, C: t = 2 weeks, D: t = 3 weeks. 195
A.67 NMR spectra; glyoxylate and chemical garden reaction under anaerobic conditions, pH 7.25. A: t = 0 weeks, B: t = 1 week, C: t = 2 weeks, D: t = 3 weeks. 196

A.68 Control NMR spectra; glyoxylate and ammonium chloride reaction under anaerobic conditions, pH 7.25. A: t = 0 weeks, B: t = 1 week, C: t = 2 weeks, D: t = 3 weeks. 197
A.69 NMR spectra; glyoxylate, ammonium chloride, and chemical garden reaction under anaerobic conditions, pH 7.25. A: t = 0 weeks, B: t = 1 week, C: t = 2 weeks, D: t = 3 weeks. 198
A.70 Control NMR spectra; pyruvate reaction under anaerobic conditions, pH 7.25. A: t = 0 weeks, B: t = 1 week, C: t = 2 weeks, D: t = 3 weeks. 199
A.71 NMR spectra; pyruvate and chemical garden reaction under anaerobic conditions, pH 7.25. A: t = 0 weeks, B: t = 1 week, C: t = 2 weeks, D: t = 3 weeks. 200
A.72 Control NMR spectra; pyruvate and ammonium chloride reaction under anaerobic conditions, pH 7.25. A: t = 0 weeks, B: t = 1 week, C: t = 2 weeks, D: t = 3 weeks. 201
A.73 NMR spectra; pyruvate, ammonium chloride and chemical garden reaction under anaerobic conditions, pH 7.25. A: t = 0 weeks, B: t = 1 week, C: t = 2 weeks, D: t = 3 weeks. 202
A.74 Control NMR spectra; glyoxylate reaction under anaerobic conditions, pH 10. A: t = 0 weeks, B: t = 1 week, C: t = 2 weeks, D: t = 3 weeks. 203
A.75 NMR spectra; glyoxylate and chemical garden reaction under anaerobic conditions, pH 10. A: t = 0 weeks, B: t = 1 week, C: t = 2 weeks, D: t = 3 weeks. 204
A.76 Control NMR spectra; glyoxylate and ammonium chloride reaction under anaerobic conditions, pH 10. A: t = 0 weeks, B: t = 1 week, C: t = 2 weeks, D: t = 3 weeks. 205
A.77 NMR spectra; glyoxylate, ammonium chloride, and chemical garden reaction under anaerobic conditions, pH 10. A: t = 0 weeks, B: t = 1 week, C: t = 2 weeks, D: t = 3 weeks. 206
A.78 Control NMR spectra; pyruvate reaction under anaerobic conditions, pH 10. A: t = 0 weeks, B: t = 1 week, C: t = 2 weeks, D: t = 3 weeks. 207
A.79 NMR spectra; pyruvate and chemical garden reaction under anaerobic conditions, pH 10. A: t = 0 weeks, B: t = 1 week, C: t = 2 weeks, D: t = 3 weeks. 208

A.80 Control NMR spectra; pyruvate and ammonium chloride reaction under anaerobic conditions, pH 10. A: t = 0 weeks, B: t = 1 week, C: t = 2 weeks, D: t = 3 weeks. 209
A.81 NMR spectra; pyruvate, ammonium chloride, and chemical garden reaction under anaerobic conditions, pH 10. A: t = 0 weeks, B: t = 1 week, C: t = 2 weeks, D: t = 3 weeks. 210
A.82 Control NMR spectra; pyruvate, glyoxylate, and ammonium chloride reaction under anaerobic conditions, pH 10. A: t = 0 weeks, B: t = 1 week, C: t = 3 weeks. 211
A.83 NMR spectra; pyruvate, glyoxylate, ammonium chloride, and chemical garden reaction under anaerobic conditions, pH 10. A: t = 0 weeks, B: t = 1 week, C: t = 2 weeks, D: t = 3 weeks. 212
A.84 Control NMR spectra; pyruvate, glyoxylate, and ammonium chloride reaction under anaerobic conditions, pH 7.25. A: t = 0 weeks, B: t = 1 week, C: t = 3 weeks. 213
A.85 NMR spectra; pyruvate, glyoxylate, ammonium chloride, and chemical garden reaction under anaerobic conditions, pH 7.25. A: t = 0 weeks, B: t = 1 week, C: t = 2 weeks, D: t = 3 weeks. 214
A.86 Control NMR spectra; glyoxylate, sodium chloride, and sodium carbonate reaction under anaerobic conditions. A: t = 0 weeks, B: t = 1 week, C: t = 3 weeks. 215
A.87 NMR spectra; glyoxylate, sodium chloride, sodium carbonate, and chemical garden reaction under anaerobic conditions. A: t = 0 weeks, B: t = 1 week, C: t = 2 weeks, D: t = 3 weeks. 216
A.88 Control NMR spectra; glyoxylate, sodium chloride, sodium carbonate, and ammonium chloride reaction under anaerobic conditions. A: t = 0 weeks, B: t = 1 week, C: t = 3 weeks. 217
A.89 NMR spectra; glyoxylate, sodium chloride, sodium carbonate, ammonium chloride, and chemical garden reaction under anaerobic conditions. A: t = 0 weeks, B: t = 1 week, C: t = 2 weeks, D: t = 3 weeks. 218
A.90 Control NMR spectra; pyruvate, sodium chloride, and sodium carbonate reaction under anaerobic conditions. A: t = 0 weeks, B: t = 1 week, C: t = 3 weeks. 219
A.91 NMR spectra; pyruvate, sodium chloride, sodium carbonate, and chemical garden reaction under anaerobic conditions. A: t = 0 weeks, B: t = 1 week, C: t = 2 weeks, D: t = 3 weeks. 220

A.92 Control NMR spectra; pyruvate, sodium chloride, sodium carbonate, and ammonium chloride reaction under anaerobic conditions. A: t = 0 weeks, B: t = 1 week, C: t = 3 weeks. 221
A.93 NMR spectra; pyruvate, sodium chloride, sodium carbonate, ammonium chloride, and chemical garden reaction under anaerobic conditions. A: t = 0 weeks, B: t = 1 week, C: t = 2 weeks, D: t = 3 weeks. 222
A.94 Control NMR spectra; glyoxylate, sodium chloride, increased sodium carbonate, and ammonium chloride reaction under anaerobic conditions. A: t = 0 weeks, B: t = 1 week, C: t = 3 weeks. 223
A.95 NMR spectra; glyoxylate, sodium chloride, increased sodium carbonate, ammonium chloride, and chemical garden reaction under anaerobic conditions. A: t = 0 weeks, B: t = 1 week, C: t = 2 weeks, D: t = 3 weeks. 224
A.96 Control NMR spectra; pyruvate, sodium chloride, sodium carbonate, and ammonium chloride reaction under anaerobic conditions. A: t = 0 weeks, B: t = 1 week, C: t = 3 weeks. 225
A.97 NMR spectra; pyruvate, sodium chloride, sodium carbonate, ammonium chloride, and chemical garden reaction under anaerobic conditions. A: t = 0 weeks, B: t = 1 week, C: t = 2 weeks, D: t = 3 weeks. 226
A.98 NMR spectrum of pyruvate, pH 7.25. 227
A.99 NMR spectrum of glyoxylate, pH 7.25. 228
A.100 NMR spectrum of D_2Or/DSS, pH 7.25. 229
A.101 NMR spectra; glycine spikes at pH 7.25. (A) – Glyoxylate, ammonia; regular/benchtop conditions. (B) – same as (A) with spike of glycine. (C) – Glyoxylate, ammonia; heated conditions. (D) – same as (C) with spike of glycine. (E) – Glyoxylate, ammonia; anaerobic conditions. (F) – same as (E) with spike of glycine. 230
A.102 NMR spectra; glycine spikes at pH 10. (A) – Glyoxylate, ammonia; regular/benchtop conditions. (B) – same as (A) with spike of glycine. (C) – Glyoxylate, ammonia; heated conditions. (D) – same as (C) with spike of glycine. (E) – Glyoxylate, ammonia; anaerobic conditions. (F) – same as (E) with spike of glycine. 231

A.103 VNIR spectra of glyoxylate, pyruvate, and ammonia under pH 10 (blue) and pH 7.25 (orange). (A) aerobic/benchtop conditions. (B) heated conditions. (C) anaerobic conditions. 235
A.104 VNIR spectra of glyoxylate in Enceladuslike salts (blue), glyoxylate and ammonia in Enceladuslike salts (orange) and glyoxylate and ammonia in Enceladuslike salts with increased salinity (green). (A) aerobic/benchtop conditions. (B) heated conditions. (C) anaerobic conditions. 235
A.105 VNIR spectra of pyruvate in Enceladuslike salts (blue), pyruvate and ammonia in Enceladuslike salts (orange) and pyruvate and ammonia in Enceladuslike salts with increased salinity (green). (A) aerobic/benchtop conditions. (B) heated conditions. (C) anaerobic conditions. 236
A.106 XRD spectrum of a chemical garden. 236
A.107 XRD spectrum of a fully oxidized chemical garden. 236
A.108 XRD spectrum of solids formed from a reaction containing glyoxylate, a chemical garden, and ammonia at pH 7.25. 237
A.109 XRD spectrum of solids formed from a reaction containing glyoxylate, a chemical garden, and ammonia at pH 10. 237
A.110 XRD spectrum of solids formed from a reaction containing pyruvate, a chemical garden, ammonia, and Enceladuslike salts. 237
A.111 XRD spectrum of solids formed from a reaction containing pyruvate, a chemical garden, ammonia, and Enceladuslike salts with increased salinity. 237
A.112 Raman spectra of solids formed from a reaction containing pyruvate, a chemical garden, and ammonia at pH 7.25 in an anaerobic environment. Separate traces denote different locations of the same sample. 238
A.113 Raman spectra of solids formed from a reaction containing glyoxylate, pyruvate, a chemical garden, and ammonia. Separate traces denote different locations of the same sample. 239
A.114 Raman spectra of solids formed from a reaction containing pyruvate, a chemical garden, and ammonia at pH 7.25 conducted in a heated environment. Separate traces denote different locations of the same sample. 240

B.1 Raman spectroscopy of pure propyne ice deposited at 75 K under low pressure, with increasing temperatures. A phase transition is observed around 105-107 K. Expanded views of various spectral regions are shown at the bottom panels. 248
B.2 Spectra at 105 K; low-temperature deposition at 75 K (increasing temperature series; warmed to 105 K), high-temperature deposition at 120 K (decreasing temperature series; cooled to 105 K), and direct deposition at 105 K comparisons. Direct deposition at 105 K has a crystalline structure. 249
B.3 Raman spectroscopy of pure propyne ice deposited at 120 K under low pressure, with decreasing temperatures. No phase transitions are observed. Expanded views of various spectral regions are shown at the bottom panels. 250
B.4 Infrared spectroscopy temperature series of pure propyne deposited at 15 K and annealed to 105 K, under vacuum. Transition from amorphous to crystalline propyne is observed between 65 K and 75 K. Spectra highlighted in purple and denoted with an asterisk (8 K, 70 K, and 80 K) are from previously published work by Hudson et al., 2021 (Figure 11-13). 251

LIST OF TABLES

Number *Page*

2.1 Percentage yields of key prebiotic molecules from glyoxylate-containing reactions conducted under benchtop conditions (oxic, room temperature). [a]: Material below detection limit. [b]: Material is present, but peak overlap prevents integration of a single peak. [c]: Insufficient data quality to calculate final molarity. 28

2.2 Percentage yields of key prebiotic molecules from glyoxylate-containing reactions conducted in heated aerobic conditions. [a]: Material below detection limit. [b]: Material is present, but peak overlap prevents integration of a single peak. 30

2.3 Percentage yields of key prebiotic molecules from glyoxylate-containing reactions conducted in anaerobic conditions. [a]: Material below detection limit. [b]: Material is present, but peak overlap prevents integration of a single peak. [c]: Insufficient data quality to calculate final molarity. 32

3.1 Lattice constants and unit cell volumes of propyne over its temperature stability range of 1 bar[a].
[a]: Values were obtained from Pawley refinements. 57

3.2 Prominent Raman features of propyne. 61

3.3 Prominent IR features of propyne and comparison to previous publication. 62

4.1 Sum of squared errors table of the closest model-data matches for both ingress and egress spots combined, ingress spots alone, and egress spots alone. Only the original 37 input profiles (36 GCM snapshots and one ALMA profile) are included. See Table C.1 in the Supplemental Information for all SSE values for original magnitude profiles. 101

4.2 Sum of squared errors table of the closest model-data matches for both ingress and egress spots combined, ingress spots alone, and egress spots alone. Input profiles include the original 36 GCM snapshots and one ALMA profile (that are shown above), and the same 37 profiles with both halved and doubled magnitudes (total of 111 input profiles). See Supplemental Information, Tables C.2 and C.3 for all SSE values for halved and doubled magnitude profiles. 102

A.1 Experimental and control reactions conducted. Conditions in every row correspond to reactions conducted both without and with a chemical garden (control). Both control and experimental reactions in each row were conducted in all three experimental conditions: benchtop, heated/aerobic, and anaerobic. (*) concentrations are approximating those of Enceladus from (Glein et al., 2020) (0.2 M NaCl and 0.07 M $NaHCO_3$); (**) concentrations refer to the same set of Enceladuslike conditions but with increased (doubled) carbonate. 129

A.2 Peaks for compounds of interest. *: Acetic acid and formic acid have NMR peaks at 2.1 ppm and 8.26 ppm, respectively. Due to the low pKa of these acids and the experimental conditions we use, these products are not formed in high quantities. References for peaks: glyoxylate: (Cui et al., 2008), glycolate, glycine, formate, pyruvate, lactate, and alanine: (Wishart et al., 2009), glycolic acid decomposition and glycolic acid oligomer: (Weber et al., 2021), acetate: (*Sodium acetate - Optional[1H NMR] - Chemical Shifts - SpectraBase* 2024) 130

A.3 Experimental and control reactions conducted. Conditions in every row correspond to reactions conducted both without and with a chemical garden (control). Both control and experimental reactions in each row were conducted in all three experimental conditions: benchtop, heated/aerobic, and anaerobic. (*) concentrations are approximating those of Enceladus from (Glein et al., 2020) (0.2 M NaCl and 0.07 M $NaHCO_3$); (**) concentrations refer to the same set of Enceladuslike conditions but with increased (doubled) carbonate. 234

A.4 Freeze-dryer procedure used to dry the remaining solid mineral after the course of the reaction. 243

C.1 Sum of squared errors table of all model-data matches for both ingress and egress spots combined, ingress spots alone, and egress spots alone (36 GCM snapshots and one ALMA profile). 254

C.2 Sum of squared errors table of all model-data matches for both ingress and egress spots combined, ingress spots alone, and egress spots alone. The profiles correspond to input profiles with doubled magnitudes (36 GCM snapshots and one ALMA profile). 255

C.3 Sum of squared errors table of all model-data matches for both ingress and egress spots combined, ingress spots alone, and egress spots alone. The profiles correspond to input profiles with halved magnitudes (36 GCM snapshots and one ALMA profile). 256

Chapter 1

INTRODUCTION

Our Solar System is a place of immense diversity. From rocky Mercury with its 600°C diurnal-nocturnal temperature dichotomy and 88-day orbit, to massive Jupiter (1300 times the volume of Earth) and its fierce storm with wind speeds exceeding 600 km/hr, to Saturn and its brilliant rings system, to the distant icy Kuiper belt objects serving as time capsules to the early days of the Solar System — these examples are but a small subset of the stunning array of variety and extremes in our own cosmic neighborhood.

But one of the biggest wonders and mysteries contained in our Solar System is showcased on our own planet: life. From subglacial lakes in Antarctica to dry barren deserts, from lush mountain jungles to the deep ocean untouched by sunlight — life on Earth thrives with innumerable adaptations in creative niches.

Science has been landmarked throughout the centuries with huge discoveries. We can describe planetary orbits with Kepler's law. Delve into the subcellular components and intricate machinery that make up cells that make up all of life. Even discover and begin to characterize exoplanets orbiting stars that are many light-years from our own. But questions surrounding the origin of life — including both how it arose on Earth and how unique the process is in the Solar System, the galaxy, the universe — remain unanswered. This work offers a small contribution toward the study of astrobiology in our Solar System by probing the chemistry of hydrothermal vent analogs and conducting a twofold characterization of the astrobiologically relevant Saturnian satellite Titan.

1.1 The origin of life on Earth

How life began on Earth remains a surprisingly hotly debated topic. The earliest direct fossil evidence for life dates back to almost 3.5 billion years — stromatolite fossils found in the Pilbara region of western Australia (Noffke et al., 2013). The requirements for life on Earth can be distilled to three components: liquid water, a source of energy, and essential chemistry (the so-called "CHNOPS" elements — carbon, hydrogen, nitrogen, oxygen, phosphorus, and sulfur) (McKay, 2014). Studies on the origin of life can be roughly divided into two major theories: terrestrial

hydrothermal springs and submarine hydrothermal vents (Longo et al., 2020). The answer to this question has enormous implications both for our understanding of the diversity of life on Earth and for our characterization of the possibilities for life on worlds beyond our own.

The terrestrial hydrothermal springs hypothesis posits that life began in volcanic hot spring pools (Damer et al., 2020). This hypothesis requires the pre-existence of biologically relevant molecules, delivered exogenously (such as via meteorite impact, (e.g., Ehrenfreund et al., 2006)). Research shows that protocells capable of encapsulating nucleic acids are able to self-assemble in thermal hot spring water (Milshteyn et al., 2018). Selection pressure on these protocells over long periods of time may have eventually led to the emergence of life on Earth.

The other prevailing theory for the origin of life on Earth is that it occurred in deep sea hydrothermal vents (Martin et al., 2006). Hydrothermal vents are found along mid-ocean ridges (Ballard et al., 1981). Magma rises from below the seafloor, heating seawater to high temperatures (hundreds of degrees Celsius). The combination of heat, seawater, organic compounds, and minerals is the basis for a myriad of chemical reactions and products (Holm et al., 2001). Instead of focusing on spontaneous vesicle formation and selection pressure, the hydrothermal vent theory posits a series of mineral-catalyzed reactions occurring at high temperature/pressure that lead to the synthesis of increasingly complex and prebiotically-relevant chemicals, ultimately giving rise to life. Chapter 2 of this work probes prebiotic chemistry using laboratory analogs of hydrothermal vents.

1.2 From deep sea hydrothermal vent to benchtop chemical garden

Some of the most essential characteristics of a hydrothermal vent can be readily reproduced in laboratory settings via simplified "chemical garden" analogs. A chemical garden is a plantlike hollow structure that forms when a hydrated metal salt is introduced into a solution containing another reactive ion (Barge, Doloboff, et al., 2012). Fossils of naturally-occurring chemical gardens that grew around springs have been discovered (e.g., Boyce et al., 1983), where these structures occurred upon the interaction of hydrothermal fluid and the ocean.

Chemical gardens spontaneously form due to disequilibria (both chemical and pH) between the two reactants (Barge, Cardoso, et al., 2015). The redox, osmotic, and pH gradients of hydrothermal vents have been proposed as the energy sources leading to the origin of life (Russell, Hall, and Turner, 1989; Russell and Hall, 1997).

However, in Chapter 2 of this work, the physical structure, osmotic gradient, and pH gradient of the chemical garden structures are not maintained due to experimental limitations. The work instead focuses on the compositional potential of chemical gardens to catalyze prebiotically-relevant reactions. While chemical gardens can be produced with a variety of metal salts, chemical gardens used in origins-of-life experiments are generally formed with Fe^{2+}/Fe^{3+}. The early Earth ocean was rich in iron, and the ocean was thought to support the growth of both iron silicates and iron oxyhydroxides (Rasmussen et al., 2015). Mixing ferrous iron and alpha keto acids (simple molecules that can be formed abiotically) yielded nine of the eleven Krebs cycle intermediates, further highlighting the relevance of iron to prebiotic chemistry (Muchowska et al., 2019).

While much is still unknown about the exact properties of early Earth vents, some work has been done to compare the compositional properties of synthetic (using sodium silicate solution) versus naturally-grown (using alkaline, silica-rich water from a spring) chemical gardens. Both types of garden have external amorphous silica layers and inner iron oxyhydroxides and iron hydroxides (Kotopoulou et al., 2021). Goethite (Fe^{3+} iron oxide-hydroxide mineral) and magnetite (Fe^{2+}/Fe^{3+} iron oxide mineral) were observed in both cases.

The work detailed in this thesis focuses on the potential role of chemical garden composition in prebiotic chemistry. Chemical gardens are reacted with the two simplest alpha keto acids (glyoxylic acid and pyruvic acid) to determine whether prebiotically-relevant molecules can be synthesized. Alpha keto acids can be abiotically produced (Marín-Yaseli et al., 2016), and have also demonstrated extensive reactivity and potential to form biologically-relevant products in conditions approximating early Earth (Muchowska et al., 2019; Stubbs et al., 2020; Barge, Flores, et al., 2019).

Previous work with chemical gardens and alpha keto acids had indicated reactivity, but the reactivity was able to be attributed to the silica solution and not necessarily to the chemical garden itself (Weber et al., 2021). The work presented here is novel in that it considers a mixture of isolated chemical gardens and alpha keto acids, and whether prebiotically-relevant chemistry can occur even in the absence of the external silica solution.

1.3 The search for life beyond Earth: ocean worlds of the Solar System

Large amounts of work have been dedicated toward furthering our understanding of how life originated on Earth, a question that remains unanswered. Science's quest to understand the origin of life on Earth is paired with an outward focus on the rest of the Solar System, an accessible microcosm within our galaxy and universe. The generalization of the study of life and its potential for originating, evolving, and thriving in locations beyond Earth presents a unique challenge when we have so much to learn still about life on our own planet. Our Solar System has eight planets and numerous other bodies: could life have existed elsewhere in the past, or be unobtrusively thriving somewhere beyond Earth at this very moment, or be waiting for one more future event that will lead to its origin?

When considering the broader notion of life in the universe, it is worth remembering: we have a sample size of one. All of our understanding of life comes from that found on Earth. From unicellular bacteria to blue whales, plankton to redwood trees, all life on Earth is carbon-based and water-dependent. While theories for alternative life forms have been proposed (e.g., inverted "azotosomes" that would thrive in a hydrophobic solvent (Stevenson et al., 2015)), much of the effort on searching for life beyond Earth comes from the lens of Earth life: namely, the search for water, chemistry, and energy.

Although Earth is the only body in our Solar System with liquid water found on its *surface*, a suite of "ocean worlds" offers an alternative for liquid water present in the Solar System. Many of our putative Solar System ocean worlds (Fig. 1.1) are moons of the outer planets: bodies with icy surfaces, subsurface water oceans (as predicted by gravity and magnetic field measurements), and rocky interiors (e.g., Fig. 1.2). The juxtaposition of rocky layer to subsurface water is a potential interface for life to thrive, exploiting gradients along the rock-water interface.

For the purposes of astrobiology, however, not all ocean worlds have equal promise. For example, Jupiter's large moon Callisto (although bigger than many of the other Solar System ocean worlds) has a heavily cratered surface that is indicative of a lack of current geological and tectonic activity (Cassen et al., 1980).

Conversely, Europa (a Jovian moon) and Enceladus and Titan (moons of Saturn) have young, relatively uncratered, and geologically active surfaces, making these prime candidates for astrobiological exploration. Europa's young surface is filled with a variety of interesting features, including hydrated salts, dark "chaos terrain," ridged plains, and a relative paucity of impact craters relative to its ocean world



Figure 1.1: A selection of the ocean worlds in the Solar System; not to scale. Image credit: Woods Hole Oceanographic Institute

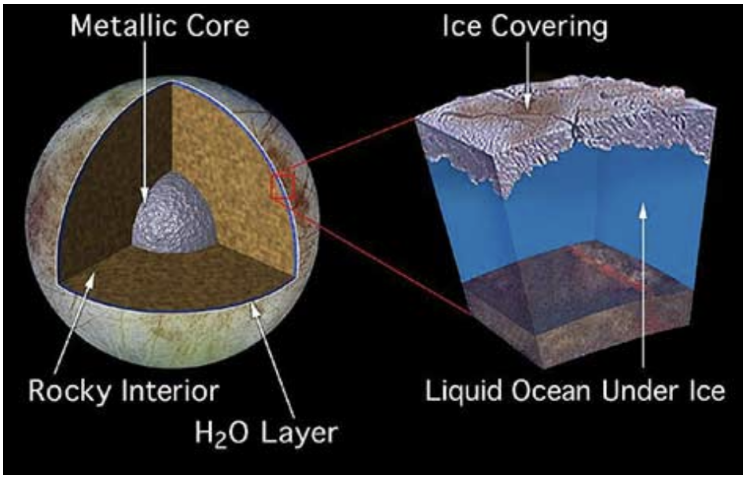


Figure 1.2: A cross section of Jupiter's moon Europa, displaying the rock-water interface posited to exist below the surface ice layer. Image credit: NASA/JPL

neighbors Ganymede and Callisto (Chyba et al., 2002). The brilliantly reflective Saturnian moon Enceladus captivated scientists with *Cassini*'s discovery of a large plume, spewing material from Enceladus' interior ocean out into space (Hansen et al., 2006). Chapter 2 of this work also considers the possibility of prebiotic chemistry occurring in Enceladus-like conditions.

While Europa and Enceladus present fascinating possibilities for past, present, or future life in our Solar System, the most striking and complex ocean world in the outer Solar System is Saturn's moon Titan. Titan's rich astrobiological potential derives from its hazy, organically rich atmosphere, its dynamic and young surface, its surface-atmosphere exchange, and the predicted presence of a subsurface water ocean. Searching for life in its subsurface water ocean is not a currently attainable feat, but many landmark discoveries related to Titan have propelled our understanding of Titan as an astrobiological candidate to new heights. The major discoveries leading to Titan's classification as a prime Solar System astrobiological target and their relationships to the thesis work are detailed below.

1.4 Titan: Before the *Cassini-Huygens* mission

Titan was one of the earliest Solar System discoveries to be made with a telescope: it was first spotted by Dutch astronomer Christiaan Huygens in the 1650s (Huygens, 1659). The next advancement in Titan science was not for several centuries: in the 1940s, Kuiper gathered visible wavelength spectra of Titan (and several other smaller Solar System bodies) and deduced that Titan was the only one to have a substantial atmosphere (Kuiper, 1944).

The first near-infrared spectrum of Titan was captured a few decades later (Fink et al., 1979). The disk-integrated spectrum was dominated by methane absorption, with several narrow "methane windows" allowing first-ever glimpses to the lower atmospheric levels and surface of Titan. Around the same time, the first spacecraft image of Titan was captured. *Pioneer 11* was the first spacecraft to pass through the Saturnian system, capturing a first close-up glimpse of a frigid world shrouded in orange haze (Figure 1.3). Shortly after, *Voyager 1* and *Voyager 2* passed closer to Titan. *Voyager 1* captured data suggesting a nitrogen-dominated atmosphere with small amounts of hydrocarbons and a surface temperature of 94.0 K (Lindal et al., 1983), but understanding of Titan remained limited.

Two major developments in the last 30 years have set the stage for this work: the remarkable thirteen year (2004-2017) mission of the *Cassini* orbiter and attached *Huygens* atmospheric probe, and the declassification of adaptive optics and subsequent use on ground-based telescopes.

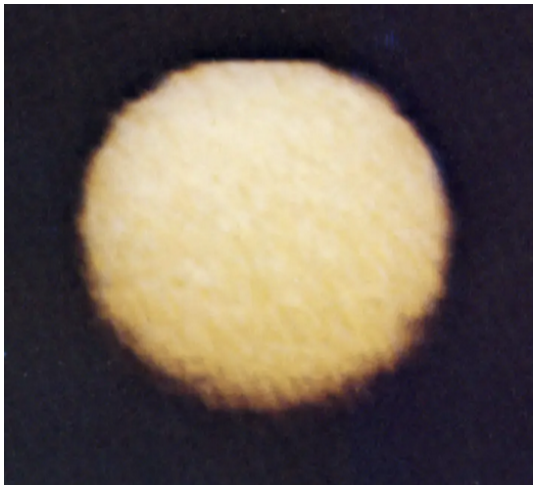


Figure 1.3: Titan as captured from 3.6 million kilometers away by *Pioneer 11* on September 3, 1979. Image credit: NASA.

1.5 The *Cassini-Huygens* mission

In 2004, the flagship NASA orbiter *Cassini* and attached ESA Titan atmospheric probe *Huygens* arrived at Saturn. *Cassini* made 126 flybys of Titan over its 13 year mission, using a suite of instruments to study Titan's atmosphere, surface, and interior. Some of the most revolutionary findings to come from the *Cassini-Huygens* mission that propelled Titan forward as an astrobiological target include:

- **Evidence for subsurface water ocean**: Prior to *Cassini*, Titan was theorized to have an ocean (e.g., Lunine, 1993), but no compelling evidence had been collected. Via gravity data collected during six Titan flybys by *Cassini*, scientists concluded that the magnitude of tidal deformations throughout Titan's orbit is consistent with the satellite having a global subsurface water ocean (Iess et al., 2012). Electric field measurements from the *Huygens* probe also support the presence of a global subsurface water ocean (Béghin et al., 2009). This finding is critical for the astrobiological potential of Titan, as any potential earthlike life would require liquid water. It is noteworthy that interior models of Titan predict a high-pressure ice layer at the bottom of Titan's surface, cutting off direct contact between Titan's ocean and its rocky core (Kalousová et al., 2020). This limits the potential for life to originate and thrive in Titan's ocean, as the ice layer would prevent nascent bacterial species from accessing and metabolizing molecules found in the core. However, modeling work has suggested that massively large impacts on Titan's surface could potentially send surface level organics down through Titan's

interior and into its subsurface ocean, which could lead to the existence of small biospheres (Affholder et al., 2025).

- **Mapping of Titan's surface, including discovery of surface hydrocarbon lakes**: *Cassini*'s instruments included the Synthetic Aperture Radar (SAR), the Imaging Science Subsystem (ISS) and the Visual and Infrared Mapping Spectrometer (VIMS)- all capable of peering through Titan's atmosphere and capturing data of Titan's surface. In 2006, radar data confirmed what had long been predicted: lakes of liquid hydrocarbons on Titan's surface (Stofan et al., 2007). Titan became the first (and to this day, only) known Solar System body besides Earth to have liquid present on its surface. Eventually, *Cassini* data of Titan's surface was combined to form a global geomorphologic map, revealing a strikingly latitudinally stratified world with polar lake regions, mid-latitude plains, and equatorial dunes (Lopes et al., 2020).

- **Seasonal variation, composition, and cloud patterns in Titan's atmosphere**: Thirteen years of flybys provided unique opportunities to study seasonal changes over nearly half of a Titan year, including the widespread changes observed during and after the 2009 equinox. The Composite Infrared Spectrometer (CIRS) studied temperature and trace organic species abundances across latitudes and longitudes (Coustenis et al., 2007). From 2009-2013, dedicated flybys with the CIRS instruments studied the atmospheric variation that accompanied equinox, noting global changes that included the brief appearance of two atmospheric circulation cells and the eventual reversal of the atmospheric circulation cell (Vinatier et al., 2015). CIRS was also used to study hazes and clouds present in Titan's atmosphere (Anderson and Samuelson, 2011). Chapter 3 builds on the remarkable findings of the CIRS instrument by conducting laboratory studies of propyne, a trace organic species in Titan's atmosphere that was monitored during *Cassini*'s mission.

- **Atmospheric measurements with high vertical resolution**: The *Huygens* descent probe is to date the only spacecraft to have landed on a body in the outer Solar System. With a slow descent over several hours, *Huygens*' suite of instruments conducted a number of experiments and measurements as it moved down through Titan's atmosphere at latitude 10.6°S (Lebreton et al., 2005). Key among these were altitude profiles and isotopic ratios of atmospheric species, chemical composition analyses for atmospheric particles that can serve as cloud condensation nuclei (Israël et al., 2005), temperature

and density profiles from 0-1500 km (Fulchignoni et al., 2005), zonal wind speeds below 150 km (Bird et al., 2005), and images of Titan's surface (Tomasko et al., 2005).

1.6 Propyne: building on the findings of *Cassini*

Titan's thick atmosphere is primarily composed of molecular nitrogen (97%) and methane (2%) (Hörst, 2017). While these species are not in themselves particularly reactive, photochemical ionization and dissociation leads to the formation of highly reactive fragments and ions, which readily recombine to form an array of complex organic species. As species recombine to form heavier and more complex molecules, they drift lower in the atmosphere, ultimately forming thick organic hazes and crusting Titan's surface (Fig. 1.4, Nixon, 2024).

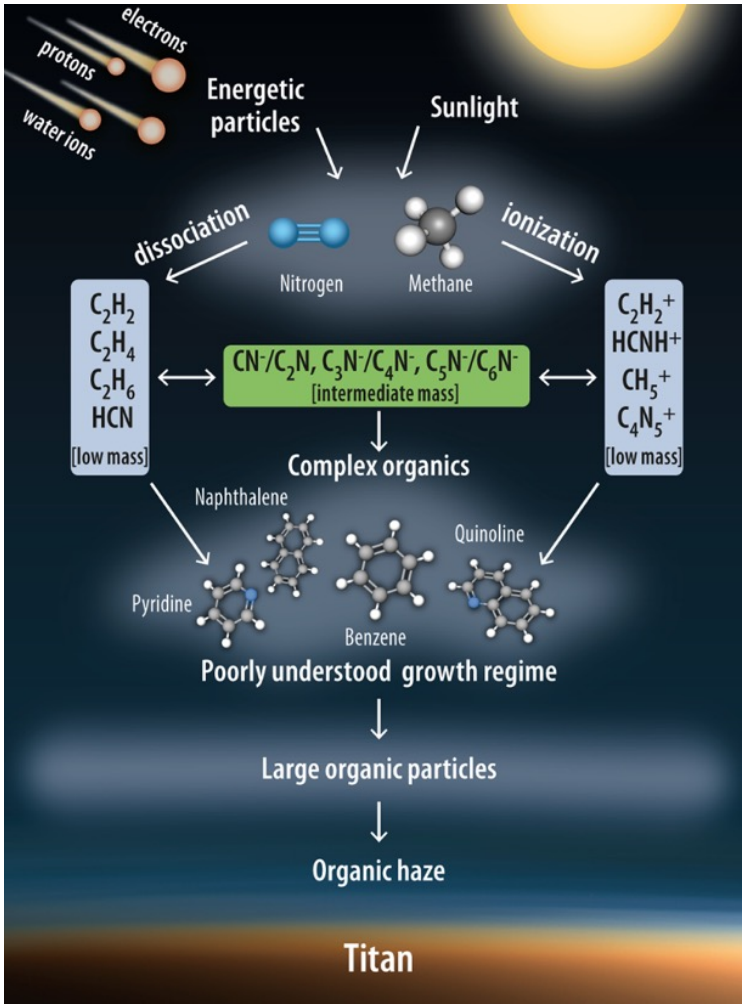


Figure 1.4: Photolysis of molecular nitrogen and methane leads to recombination and formation of complex organic molecules. Figure from Nixon, 2024.

To date, 22 photochemically produced species have been discovered in Titan's atmosphere through a combination of space-based telescopes, ground-based telescopes, and *Cassini* data (Hörst, 2017; Nixon, 2024). Twice in a Titan year (29.5 Earth years) – at autumnal equinox and at vernal equinox – Titan's atmosphere is predicted to undergo a circulation reversal, with photochemically produced organics being enriched at the winter pole (Teanby et al., 2012). Many photochemically-produced organics also settle on Titan's surface (Anderson, Samuelson, and Nna-Mvondo, 2018).

As discussed in the previous section, the CIRS instrument has contributed immensely to our study and understanding of Titan's atmospheric organics. Laboratory reconstructions of stratospheric clouds detected by CIRS have revealed partial information about their compositions, but laboratory and spacecraft spectra still show significant discrepancies from each other, and additional laboratory work is necessary.

One organic species of interest is propyne (C_3H_4) which was detected in vapor phase by the *Voyager 1* spacecraft (Maguire et al., 1981). Solid propyne has not yet been detected at Titan, but if it is present then it is a potential contender for mixed-species clouds on Titan. Before propyne can be explored in cloud-analog mixtures, the molecule itself needs to be better understood. The work detailed here dives into pure, solid propyne, characterizing it with infrared spectroscopy, Raman spectroscopy, and X-ray diffraction. It includes the first published Raman spectra of amorphous and crystalline propyne ice.

1.7 Ground-based observations of Titan with adaptive optics

While having a spacecraft operate in situ in the Saturnian system undeniably yields the best data for Titan, practical and financial reasons limit the time spans for which in situ data can be collected. The other major recent advancement to Titan science has been the addition of adaptive optics (AO) systems to large ground-based telescopes around the world (Roddier, 1999). AO corrects for turbulence created by Earth's atmosphere and allows the observation of astronomical objects with vastly improved resolution. With AO-equipped telescopes, images and spectra of Titan have greatly improved. Some of adaptive optics' most relevant contributions to Titan science and its astrobiological relevance are outlined below:

- **Large cloud activity:** Titan is the only planetary body in the Solar System besides Earth that is known to have a precipitation cycle, including clouds, lakes, and rain. Titan has transient clouds throughout its seasons, but occasionally

large, widespread storm clouds are observed. The spatial resolution power of AO-equipped telescopes allows direct imaging of these cloud outburst events from Earth (e.g., Schaller et al., 2006) and a window into meteorology patterns on Titan.

- **Latitudinal seasonal haze evolution:** The photochemically-produced organic haze present in Titan's atmosphere is one of its most compelling lines of evidence for astrobiology. Using spectroscopy, AO, and radiative transfer models (mapping the passage of light through an atmosphere), organic haze behaviors can be mapped across seasons and latitudes (e.g., Ádámkovics et al., 2017; Nichols-Fleming et al., 2021).

- **Zonal wind profiles from spatially-resolved stellar occultations:** Stellar occultations by planetary bodies with dense atmospheres afford a unique chance to characterize zonal (east-west) winds. Although this technique has been leveraged by non-AO telescopes as well (e.g., Hubbard et al., 1993; Sicardy et al., 2006), the incorporation of AO allows study of stellar occultations of dimmer stars and produces spatially resolved, directly imaged data of refracted starlight around Titan's limb (e.g., Bouchez, 2004). As the refracted light patterns are highly sensitive to non-spherical distortions (caused by zonal winds in Titan's middle atmosphere), stellar occultation data provides insight into middle atmosphere zonal wind patterns at a given time in Titan's year. Middle atmosphere zonal winds affect the transport patterns of organic hazes in Titan's atmosphere before their eventual deposition on Titan's surface. Chapter 4 of this work explores one such instance of spatially-resolved data of a Titan stellar occultation captured with an AO-equipped telescope.

1.8 Stellar occultations: zonal wind snapshots

A stellar occultation is serendipitious. The alignment of a Solar System body, a suitably bright star, and a powerful enough telescope — on a clear night and with no instrument failures — is no small feat. Adding to the difficulty, the variation between sidereal and non-sidereal rates means that most occultations last on the order of minutes or seconds, giving a very small window to collect critical data on the event.

When the occulting body has an atmosphere, the light from the occulted star is refracted and focused by the atmosphere, creating a phenomenon known as a "caustic" (concentration of light rays) at the center of the event. The fast motion of

light around the limb of a planetary body during the central time of an occultation is known as the “central flash", and the distribution of refracted light is highly sensitive to zonal winds.

On Titan, occultations probe an altitude of roughly 180-500 km, corresponding to Titan’s middle atmosphere. The middle atmosphere serves as a critical bridge between the upper atmosphere and the lower atmosphere/surface. In the upper atmosphere, molecular nitrogen and methane are being dissociated and ionized, generating energetic fragments that readily recombine to form Titan’s vast inventory of organic species (see Fig. 1.4). The lower atmosphere is filled with dense haze, with organic species depositing on the surface and interacting with its topology. Characterizing dynamics in the middle atmosphere is critical for understanding the passage and distribution of photochemically produced organics from upper to lower atmosphere.

An occultation probes a moment in time within the long Titan year. Titan’s middle atmosphere zonal winds are generally thought to be higher in the hemisphere experiencing winter, with an atmospheric circulation cell shift occurring around autumnal and vernal equinox (Lombardo et al., 2023). The work presented here offers a zonal wind analysis for a moment in the Titan year (late northern summer)- the data represent the first stellar occultation to be captured during Titan’s late northern summer and only the second successful collection of spatially-resolved Titan occultation data. These data present a window into middle atmosphere dynamics during late northern summer and the opportunity to contextualize them within the broader data and model landscape of Titan’s yearlong dynamics.

1.9 Thesis overview

This thesis broadly addresses astrobiologically relevant bodies within our Solar System. It begins with an inward lens, considering how life originated on our own planet, and extrapolating that to the astrobiologically relevant Saturnian moon Enceladus. I study laboratory analogs of hydrothermal vents and probe potential chemistry that could have given rise to the origin of life, conducting reactions with chemical gardens and simple organics in different temperatures, solutions, and conditions. The thesis then moves outward in the Saturnian system to Saturn’s largest moon Titan, presenting a laboratory characterization and an observational astronomy study of its atmosphere. I conduct an in-depth characterization of propyne, a photochemically-produced organic species in Titan’s atmosphere that may be a

component of its stratospheric ice clouds. I study the zonal wind profile of Titan's middle atmosphere during late northern summer, which directly relates to the vertical transport of organics through the atmosphere. The chapters are detailed below:

- **Chemical gardens as analogs for prebiotic chemistry on ocean worlds**. Chemical gardens are spontaneously formed, inorganic structures that mimic the properties of hydrothermal vents. This work uses nuclear magnetic resonance (NMR) spectroscopy, visible/near-infrared (VNIR) spectroscopy, Raman spectroscopy, and X-ray diffraction (XRD) to characterize the behavior of simple alpha keto acids (precursors to amino acids) in the presence of chemical gardens. In conditions approximating the early Earth, reactions containing alpha keto acids and chemical gardens generated prebiotically-relevant molecules. As the reactants are present in geological settings, it is possible that similar processes led to the first synthesis of critical biological molecules on Earth. Enceladuslike conditions are also tested. This work presents the first analysis of alpha keto acids reacted with chemical gardens in the absence of the reactive silicate solution. It is a closer look at the effect of chemical garden composition on reactions containing alpha keto acids.

- **Propyne: Determination of Physical Properties and Unit Cell Parameters under Titan-Relevant Conditions**. Propyne is among the inventory of photochemically-produced organics present in Titan's atmosphere and a potential component of Titan's stratospheric clouds (Anderson, Samuelson, and Nna-Mvondo, 2018). This work is a first step toward understanding the behavior of propyne by itself in Titan's atmosphere, in order to ultimately characterize it in laboratory analogs of clouds. This work is a bulk structural characterization via infrared spectroscopy, Raman spectroscopy, and X-ray diffraction to study the properties and transitions of propyne ice over a range of Titan-relevant temperatures. It presents the Raman spectra of amorphous and crystalline propyne ice for the first time.

- **Zonal winds in Titan's middle atmosphere from a stellar occultation observed with Keck adaptive optics**. Titan exhibits dynamic seasonal variation over the course of its 29.5 Earth year orbit. One of the regions of interest that remains challenging to probe with existing instrumentation is Titan's middle atmosphere (~100-500 km altitude). This work presents spatially resolved stellar occultation data where refracted light from an occulted star is visible

along Titan's limb. Characterization via a forward model and comparison to data from the Atacama Large Millimeter Array (ALMA) radio telescope are conducted. Occultation data support the findings of General Circulation Models (GCMs) and ALMA Doppler shift data that winds are higher at southern latitudes than at northern latitudes during northern summer. These data are the first stellar occultation data to be captured during Titan's late northern summer, offering insight into this key period preceding the widespread equinoctial change.

References

Ádámkovics, Máté and Imke de Pater (July 2017). "Observations of the global haze redistribution on Titan from 2006 to 2015 with OSIRIS at Keck". In: *Icarus* 290. ADS Bibcode: 2017Icar..290..134A, pp. 134–149. ISSN: 0019-1035. DOI: 10.1016/j.icarus.2017.02.015. URL: https://ui.adsabs.harvard.edu/abs/2017Icar..290..134A.

Affholder, Antonin et al. (Apr. 2025). "The Viability of Glycine Fermentation in Titan's Subsurface Ocean". In: *The Planetary Science Journal* 6.4. Publisher: IOP Publishing, p. 86. ISSN: 2632-3338. DOI: 10.3847/PSJ/adbc66. URL: https://iopscience.iop.org/article/10.3847/PSJ/adbc66/meta (visited on 08/31/2025).

Anderson, Carrie M., R. E. Samuelson, and D. Nna-Mvondo (Nov. 2018). "Organic Ices in Titan's Stratosphere". In: *Space Science Reviews* 214.8, p. 125. ISSN: 1572-9672. DOI: 10.1007/s11214-018-0559-5. URL: https://doi.org/10.1007/s11214-018-0559-5.

Anderson, Carrie M. and Robert E. Samuelson (Apr. 2011). "Titan's aerosol and stratospheric ice opacities between 18 and 500 μm: Vertical and spectral characteristics from Cassini CIRS". In: *Icarus* 212.2, pp. 762–778. ISSN: 0019-1035. DOI: 10.1016/j.icarus.2011.01.024. URL: https://www.sciencedirect.com/science/article/pii/S0019103511000352.

Ballard, Robert D. et al. (Sept. 1981). "East Pacific rise at 21°N: The volcanic, tectonic, and hydrothermal processes of the central axis". In: *Earth and Planetary Science Letters* 55.1, pp. 1–10. ISSN: 0012-821X. DOI: 10.1016/0012-821X(81)90081-9. URL: https://www.sciencedirect.com/science/article/pii/0012821X81900819.

Barge, Laura M., Silvana S. S. Cardoso, et al. (Aug. 2015). "From Chemical Gardens to Chemobrionics". In: *Chemical Reviews* 115.16. Publisher: American Chemical Society, pp. 8652–8703. ISSN: 0009-2665. DOI: 10.1021/acs.chemrev.5b00014. URL: https://doi.org/10.1021/acs.chemrev.5b00014.

Barge, Laura M., Ivria J. Doloboff, et al. (Feb. 2012). "Characterization of Iron – Phosphate – Silicate Chemical Garden Structures". In: *Langmuir* 28.8. Publisher:

American Chemical Society, pp. 3714–3721. ISSN: 0743-7463. DOI: 10.1021/la203727g. URL: https://doi.org/10.1021/la203727g.

Barge, Laura M., Erika Flores, et al. (Mar. 2019). "Redox and pH gradients drive amino acid synthesis in iron oxyhydroxide mineral systems". In: *Proceedings of the National Academy of Sciences of the United States of America* 116.11, pp. 4828–4833. ISSN: 1091-6490. DOI: 10.1073/pnas.1812098116.

Béghin, Christian et al. (Dec. 2009). "New insights on Titan's plasma-driven Schumann resonance inferred from Huygens and Cassini data". In: *Planetary and Space Science* 57.14, pp. 1872–1888. ISSN: 0032-0633. DOI: 10.1016/j.pss.2009.04.006. URL: https://www.sciencedirect.com/science/article/pii/S0032063309001020.

Bird, Michael K. et al. (Dec. 2005). "The vertical profile of winds on Titan". In: *Nature* 438.7069. Publisher: Nature Publishing Group, pp. 800–802. ISSN: 1476-4687. DOI: 10.1038/nature04060. URL: https://www.nature.com/articles/nature04060.

Bouchez, Antonin Henri (2004). "Seasonal trends in Titan's atmosphere: Haze, wind, and clouds". ISBN: 9780496723560 Publication Title: ProQuest Dissertations and Theses. Ph.D. United States – California: California Institute of Technology. URL: https://www.proquest.com/docview/305203060/abstract/7887C087627C4A4EPQ/1.

Boyce, A. J., M. L. Coleman, and M. J. Russell (Dec. 1983). "Formation of fossil hydrothermal chimneys and mounds from Silvermines, Ireland". In: *Nature* 306.5943, pp. 545–550. ISSN: 0028-0836, 1476-4687. DOI: 10.1038/306545a0. URL: https://www.nature.com/articles/306545a0 (visited on 08/30/2025).

Cassen, Patrick, Stanton J. Peale, and Ray T. Reynolds (Feb. 1980). "On the comparative evolution of Ganymede and Callisto". In: *Icarus* 41.2, pp. 232–239. ISSN: 0019-1035. DOI: 10.1016/0019-1035(80)90006-8. URL: https://www.sciencedirect.com/science/article/pii/0019103580900068.

Chyba, Christopher F. and Cynthia B. Phillips (Feb. 2002). "Europa as an Abode of Life". In: *Origins of life and evolution of the biosphere* 32.1, pp. 47–67. ISSN: 1573-0875. DOI: 10.1023/A:1013958519734. URL: https://doi.org/10.1023/A:1013958519734.

Coustenis, Athena et al. (July 2007). "The composition of Titan's stratosphere from Cassini/CIRS mid-infrared spectra". In: *Icarus* 189.1, pp. 35–62. ISSN: 0019-1035. DOI: 10.1016/j.icarus.2006.12.022. URL: https://www.sciencedirect.com/science/article/pii/S0019103507000279.

Damer, Bruce and David Deamer (Apr. 2020). "The Hot Spring Hypothesis for an Origin of Life". In: *Astrobiology* 20.4. Publisher: Mary Ann Liebert, Inc., publishers, pp. 429–452. ISSN: 1531-1074. DOI: 10.1089/ast.2019.2045. URL: https://www.liebertpub.com/doi/10.1089/ast.2019.2045.

Ehrenfreund, Pascale and Mark A. Sephton (2006). "Carbon molecules in space: from astrochemistry to astrobiology". In: *Faraday Discussions* 133.0. Publisher: Royal Society of Chemistry, pp. 277–288. DOI: 10.1039/B517676J. URL: https://pubs.rsc.org/en/content/articlelanding/2006/fd/b517676j.

Fink, U. and H.P. Larson (Nov. 1979). "The infrared spectra of Uranus, Neptune, and Titan from 0.8 to 2.5 microns". In: *Astrophysical Journal* 233.3, pp. 1021–1040. URL: https://adsabs.harvard.edu/full/1979ApJ...233.1021F7.

Fulchignoni, Marcello et al. (Dec. 2005). "In situ measurements of the physical characteristics of Titan's environment". In: *Nature* 438.7069. Publisher: Nature Publishing Group, pp. 785–791. ISSN: 1476-4687. DOI: 10.1038/nature04314. URL: https://www.nature.com/articles/nature04314.

Hansen, Candice J. et al. (Mar. 2006). "Enceladus' Water Vapor Plume". In: *Science* 311.5766. Publisher: American Association for the Advancement of Science, pp. 1422–1425. DOI: 10.1126/science.1121254. URL: https://www.science.org/doi/10.1126/science.1121254.

Holm, Nils G. and Jean Luc Charlou (Aug. 2001). "Initial indications of abiotic formation of hydrocarbons in the Rainbow ultramafic hydrothermal system, Mid-Atlantic Ridge". In: *Earth and Planetary Science Letters* 191.1, pp. 1–8. ISSN: 0012-821X. DOI: 10.1016/S0012-821X(01)00397-1. URL: https://www.sciencedirect.com/science/article/pii/S0012821X01003971.

Hörst, Sarah M. (2017). "Titan's atmosphere and climate". In: *Journal of Geophysical Research: Planets* 122.3, pp. 432–482. ISSN: 2169-9100. DOI: 10.1002/2016JE005240. URL: https://onlinelibrary.wiley.com/doi/abs/10.1002/2016JE005240.

Hubbard, William B. et al. (Mar. 1993). "The occultation of 28 SGR by Titan." In: *Astronomy and Astrophysics* 269. ADS Bibcode: 1993A&A...269..541H, pp. 541–563. ISSN: 0004-6361. URL: https://ui.adsabs.harvard.edu/abs/1993A&A...269..541H.

Huygens, Christiaan (1659). *Systema Saturnium*. Hagae-Comitis. URL: https://www.loc.gov/item/2021666744/.

Iess, Luciano et al. (July 2012). "The Tides of Titan". In: *Science* 337.6093. Publisher: American Association for the Advancement of Science, pp. 457–459. DOI: 10.1126/science.1219631. URL: https://www.science.org/doi/10.1126/science.1219631.

Israël, G. et al. (Dec. 2005). "Complex organic matter in Titan's atmospheric aerosols from in situ pyrolysis and analysis". In: *Nature* 438.7069. Publisher: Nature Publishing Group, pp. 796–799. ISSN: 1476-4687. DOI: 10.1038/nature04349. URL: https://www.nature.com/articles/nature04349.

Kalousová, Klára and Christophe Sotin (Sept. 2020). "Dynamics of Titan's high-pressure ice layer". In: *Earth and Planetary Science Letters* 545, p. 116416. ISSN: 0012-821X. DOI: 10.1016/j.epsl.2020.116416. URL: https://www.sciencedirect.com/science/article/pii/S0012821X20303605 (visited on 08/31/2025).

Kotopoulou, Electra et al. (Jan. 2021). "Nanoscale Anatomy of Iron-Silica Self-Organized Membranes: Implications for Prebiotic Chemistry". In: *Angewandte Chemie (International Ed. in English)* 60.3, pp. 1396–1402. ISSN: 1433-7851. DOI: 10.1002/anie.202012059. URL: https://www.ncbi.nlm.nih.gov/pmc/articles/PMC7839773/.

Kuiper, Gerard (1944). "Titan: a Satellite with an Atmosphere". In: *Astrophysical Journal* 100, pp. 378–383. URL: https://articles.adsabs.harvard.edu//full/1944ApJ...100..378K/0000378.000.html.

Lebreton, Jean-Pierre et al. (Dec. 2005). "An overview of the descent and landing of the Huygens probe on Titan". In: *Nature* 438.7069. Publisher: Nature Publishing Group, pp. 758–764. ISSN: 1476-4687. DOI: 10.1038/nature04347. URL: https://www.nature.com/articles/nature04347.

Lindal, Gunnar F. et al. (Feb. 1983). "The atmosphere of Titan: An analysis of the Voyager 1 radio occultation measurements". In: *Icarus* 53.2, pp. 348–363. ISSN: 0019-1035. DOI: 10.1016/0019-1035(83)90155-0. URL: https://www.sciencedirect.com/science/article/pii/0019103583901550.

Lombardo, Nicholas A. and Juan M. Lora (Jan. 2023). "Influence of observed seasonally varying composition on Titan's stratospheric circulation". In: *Icarus* 390. ADS Bibcode: 2023Icar..39015291L, p. 115291. ISSN: 0019-1035. DOI: 10.1016/j.icarus.2022.115291. URL: https://ui.adsabs.harvard.edu/abs/2023Icar..39015291L.

Longo, Alex and Bruce Damer (Apr. 2020). "Factoring Origin of Life Hypotheses into the Search for Life in the Solar System and Beyond". In: *Life* 10.5, p. 52. ISSN: 2075-1729. DOI: 10.3390/life10050052. URL: https://www.ncbi.nlm.nih.gov/pmc/articles/PMC7281141/.

Lopes, Rosaly M. C. et al. (Mar. 2020). "A Global Geomorphologic Map of Saturn's Moon Titan". In: *Nature Astronomy* 4, pp. 228–233. ISSN: 2397-3366. DOI: 10.1038/s41550-019-0917-6. URL: https://www.ncbi.nlm.nih.gov/pmc/articles/PMC7271969/.

Lunine, Jonathan I. (1993). "Does Titan have an ocean? A review of current understanding of Titan's surface". In: *Reviews of Geophysics* 31.2. _eprint: https://onlinelibrary.wiley.com/doi/p pp. 133–149. ISSN: 1944-9208. DOI: 10.1029/92RG02794. URL: https://onlinelibrary.wiley.com/doi/abs/10.1029/92RG02794.

Maguire, William C. et al. (Aug. 1981). "C3H8 and C3H4 in Titan's atmosphere". In: *Nature* 292.5825. Number: 5825 Publisher: Nature Publishing Group, pp. 683–

686. ISSN: 1476-4687. DOI: 10.1038/292683a0. URL: https://www.nature.com/articles/292683a0.

Marín-Yaseli, Margarita R. et al. (2016). "The Role of Aqueous Aerosols in the "Glyoxylate Scenario": An Experimental Approach". In: *Chemistry – A European Journal* 22.36, pp. 12785–12799. ISSN: 1521-3765. DOI: 10.1002/chem.201602195. URL: https://onlinelibrary.wiley.com/doi/abs/10.1002/chem.201602195.

Martin, William and Michael J. Russell (Nov. 2006). "On the origin of biochemistry at an alkaline hydrothermal vent". In: *Philosophical Transactions of the Royal Society B: Biological Sciences* 362.1486. Publisher: Royal Society, pp. 1887–1926. DOI: 10.1098/rstb.2006.1881. URL: https://royalsocietypublishing.org/doi/full/10.1098/rstb.2006.1881.

McKay, Christopher P. (Sept. 2014). "Requirements and limits for life in the context of exoplanets". In: *Proceedings of the National Academy of Sciences* 111.35. Publisher: Proceedings of the National Academy of Sciences, pp. 12628–12633. DOI: 10.1073/pnas.1304212111. URL: https://www.pnas.org/doi/abs/10.1073/pnas.1304212111.

Milshteyn, Daniel et al. (June 2018). "Amphiphilic Compounds Assemble into Membranous Vesicles in Hydrothermal Hot Spring Water but Not in Seawater". In: *Life* 8.2. Number: 2 Publisher: Multidisciplinary Digital Publishing Institute, p. 11. ISSN: 2075-1729. DOI: 10.3390/life8020011. URL: https://www.mdpi.com/2075-1729/8/2/11.

Muchowska, Kamila B., Sreejith J. Varma, and Joseph Moran (May 2019). "Synthesis and breakdown of universal metabolic precursors promoted by iron". In: *Nature* 569.7754. Number: 7754 Publisher: Nature Publishing Group, pp. 104–107. ISSN: 1476-4687. DOI: 10.1038/s41586-019-1151-1. URL: https://www.nature.com/articles/s41586-019-1151-1.

Nichols-Fleming, Fiona et al. (Sept. 2021). "Tracking Short-term Variations in the Haze Distribution of Titan's Atmosphere with SINFONI VLT". In: *The Planetary Science Journal* 2.5. Publisher: IOP Publishing, p. 180. ISSN: 2632-3338. DOI: 10.3847/PSJ/abffd7. URL: https://iopscience.iop.org/article/10.3847/PSJ/abffd7/meta.

Nixon, Conor A. (Mar. 2024). "The Composition and Chemistry of Titan's Atmosphere". In: *ACS Earth and Space Chemistry* 8.3. Publisher: American Chemical Society, pp. 406–456. DOI: 10.1021/acsearthspacechem.2c00041. URL: https://doi.org/10.1021/acsearthspacechem.2c00041.

Noffke, Nora et al. (Dec. 2013). "Microbially Induced Sedimentary Structures Recording an Ancient Ecosystem in the ca. 3.48 Billion-Year-Old Dresser Formation, Pilbara, Western Australia". In: *Astrobiology* 13.12, pp. 1103–1124. ISSN: 1531-1074. DOI: 10.1089/ast.2013.1030. URL: https://www.ncbi.nlm.nih.gov/pmc/articles/PMC3870916/.

Rasmussen, Birger et al. (Apr. 2015). "Precipitation of iron silicate nanoparticles in early Precambrian oceans marks Earth's first iron age". In: *Geology* 43.4, pp. 303–306. ISSN: 0091-7613. DOI: 10.1130/G36309.1. URL: https://doi.org/10.1130/G36309.1 (visited on 08/30/2025).

Roddier, François (June 1999). *Adaptive Optics in Astronomy*. Google-Books-ID: 4n5tBN21LRsC. Cambridge University Press. ISBN: 978-0-521-55375-9.

Russell, Michael J. and A. J. Hall (May 1997). "The emergence of life from iron monosulphide bubbles at a submarine hydrothermal redox and pH front". In: *Journal of the Geological Society* 154.3, pp. 377–402. ISSN: 0016-7649, 2041-479X. DOI: 10.1144/gsjgs.154.3.0377. URL: https://www.lyellcollection.org/doi/10.1144/gsjgs.154.3.0377.

Russell, Michael J., Allan J. Hall, and Dugald Turner (1989). "In vitro growth of iron sulphide chimneys: possible culture chambers for origin-of-life experiments". In: *Terra Nova* 1.3, pp. 238–241. ISSN: 1365-3121. DOI: 10.1111/j.1365-3121.1989.tb00364.x. URL: https://onlinelibrary.wiley.com/doi/abs/10.1111/j.1365-3121.1989.tb00364.x.

Schaller, Emily L. et al. (May 2006). "A large cloud outburst at Titan's south pole". In: *Icarus* 182.1, pp. 224–229. ISSN: 0019-1035. DOI: 10.1016/j.icarus.2005.12.021. URL: https://www.sciencedirect.com/science/article/pii/S0019103505005038.

Sicardy, Bruno et al. (2006). "The two Titan stellar occultations of 14 November 2003". In: *Journal of Geophysical Research: Planets* 111.E11. ISSN: 2156-2202. DOI: 10.1029/2005JE002624. URL: https://onlinelibrary.wiley.com/doi/abs/10.1029/2005JE002624.

Stevenson, James, Jonathan Lunine, and Paulette Clancy (Feb. 2015). "Membrane alternatives in worlds without oxygen: Creation of an azotosome". In: *Science Advances* 1.1, e1400067. ISSN: 2375-2548. DOI: 10.1126/sciadv.1400067.

Stofan, Ellen R. et al. (Jan. 2007). "The lakes of Titan". In: *Nature* 445.7123. Publisher: Nature Publishing Group, pp. 61–64. ISSN: 1476-4687. DOI: 10.1038/nature05438. URL: https://www.nature.com/articles/nature05438.

Stubbs, R. Trent et al. (Nov. 2020). "A plausible metal-free ancestral analogue of the Krebs cycle composed entirely of α-ketoacids." In: *Nature chemistry* 12.11, pp. 1016–1022. ISSN: 1755-4330. DOI: 10.1038/s41557-020-00560-7. URL: https://www.ncbi.nlm.nih.gov/pmc/articles/PMC8570912/.

Teanby, Nicholas A. et al. (Nov. 2012). "Active upper-atmosphere chemistry and dynamics from polar circulation reversal on Titan". In: *Nature* 491.7426. Publisher: Nature Publishing Group, pp. 732–735. ISSN: 1476-4687. DOI: 10.1038/nature11611. URL: https://www.nature.com/articles/nature11611.

Tomasko, Martin G. et al. (Dec. 2005). "Rain, winds and haze during the Huygens probe's descent to Titan's surface". In: *Nature* 438.7069. Publisher: Nature Publishing Group, pp. 765–778. ISSN: 1476-4687. DOI: 10.1038/nature04126. URL: https://www.nature.com/articles/nature04126.

Vinatier, Sandrine et al. (Apr. 2015). "Seasonal variations in Titan's middle atmosphere during the northern spring derived from Cassini/CIRS observations". In: *Icarus* 250, pp. 95–115. ISSN: 0019-1035. DOI: 10.1016/j.icarus.2014.11.019. URL: https://www.sciencedirect.com/science/article/pii/S0019103514006472.

Weber, Jessica M. and Laura M. Barge (2021). "Iron-Silicate Chemical Garden Morphology and Silicate Reactivity with Alpha-Keto Acids". In: *ChemSystemsChem* 3.3, e2000058. ISSN: 2570-4206. DOI: 10.1002/syst.202000058. URL: https://onlinelibrary.wiley.com/doi/abs/10.1002/syst.202000058.

Chapter 2

CHEMICAL GARDENS AS ANALOGS FOR PREBIOTIC CHEMISTRY ON OCEAN WORLDS

Marlin, Theresa C., Jessica M. Weber, Rachel Y. Sheppard, Scott Perl, Derek Diener, Marc M. Baum, Laura M. Barge (Jan. 2025). "Chemical gardens as analogs for prebiotic chemistry on ocean worlds". English. In: *Chem* 11.1. Publisher: Elsevier. ISSN: 2451-9294, 2451-9308. DOI: 10.1016/j.chempr.2024.08.012. URL: https://www.cell.com/chem/abstract/S2451-9294(24)00427-3.

Abstract

Various studies have hypothesized that life on Earth may have originated near seafloor, mineral-rich hydrothermal vents. The use of laboratory analogs of these environments, such as chemical gardens, allows the creation of controlled, manipulable systems for studying potential prebiotic chemistry and origins-of-life scenarios on Earth and beyond. In this study, we tested reactions of prebiotically relevant organic anions, pyruvate and glyoxylate, in the presence of chemical gardens under a set of conditions relevant to the early Earth and the Saturnian moon Enceladus. Reactions were run for up to 3 weeks and then analyzed. Prebiotically relevant molecules were synthesized from organics reacted in the presence of chemical gardens under early-Earth-like conditions. As our reactants are readily available in geological settings, it is possible that similar self-organized structures could have played a role in prebiotic chemistry on early Earth or potentially even on other ocean-containing places in the Solar System.

2.1 Introduction

Chemical gardens (CGs) are spontaneously precipitated hollow-tube-like semipermeable structures that form upon the addition of a metal salt to an aqueous salt solution that have been used in a variety of fields. (Russell, Hall, and Turner, 1989; Barge, Cardoso, et al., 2015; Cartwright et al., 2002) Any one of a number of metal salts can be used as the secondary "seed" component (Barge, Cardoso, et al., 2015; Cartwright et al., 2002). The CG itself is an intricate and heterogeneous structure, with the membrane consisting of interior layers of metal hydroxide precipitates and exterior layers of amorphous silica (Hazlehurst, 1941; Kotopoulou et al., 2021). Eventually, the gradients created by precipitation, diffusion, and transport of species across the membrane decay toward equilibrium (Barge, Cardoso, et al., 2015; Glaab et al., 2012).

As CGs can be controlled in a laboratory setting, they are attractive abiotic mineral analogs for chimneys formed at hydrothermal vents, (Barge, Cardoso, et al., 2015; Mielke et al., 2010) which can be defined as geochemically reactive regions (often along mid-ocean ridges) that are rich in metals and minerals and eject hot, chemically and minerally rich fluids (Martin et al., 2008; Kelley et al., 2005). Hydrothermal vents have been posited as a potential location for the origins of life for nearly a century due to their ambient redox and pH disequilibria as well as an abundance of reactive minerals (Martin et al., 2008; Russell and Hall, 1997; Corliss et al., 1981; Baross et al., 1985; Russell, Barge, et al., 2014; Sojo et al., 2016). Hydrothermal vents have existed on Earth since the Hadean geological eon (corresponding to 4.6-4.0 billion years ago) (Martin et al., 2008; Miyazaki et al., 2022). Importantly, simulating an "early Earth" hydrothermal vent in the laboratory requires an anaerobic environment, as prior to the Great Oxidation Event ~2.4 billion years ago, Earth's atmosphere contained no oxygen (Lyons et al., 2014). Scientific interest in hydrothermal vents and their prebiotic potential is not limited to early Earth. The NASA "roadmap to ocean worlds" emphasizes the identification, characterization, and evaluation of the potential for life on other Solar System "ocean worlds" (bodies with liquid-water oceans underneath their surfaces), with a focus on some outer Solar System moons (Hendrix et al., 2019). Water-rock (ocean floor) interactions and hydrothermal vents have also been hypothesized to exist on some of these ocean worlds, e.g., Jupiter's moon Europa and Saturn's moon Enceladus (Vance, Harnmeijer, et al., 2007; Vance and Melwani Daswani, 2020; Choblet et al., 2017; Hsu et al., 2015; Vance, Hand, et al., 2016). Ocean worlds are thus key candidates for understanding the origins of life and possible life detection with future space missions

(*Origins, Worlds, and Life* 2022). Enceladus, in particular, is of astrobiological interest because organic molecules and hydrogen have been detected being ejected from the subsurface water ocean into space via a large plume (Waite et al., 2017; Postberg et al., 2018; Khawaja et al., 2019). Some have proposed that these organics could be produced abiotically and might be indicators of extant prebiotic chemistry (Khawaja et al., 2019; Kahana et al., 2019). Research incorporating data from the *Cassini* mission (a spacecraft mission to the Saturnian system that operated from 2004-2017) and numerical modeling has yielded a predicted ocean composition for Enceladus' subsurface water ocean, which is proposed to be enriched in carbonate and chloride (Glein et al., 2020).

In this study, we used CGs as laboratory hydrothermal vent chimney analogs under simulated early Earth and Enceladus conditions to explore prebiotic chemistry potential in ocean floor environments. Hydrothermal vent chimneys have some structural similarities to CGs, as their precipitate structures allow bidirectional ion transport between the hydrothermal vent fluid and seawater, as well as separation between fluids and thus sustained pH and redox disequilibria (Russell, Hall, and Turner, 1989; Russell and Hall, 1997). CGs can approximate several key features of hydrothermal vents in laboratory settings, such as electrochemical gradients, and injection CG experiments simulating hydrothermal chimneys have been used to simulate proposed prebiotic systems on the early Earth (Glaab et al., 2012; Barge, Doloboff, et al., 2012; Barge, Cardoso, et al., 2015).

CGs are complex structures that have been explored as solid reactants and/or catalysts in a prebiotic context: in particular, within systems containing iron (or another metal) and silicate (Barge, Doloboff, et al., 2012; Omran et al., 2023; Mattia Bizzarri et al., 2018; Saladino et al., 2016; Weber et al., 2021). For example, Fe-silicate CG precipitates were shown to facilitate adsorption of formamide and pyruvate and subsequent synthesis of amino acids, carboxylic acids, and nucleobases (Mattia Bizzarri et al., 2018; Saladino et al., 2016). In a previous study, the synthesis of glycine and glycolate was observed in the presence of alpha-keto acids in Fe-silicate CGs, but this was determined to be mediated by the exterior silicate solution and not the CG precipitates themselves (Weber et al., 2021). The effects of phosphate, amino acids, ammonia, and alpha-keto acids on Fe-silicate CG formation and morphology have also been studied (Barge, Doloboff, et al., 2012; Weber et al., 2021; Hooks et al., 2020; Borrego-Sánchez et al., 2022).

Herein, we sought to explore the reactivity of Fe-silicate CG mineral structures under lab-simulated early-Earth- and Enceladus-relevant conditions. This work seeks to expand on previous work conducted with alpha-keto acids and iron-silicate CGs (Weber et al., 2021) to determine whether the CG precipitates are capable of facilitating reactions with alpha-keto acids in the absence of the sodium silicate solution. In particular we chose to focus on the simplest alpha-keto acids, pyruvate and glyoxylate (conjugate bases of pyruvic acid and glyoxylic acid, respectively); these have been previously used in protometabolism studies that have shown their central role in reaction networks producing intermediates and analogs of the reductive citric acid/tricarboxylic acid (rTCA) cycle (Muchowska, Varma, and Moran, 2019; Muchowska, Varma, Chevallot-Beroux, et al., 2017; Stubbs et al., 2020). Pyruvate and glyoxylate can form a variety of products abiotically in aqueous solution and also in the presence of minerals or metals (Muchowska, Varma, and Moran, 2019; Muchowska, Varma, Chevallot-Beroux, et al., 2017; Stubbs et al., 2020; Barge, Flores, VanderVelde, et al., 2020; Barge, Flores, Baum, et al., 2019). Although neither glyoxylate nor pyruvate has been discovered yet on Enceladus, abiotic formation pathways exist (Marín-Yaseli et al., 2016) and studying these organics in Enceladus-like environments provides a valuable groundwork for the potential behavior of these organics on a different Solar System body. As there are limited in situ data from the *Cassini* mission, the organic inventory of Enceladus remains largely unexplored. Previously, we have studied reactions of these precursors with Fe-hydroxide minerals — which are highly reactive and relevant to early Earth prebiotic systems (Russell, 2018) — and observed that the pH and Fe redox state are key factors in determining product distribution (Barge, Flores, VanderVelde, et al., 2020; Barge, Flores, Baum, et al., 2019). Fe-silicate CGs are gradient systems containing a range of pH and mineralogical conditions, likely including Fe hydroxides in the interior (Cartwright et al., 2002; Kotopoulou et al., 2021). so it is possible that similar prebiotic reactions that have previously been observed in batch experiments may also occur in an Fe-containing CG system.

We sought to include Enceladus-relevant conditions in our reactions to test whether, if these prebiotic organics are present, Fe-silicate CG precipitates could drive similar reactions in other ocean-world contexts beyond our own planet. Previous studies have synthesized carbonate-hydroxide CGs in Enceladus-like conditions (Cardoso et al., 2019); in this work, we focused on Fe-silicate precipitation systems and incorporation of CGs into solutions containing prebiotic organics and a lab-simulated

Enceladus ocean solution (with sodium carbonate and sodium chloride added) based on a recently published model for the conditions of that moon (Glein et al., 2020).

2.2 Results

CG growth displays minimal variation

Upon addition of the $FeCl_2 \cdot 4H_2O$ salt to the silicate solution (~ 4 M), CG growth began almost immediately (Figure 2.1A). The gardens appeared to be fully formed within a few hours, but were allowed a full week to complete growth prior to using them in reactions (Figure 2.1B). CGs were composed primarily of thin (~2 mm diameter) vertical tubes, with some gardens containing one or several thicker (~5 mm diameter) tubes. CG structure was similar between experiments, although some heterogeneity was observed. Tubes varied in height from about one centimeter (most common) to several centimeters (a few per CG) to the top of the silicate solution (though this was rare and did not occur for all CGs) (Figure 2.1). Isolated CG masses prior to addition to the reactions varied from 0.7 to 1.1 g once filtered. As the CGs were grown on the benchtop, oxidation was observed during synthesis and upon filtration, which was also performed on the benchtop. All CGs, once formed, were stored in a nitrogen-filled Coy glove box until used in reactions.

Organic analysis demonstrates formation of various prebiotically relevant precursors

A full proposed reaction/pathway schematic can be found in Figure 2.2. Reactions conducted are listed in Table A.1 and pictured in Figure A.1. Key prebiotic products of interest (Table A.2) were searched for in all spectra (Tables 2.1, 2.2, and 2.3; Figures A.2-A.100; Table A.3). Glycolate formation (indicated by a ^{1}H NMR singlet peak at 3.93 ppm) was observed in most of the reactions containing only glyoxylate, regardless of whether ammonia was present or of other conditions; glycine was sometimes also observed. Glycine formation occurred only in the presence of glyoxylate and ammonia and in the absence of Enceladus-relevant salts. Glycine formation was difficult to characterize, as it produced only a singlet peak around 3.5 ppm and the peak shifted between 3.40 and 3.55 ppm with varying pH (see Figures A.101-A.102), though glycine formation was confirmed by spiking reaction mixtures with an authentic sample. In instances where product peaks could be isolated and integrated, calculated yields are presented in Tables 2.1, 2.2, and 2.3. Overall, heated conditions led to higher product yield.

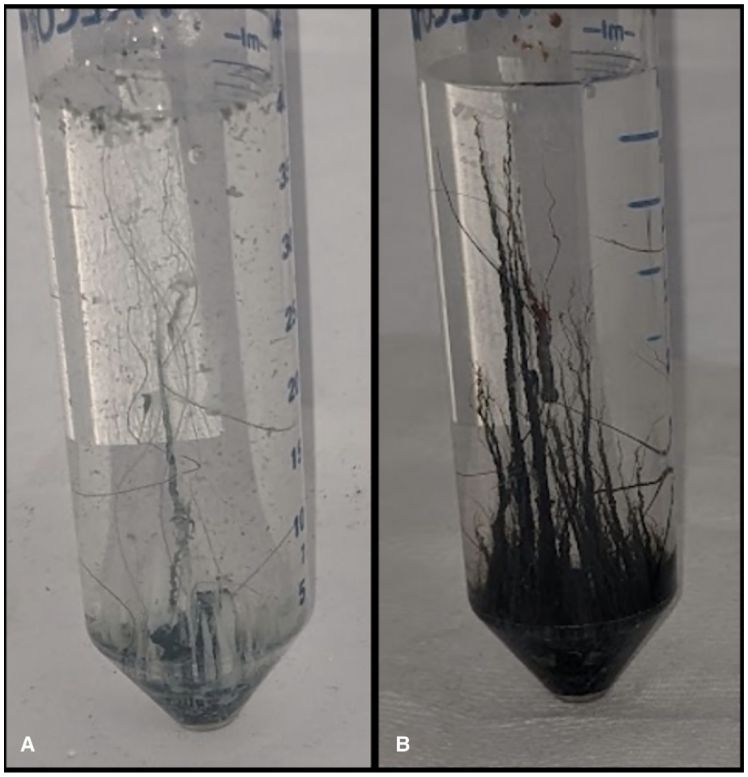


Figure 2.1: *CG growth with time*. Iron silicate CG in sodium silicate solution after (A) 5 min and (B) 1 week of growth.

Molecule Timepoint	Glycolate t = 0	Glycolate t = 1	Glycolate t = 2	Glycolate t = 3	Glycine t = 1	Glycine t = 2	Glycine t = 3	Formate t = 0	Formate t = 1	Formate t = 2	Formate t = 3
GA, pH 7.25	0.38	0.50	0.51	0.28	–[a]	–	–	0.98	6.2	11	8.1
GA + NH_3, pH 7.25	0.25	0.79	~~~[b]	0.85	0.068	0.083	0.25	0.52	4.1	6.9	6.4
GA, pH 10	0.50	0.53	0.40	0.20	–	–	–	1.0	11	14	12
GA + NH_3, pH 10	–	0.57	~~~	0.54	0.20	0.18	0.18	0.50	4.2	6.9	6.1
GA + PA + NH_3, pH 7.25	~~~	~~~	~~~	~~~	~~[c]	~~	~~	1.0	4.6	6.7	8.4
GA + PA + NH_3, pH 10	~~~	~~~	~~~	~~~	~~[c]	~~	~~	1.2	4.7	5.5	7.6
GA (Enceladus-like)	0.40	0.43	0.47	0.53	–	–	–	0.93	12	19	20
GA + NH_3 (Enceladus-like)	0.33	0.30	0.36	0.30	–	–	–	0.73	10	15	16
GA + NH_3 (Enceladus-like, inc. carbonate)	0.32	0.37	0.38	0.33	–	–	–	0.80	9.6	17	19

Table 2.1: Percentage yields of key prebiotic molecules from glyoxylate-containing reactions conducted under benchtop conditions (oxic, room temperature).
[a]: Material below detection limit.
[b]: Material is present, but peak overlap prevents integration of a single peak.
[c]: Insufficient data quality to calculate final molarity.

Molecule Timepoint	Glycolate t = 0	Glycolate t = 1	Glycolate t = 2	Glycolate t = 3	Glycine t = 1	Glycine t = 2	Glycine t = 3	Formate t = 0	Formate t = 1	Formate t = 2	Formate t = 3
GA, pH 7.25	0.11	3.0	3.3	3.3	–[a]	–	–	0.40	15	17	18
GA + NH_3, pH 7.25	0.075	4.7	5.5	5.6	0.64	0.89	1.1	0.23	4.7	7.6	9.1
GA, pH 10	–	3.7	3.6	4.1	–	–	–	0.30	19	20	22
GA + NH_3, pH 10	0.088	4.2	4.7	5.1	0.51	0.83	1.2	0.56	4.5	7.3	10
GA + PA + NH_3, pH 7.25	–	1.4	1.7	1.3	~~~[b]	~~~	~~~	0.35	8.3	9.0	10
GA + PA + NH_3, pH 10	–	1.3	1.3	1.2	~~~	~~~	~~~	0.25	6.1	9.1	9.4
GA (Enceladus-like)	0.47	6.0	5.8	5.8	–	–	–	0.57	12	11	12
GA + NH_3 (Enceladus-like)	0.42	5.2	5.0	5.6	–	–	–	0.67	14	13	11
GA + NH_3 (Enceladus-like, inc. carbonate)	0.32	5.7	5.7	5.6	–	–	–	0.43	13	12	12

Table 2.2: Percentage yields of key prebiotic molecules from glyoxylate-containing reactions conducted in heated aerobic conditions.
[a]: Material below detection limit.
[b]: Material is present, but peak overlap prevents integration of a single peak.

Molecule Timepoint	Glycolate t = 0	Glycolate t = 1	Glycolate t = 2	Glycolate t = 3	Glycine t = 1	Glycine t = 2	Glycine t = 3	Formate t = 0	Formate t = 1	Formate t = 2	Formate t = 3
GA, pH 7.25	0.28	3.6	5.5	7.6	–[a]	–	–	0.18	1.4	1.1	0.93
GA + NH_3, pH 7.25	0.25	1.9	2.2	∼∼	0.38	0.81	∼∼	0.43	1.1	1.1	1.5
GA, pH 10	–	5.1	6.5	6.3	–	–	–	0.53	1.3	1.7	1.8
GA + NH_3, pH 10	0.20	1.1	1.4	1.2	0.53	0.79	1.1	1.1	1.1	1.1	1.5
GA + PA + NH_3, pH 7.25	–	∼∼∼[b]	∼∼∼	∼∼∼	∼∼[c]	∼∼	∼∼	0.37	1.1	1.1	∼∼
GA + PA + NH_3, pH 10	∼∼	∼∼∼	∼∼∼	∼∼∼	∼∼	∼∼	∼∼	1.3	0.97	0.50	0.37
GA (Enceladus-like)	0.45	0.61	1.4	1.6	–	–	–	0.43	2.3	1.8	1.5
GA + NH_3 (Enceladus-like)	0.48	0.88	0.98	1.0	–	–	–	0.47	0.37	0.90	1.1
GA + NH_3 (Enceladus-like, inc. carbonate)	0.33	0.88	0.92	1.0	–	–	–	0.40	0.70	0.80	1.1

Table 2.3: Percentage yields of key prebiotic molecules from glyoxylate-containing reactions conducted in anaerobic conditions.

[a]: Material below detection limit.

[b]: Material is present, but peak overlap prevents integration of a single peak.

[c]: Insufficient data quality to calculate final molarity.

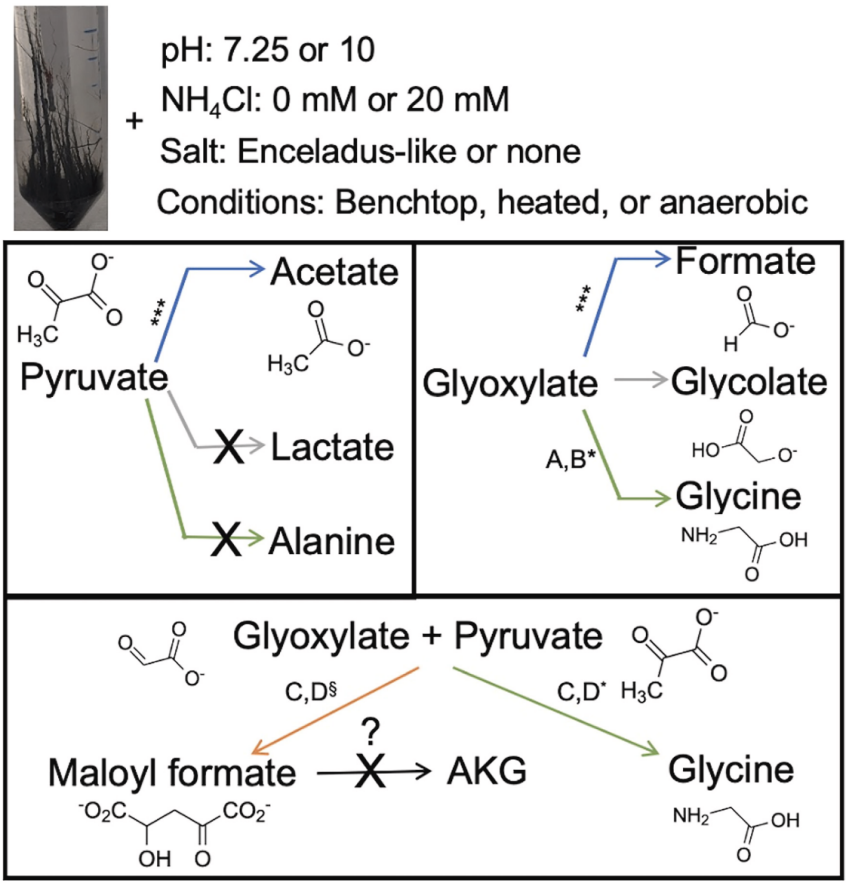


Figure 2.2: *Organic analysis demonstrates limited formation of glycine and maloyl formate, broad formation of acetate, formate, and glycolate*. Products formed from pyruvate and/or glyoxylate under prebiotic and/or Enceladus conditions. Reaction conditions leading to product formation include the following: (A) glyoxylate, NH_3, and CG (pH 7.25); (B) glyoxylate, NH_3, and CG (pH 10); (C) glyoxylate, pyruvate, NH_3, and CG (pH 10); and (D) glyoxylate, pyruvate, NH_3, and CG (pH 7.25).
***: product was observed in all reactions.
X: product was not observed in any reactions.
*: Product observed under benchtop, anaerobic, and heated conditions.
§: Product observed under benchtop and anaerobic conditions only.
AKG: alpha-ketoglutarate. Blue reactions: decomposition; gray reactions: reduction; green reactions: reductive amination; orange reaction: aldol addition.

Formate, a decomposition product of glyoxylate, was observed in most glyoxylate-CG reactions (Figure 2.3). Its formation occurred regardless of condition, pH, or salts present. Formate yields were much higher for aerobic reactions (benchtop or heated) than for anaerobic reactions. Formate yields were also higher when ammonia was absent (except in cases of Enceladus-like solutions). In pyruvate-only reactions, most of the NMR spectra contained too many peaks to allow identification

of every product; however, the spectral fingerprint was largely the same regardless of pH or whether ammonia was added. The pyruvate-containing samples, although generating a large number of peaks throughout the course of the reaction, did not definitively produce alanine or lactate under any of the reaction conditions tested. Our NMR system is capable of detections as low as 0.1% (alanine) and 0.5% (formate), so non-detection of these compounds indicates a percentage yield lower than this.

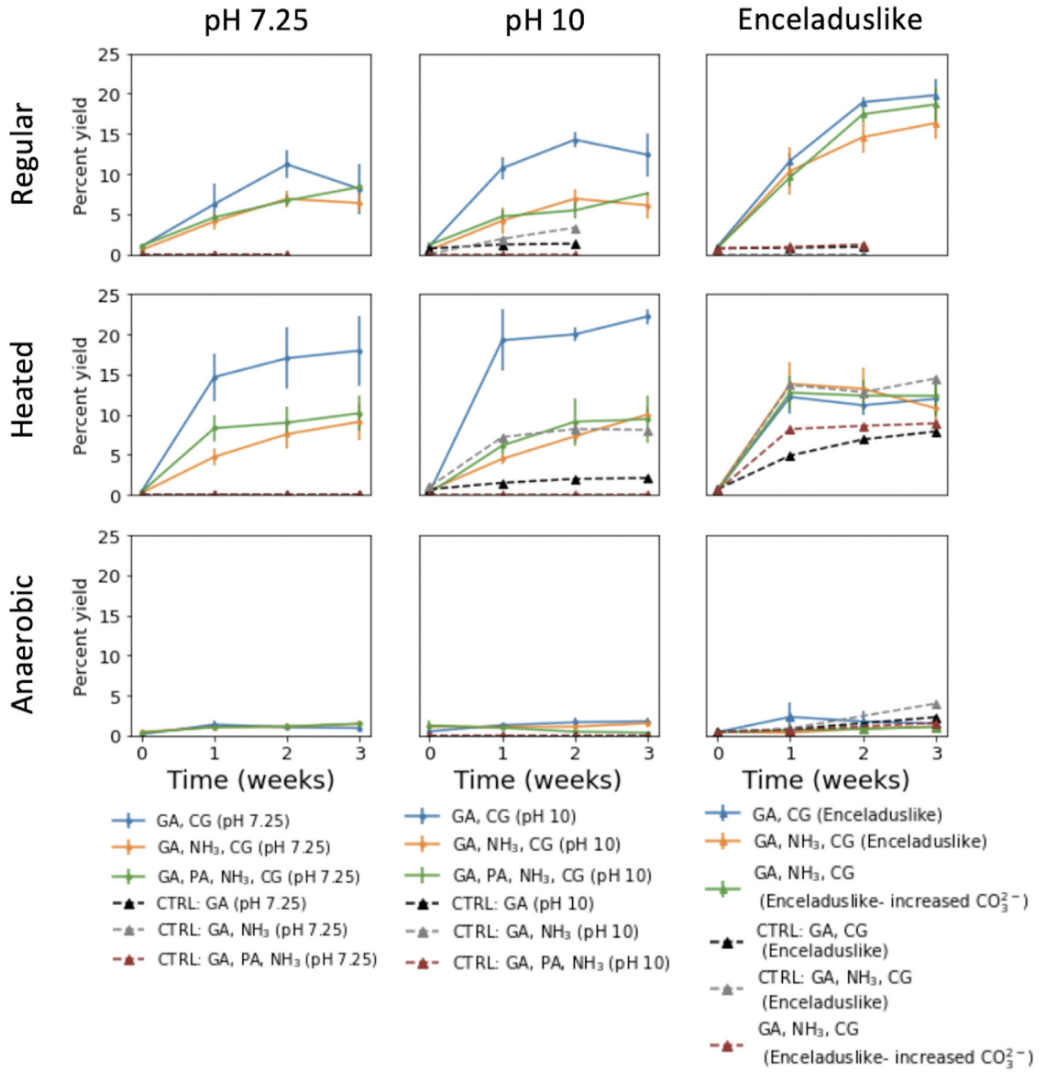


Figure 2.3: *Formate yields varied depending on the conditions and components of the reactions.*. In all instances, the presence of a CG increased formate production. Formate production was inhibited under anaerobic conditions. GA, glyoxylate; PA, pyruvate. The presence of ammonia led to decreased formate production in instances when Enceladus-like salts were not present.

The presence of the CG almost always caused variation in reactivity and product formation compared with the corresponding (CG-free) control. Control reactions (without any CG) exhibited less product formation (both in terms of product abundance and diversity). Products from glyoxylate control reactions included glycolate (particularly at high pH or with Enceladus salts) and formate. Products from pyruvate control reactions included acetate and pyruvic acid decomposition (particularly with Enceladus salts). Control reactions containing both glyoxylate and pyruvate showed marked differences from the corresponding CG-containing reactions: although additional peaks indicated that products were formed, we did not observe any of the individual products (glycine, alanine, glycolate, and lactate) that could potentially be formed in pyruvate- or glyoxylate-only experiments with Fe-hydroxide minerals (Barge, Flores, VanderVelde, et al., 2020; Barge, Flores, Baum, et al., 2019). For oxic/benchtop reactions (room temperature and heated), the CG-containing reactions exhibited many more peaks than their corresponding control spectra. However, in the case of the anaerobic reactions containing both pyruvate and glyoxylate, both control and CG-containing reactions had many peaks, albeit not matching ones. Interestingly, peaks potentially corresponding to maloyl formate around 3.0 ppm (Stubbs et al., 2020) were observed in the anaerobic and aerobic pyruvate + glyoxylate + CG reactions (e.g., Figure 2.4).

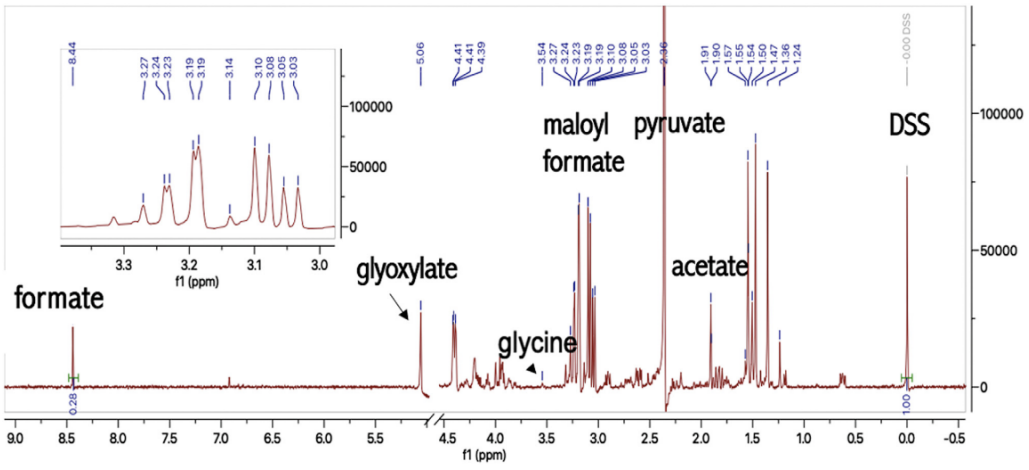


Figure 2.4: *Product formation observed in reactions containing pyruvate, glyoxylate, and ammonia*. NMR spectrum of a chemical garden, glyoxylate, pyruvate, and NH_3 at pH 10. Benchtop conditions, t = 2 weeks.

In glyoxylate experiments, the peaks produced did not appear substantially different under Enceladus conditions (glycolate was still formed). In pyruvate experiments without ammonia, the same peaks were observed whether or not Enceladus condi-

tions were used; however, when ammonia was added, additional peaks around 1-2 and 3-4 ppm were observed — unlike in the experiments without Enceladus salts, where the addition of ammonia to pyruvate experiments did not produce new peaks. The difference in reaction behavior with and without CGs varied according to experimental condition. For reactions conducted at room temperature (aerobic and anaerobic) with Enceladus salts, additional peaks were formed in the CG-containing reaction. However, for heated reactions containing Enceladus salts, the same peaks were observed regardless of the presence of the CG.

VNIR reflectance spectroscopy indicates diverse solid formation in CG reactions

Visible near-infrared (VNIR) reflectance spectroscopy was used to determine whether there were any changes to the CG material during the course of the reaction (Figures 2.5 and A.103–A.105). When reactions were conducted at 70°C, spectra suggested that the composition of VNIR-active minerals was largely similar across samples. Heated reactions containing only pyruvate or pyruvate + glyoxylate displayed no differences in VNIR spectra between experiments of varying pH or with Enceladus salts (Figures 2.5B and 2.5E). For glyoxylate, a slight dip in the spectrum around 2.1 μm was observed whenever ammonia was present (Figure 2.5B) but not when Enceladus salts were also present.

All samples had strong Fe absorptions, from ~0.35-1.0 μm, caused by charge transfer and crystal field splitting. Under regular and heated conditions, these Fe absorptions were relatively consistent, with band centers around 0.5 and 0.9 μm, consistent with ferric Fe (Rudolph et al., 2022). Glyoxylate conditions appeared to produce absorptions consistent with hematite, with a flatter slope of 0.45-0.48 μm (Sheppard et al., 2019). Under anaerobic conditions, the Fe absorptions were notably more complex and overlapping, with a decrease in the 0.5-μm absorption and an additional Fe absorption near 0.7 μm. This is consistent with complex Fe phases that may be amorphous or mixed valence (Rudolph et al., 2022; Sheppard et al., 2019). There was no spectral evidence of hematite.

However, when reactions were conducted in an anaerobic room-temperature environment, more differences in spectral features were observed between CGs formed in the presence of pyruvate vs. those formed in the presence of glyoxylate. Pyruvate reactions displayed varied features at ~1.7 and 2.5 μm, regardless of pH, when ammonia was present (Figure 2.5F). This signature was not as readily observed in

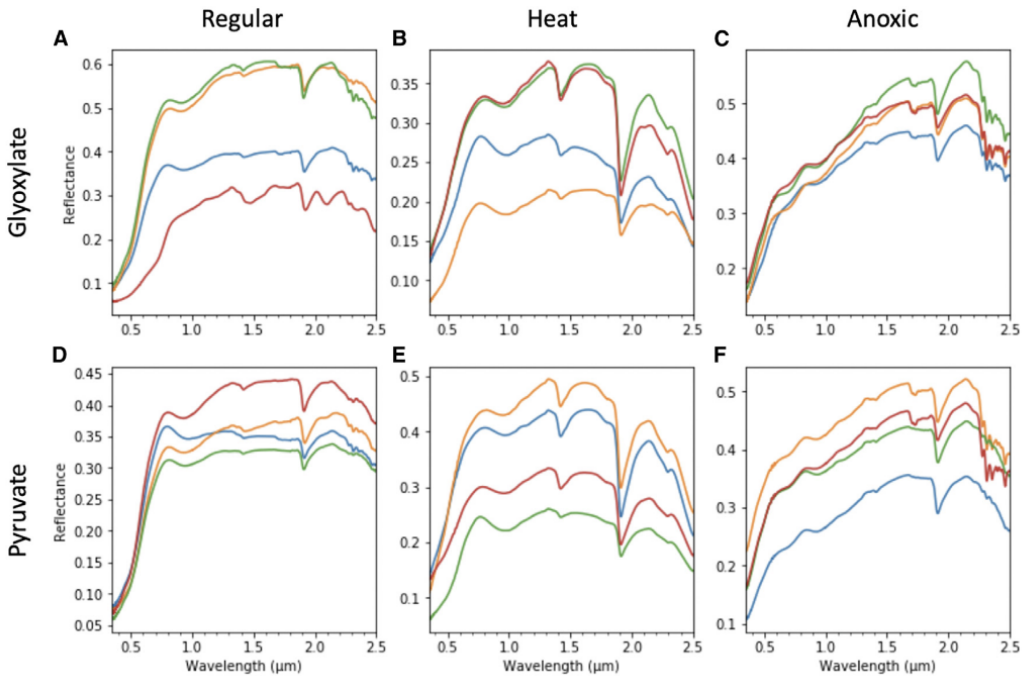


Figure 2.5: *VNIR reflectance spectroscopy indicates diverse solid formation in CG reactions*. VNIR reflectance spectra of various CG precipitates following 3 weeks of reactions. Blue: pH 7.25, no NH_4Cl; orange: pH 7.25, added NH_4Cl; green: pH 10, no NH_4Cl; red: pH 10, added NH_4Cl.
(A) Glyoxylate and benchtop.
(B) Glyoxylate and heated.
(C) Glyoxylate and anaerobic.
(D) Pyruvate and benchtop.
(E) Pyruvate and heated.
(F) Pyruvate and anaerobic.

experiments with Enceladus salts (Figures A.104 and A.105). Anaerobic glyoxylate-only experiments exhibited strong spectral features as well, which, unlike pyruvate, appeared whether or not ammonia was present (Figure 2.5C). These differences observed in an anaerobic environment were not present when reactions were conducted on the benchtop (Figures 2.5A–2.5D).

Variations in absorptions at longer wavelengths of the reflectance spectra were related to different components experiencing vibrations, including organics, salts, and clay minerals. For example, all the samples under regular and anaerobic conditions had complex absorptions related to the presence of organics at ~2.2-2.5 μm, consistent with additives in those systems. These organics-related features are consistent with ammonia, possibly present as ammoniated clay (Ehlmann, Hodyss,

et al., 2018). Notably, samples from heated conditions lacked these organic-related absorptions and instead had a consistent check-mark-shaped absorption at 2.29 μm, consistent with Fe-bearing clay minerals such as nontronite (Bishop et al., 2008; Ehlmann, Mustard, et al., 2008). The heated condition spectra also had a convexity in their spectral shape at wavelengths longer than 2.29 μm, which is consistent with the presence of sulfate (Viviano et al., 2014).

XRD and Raman spectroscopy suggest amorphous silica and halite formation

X-ray diffraction (XRD) was conducted to obtain chemical characterization of the CG materials formed in these reactions (Figures A.106–A.111). The unreacted CG (Figure A.106) had an elevated baseline, suggestive of amorphous silica. The same trends were observed in the fully oxidized, unreacted CG (Figure A.107). XRD characterization of the CG precipitate formed in reactions containing glyoxylate and ammonium chloride were again interpreted as amorphous (Figures A.108 and A.109). Slight peaks are present at 32° and 46°, representative of the mineral halite (sodium chloride). This is in line with previously published CG studies (Borrego-Sánchez et al., 2022). No other minerals were readily observed. The CG precipitate in reactions containing pyruvate, ammonium chloride, and Enceladus-like salts (Figures A.110 and A.111) showed a similar pattern, with more pronounced halite peaks, which is likely a direct effect of the additional sodium chloride present. Raman spectroscopy was also performed to validate these results (Figures A.112-A.114).

2.3 Discussion

CGs have been of longstanding interest to the origins-of-life research community (Barge, Cardoso, et al., 2015); this is due to their self-organizational properties, the sustained disequilibria that are observed, and the reactive materials that make up the precipitate itself. CGs' role as simple and easily constructed laboratory analogs for hydrothermal vent chimneys makes them a valuable tool for studying the potential prebiotic properties of similar precipitates that may have existed on early Earth and other worlds (Mielke et al., 2010; Hsu et al., 2015; Barge, Cardoso, et al., 2015; Cardoso et al., 2019; Garcia-Ruiz, Juan M et al., 2017). Previous laboratory work demonstrated the role of CGs in the synthesis of nucleobases (Mattia Bizzarri et al., 2018) as well as their reactivity in the presence of simple alpha-keto acids (Weber et al., 2021). Here, we demonstrate that CGs in the presence of pyruvate and

glyoxylate can produce molecules with relevance to prebiotic and protometabolic chemistry under early Earth and Enceladus conditions.

We considered three different experimental environments: "regular" benchtop reactions as a reference point, an oxygen-free environment (to simulate an anaerobic early Earth), and an environment under sustained moderate heat (simulating the heated environment around a hydrothermal vent) — all of which could have different effects on the CG precipitate properties and concomitant organic reactions. Usage of multiple analytical techniques (VNIR reflectance spectroscopy, Raman spectroscopy, and XRD) allowed a multifaceted view of the solid-phase materials formed in our reactions. It is worth noting that heated reactions were conducted in a hot water bath and not on a heated stir plate. This means that, unlike the other two types of reaction environments, the heated reactions did not undergo any stirring. Although the CGs in anaerobic and regular environments were well-stirred and thus ended up ground into a more powder-like consistency, the ones in the heated environments remained discrete chunks of up to ~5 mm diameter. This means that the amount of solid surface area making contact with the liquid was lower for the heated reactions and the resulting mixtures were less well mixed. XRD indicated the overall amorphous character of the minerals formed as well as the presence of halite — particularly in Enceladus-salt experiments — while VNIR indicated the presence of Fe minerals with various valence states. These observations are consistent with the expected amorphous silica and Fe-oxyhydroxides that should be present in this type of Fe-silicate CG precipitate (Barge, Cardoso, et al., 2015; Hazlehurst, 1941; Kotopoulou et al., 2021).

Under all the conditions tested, glycolate, formate, and sometimes glycine, the simplest amino acid, were generated. This finding demonstrates that simple prebiotically relevant molecules can be generated in the presence of CGs, even in the absence of the reactive exterior silicate solution. The solution pH led to shifts in the location of the ^{1}H NMR peak for glycine (range: 3.40-3.54 ppm), but it did not substantially affect the reaction outcomes in any of the experimental conditions. The expected products derived from pyruvate (lactate and alanine) (Barge, Flores, Baum, et al., 2019) were not observed in any of our tested conditions; however, it should be noted that although the small subset of molecules we specifically looked for were not observed, the pyruvate reactions appeared to be very active chemically, exhibiting a large number of NMR peaks. Interestingly, while glycine was able to be easily identified in reactions initiated with only glyoxylate, any reactions initiated

with both glyoxylate and pyruvate contained a much more complex series of peaks and the identification of glycine by ^{1}H NMR spectroscopy was accordingly more challenging. Although the products formed in any pyruvate-containing reactions were not immediately identifiable, the presence of many products and high reactivity is interesting for origins-of-life scenarios.

The possible production of maloyl formate in our pyruvate + glyoxylate + CG reactions is consistent with previous work (Stubbs et al., 2020) in which its formation was proposed to be due to an aldol addition of glyoxylate to pyruvate. In our experiments, the CG appears to be necessary for the formation of maloyl formate at room temperature because none of the compound was formed when the CG was absent nor when the experiment was heated. If maloyl formate was being produced in our experiments by a similar mechanism as proposed in the referenced previous work (Stubbs et al., 2020), then it is interesting that we do not also see further downstream products, e.g., alpha-ketoglutarate (potentially formed from further reaction with glyoxylate and also important for prebiotic rTCA cycle-like reactions). It is possible that the presence of the CG precipitates caused maloyl formate formation via a different mechanism or that all of the glyoxylate in our experiments (which started with a 1:1 glyoxylate:pyruvate ratio) was consumed in the initial reaction so that further reactions could not occur. The potential maloyl formate product in our experiments appears to be stable for the 2- to 3-week experiment duration, which suggests that, in a geological environment, it might be able to persist in solution to eventually react further if more glyoxylate (or other reactants) became available.

In these experiments, we aimed to investigate the effects of specific inorganic parameters (Fe-Si CGs, ammonia, and carbonate) on the organic reactions of our two precursors and determine likely products that would form. Therefore, as is typical for prebiotic reaction studies, we used organic concentrations that were higher than would be expected in a geological setting in order to facilitate product detection. In a planetary setting, specific organic/mineral reactions would be taking place in the presence of many other components and reaction systems. Local concentrations of organics would be determined not only by their production in prebiotic reactions but also by their specific propensities to concentrate in mineral surfaces, pores, and gels (Arrabito et al., 2019; Erastova et al., 2017; Westall et al., 2018). However the components of our experiments (Fe, silica, water, alpha-keto acids, and ammonia) can easily be envisaged in an early Earth context: silica and Fe hydroxides were abundant in the early Earth's oceans (Tosca et al., 2016; Halevy et al., 2017) and

pyruvate and glyoxylate can be prebiotically/abiotically synthesized (Cody et al., 2000; Eckhardt et al., 2019; Eggins et al., 1988; Mohammed et al., 2017; Varma et al., 2018). Our results suggest potential pathways for key protometabolic compounds to be produced in environments where CG-like precipitates may occur—for example, from precipitation of metals in natural silica-rich waters in serpentinizing systems (Hazlehurst, 1941; Garcia-Ruiz, Juan M et al., 2017).

Additionally, the presence of salts and other components in an ocean-world setting may affect protometabolic reactions. For example, in contrast to our glyoxylate experiments conducted in MilliQ water, the same reactions carried out in the presence of Enceladus-relevant salts (Glein et al., 2020) did not lead to glycine synthesis, suggesting that glycine formation via this mechanism would require an environment with low salt content. Glycolate formation was still observed in reactions with Enceladus salts. At least, these particular reactions demonstrate a clear sensitivity of glycine formation to the salinity of the solution. However, reactivity (in terms of ^{1}H NMR peaks observed) was overall still high, even in Enceladus-like solutions with increased salinity, demonstrating that similar reactions may be able to occur in Enceladus' ocean and similarly salty oceans on other planetary bodies. Further exploration of different salt combinations and concentrations would be valuable for determining the effect of salinity on prebiotic rTCA-type reactions to determine what kinds of geological environments would favor this chemistry.

We have demonstrated that pyruvate and/or glyoxylate are able to react in the presence of Fe-silicate CG precipitates — under benchtop (oxic) conditions, anaerobic environments, and heated environments — and in the presence of Enceladus-relevant salts. CG precipitates exhibited amorphous material and mixed-valence Fe minerals as well as salts (halite), especially under simulated Enceladus conditions. Organic reactivity varied, depending on the conditions, producing expected products (glycine and glycolate) from glyoxylate reactions. Unidentified organic products, but not the expected alanine or lactate, were observed from pyruvate reactions. In mixed pyruvate-glyoxylate-ammonia-CG experiments, maloyl formate was potentially formed in the presence of CG precipitates and at room temperature, indicating that some hypothesized prebiotic rTCA cycle reactions (Stubbs et al., 2020) could occur in systems containing CGs. Enceladus-relevant salts were observed to affect some glyoxylate reactions, inhibiting the formation of glycine in the presence of sodium chloride/sodium carbonate and inhibiting glycolate formation with increasing sodium carbonate concentration. Because the components of our reaction system

(Fe, silica, and sodium chloride/sodium carbonate) are readily available in geological settings, it is possible that self-organized CG structures such as these could have played a role in prebiotic TCA cycle reactions on early Earth and potentially on ocean worlds such as Enceladus.

2.4 Experimental Procedures

Conducted work

All experimental procedures used in this work are standard and are described in detail in the supplemental information.

2.5 Acknowledgements

The authors would like to thank Dr. David Vander Velde for useful input on ^{1}H NMR analysis and for running the samples. T.C.M. was funded by an NSF graduate research fellowship. J.M.W. and L.M.B. were supported by the NASA Astrobiology Institute (Icy Worlds) and the NASA-NSF Ideas Lab for the Origins of Life ("Becoming Biotic"). This work was performed at the Jet Propulsion Laboratory, California Institute of Technology, under a contract with NASA (80NM0018D004).

2.6 Author Contributions

T.C.M. conducted the experimental reactions, data processing, and analysis and wrote the original draft of the manuscript. L.M.B. and J.M.W. conceived of the experiment design and assisted with discussion, organization, and writing of the manuscript. J.M.W. additionally helped with the VNIR and Raman spectroscopy data collection. R.Y.S. led the VNIR spectroscopy data collection and analysis. S.P. led the Raman spectroscopy data collection and processing. D.D. and M.M.B. collected the XRD data.

References

Arrabito, Giuseppe et al. (July 2019). "Layered Double Hydroxides: A Toolbox for Chemistry and Biology". In: *Crystals* 9.7. Number: 7 Publisher: Multidisciplinary Digital Publishing Institute, p. 361. ISSN: 2073-4352. DOI: 10.3390/cryst9070361. URL: https://www.mdpi.com/2073-4352/9/7/361.

Barge, Laura M., Silvana S. S. Cardoso, et al. (Aug. 2015). "From Chemical Gardens to Chemobrionics". In: *Chemical Reviews* 115.16. Publisher: American Chemical Society, pp. 8652–8703. ISSN: 0009-2665. DOI: 10.1021/acs.chemrev.5b00014. URL: https://doi.org/10.1021/acs.chemrev.5b00014.

Barge, Laura M., Ivria J. Doloboff, et al. (Feb. 2012). "Characterization of Iron – Phosphate – Silicate Chemical Garden Structures". In: *Langmuir* 28.8. Publisher: American Chemical Society, pp. 3714–3721. ISSN: 0743-7463. DOI: 10.1021/la203727g. URL: https://doi.org/10.1021/la203727g.

Barge, Laura M., E. Flores, D. G. VanderVelde, et al. (2020). "Effects of Geochemical and Environmental Parameters on Abiotic Organic Chemistry Driven by Iron Hydroxide Minerals". In: *Journal of Geophysical Research: Planets* 125.11, e2020JE006423. ISSN: 2169-9100. DOI: 10.1029/2020JE006423. URL: https://onlinelibrary.wiley.com/doi/abs/10.1029/2020JE006423.

Barge, Laura M., Erika Flores, Marc M. Baum, et al. (Mar. 2019). "Redox and pH gradients drive amino acid synthesis in iron oxyhydroxide mineral systems". In: *Proceedings of the National Academy of Sciences of the United States of America* 116.11, pp. 4828–4833. ISSN: 1091-6490. DOI: 10.1073/pnas.1812098116.

Baross, John A. and Sarah E. Hoffman (Dec. 1985). "Submarine hydrothermal vents and associated gradient environments as sites for the origin and evolution of life". In: *Origins of Life and Evolution of the Biosphere* 15.4, pp. 327–345. ISSN: 0169-6149, 1573-0875. DOI: 10.1007/BF01808177. URL: http://link.springer.com/10.1007/BF01808177.

Bishop, J. L. et al. (Mar. 2008). "Reflectance and emission spectroscopy study of four groups of phyllosilicates: smectites, kaolinite-serpentines, chlorites and micas". In: *Clay Minerals* 43.1, pp. 35–54. ISSN: 0009-8558. DOI: 10.1180/claymin.2008.043.1.03. URL: https://doi.org/10.1180/claymin.2008.043.1.03.

Borrego-Sánchez, Ana et al. (Aug. 2022). "The Effect of the Presence of Amino Acids on the Precipitation of Inorganic Chemical-Garden Membranes: Biomineralization at the Origin of Life". In: *Langmuir* 38.34. Publisher: American Chemical Society, pp. 10538–10547. ISSN: 0743-7463. DOI: 10.1021/acs.langmuir.2c01345. URL: https://doi.org/10.1021/acs.langmuir.2c01345.

Cardoso, Silvana S. S., Julyan H. E. Cartwright, and C. Ignacio Sainz-Díaz (Feb. 2019). "Carbonate-hydroxide chemical-garden tubes in the soda ocean of Enceladus: Abiotic membranes and microtubular forms of calcium carbonate". In: *Icarus* 319, pp. 337–348. ISSN: 0019-1035. DOI: 10.1016/j.icarus.2018.09.020. URL: https://www.sciencedirect.com/science/article/pii/S0019103518302896.

Cartwright, Julyan H. E. et al. (Dec. 2002). "Formation of Chemical Gardens". In: *Journal of Colloid and Interface Science* 256.2, pp. 351–359. ISSN: 0021-9797. DOI: 10.1006/jcis.2002.8620. URL: https://www.sciencedirect.com/science/article/pii/S0021979702986200.

Choblet, Gaël et al. (Dec. 2017). "Powering prolonged hydrothermal activity inside Enceladus". In: *Nature Astronomy* 1.12. Number: 12 Publisher: Nature Publishing

Group, pp. 841–847. ISSN: 2397-3366. DOI: 10.1038/s41550-017-0289-8. URL: https://www.nature.com/articles/s41550-017-0289-8.

Cody, George D. et al. (Aug. 2000). "Primordial Carbonylated Iron-Sulfur Compounds and the Synthesis of Pyruvate". In: *Science* 289.5483. Publisher: American Association for the Advancement of Science, pp. 1337–1340. DOI: 10.1126/science.289.5483.1337. URL: https://www.science.org/doi/full/10.1126/science.289.5483.1337.

Corliss, John B., J. Baross, and S. Hoffman (1981). "An Hypothesis Concerning the Relationships Between Submarine Hot Springs and the Origin of Life on Earth". In: *Oceanologica Acta, Special issue*. URL: https://www.semanticscholar.org/paper/An-Hypothesis-Concerning-the-Relationships-Between-Corliss-Baross/44077224e169b5f54bd5f8bdcbc083e647ca9b3a.

Eckhardt, André K. et al. (2019). "Formation of Glyoxylic Acid in Interstellar Ices: A Key Entry Point for Prebiotic Chemistry". In: *Angewandte Chemie International Edition* 58.17, pp. 5663–5667. ISSN: 1521-3773. DOI: 10.1002/anie.201901059. URL: https://onlinelibrary.wiley.com/doi/abs/10.1002/anie.201901059.

Eggins, Brian R et al. (Jan. 1988). "Carbon dioxide fixation by electrochemical reduction in water to oxalate and glyoxylate". In: *Tetrahedron Letters* 29.8, pp. 945–948. ISSN: 0040-4039. DOI: 10.1016/S0040-4039(00)82489-2. URL: https://www.sciencedirect.com/science/article/pii/S0040403900824892.

Ehlmann, Bethany L., Robert Hodyss, et al. (2018). "Ambient and cold-temperature infrared spectra and XRD patterns of ammoniated phyllosilicates and carbonaceous chondrite meteorites relevant to Ceres and other solar system bodies". In: *Meteoritics & Planetary Science* 53.9, pp. 1884–1901. ISSN: 1945-5100. DOI: 10.1111/maps.13103. URL: https://onlinelibrary.wiley.com/doi/abs/10.1111/maps.13103.

Ehlmann, Bethany L., John F. Mustard, et al. (Dec. 2008). "Orbital identification of carbonate-bearing rocks on Mars". In: *Science (New York, N.Y.)* 322.5909, pp. 1828–1832. ISSN: 1095-9203. DOI: 10.1126/science.1164759.

Erastova, Valentina et al. (Dec. 2017). "Mineral surface chemistry control for origin of prebiotic peptides". In: *Nature Communications* 8.1. Publisher: Nature Publishing Group, p. 2033. ISSN: 2041-1723. DOI: 10.1038/s41467-017-02248-y. URL: https://www.nature.com/articles/s41467-017-02248-y.

Garcia-Ruiz, Juan M et al. (Mar. 2017). "Biomimetic mineral self-organization from silica-rich spring waters". In: *Science Advances* 3.1602285. DOI: 10.1126/sciadv.1602285. URL: https://www.science.org/doi/10.1126/sciadv.1602285.

Glaab, Fabian et al. (2012). "Formation and Evolution of Chemical Gradients and Potential Differences Across Self-Assembling Inorganic Membranes". In: *Angewandte Chemie International Edition* 51.18, pp. 4317–4321. ISSN: 1521-3773. DOI: 10.1002/anie.201107754. URL: https://onlinelibrary.wiley.com/doi/abs/10.1002/anie.201107754.

Glein, Christopher R. and J. Hunter Waite (Feb. 2020). "The Carbonate Geochemistry of Enceladus' Ocean". In: *Geophysical Research Letters* 47, e85885. ISSN: 0094-8276. DOI: 10.1029/2019GL085885. URL: https://ui.adsabs.harvard.edu/abs/2020GeoRL..4785885G.

Halevy, Itay et al. (Feb. 2017). "A key role for green rust in the Precambrian oceans and the genesis of iron formations". In: *Nature Geoscience* 10.2. Number: 2 Publisher: Nature Publishing Group, pp. 135–139. ISSN: 1752-0908. DOI: 10.1038/ngeo2878. URL: https://www.nature.com/articles/ngeo2878.

Hazlehurst, Thomas H. (June 1941). "Structural precipitates: The silicate garden type". In: *Journal of Chemical Education* 18.6. Publisher: American Chemical Society, p. 286. ISSN: 0021-9584. DOI: 10.1021/ed018p286. URL: https://doi.org/10.1021/ed018p286.

Hendrix, Amanda R. et al. (Jan. 2019). "The NASA Roadmap to Ocean Worlds". In: *Astrobiology* 19.1. Publisher: Mary Ann Liebert, Inc., publishers, pp. 1–27. ISSN: 1531-1074. DOI: 10.1089/ast.2018.1955. URL: https://www.liebertpub.com/doi/10.1089/ast.2018.1955.

Hooks, Michelle R. et al. (June 2020). "Effects of Amino Acids on Iron-Silicate Chemical Garden Precipitation". In: *Langmuir* 36.21. Publisher: American Chemical Society, pp. 5793–5801. ISSN: 0743-7463. DOI: 10.1021/acs.langmuir.0c00502. URL: https://doi.org/10.1021/acs.langmuir.0c00502.

Hsu, Hsiang-Wen et al. (Mar. 2015). "Ongoing hydrothermal activities within Enceladus". In: *Nature* 519.7542. Number: 7542 Publisher: Nature Publishing Group, pp. 207–210. ISSN: 1476-4687. DOI: 10.1038/nature14262. URL: https://www.nature.com/articles/nature14262.

Kahana, Amit, Philippe Schmitt-Kopplin, and Doron Lancet (Oct. 2019). "Enceladus: First Observed Primordial Soup Could Arbitrate Origin-of-Life Debate". In: *Astrobiology* 19.10. Publisher: Mary Ann Liebert, Inc., publishers, pp. 1263–1278. ISSN: 1531-1074. DOI: 10.1089/ast.2019.2029. URL: https://www.liebertpub.com/doi/10.1089/ast.2019.2029.

Kelley, Deborah S. et al. (Mar. 2005). "A serpentinite hosted ecosystem: the Lost City hydrothermal field". In: *Science* 307.5714. Publisher: American Association for the Advancement of Science, pp. 1428–1434. DOI: 10.1126/science.1102556. URL: https://www.science.org/doi/full/10.1126/science.1102556.

Khawaja, Nozair et al. (Nov. 2019). "Low-mass nitrogen-, oxygen-bearing, and aromatic compounds in Enceladean ice grains". In: *Monthly Notices of the Royal*

Astronomical Society 489.4, pp. 5231–5243. ISSN: 0035-8711. DOI: 10.1093/mnras/stz2280. URL: https://doi.org/10.1093/mnras/stz2280.

Kotopoulou, Electra et al. (Jan. 2021). "Nanoscale Anatomy of Iron-Silica Self-Organized Membranes: Implications for Prebiotic Chemistry". In: *Angewandte Chemie (International Ed. in English)* 60.3, pp. 1396–1402. ISSN: 1433-7851. DOI: 10.1002/anie.202012059. URL: https://www.ncbi.nlm.nih.gov/pmc/articles/PMC7839773/.

Lyons, Timothy W., Christopher T. Reinhard, and Noah J. Planavsky (Feb. 2014). "The rise of oxygen in Earth's early ocean and atmosphere". In: *Nature* 506.7488. Publisher: Nature Publishing Group, pp. 307–315. ISSN: 1476-4687. DOI: 10.1038/nature13068. URL: https://www.nature.com/articles/nature13068.

Marín-Yaseli, Margarita R. et al. (2016). "The Role of Aqueous Aerosols in the "Glyoxylate Scenario": An Experimental Approach". In: *Chemistry – A European Journal* 22.36, pp. 12785–12799. ISSN: 1521-3765. DOI: 10.1002/chem.201602195. URL: https://onlinelibrary.wiley.com/doi/abs/10.1002/chem.201602195.

Martin, William et al. (Nov. 2008). "Hydrothermal vents and the origin of life". In: *Nature Reviews Microbiology* 6.11. Number: 11 Publisher: Nature Publishing Group, pp. 805–814. ISSN: 1740-1534. DOI: 10.1038/nrmicro1991. URL: https://www.nature.com/articles/nrmicro1991.

Mattia Bizzarri, Bruno et al. (2018). "Silica Metal Oxide Vesicles Catalyze Comprehensive Prebiotic Chemistry". In: *Chemistry – A European Journal* 24.32, pp. 8126–8132. ISSN: 1521-3765. DOI: 10.1002/chem.201706162. URL: https://onlinelibrary.wiley.com/doi/abs/10.1002/chem.201706162.

Mielke, Randall E. et al. (Oct. 2010). "Design, fabrication, and test of a hydrothermal reactor for origin-of-life experiments". In: *Astrobiology* 10.8. Publisher: Mary Ann Liebert, Inc., publishers, pp. 799–810. ISSN: 1531-1074. DOI: 10.1089/ast.2009.0456. URL: https://www.liebertpub.com/doi/full/10.1089/ast.2009.0456.

Miyazaki, Yoshinori and Jun Korenaga (Mar. 2022). "A wet heterogeneous mantle creates a habitable world in the Hadean". In: *Nature* 603.7899. Publisher: Nature Publishing Group, pp. 86–90. ISSN: 1476-4687. DOI: 10.1038/s41586-021-04371-9. URL: https://www.nature.com/articles/s41586-021-04371-9.

Mohammed, Fiaz S. et al. (Jan. 2017). "A Plausible Prebiotic Origin of Glyoxylate: Nonenzymatic Transamination Reactions of Glycine with Formaldehyde". In: *Synlett* 28.1. Company: Georg Thieme Verlag Distributor: Georg Thieme Verlag Institution: Georg Thieme Verlag Label: Georg Thieme Verlag Publisher: Georg Thieme Verlag, pp. 93–97. ISSN: 0936-5214, 1437-2096. DOI: 10.1055/s-0036-1588657. URL: http://www.thieme-connect.de/DOI/DOI?10.1055/s-0036-1588657.

Muchowska, Kamila B., Sreejith J. Varma, Elodie Chevallot-Beroux, et al. (Nov. 2017). "Metals promote sequences of the reverse Krebs cycle". In: *Nature Ecology & Evolution* 1.11. Number: 11 Publisher: Nature Publishing Group, pp. 1716–1721. ISSN: 2397-334X. DOI: 10.1038/s41559-017-0311-7. URL: https://www.nature.com/articles/s41559-017-0311-7.

Muchowska, Kamila B., Sreejith J. Varma, and Joseph Moran (May 2019). "Synthesis and breakdown of universal metabolic precursors promoted by iron". In: *Nature* 569.7754. Number: 7754 Publisher: Nature Publishing Group, pp. 104–107. ISSN: 1476-4687. DOI: 10.1038/s41586-019-1151-1. URL: https://www.nature.com/articles/s41586-019-1151-1.

Omran, Arthur et al. (June 2023). "Serpentinization-Associated Mineral Catalysis of the Protometabolic Formose System". In: *Life* 13.6. Number: 6 Publisher: Multidisciplinary Digital Publishing Institute, p. 1297. ISSN: 2075-1729. DOI: 10.3390/life13061297. URL: https://www.mdpi.com/2075-1729/13/6/1297.

Origins, Worlds, and Life (2022). *Origins, Worlds, and Life: A Decadal Strategy for Planetary Science and Astrobiology 2023-2032*. Washington, D.C.: National Academies Press. ISBN: 978-0-309-47578-5. DOI: 10.17226/26522. URL: https://www.nap.edu/catalog/26522.

Postberg, Frank et al. (June 2018). "Macromolecular organic compounds from the depths of Enceladus". In: *Nature* 558.7711. Publisher: Nature Publishing Group, pp. 564–568. ISSN: 1476-4687. DOI: 10.1038/s41586-018-0246-4. URL: https://www.nature.com/articles/s41586-018-0246-4.

Rudolph, Amanda et al. (2022). "The Distribution of Clay Minerals and Their Impact on Diagenesis in Glen Torridon, Gale Crater, Mars". In: *Journal of Geophysical Research: Planets* 127.10, e2021JE007098. ISSN: 2169-9100. DOI: 10.1029/2021JE007098. URL: https://onlinelibrary.wiley.com/doi/abs/10.1029/2021JE007098.

Russell, Michael J. (Sept. 2018). "Green Rust: The Simple Organizing 'Seed' of All Life?" In: *Life* 8.3. Number: 3 Publisher: Multidisciplinary Digital Publishing Institute, p. 35. ISSN: 2075-1729. DOI: 10.3390/life8030035. URL: https://www.mdpi.com/2075-1729/8/3/35.

Russell, Michael J., Laura M. Barge, et al. (Apr. 2014). "The Drive to Life on Wet and Icy Worlds". In: *Astrobiology* 14.4. Publisher: Mary Ann Liebert, Inc., publishers, pp. 308–343. ISSN: 1531-1074. DOI: 10.1089/ast.2013.1110. URL: https://www.liebertpub.com/doi/full/10.1089/ast.2013.1110.

Russell, Michael J. and A. J. Hall (May 1997). "The emergence of life from iron monosulphide bubbles at a submarine hydrothermal redox and pH front". In: *Journal of the Geological Society* 154.3, pp. 377–402. ISSN: 0016-7649, 2041-479X. DOI: 10.1144/gsjgs.154.3.0377. URL: https://www.lyellcollection.org/doi/10.1144/gsjgs.154.3.0377.

Russell, Michael J., Allan J. Hall, and Dugald Turner (1989). "In vitro growth of iron sulphide chimneys: possible culture chambers for origin-of-life experiments". In: *Terra Nova* 1.3, pp. 238–241. ISSN: 1365-3121. DOI: 10.1111/j.1365-3121.1989.tb00364.x. URL: https://onlinelibrary.wiley.com/doi/abs/10.1111/j.1365-3121.1989.tb00364.x.

Saladino, Raffaele et al. (May 2016). "A Global Scale Scenario for Prebiotic Chemistry: Silica-Based Self-Assembled Mineral Structures and Formamide". In: *Biochemistry* 55.19. Publisher: American Chemical Society, pp. 2806–2811. ISSN: 0006-2960. DOI: 10.1021/acs.biochem.6b00255. URL: https://doi.org/10.1021/acs.biochem.6b00255.

Sheppard, Rachel Y. et al. (May 2019). "Characterization of Iron in Lake Towuti sediment". In: *Chemical Geology* 512, pp. 11–30. ISSN: 0009-2541. DOI: 10.1016/j.chemgeo.2019.02.029. URL: https://www.sciencedirect.com/science/article/pii/S0009254119300798.

Sojo, Victor et al. (Feb. 2016). "The Origin of Life in Alkaline Hydrothermal Vents". In: *Astrobiology* 16.2. Publisher: Mary Ann Liebert, Inc., publishers, pp. 181–197. ISSN: 1531-1074. DOI: 10.1089/ast.2015.1406. URL: https://www.liebertpub.com/doi/full/10.1089/ast.2015.1406.

Stubbs, R. Trent et al. (Nov. 2020). "A plausible metal-free ancestral analogue of the Krebs cycle composed entirely of α-ketoacids." In: *Nature chemistry* 12.11, pp. 1016–1022. ISSN: 1755-4330. DOI: 10.1038/s41557-020-00560-7. URL: https://www.ncbi.nlm.nih.gov/pmc/articles/PMC8570912/.

Tosca, Nicholas J., Stephen Guggenheim, and Peir K. Pufahl (Mar. 2016). "An authigenic origin for Precambrian greenalite: Implications for iron formation and the chemistry of ancient seawater". In: *GSA Bulletin* 128.3-4, pp. 511–530. ISSN: 0016-7606. DOI: 10.1130/B31339.1. URL: https://doi.org/10.1130/B31339.1.

Vance, Steven, Jelte Harnmeijer, et al. (Dec. 2007). "Hydrothermal systems in small ocean planets". In: *Astrobiology* 7.6. Publisher: Mary Ann Liebert, Inc., publishers, pp. 987–1005. ISSN: 1531-1074. DOI: 10.1089/ast.2007.0075. URL: https://www.liebertpub.com/doi/10.1089/ast.2007.0075.

Vance, Steven D., K. P. Hand, and R. T. Pappalardo (2016). "Geophysical controls of chemical disequilibria in Europa". In: *Geophysical Research Letters* 43.10, pp. 4871–4879. ISSN: 1944-8007. DOI: 10.1002/2016GL068547. URL: https://onlinelibrary.wiley.com/doi/abs/10.1002/2016GL068547.

Vance, Steven D. and M. Melwani Daswani (Jan. 2020). "Serpentinite and the search for life beyond Earth". In: *Philosophical Transactions of the Royal Society A: Mathematical, Physical and Engineering Sciences* 378.2165. Publisher: Royal Society, p. 20180421. DOI: 10.1098/rsta.2018.0421. URL: https://royalsocietypublishing.org/doi/10.1098/rsta.2018.0421.

Varma, Sreejith J. et al. (June 2018). "Native iron reduces CO2 to intermediates and end-products of the acetyl-CoA pathway". In: *Nature Ecology & Evolution* 2.6. Number: 6 Publisher: Nature Publishing Group, pp. 1019–1024. ISSN: 2397-334X. DOI: 10.1038/s41559-018-0542-2. URL: https://www.nature.com/articles/s41559-018-0542-2.

Viviano, Christina E. et al. (2014). "Revised CRISM spectral parameters and summary products based on the currently detected mineral diversity on Mars". In: *Journal of Geophysical Research: Planets* 119.6, pp. 1403–1431. ISSN: 2169-9100. DOI: 10.1002/2014JE004627. URL: https://onlinelibrary.wiley.com/doi/abs/10.1002/2014JE004627.

Waite, J. Hunter et al. (Apr. 2017). "Cassini finds molecular hydrogen in the Enceladus plume: Evidence for hydrothermal processes". In: *Science (New York, N.Y.)* 356.6334, pp. 155–159. ISSN: 1095-9203. DOI: 10.1126/science.aai8703.

Weber, Jessica M. and Laura M. Barge (2021). "Iron-Silicate Chemical Garden Morphology and Silicate Reactivity with Alpha-Keto Acids". In: *ChemSystemsChem* 3.3, e2000058. ISSN: 2570-4206. DOI: 10.1002/syst.202000058. URL: https://onlinelibrary.wiley.com/doi/abs/10.1002/syst.202000058.

Westall, F. et al. (Mar. 2018). "A Hydrothermal-Sedimentary Context for the Origin of Life". In: *Astrobiology* 18.3. Publisher: Mary Ann Liebert, Inc., publishers, pp. 259–293. ISSN: 1531-1074. DOI: 10.1089/ast.2017.1680. URL: https://www.liebertpub.com/doi/10.1089/ast.2017.1680.

Chapter 3

PROPYNE: DETERMINATION OF PHYSICAL PROPERTIES AND UNIT CELL PARAMETERS UNDER TITAN-RELEVANT CONDITIONS

Marlin, Theresa C., Morgan L. Cable, Tuan Vu, Helen E. Maynard-Casely, Melissa Ugelow, Carrie Anderson, Robert Hodyss (May 2024). "Propyne: Determination of Physical Properties and Unit Cell Parameters under Titan-Relevant Conditions". In: *ACS Earth and Space Chemistry* 8.5. Publisher: American Chemical Society, pp. 957–964. DOI: 10.1021/acsearthspacechem.3c00303.

Abstract

With its large size, dense atmosphere, methane-based hydrological-like cycle, and diverse surface features, the Saturnian moon Titan is one of the most unique of the outer Solar System satellites. Study of the photochemically produced molecules in Titan's atmosphere is critical in order to understand the mechanics of the atmosphere and, by extension, the interactions between atmosphere, surface, and subsurface water ocean. One example is propyne vapor, a photochemically produced species in Titan's upper atmosphere expected to condense in Titan's stratosphere at lower altitudes. Propyne may also be a trace species in Titan's stratospheric co-condensed ice clouds detected by the *Cassini* Composite Infrared Spectrometer (CIRS). Bulk structural characterization of propyne ice is currently incomplete and is lacking in published laboratory Raman spectra and X-ray diffraction data. Here, we present a laboratory characterization of propyne ice, including the first published X-ray diffraction and Raman spectroscopy results for propyne ice.

3.1 Introduction

Complex photochemistry in the upper atmosphere of Saturn's moon Titan produces a variety of hydrocarbon, nitrile, and other species with varying distributions throughout the moon's thick atmosphere (Hörst, 2017; Vuitton, Yelle, et al., 2019; Cable, Runčevski, et al., 2021). Among these species, propyne (methylacetylene; $HC{\equiv}C\text{-}CH_3$) vapor is formed in Titan's upper atmosphere via the following reactions (Vuitton, Dutuit, et al., 2014):

Formation: of allene, propyne's isomer:

$$CH + C_2H_4 \rightarrow CH_2CCH_2 + H \tag{3.1}$$

H exchange reaction to form propyne:

$$H + CH_2CCH_2 \rightarrow H + CH_3CCH \tag{3.2}$$

alternative reaction to form propyne:

$$H + C_3H_3 + M^* \rightarrow CH_3CCH + M \tag{3.3}$$

recombination reaction:

$$H + CH_3CCH + M \rightarrow C_3H_5 + M \tag{3.4}$$

degradation by photolysis:

$$C_3H_4 + h\nu \rightarrow C_3H_3 + H \tag{3.5}$$

*: M denotes a neutral body (e.g., N_2) that is required for energy balance in the termolecular reactions.

Propyne gas was first detected in Titan's stratosphere by the InfraRed Interferometer Spectrometer (IRIS) onboard the *Voyager 1* spacecraft in 1981, where the spacecraft passed by Titan shortly after northern spring equinox (Maguire et al., 1981). Nearly one Saturnian year later, the arrival of the *Cassini* spacecraft allowed further observations of these gas species at an analogous time in Titan's seasonal cycle.

Propyne's abundance and distribution in Titan's atmosphere undergo seasonal variation. Titan is predicted to have one pole-to-pole global atmospheric circulation cell with upwelling at the summer pole and subsiding at the winter pole (Teanby, Irwin, Nixon, et al., 2012). Photochemical trace species abundance in Titan's atmosphere is correlated with the satellite's seasons, with increased enrichment occurring at the

winter pole as the global circulation cell carries the organics from the upper stratosphere (Mathé et al., 2020). The atmospheric distribution of propyne was studied contemporaneously with *Cassini* and the Atacama Large Millimeter/submillimeter Array (ALMA). Prior to northern spring equinox, propyne abundance was enriched in the north (Teanby, Irwin, Kok, et al., 2009). ALMA observations in 2012 (shortly after northern spring equinox) revealed a sustained presence of propyne in the northern regions as well as several other photochemically produced trace species (Cordiner et al., 2015). It was theorized that these species were left over from northern winter, when they had been deposited by the reversed global circulation cell and were undergoing slow photochemical destruction. Data from 2010 to 2015 taken by the *Cassini* Composite InfraRed Spectrometer (CIRS) shows the abundance of propyne steadily increasing at southern polar latitudes as the pole transitions into winter (Coustenis, Jennings, Achterberg, Bampasidis, Lavvas, et al., 2016). The southern increase of propyne abundance was separately confirmed with ALMA data (Thelen et al., 2019). While the enrichment of trace species in southern regions was detectable shortly (several Earth years) after equinox, the decrease in trace species in the north was not widespread until six earth years post-equinox (Coustenis, Jennings, Achterberg, Bampasidis, Nixon, et al., 2018). Even then, propyne persisted in the north: data collected five to seven years after equinox revealed constant amounts of propyne in Titan's mid-northern latitudes (Sylvestre et al., 2018). However, its vertical distribution does experience shorter-scale seasonal variation, steepening as the northern hemisphere passes into spring (Lombardo et al., 2019; Vinatier et al., 2015). Despite the prevalence of propyne vapor in Titan's atmosphere throughout a Titan year, pure stratospheric propyne ice has not yet been detected.

Organic ice particles formed in the stratosphere, such as propyne, slowly drift downward. They eventually make their way to the troposphere and are theorized to deposit on Titan's organic-laden surface (Anderson et al., 2018). The deposition rate of propyne onto the surface can be calculated based on modeled condensation flux (Vuitton, Dutuit, et al., 2014). The condensation flux of propyne in Titan's atmosphere has been calculated in several models, but wide variation exists among these values. Krasnopolsky (2009), Lara et al. (1996), and Yung et al. (1984) have predicted column-integrated condensation fluxes of 2.6×10^6 molecules/(cm^2·s), 1.1×10^4 molecules/(cm^{2}s), and 5.7×10^7 molecules/(cm^{2}s), respectively, which (assuming a density of 1000 kg/m^3) corresponds to a propyne deposition rate of 0.23-1200 μm/Myr on Titan's surface (Krasnopolsky, 2009; Lara et al., 1996; Yung et al., 1984). Once deposited, propyne may interact with other organic

species to form surface co-crystals or other cryominerals, as has been experimentally demonstrated to be feasible with other abundant and trace species in Titan-relevant conditions (Cable, Runčevski, et al., 2021; Cable, Vu, Malaska, et al., 2020; Cable, Vu, Malaska, et al., 2019; Maynard-Casely et al., 2016). Co-crystal formation is proposed on Titan via either interactions between photochemical surface deposits and liquid hydrocarbon regions or via solid-state chemistry (Cable, Vu, Maynard-Casely, et al., 2018).

Before propyne's behavior as a co-condensate in stratospheric ice clouds or as a component of a surface co-crystal can be fully understood, pure propyne ice must be fully characterized under Titan-relevant conditions. Additionally, we conducted experiments on pure propyne in conditions that were not Titan-relevant in order to deepen the overall understanding of the chemical and physical properties of this molecular solid. Laboratory characterization of propyne to date has been minimal, with only three laboratory studies found in the literature (Kalasinsky et al., 1983; Crawford, 1940; Hudson, Gerakines, et al., 2021). The two studies published in 1940 and 1983 contain Raman spectra for propyne in liquid and gas phases as well as the infrared spectrum for the gas phase (Kalasinsky et al., 1983; Crawford, 1940) (1940: ~300 to ~3300 cm^{-1}; 1983: 100 to 3400 cm^{-1}; temperature and pressure were not specified). The third study in 2021 was recently published, reporting an infrared temperature series of propyne ice, T_{min} = 8 K, under ultrahigh vacuum (500 to 3600 cm^{-1}) (Hudson, Gerakines, et al., 2021); but to the best of our knowledge, no complementary Raman spectra have been published for solid propyne. Raman spectroscopy provides a powerful tool for bulk structural ice characterization and the identification of phases. Here, we report X-ray diffraction data (collected between 1.5 and 8.5 Å), solid phase Raman spectra (50 to 4000 cm^{-1}), and infrared spectra (600 to 4000 cm^{-1}) in conditions relevant to Titan's atmosphere. To the best of our knowledge, X-ray diffraction data and solid-phase Raman data of propyne have not been made publicly available prior to this work. Our data provide broad qualitative information about bulk structural properties of propyne and provide a foundation for the chemical and physical behaviors of this molecule.

3.2 Experimental Methods

The experimental methods used to gather X-ray diffraction (XRD), Raman, and Infrared (IR) data are described below. Note that none of our methods employed unusually dangerous or hazardous components.

X-ray Diffraction

To gain insights into the bulk structural characteristics of solid propyne, a synchrotron powder diffraction experiment was carried out using the mail-in program at Argonne National Laboratory's Advanced Photon Source (APS) 11-BM beamline. Propyne gas was first condensed via a vacuum manifold into a 0.9 mm borosilicate capillary (Charles Supper Co., Inc.) submerged under liquid nitrogen. While propyne was still frozen, a butane torch was used to flame cut and seal the capillary tube at the appropriate length for the provided sample container. The tube was then allowed to warm up to room temperature, where the propyne melts and equilibrates with its vapor pressure in the headspace (~5 bar). After confirmation that the capillary can withstand this pressure for several days, it was then inserted into a Kapton sleeve and mounted onto the provided sample base and covered by a magnetic cap. Afterward, the sample was shipped to the APS facility, where it was frozen at 90 K and diffraction patterns acquired at various temperatures (90, 100, 120, 140, and 160 K) over the allocated beam time of 8 h. The incident X-ray beam for these collections was λ = 0.458155 Å, with a multianalyzer detection system also used for all data collections.

The synchrotron data were supplemented with experiments prepared in a similar manner using a laboratory Bruker D8 DISCOVER DaVinci instrument. This instrument is equipped with a Cu Kα X-ray source (λ = 1.5406 Å), a linear energy-dispersive LynxEye XE-T 1D detector, and an Oxford Cryosystems 800 cryostream for temperature control to within ± 1 K. Here, a capillary containing liquid propyne was first frozen at 85 K, followed by incremental increases in temperature every 5 K until 120 K. Diffraction patterns were recorded at each temperature point for ~1 h over the 2θ range of 10-60° (angular resolution of 0.02°). Refinements of all experimental patterns from both the synchrotron and laboratory data were undertaken using the Topas suite (version 6) (Coelho, 2018).

Raman

Raman spectra were collected using a high-resolution confocal dispersive micro-Raman spectrometer (Horiba Jobin Yvon LabRam HR), equipped with a 532 nm laser operating at 50 mW, an 1800 grooves/mm diffraction grating, and a 50× Olympus BXFM objective. The system utilized an Oxford MicroStatN liquid nitrogen-cooled vacuum cryostage mounted to the XYZ motorized translation stage underneath the objective turret; the cryostage is capable of reaching temperatures as low as 75 ± 0.5 K. Deposition of the propyne onto the sample plate was conducted through

a 1/16 in. stainless steel tube to control where the deposition occurred. The obtained Raman spectra cover the 50-4000 cm^{-1} frequency range at a 0.4 cm^{-1}/px resolution. The silicon 520.7 cm^{-1} peak was used for frequency calibration. Between two and four spectral accumulations were obtained per final spectrum in order to improve the signal-to-noise ratio.

Multiple temperature dependence studies were conducted. In the first, propyne (Aldrich, >97% purity) was deposited from the gas phase into the cryostage at the lower temperature limit of the system, 75 K. Raman spectra were collected in 5 K increments from 75 to 120 K (with an equilibration time of 5 min at each temperature point). The converse of this experiment was also conducted, with deposition at 120 K followed by cooling in 5 K increments (with the same equilibration time) and corresponding spectral collection until the lower temperature limit of the system was reached. A third experiment was performed in which propyne was condensed at a midpoint of 105 K.

Infrared

The experimental apparatus used for the acquisition of infrared spectra has been described elsewhere (Mahjoub et al., 2018; Johnson et al., 2019; Hodyss et al., 2019). Briefly, propyne ice films were deposited at 15 K on a CsI window cooled by a closed cycle He refrigerator (ARS 202B) at a rate of 4.5 μm/h. The temperature of the window was controlled with a resistive heater and monitored with a Si diode thermometer (DT-670, ± 0.5 K) affixed to the copper window frame. The thickness of the ice film was monitored during growth by laser interferometry (laser wavelength = 637 nm, laser/detector angle ~5°) and was approximately 0.6 μm using an n_0 from the literature that was measured at 15 K and 670 nm (n_0 = 1.370) (Hudson, Gerakines, et al., 2021).

The window is contained within an ultrahigh vacuum system that routinely reaches a base pressure less than 5×10^{-10} Torr. Gas samples are introduced into the vacuum chamber through a separate turbo-pumped line with a base pressure of no more than 1×10^{-6} Torr. The flow of gas into the chamber is regulated with a precision leak valve (VACGEN, LVM Series). The gas enters the chamber through a 1/16 in. diameter stainless-steel tube directed at the deposition window, whose tip is approximately 5 cm from the deposition window. Propyne was used without further purification. No evidence of contaminants was observed in the resultant spectra for propyne.

IR spectra were recorded in transmission with a Nicolet 6700 FTIR spectrometer, at a resolution of 2 cm^{-1} full width at half-maximum. Each spectrum ranged from 600 to 4000 cm^{-1} and is the result of 1000 coadded single scan spectra. Samples were equilibrated for 5 min at the temperature of interest before spectra were collected. Samples were collected in 10 K increments from 15 to 105 K, the latter temperature being the point at which propyne sublimated.

3.3 Results

X-ray Diffraction

Figure 3.1 shows the diffraction pattern of propyne at 90 K obtained from the synchrotron experiment. Indexing of this pattern showed that the observed Bragg peaks could be fit with an orthorhombic unit cell with a = 15.89410(11) Å, b = 13.2987(1) Å and c = 5.7070(6) Å, resulting in a volume of 1206.30(2) $Å^3$. Fitting first with a P222 unit cell revealed a number of systematic absences (in 0kl, h0l, hk0, h00, 0k0, and 00l reflections) that supported the assignment of *Pbca* as the space group for this phase.

Figure 3.2 shows the laboratory XRD patterns of propyne as a function of temperature. A comparison with Figure 3.1 confirms that propyne adopts the same orthorhombic structure as in the synchrotron experiment and maintains this singular crystalline phase between 85 and 120 K. Using the determined *Pbca* space group, Pawley refinements are performed on each of the obtained experimental patterns (from both synchrotron and laboratory sources). The detailed lattice parameters as a function of the temperature are listed in Table 3.1. The relative expansion, where the values are normalized to those at the coldest temperature (85 K), is plotted in Figure 3.3.

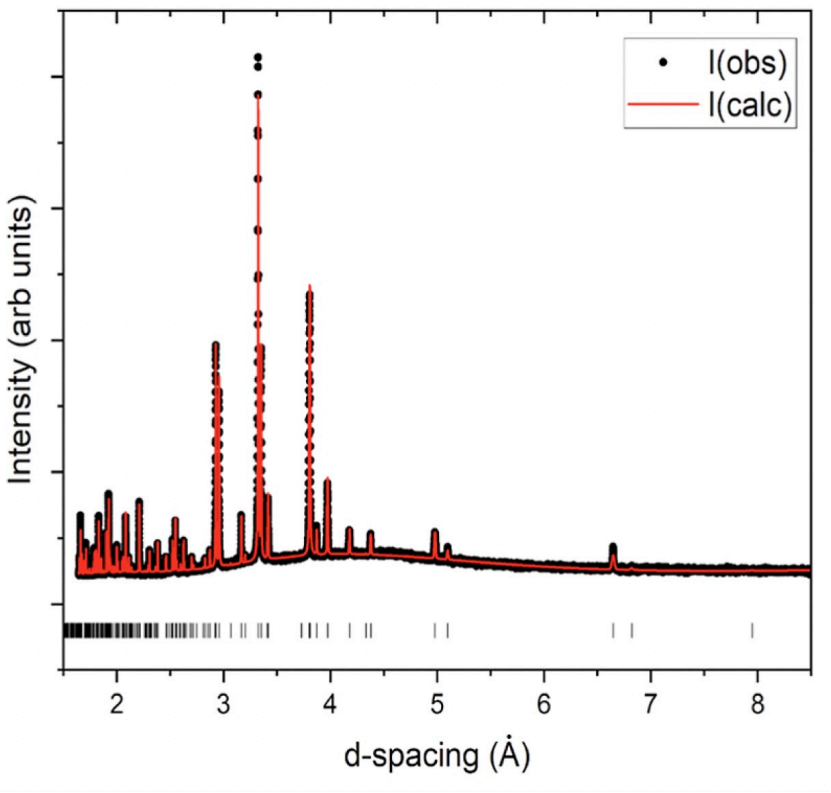


Figure 3.1: Pawley fit of the 90 K synchrotron diffraction data to the *Pbca* unit cell, a = 15.89410(11) Å, b = 13.2987(1) Å, and c = 5.7070(6) Å. Tick marks below the data indicate the expected positions of Bragg peaks from this unit cell. The fit of these data yielded R_{wp} = 8.46%, R_p = 6.21% with peaks described by a Thomson-Cox Hastings model and background by a 7-order Chebyshev polynomial (additional large-width peak included in the background to describe amorphous scattering from the silicate capillary).

Temperature (K)	a (Å)	b (Å)	c (Å)	V (Å^3)
85	15.892(6)	13.287(4)	5.714(7)	1206.6
90	15.902(2)	13.314(7)	5.717(5)	1210.4
95	15.906(0)	13.325(0)	5.718(0)	1211.9
100	15.907(1)	13.342(2)	5.723(2)	1214.6
105	15.914(0)	13.364(0)	5.729(0)	1218.3
110	15.918(0)	13.390(0)	5.735(0)	1222.4
115	15.923(0)	13.418(0)	5.744(0)	1227.4
120	15.926(0)	13.432(0)	5.746(0)	1229.2
140	15.936(0)	13.500(0)	5.763(1)	1239.9
160	15.955(0)	13.573(3)	5.784(1)	1252.5

Table 3.1: Lattice constants and unit cell volumes of propyne over its temperature stability range of 1 bar[a].
[a]: Values were obtained from Pawley refinements.

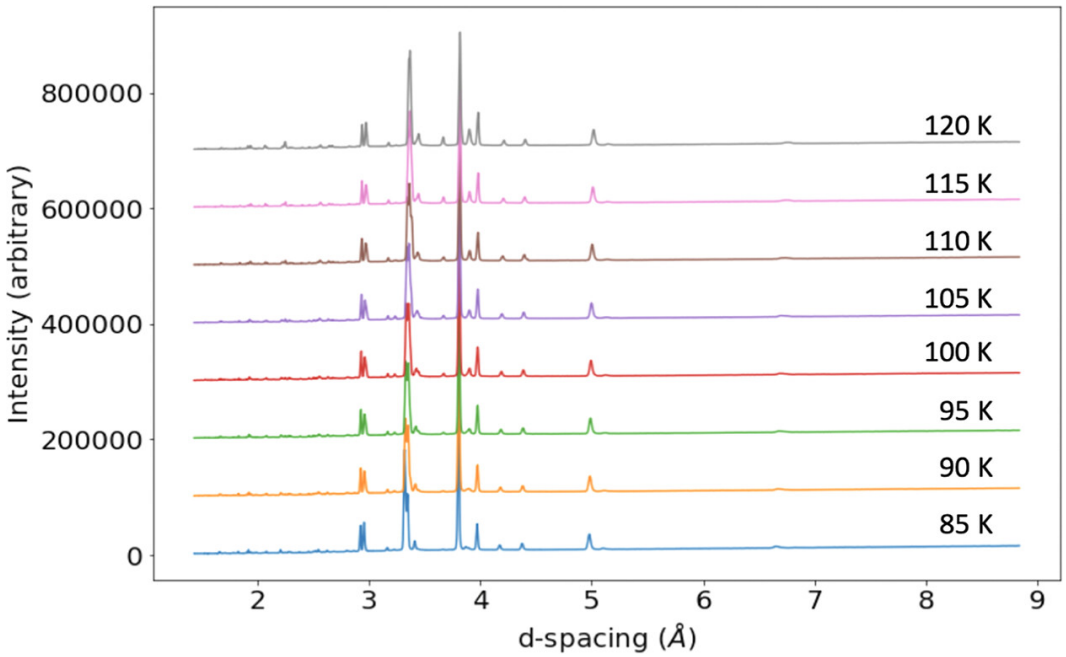


Figure 3.2: Diffraction patterns of propyne obtained on the laboratory X-ray source (λ = 1.5406 Å) as a function of temperatures. The sample was first frozen at 85 K, followed by an incremental temperature increase every 5 K.

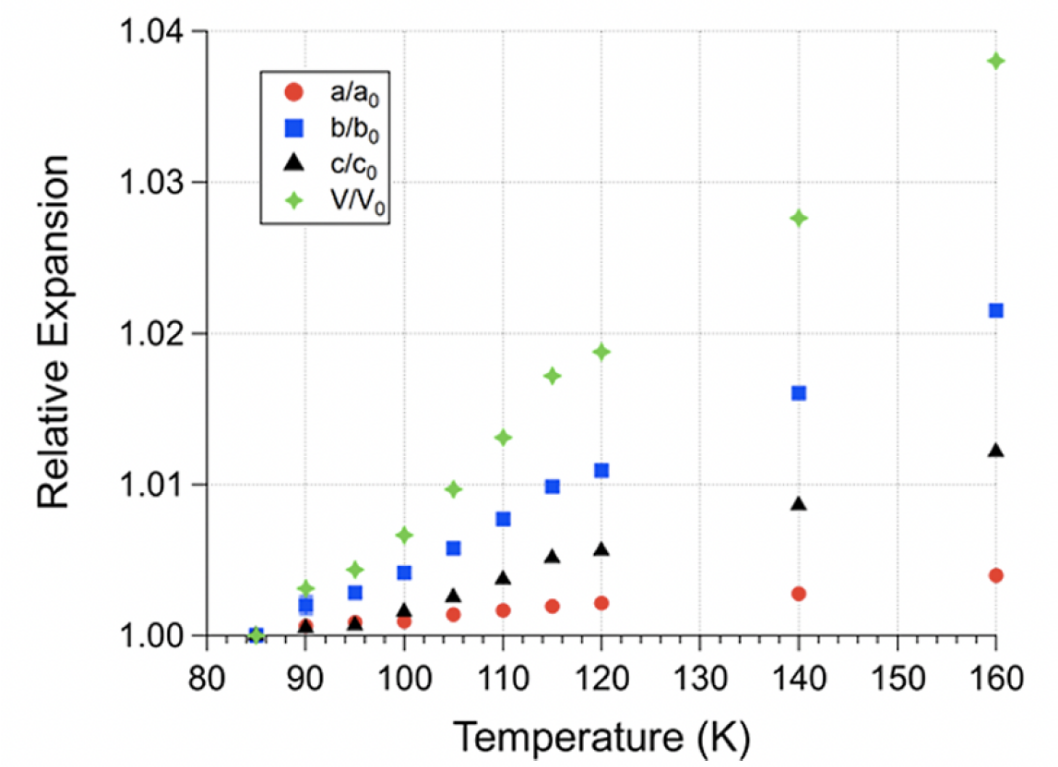


Figure 3.3: Thermal expansion of propyne as derived from Pawley refinements (Table 3.1). Lattice constants and unit cell volumes are normalized to those at the coldest temperature under study (85 K).

Raman

At 125 K under low pressure, the propyne sublimated before a full spectrum could be collected. Thus, spectra for the vacuum series were collected in the range of 75 to 120 K. Deposition at 75 K yielded amorphous-phase propyne, while a deposition at 120 K was crystalline (Figure 3.4). When propyne was incrementally heated following deposition at 75 K, a gradual amorphous-to-crystalline phase transition appeared to occur between 105 and 107 K (Figure B.1). Direct deposition at 105 K corresponded to a crystalline structure (Figure B.2, purple/top trace), and subsequent cooling from a higher-temperature deposition yielded no structural change as the propyne remained in the crystalline phase (Figure B.3).

The difference between the crystalline and amorphous phases can be observed through differentiated features across the Raman spectra. The most diagnostic region of this transition is between 600 and 700 cm^{-1} (H-C≡C bend), where three distinct peaks at low temperature are replaced by a triplet and a doublet at 120 K

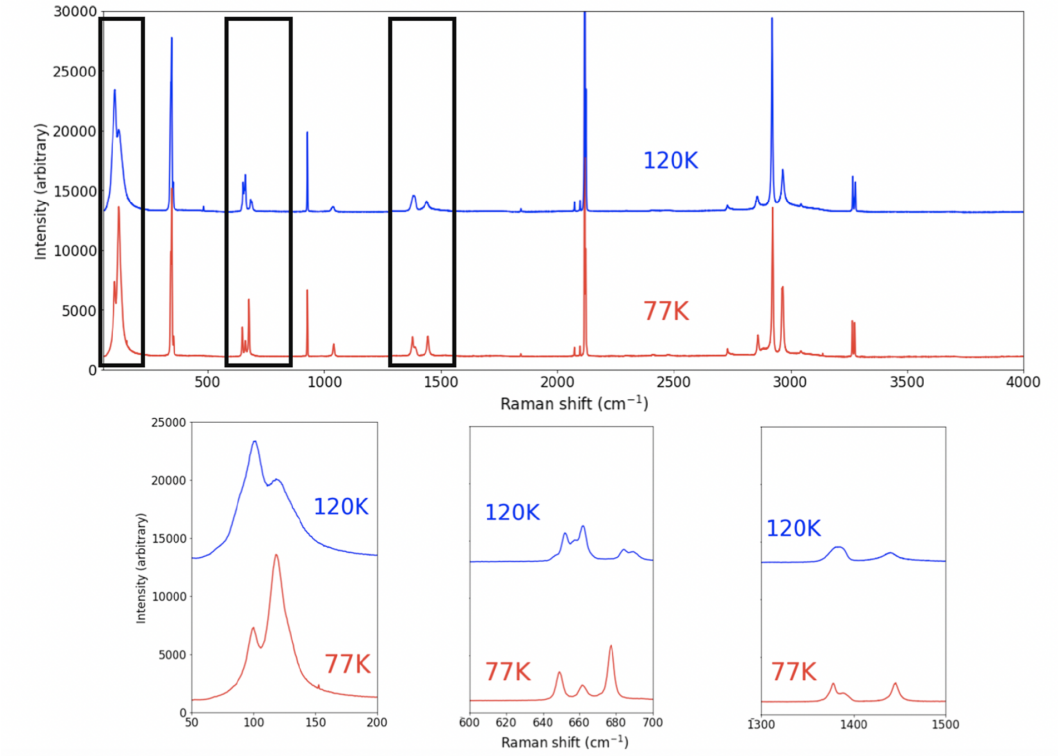


Figure 3.4: Thermal expansion of propyne as derived from Pawley refinements (Table 3.1). Lattice constants and unit cell volumes are normalized to those at the coldest temperature under study (85 K).

(Figure 3.4, second panel). A change in the lattice peak shape accompanies the transition (Figure 3.4, first panel) as well as shifts in peak shape in the CH_3 s-deform and CH_3 d-deform regions (1300-1500 cm^{-1}; Figure 3.4, third panel) and the C-C≡C bend region (300-400 cm^{-1}). Although the H-C≡C bend is a key diagnostic band for changes in the propyne crystal structure, this region is not diagnostic across all alkyne ices: it does not demonstrate appreciable change in previously published infrared data of acetylene (ethyne) (Hudson, Ferrante, et al., 2014). To our knowledge, no detailed studies of larger alkyne ices have been conducted, so it is yet undetermined if this region is broadly diagnostic for nonsymmetric alkynes. Peak positions and assignments are in Table 3.2 (amorphous propyne, 77 K; crystalline propyne, cooled from 120 to 77 K). Assignments are based on previously published works (Kalasinsky et al., 1983; Shimanouchi, 1972).

Description	Amorphous, 77 K		Crystalline, 77 K	
	Wavenumber (cm^{-1})	Peak character	Wavenumber (cm^{-1})	Peak character
Lattice	100	doublet	105	doublet
Lattice	118	doublet	126	doublet
C-C≡C bend	339	doublet		
C-C≡C bend	343	doublet	343	
H-C≡C bend	649		653	triplet
H-C≡C bend			658	triplet
H-C≡C bend	661		663	triplet
H-C≡C bend	677		686	doublet
H-C≡C bend			693	doublet
C-C stretch	928		928	
CH_3 rock	1040		1037	
CH_3 s-deform	1378		1379	
CH_3 d-deform	1446		1438	
C≡C stretch	2117	doublet	2117	doublet
C≡C stretch	2122	doublet	2122	doublet
CH_3 s-stretch	2924		2921	
CH_3 d-stretch	2964	doublet		
CH_3 d-stretch	2968	doublet	2967	
H-C≡ stretch	3265		3264	
H-C≡ stretch	3275		3276	

Table 3.2: Prominent Raman features of propyne.

Infrared

The infrared spectroscopy temperature series data support the XRD crystalline transition temperature (T_{crys} < 85 K), in contrast with the high crystalline temperature transition that resulted from the Raman experiments (T_{crys} ~ 105 K). A sharp change is observed in the infrared spectra between 65 and 75 K, which can be ascribed to an amorphous-to-crystalline transition (Figure 3.5). The most apparent indication is in the 600-750 cm^{-1} region (H-C≡C bend), where a single broad peak at lower temperatures splits into three distinct peaks at and above 75 K. A narrowing and sharpening are also observed for the 3270 cm^{-1} peak (H-C≡ stretch) during the amorphous to crystalline transition. Significant peak wavenumbers and assignments can be found in Table 3.3 (amorphous propyne, 65 K; crystalline propyne, 75 K). Assignments are based on several previously published works (Crawford, 1940; Hudson, Gerakines, et al., 2021; Shimanouchi, 1972; Whitmer, 1974). A full temperature series for IR can be found in Figure B.4.

Description	Wavenumber (cm^{-1})			
	Amorphous, 15 K	Amorphous, 8 K (Hudson et al.)	Crystalline, 70 K	Crystalline, 80 K (Hudson et al.)
H-C≡C bend	649	645	651	(not reported)
H-C≡C bend			679	678
H-C≡C bend			701	700
C-H bend	1437	1437	1440	1441
C≡C stretch	2123	2124	2117	2117
H-C≡C stretch			3266	3266
H-C≡C stretch	3279	3280	3271	(not reported)

Table 3.3: Prominent IR features of propyne and comparison to previous publication.

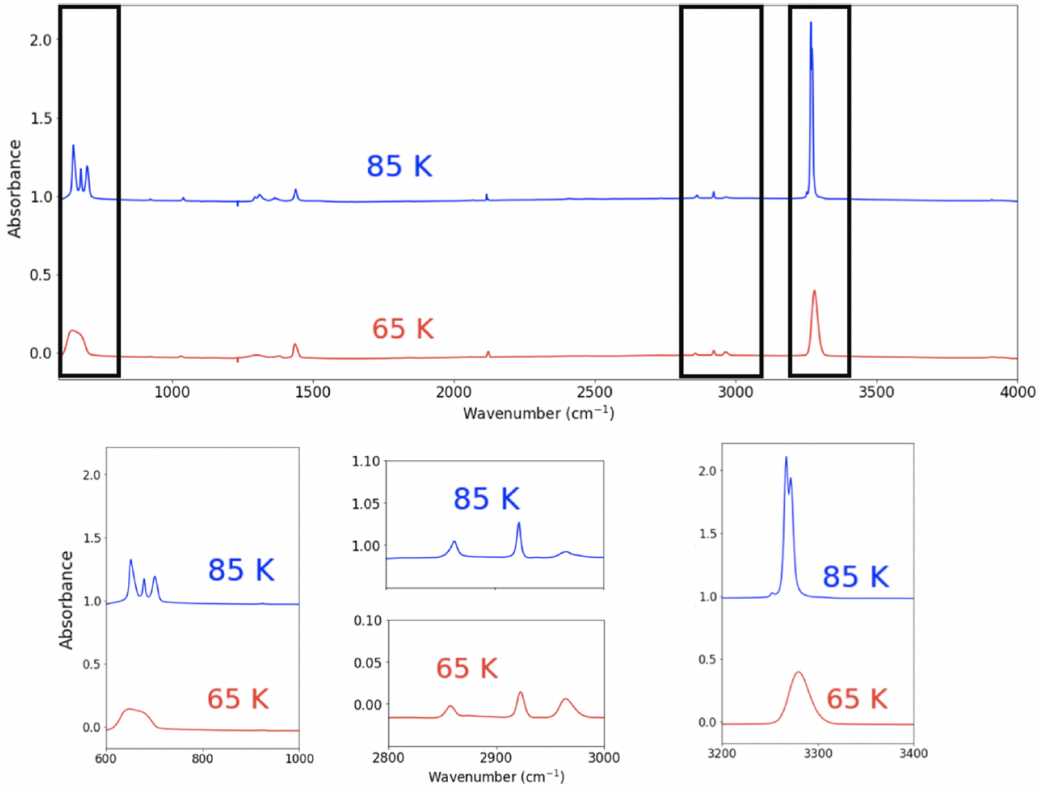


Figure 3.5: Infrared spectra of the amorphous phase (red trace; bottom) and crystalline (blue trace; top) phase propyne ice. Expanded views of characteristic spectral regions are highlighted in the bottom panels.

3.4 Discussion

X-ray Diffraction

The XRD results indicate that there is only one crystalline phase of propyne observed, consistent with previously published vibrational spectroscopic measurements (Hud-

son, Gerakines, et al., 2021). Indexing of the synchrotron data suggests that the crystal structure consists of two independent molecules, justified by the calculated density from the volume of the determined unit cell. The general position in the *Pbca* space group has a multiplicity of 8 — hence pursuing a structure solution with one molecule would result in an unlikely density of 441.05 kg m^{-3}. With two molecules each at a general position, the resultant density is 882.10 kg m^{-3}, on par with the behavior of other small organic solids (877.0 kg m^{-3} for butadiene at 90 K 34 and 830 kg m^{-3} for propane at 30 K 35). A previously published propyne study (Hudson, Gerakines, et al., 2021) measured a density of 866 kg m^{-3} at 80 K, a value in very good agreement to that reported here (determined at 90 K). The interpretation of two independent molecules per unit cell is further supported by the obtained Raman spectra (Figure 3.4), where two peaks are observed for the terminal H-C≡ stretch at 3264 and 3276 cm^{-1} (Table 3.2, indicating two distinct chemical environments for the propyne molecule in the crystalline solid phase. Using this experimentally determined density, we can recalculate the deposition rate on Titan's surface based on published Titan atmosphere models from 0.23-1200 to 0.26-1400 μm/Myr.

While the quality of the powder diffraction data is insufficient to yield a viable crystal structure, the temperature series does indicate significant anisotropy in thermal expansion, with the majority occurring along the b axis. The unit cell volume is found to expand by ∼4% over the temperature range between 85 and 160 K. Such anisotropic behavior and magnitude of expansion are on par with the behavior of other small organic solids that have been characterized under Titan-relevant conditions (e.g., butadiene (Vu et al., 2022), benzene (Czaplinski et al., 2020)).

Raman

The unexpectedly high crystalline phase transition temperature is most likely attributed to the high deposition rate of the Raman system. As early as 1951, it has been noted in literature that the rate and temperature of initial condensation of the compound affect the amorphous-to-crystalline temperature transition (Malherbe et al., 1951). Our infrared spectroscopy system is capable of temperatures approximately 60 K lower than the lowest that our Raman spectroscopy system can reach. The rate of deposition in the infrared spectrometer system was 0.075 μm/min, while that in the Raman spectroscopy system is significantly faster. It seems that the Raman vacuum cryostage is vulnerable to these variations, as the 105 K ice film warmed from 75 K was in mid amorphous-to-crystalline transition, but a direct

deposit at 105 K was entirely crystalline. The 340 cm^{-1} feature seems particularly sensitive to the deposition environment (Figure S2). Although the direct deposition spectral trace (purple; top, deposited at 105 K) is nearly indistinguishable from the crystalline phase observed in the decreasing temperature series (green; middle, deposited at 120 K), the 340 cm^{-1} feature exhibits variation. The direct deposition feature has the primary peak and two pronounced shoulders, while the decreasing temperature feature at this frequency has only one slight shoulder.

Infrared

The observed 75 K crystalline transition temperature, determined from infrared spectroscopy experiments, is consistent with those published by Hudson et al. (2021). Hudson et al. reported that the amorphous-to-crystalline phase change for propyne occurred around 70 K and was completed by 80 K. Note that Hudson et al. did not perform propyne experiments at 75 K. Minor differences in the amorphous-to-crystalline phase change temperatures between our work and that of Hudson et al. can be attributed to variations in deposition and annealing temperatures, deposition rates, and experimental procedures and setups. Our IR spectroscopy results affirm the XRD results that propyne is crystalline at 85 K and reinforces the impact of the fast deposition rate of the Raman experiments, which is the primary cause of the 30 K increase in the observed amorphous-to-crystalline transition temperature of 105 K. We do note that the IR and Raman vacuum system pressures were not identical, which could cause additional [minor] variations among the observed amorphous-to-crystalline transition temperatures.

3.5 Conclusions

We present the first X-ray diffraction and Raman spectroscopy data of propyne ice. From infrared spectroscopy, Raman spectroscopy, X-ray diffraction, and thermal expansion data, it can be concluded that propyne has one solid amorphous phase and one solid crystalline phase, a finding that is in agreement with previous work (Hudson, Gerakines, et al., 2021). From XRD, we conclude that the propyne structure is orthorhombic, with a crystalline transition temperature less than 85 K and a corresponding density of 882.10 kg m^{-3}. This density is consistent with that calculated by Hudson et al. (2021) at 80 K. From the IR spectroscopy experiments, we determined a crystalline transition temperature of 75 K, consistent with that of Hudson et al. (2021). Thus, if pure propyne were to condense in Titan's stratosphere, it would condense in its crystalline phase.

3.6 Author Information

Corresponding Author

Theresa C. Marlin — NASA Jet Propulsion Laboratory, California Institute of Technology, Pasadena, California 91109, United States; Division of Geological and Planetary Sciences, California Institute of Technology, Pasadena, California 91125, United States; orcid.org/0009-0003- 0670-5474; Email: tmarlin@caltech.edu

Authors

Morgan L. Cable — NASA Jet Propulsion Laboratory, California Institute of Technology, Pasadena, California 91109, United States; orcid.org/0000-0002-3680-302X

Tuan H. Vu — NASA Jet Propulsion Laboratory, California Institute of Technology, Pasadena, California 91109, United States; orcid.org/0000-0001-6839-9765

Helen E. Maynard-Casely — Australian Nuclear Science and Technology Organisation, Kirrawee DC, New South Wales 2234, Australia; orcid.org/0000-0001-6364-9665 Melissa Ugelow — NASA Goddard Space Flight Center, Greenbelt, Maryland 20771, United States

Carrie Anderson — NASA Goddard Space Flight Center, Greenbelt, Maryland 20771, United States

Robert Hodyss — NASA Jet Propulsion Laboratory, California Institute of Technology, Pasadena, California 91109, United States

Author Contributions

The manuscript was written through contributions of all authors. All authors have approved the final version of the manuscript.

Funding

T.C.M. was funded by NSF GRFP. All other authors were funded by a *Cassini* Data Analysis Program grant.

Notes

The authors declare no competing financial interest.

3.7 Acknowledgements

This work was conducted at the Jet Propulsion Laboratory, California Institute of Technology, under a contract with the National Aeronautics and Space Administration (80NM0018D0004). Reference herein to any specific commercial product, process, or service by trade name, trademark, manufacturer, or otherwise does not constitute or imply its endorsement by the United States Government or the Jet Propulsion Laboratory, California Institute of Technology. T.C.M. was funded by NSF GRFP. All other authors were funded by a *Cassini* Data Analysis Program grant. This research used resources of the Advanced Photon Source, a U.S. Department of Energy (DOE) Office of Science user facility operated for the DOE Office of Science by Argonne National Laboratory under Contract no. DE-AC02-06CH11357.
©2023. All rights reserved.

3.8 Abbreviations

ALMA, Atacama Large Millimeter/submillimeter Array; CIRS, Composite InfraRed Spectrometer; XRD, X-ray Diffraction

References

Anderson, Carrie M., R. E. Samuelson, and D. Nna-Mvondo (Nov. 2018). "Organic Ices in Titan's Stratosphere". In: *Space Science Reviews* 214.8, p. 125. ISSN: 1572-9672. DOI: 10.1007/s11214-018-0559-5. URL: https://doi.org/10.1007/s11214-018-0559-5.

Cable, Morgan L., Tomče Runčevski, et al. (Aug. 2021). "Titan in a Test Tube: Organic Co-crystals and Implications for Titan Mineralogy". In: *Accounts of Chemical Research* 54.15. Publisher: American Chemical Society, pp. 3050–3059. ISSN: 0001-4842. DOI: 10.1021/acs.accounts.1c00250. URL: https://doi.org/10.1021/acs.accounts.1c00250.

Cable, Morgan L., Tuan H. Vu, Michael J. Malaska, et al. (Dec. 2019). "A Co-Crystal between Acetylene and Butane: A Potentially Ubiquitous Molecular Mineral on Titan". In: *ACS Earth and Space Chemistry* 3, pp. 2808–2815. DOI: 10.1021/acsearthspacechem.9b00275. URL: https://ui.adsabs.harvard.edu/abs/2019ESC.....3.2808C.

– (Aug. 2020). "Properties and Behavior of the Acetonitrile–Acetylene Co-Crystal under Titan Surface Conditions". In: *ACS Earth and Space Chemistry* 4.8. Publisher: American Chemical Society, pp. 1375–1385. DOI: 10.1021/acsearthspacechem.0c00129. URL: https://doi.org/10.1021/acsearthspacechem.0c00129.

Cable, Morgan L., Tuan H. Vu, Helen E. Maynard-Casely, et al. (Apr. 2018). "The Acetylene-Ammonia Co-crystal on Titan". In: *ACS Earth and Space Chem-*

istry 2.4. Publisher: American Chemical Society, pp. 366–375. DOI: 10.1021/acsearthspacechem.7b00135.

Coelho, Alan A. (Feb. 2018). "TOPAS and TOPAS-Academic: an optimization program integrating computer algebra and crystallographic objects written in C++". In: *Journal of Applied Crystallography* 51.1. Publisher: International Union of Crystallography, pp. 210–218. ISSN: 1600-5767. DOI: 10.1107/S1600576718000183. URL: https://journals.iucr.org/j/issues/2018/01/00/jo5037/.

Cordiner, Martin A. et al. (Feb. 2015). "Ethyl Cyanide on Titan: Spectroscopic Detection and Mapping Using ALMA". In: *The Astrophysical Journal* 800.1. Publisher: American Astronomical Society, p. L14. ISSN: 2041-8205. DOI: 10.1088/2041-8205/800/1/L14. URL: https://doi.org/10.1088/2041-8205/800/1/l14.

Coustenis, Athena, D. E. Jennings, R. K. Achterberg, G. Bampasidis, C. A. Nixon, et al. (Feb. 2018). "Seasonal Evolution of Titan's Stratosphere Near the Poles". In: *The Astrophysical Journal* 854.2. Publisher: American Astronomical Society, p. L30. ISSN: 2041-8205. DOI: 10.3847/2041-8213/aaadbd. URL: https://doi.org/10.3847/2041-8213/aaadbd.

Coustenis, Athena, Donald E. Jennings, Richard K. Achterberg, Georgios Bampasidis, Panayiotis Lavvas, et al. (May 2016). "Titan's temporal evolution in stratospheric trace gases near the poles". In: *Icarus*. Titan's Surface and Atmosphere 270, pp. 409–420. ISSN: 0019-1035. DOI: 10.1016/j.icarus.2015.08.027. URL: https://www.sciencedirect.com/science/article/pii/S0019103515003711.

Crawford, Bryce L. (July 1940). "Infra-Red and Raman Spectra of Polyatomic Molecules XII. Methyl Acetylene". In: *The Journal of Chemical Physics* 8.7. Publisher: American Institute of Physics, pp. 526–531. ISSN: 0021-9606. DOI: 10.1063/1.1750706. URL: https://aip.scitation.org/doi/10.1063/1.1750706.

Czaplinski, Ellen et al. (Dec. 2020). "Experimental Investigation of the Acetylene–Benzene Cocrystal on Titan". In: *The Planetary Science Journal* 1.3. Publisher: IOP Publishing, p. 76. ISSN: 2632-3338. DOI: 10.3847/PSJ/abbf57. URL: https://iopscience.iop.org/article/10.3847/PSJ/abbf57/meta.

Hodyss, Robert et al. (Apr. 2019). "Ultraviolet Spectroscopy and Photochemistry of SO2/H2O Ices". In: *ACS Earth and Space Chemistry* 3.4. Publisher: American Chemical Society, pp. 663–668. DOI: 10.1021/acsearthspacechem.9b00034. URL: https://doi.org/10.1021/acsearthspacechem.9b00034.

Hörst, Sarah M. (2017). "Titan's atmosphere and climate". In: *Journal of Geophysical Research: Planets* 122.3, pp. 432–482. ISSN: 2169-9100. DOI: 10.1002/2016JE005240. URL: https://onlinelibrary.wiley.com/doi/abs/10.1002/2016JE005240.

Hudson, Reggie L., R. F. Ferrante, and M. H. Moore (Jan. 2014). "Infrared spectra and optical constants of astronomical ices: I. Amorphous and crystalline acetylene". In: *Icarus* 228, pp. 276–287. ISSN: 0019-1035. DOI: 10.1016/j.icarus.2013.08.029. URL: https://www.sciencedirect.com/science/article/pii/S0019103513003783.

Hudson, Reggie L., Perry A. Gerakines, et al. (Jan. 2021). "Infrared spectra and optical constants of astronomical ices: III. Propane, propylene, and propyne". In: *Icarus* 354, p. 114033. ISSN: 0019-1035. DOI: 10.1016/j.icarus.2020.114033. URL: https://www.sciencedirect.com/science/article/pii/S0019103520303924.

Johnson, Paul V., Charles R. Markus, and Robert Hodyss (Nov. 2019). "Photochemistry of Ozone–Water Ices". In: *ACS Earth and Space Chemistry* 3.11. Publisher: American Chemical Society, pp. 2430–2436. DOI: 10.1021/acsearthspacechem.9b00189. URL: https://doi.org/10.1021/acsearthspacechem.9b00189.

Kalasinsky, Victor F. and T. S. Little (Aug. 1983). "Raman spectra and vibrational dephasing of methylacetylene". In: *Journal of Raman Spectroscopy* 14.4, pp. 253–258. ISSN: 03770486. DOI: 10.1002/jrs.1250140408. URL: https://onlinelibrary.wiley.com/doi/10.1002/jrs.1250140408.

Krasnopolsky, Vladimir A. (May 2009). "A photochemical model of Titan's atmosphere and ionosphere". In: *Icarus* 201.1, pp. 226–256. ISSN: 0019-1035. DOI: 10.1016/j.icarus.2008.12.038. URL: https://www.sciencedirect.com/science/article/pii/S0019103509000062.

Lara, Luisa M. et al. (1996). "Vertical distribution of Titan's atmospheric neutral constituents". In: *Journal of Geophysical Research: Planets* 101.E10, pp. 23261–23283. ISSN: 2156-2202. DOI: 10.1029/96JE02036. URL: https://onlinelibrary.wiley.com/doi/abs/10.1029/96JE02036.

Lombardo, Nicholas A et al. (Jan. 2019). "Spatial and seasonal variations in C3Hx hydrocarbon abundance in Titan's stratosphere from Cassini CIRS observations". In: *Icarus* 317, pp. 454–469. ISSN: 0019-1035. DOI: 10.1016/j.icarus.2018.08.027. URL: https://www.sciencedirect.com/science/article/pii/S0019103518300939.

Maguire, William C. et al. (Aug. 1981). "C3H8 and C3H4 in Titan's atmosphere". In: *Nature* 292.5825. Number: 5825 Publisher: Nature Publishing Group, pp. 683–686. ISSN: 1476-4687. DOI: 10.1038/292683a0. URL: https://www.nature.com/articles/292683a0.

Mahjoub, Ahmed and Robert Hodyss (Dec. 2018). "Thermal Reaction in Cometary and Pre-cometary Ices: Formation of Thiocarbamate in OCS-CH_3NH_2 Mixed Ices". In: *The Astrophysical Journal* 869.2. Publisher: The American Astronomical Society, p. 98. ISSN: 0004-637X. DOI: 10.3847/1538-4357/aaec09. URL: https://dx.doi.org/10.3847/1538-4357/aaec09.

Malherbe, F. E. and H. J. Bernstein (Dec. 1951). "Infrared Spectra of Rapidly Solidified Vapors". In: *The Journal of Chemical Physics* 19.12. Publisher: American Institute of Physics, pp. 1607–1608. ISSN: 0021-9606. DOI: 10.1063/1.1748132. URL: https://aip.scitation.org/doi/10.1063/1.1748132 (visited on 01/16/2023).

Mathé, Christophe et al. (July 2020). "Seasonal changes in the middle atmosphere of Titan from Cassini/CIRS observations: Temperature and trace species abundance profiles from 2004 to 2017". In: *Icarus*. Cassini Mission Science Results 344, p. 113547. ISSN: 0019-1035. DOI: 10.1016/j.icarus.2019.113547. URL: https://www.sciencedirect.com/science/article/pii/S0019103519304774.

Maynard-Casely, Helen E. et al. (May 2016). "A co-crystal between benzene and ethane: a potential evaporite material for Saturn's moon Titan". In: *IUCrJ* 3.3. Publisher: International Union of Crystallography, pp. 192–199. ISSN: 2052-2525. DOI: 10.1107/S2052252516002815. URL: //scripts.iucr.org/cgi-bin/paper?bi5052.

Shimanouchi, Takehiko (1972). "Tables of Molecular Vibrational Frequencies Consolidated Volume I". In: pp. 1–160.

Sylvestre, Melody et al. (Jan. 2018). "Seasonal evolution of C2N2, C3H4, and C4H2 abundances in Titan's lower stratosphere". In: *Astronomy & Astrophysics* 609. Publisher: EDP Sciences, A64. ISSN: 0004-6361, 1432-0746. DOI: 10.1051/0004-6361/201630255. URL: https://www.aanda.org/articles/aa/abs/2018/01/aa30255-16/aa30255-16.html.

Teanby, Nicholas A., P. G. J. Irwin, R. de Kok, et al. (Aug. 2009). "Titan's stratospheric C2N2, C3H4, and C4H2 abundances from Cassini/CIRS far-infrared spectra". In: *Icarus* 202.2, pp. 620–631. ISSN: 0019-1035. DOI: 10.1016/j.icarus.2009.03.022. URL: https://www.sciencedirect.com/science/article/pii/S001910350900133X.

Teanby, Nicholas A., P. G. J. Irwin, Conor A. Nixon, et al. (Nov. 2012). "Active upper-atmosphere chemistry and dynamics from polar circulation reversal on Titan". In: *Nature* 491.7426. Publisher: Nature Publishing Group, pp. 732–735. ISSN: 1476-4687. DOI: 10.1038/nature11611. URL: https://www.nature.com/articles/nature11611.

Thelen, Alexander E. et al. (Feb. 2019). "Abundance measurements of Titan's stratospheric HCN, HC3N, C3H4, and CH3CN from ALMA observations". In: *Icarus* 319, pp. 417–432. ISSN: 0019-1035. DOI: 10.1016/j.icarus.2018.09.023. URL: https://www.sciencedirect.com/science/article/pii/S0019103518304184.

Vinatier, Sandrine et al. (Apr. 2015). "Seasonal variations in Titan's middle atmosphere during the northern spring derived from Cassini/CIRS observations". In: *Icarus* 250, pp. 95–115. ISSN: 0019-1035. DOI: 10.1016/j.icarus.2014.11.

019. URL: https://www.sciencedirect.com/science/article/pii/S0019103514006472.

Vu, Tuan H. et al. (Oct. 2022). "1,3-Butadiene on Titan: Crystal Structure, Thermal Expansivity, and Raman Signatures". In: *ACS Earth and Space Chemistry* 6.10. Publisher: American Chemical Society, pp. 2274–2281. DOI: 10.1021/acsearthspacechem.1c00364. URL: https://doi.org/10.1021/acsearthspacechem.1c00364 (visited on 03/21/2023).

Vuitton, Veronique, O. Dutuit, et al. (2014). "Chemistry of Titan's atmosphere". In: *Titan: Interior, Surface, Atmosphere, and Space Environment*. Ed. by Caitlin A. Griffith et al. Cambridge Planetary Science. Cambridge: Cambridge University Press, pp. 224–284. ISBN: 978-0-521-19992-6. DOI: 10.1017/CBO9780511667398.010. URL: https://www.cambridge.org/core/books/titan/chemistry-of-titans-atmosphere/3BF6496A74C040D542A643300F58C2F7.

Vuitton, Veronique, R. V. Yelle, et al. (May 2019). "Simulating the density of organic species in the atmosphere of Titan with a coupled ion-neutral photochemical model". In: *Icarus* 324, pp. 120–197. ISSN: 0019-1035. DOI: 10.1016/j.icarus.2018.06.013. URL: https://www.sciencedirect.com/science/article/pii/S0019103517307522.

Whitmer, John C. (1974). "Normal coordinates and potential energy distributions of methyl acetylene and some halogen substituted analogues". In: DOI: 10.1016/0022-2860(74)80044-X.

Yung, Yuk L., M. Allen, and J. P. Pinto (July 1984). "Photochemistry of the atmosphere of Titan: comparison between model and observations". In: *The Astrophysical Journal. Supplement Series* 55.3, pp. 465–506. ISSN: 0067-0049. DOI: 10.1086/190963.

Chapter 4

ZONAL WINDS IN TITAN'S MIDDLE ATMOSPHERE FROM A STELLAR OCCULTATION OBSERVED WITH KECK ADAPTIVE OPTICS

Marlin, Theresa C., Eliot F. Young, Katherine de Kleer, Martin Cordiner, Nicholas A. Lombardo, Imke de Pater, Juan M. Lora, Paul Corlies, Richard Cosentino, Conor Nixon, Sébastien Rodriguez, Alexander Thelen (Dec. 2025). "Zonal Winds in Titan's Middle Atmosphere from a Stellar Occultation Observed with Keck Adaptive Optics". In: *The Planetary Science Journal* 6.12, p. 286. DOI: 10.3847/PSJ/ae03a6. URL: https://doi.org/10.3847/PSJ/ae03a6.

Abstract

We present spatially resolved Keck/NIRC2 images of a stellar occultation by Titan on 2022 September 5 and compare them to predictions from concurrent Atacama Large Millimeter/submillimeter Array (ALMA) observations and a suite of general circulation model (GCM) simulations. ALMA data and GCM simulations can predict middle atmosphere zonal wind distributions, which in turn produce diagnostic occultation image sequences. We construct an occultation forward model using the temperature profile measured by the Huygens Atmospheric Structure Instrument, which is then distorted using latitudinal zonal wind profiles from the ALMA data or GCM simulations. The occultation forward model yields simulated light distributions around Titan's limb, which we compare directly to the light distributions observed during the occultation. The GCM zonal wind profile corresponding to slightly before the time of the stellar occultation provides the best overall match to the data. The ALMA wind profile provided the best match to the occultation data when only the ingress data were considered, but did not perform as well when data from ingress and egress were combined. Our data support the presence of stronger winds in the southern hemisphere during late northern summer.

4.1 Introduction

Titan's thick, hazy atmosphere is the site of photochemical dissociation of the atmospheric constituents molecular nitrogen (N_2) and methane (CH_4), and subsequent recombination and synthesis of complex organic species (Willacy et al., 2022; Nixon, 2024). Photochemical pathways in Titan's atmosphere generate heavier molecules that descend through the atmosphere, and eventually get deposited across Titan's geologically varied surface (Brown et al., 2010; Hörst, 2017). The intimate interactions of Titan's surface and atmosphere result in an active world (MacKenzie et al., 2021), where molecules created by complex chemistry high in the atmosphere eventually reach the dunes, lakes, plains, and mountains of Titan, crusting the water-ice surface and settling in the polar lakes (Soderblom et al., 2007; Clark et al., 2010).

The composition of Titan's atmosphere is also dependent on the satellite's atmospheric dynamics (Flasar and Achterberg, 2008), which undergo seasonal variations over the course of Saturn's 29.5 Earth year orbit (Teanby, Irwin, Nixon, et al., 2012; Teanby, Kok, et al., 2008; Teanby, Irwin, Kok, et al., 2007). We use solar longitude (L_s) as a metric of where Titan is in its orbit around the Sun in order to compare data from across different times in Titan's year. $L_s = 0°$ refers to northern vernal equinox, $L_s = 90°$ is northern summer solstice, $L_s = 180°$ is northern autumnal equinox, and $L_s = 270°$ is northern winter solstice. The middle atmosphere is thought to most often have a single thermally direct circulation cell that stretches from pole to pole, with upwelling at the summer pole and subsidence at the winter pole (Teanby, Irwin, Nixon, et al., 2012). During vernal and autumnal equinox, the circulation cell reverses, and the atmosphere is predicted to briefly sustain two equator-to-pole circulation cells (Hörst, 2017). General circulation model (GCM) simulations likewise predict that the middle atmospheric zonal winds follow a cyclical pattern over the course of a Titan year, with rapid changes occurring around the equinoxes (Hourdin et al., 1995; Newman et al., 2011; Lombardo et al., 2023b; Lombardo et al., 2023a).

Complete characterization of Titan's atmospheric dynamics relies on accurate measurements of Titan's atmospheric winds, which are challenging to acquire directly. Efforts to study Titan's middle atmospheric zonal winds have included applying the thermal wind equation to *Cassini* Composite InfraRed Spectrometer (CIRS) temperature measurements (Achterberg, Conrath, et al., 2008; Achterberg, Gierasch, et al., 2011; Achterberg, 2023), measurements of the Doppler shifts of atmospheric

species' emission lines (e.g., Lellouch et al., 2019a; Cordiner et al., 2020) and analysis of stellar occultation data (e.g., Sicardy et al., 2006; Zalucha et al., 2007). Each of these methods has its shortcomings: CIRS is limited in temporal and spatial scope by *Cassini*'s lifespan and Titan fly-bys and is also unable to retrieve wind speeds near the equator; stellar occultations are dependent on a fortuitous alignment of a sufficiently bright star, Titan, and an adequate telescope on a clear night; and Doppler shift measurements predict a single zonal wind profile for a range of altitudes that corresponds to the peak of the measured molecule's contribution function. However, when used in concert, these techniques provide insight into a challenging and essential region of Titan's atmosphere. In this paper, we present both spatially-resolved data from a 2022 stellar occultation (L_s = 160°) captured with adaptive optics (AO) and Doppler shift measurements of millimeter emission lines of the CH_3CN molecule, whose contribution function peaks around 300 km in Titan's atmosphere. We use a forward model to compare our occultation data to a wind field derived from the Atacama Large Millimeter/submillimeter Array (ALMA) Doppler shift measurements, as well as to wind fields from an existing GCM simulation for Titan's middle atmosphere. The altitude ranges for these three methods are complementary, with occultation data probing altitudes of roughly 180-500 km, CH_3CN Doppler shift measurements centering around 200-400 km (with limited sensitivity up to 800 km), and GCM simulations providing predictions for altitudes up to 650 km.

Titan's zonal winds via stellar occultations

While occultations are often used to infer shape or ring properties of Solar System bodies, a stellar occultation by a body with a thick atmosphere presents special opportunities for atmospheric characterization. During a stellar occultation, Titan's thick atmosphere refracts starlight rays, causing light "spots" to be visible around the limb of the moon, even when an occulted star is physically located behind Titan's disk. The behavior and characteristics of these lightspots are sensitive to Titan's atmospheric density field between the stratosphere and mesosphere (altitudes of roughly 180–500 km): rays at lower altitudes are attenuated by differential refraction, while the density gradient at higher altitudes is too slight to sufficiently bend rays when the star is behind Titan's disk. Integrated line-of-sight refractivities can be calculated from densities, which allow tracing of starlight as it is bent by Titan's atmosphere. The location of the observed refracted starlight is highly sensitive to nonspherical atmospheric distortions, which are in turn related to atmospheric zonal

wind patterns. Thus, by modeling the behavior of the starlight as it passes through Titan's atmosphere, Titan's zonal wind behavior can be estimated at the time of the occultation.

The occultation shadow cast by Titan on Earth is not completely devoid of starlight: the light refracted by Titan's limb fills the shadow in ways that depend on the non-spherical shape of Titan's atmosphere. A uniformly rotating body with an atmosphere has an oblate shape that depends on the body's gravitational field and the rotation period. A common approximation uses the gravitational J_2 term, the equatorial radius (a), the uniform angular velocity (ω) and the surface gravity (g) to express the eccentricity (e) of the atmosphere (Eq. 6 from Hubbard et al., 1993):

$$e = \frac{3}{2}J_2 + \frac{1}{2}\frac{a\omega^2}{g}. \tag{4.1}$$

Oblate planets have a bright diamond-shape caustic feature in the middle of the shadow (where "caustic" means a concentration of light rays), and observers on chords that intersect this caustic see bright features near the midpoint of the occultation, referred to as "central flash" features. The caustic and central flash features are highly sensitive to deviations from oblateness (Figure 4.1). The high sensitivity of central flash features to nonspherical atmospheric distortions and therefore zonal wind patterns allows zonal wind profiles to be studied via investigation of central flash features.

Previous investigations (e.g., Hubbard et al., 1993) have used central flash features to deduce zonal winds as a function of latitude. Hubbard et al., 1993 observed Titan occulting the bright (V_{mag} 5.4) star 28 Sagittarius (28 Sgr), with the center of the occultation path crossing over densely populated areas with a number of observatories. Using a "picket fence" series of observations located at different latitudes, observers were able to collect 23 lightcurves of Titan as it passed in front of 28 Sgr. Although no spatially resolved data were obtained, Hubbard et al., 1993 acquired central flash data during the middle of the event from 8 of their 15 sites. They showed that these central flashes were inconsistent with a simple oblate model of Titan's atmosphere, regardless of whether Titan's solid-body rotation or a faster rotation (i.e., a superrotating atmosphere) was assumed. Instead, their best-fit model required fast zonal winds with peak velocities of ~175 m s^{-1} at latitudes near 65°N and 65°S, and much slower winds (~90 m s^{-1}) near the equator.

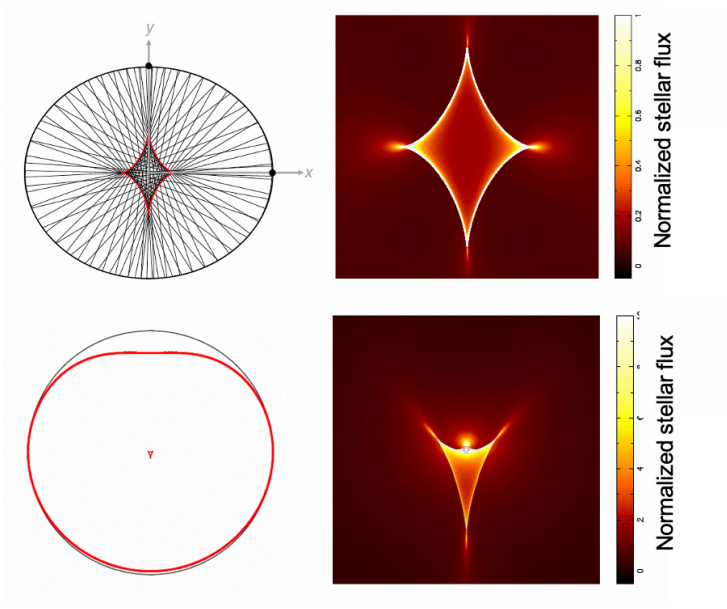


Figure 4.1: The top panels show the diamond-shaped caustic (concentration of light rays) that results from a planet with a uniformly rotating, oblate atmosphere (depicted as a black oval, top left panel). The black lines represent refracted starlight, and the caustic is highlighted in red. The top right panel depicts a magnified version of the caustic for the atmosphere on the left, showing the abrupt variations in flux that are present. Observation chords intersecting the caustic show rapid changes in flux at the center of an occultation event, allowing observers to determine the shape of the caustic. The bottom panels show the caustic that is formed in an alternative case: when the atmosphere is not uniformly rotating, but rather has a strong zonal wind in the north causing atmospheric distortion (highlighted by the red flattened circle outline). The distorted atmosphere produces a triangle-shaped caustic (the red triangle in the middle of the bottom left panel); the caustic and its flux variations are depicted in the bottom right panel. As in the case of the oblate atmosphere, observation chords that intersect the caustic capture variations in flux that allow mapping of the caustic. As caustics are highly sensitive to nonspherical distortions, observations of the central flash allow observers to determine the shape of Titan's atmosphere and therefore the zonal wind profile at the time of the occultation. (From Figs. 9 and 10 of Sicardy, 2022).

AO images of Titan during an occultation have only been obtained once before, when Bouchez, 2004 observed Titan pass in front of a double star on 2001-12-20 ($L_s \sim 265°$) with the PHARO instrument on the Hale telescope at Palomar Observatory. While 1D lightcurves offer a single metric — total flux as a function of time over the course of the occultation — spatially-resolved occultation images reveal the distribution of light around the limb and the angle of offset between near-

and far-limb spots. From these data, Bouchez derived a zonal wind profile that is qualitatively similar to that of Hubbard et al., 1993 (winds less than ~80 m s^{-1} near the equator, winds over 180 m s^{-1} at latitudes that are 50°N and 50°S of the minimum), but with different latitudes marking the maximum and minimum zonal winds (Bouchez, 2004).

In this paper we report on image sequences taken during an occultation in which Titan's disk was resolved with Keck's AO system. The 2022 September 5 observations at Maunakea are noteworthy in that the center of the occultation shadow path passed within a few tens of kilometers of the Keck II and Gemini North telescopes. The Titan-star offset in this occultation data set is the smallest that has ever been captured with AO.

Titan's zonal winds via Doppler shift emission measurements

The first direct detection of zonal winds in Titan's upper stratosphere/lower mesosphere (z = 300-450 km) was by Moreno et al., 2005, using spatially resolved, ground-based microwave spectroscopy of Titan's entire Earth-facing hemisphere with the Plateau de Bure interferometer. The line-of-sight wind speeds at the limb were calculated from observed frequency shifts of molecular emission lines, which occur as a result of the Doppler effect. Observations conducted with the extended Submillimeter Array around northern spring equinox (L_s = 355° and L_s = 5°) suggested a rapid increase in stratospheric wind speed following equinox, although the data were too coarse to be latitudinally resolved (Light et al., 2024). Lellouch et al., 2019b used ALMA to derive Doppler wind maps for six gases, covering eight different altitudes in the range $z \sim$ 300-1000 km. The combined spectral/spatial resolution and sensitivity of ALMA allow the Doppler shifts of the observed emission lines to be measured as a function of position across Titan's disk, from which the zonal wind speeds as a function of latitude can be derived. While the stratospheric (~50-400 km) zonal wind speeds were found to peak south of the equator, an unexpectedly intense, superrotating equatorial jet was found at thermospheric altitudes ~700-1000 km. The time variability and dynamical stability of these jets was subsequently investigated in a follow-up ALMA study (Cordiner et al., 2020).

Titan's zonal winds inferred from thermal wind measurements

Most of what is assumed about Titan's middle atmospheric zonal winds is derived from the cyclostrophic thermal wind equation, which relates the meridional temperature gradient to the wind shear along an axis parallel to Titan's rotation axis

(Flasar, Achterberg, et al., 2005). Using this method relies on an accurate boundary condition for the zonal winds at the 10^3 Pa (0.01 bar) level in the atmosphere (100 km), which is assumed to be 4 × Titan's solid-body rotation rate (Flasar, Achterberg, et al., 2005; Achterberg, Conrath, et al., 2008; Achterberg, Gierasch, et al., 2011; Sharkey et al., 2021; Achterberg, 2023), consistent with measurements using the Huygens probe (Bird et al., 2005).

Sharkey et al., 2021 used this method of inferring the zonal winds from thermal measurements to describe the seasonality of Titan's middle atmospheric jet from CIRS measurements. They found that the jet underwent substantial morphological changes over the duration of the *Cassini* mission, with the core of the jet (the region with the strongest winds) migrating from the low winter latitudes (up to ~30°N, with data unavailable near the equator) in 2007 to the high autumn latitudes (peak around 60°S) in 2015. There was a similar change in the altitude of the jet, with the fastest winds found higher in the atmosphere near equinox (~500 km) than near solstice (~300 km). The jet reached a maximum speed that exceeded 240 m s^{-1} in mid-autumn, and was weakest near solstice, with a speed closer to 180 m s^{-1}.

Titan's zonal winds simulated with General Circulation Models

GCMs are useful tools in assessing the roles that different physical processes play in driving the circulation of an atmosphere. The first fully three-dimensional GCM of Titan's atmosphere was reported by Hourdin et al., 1995. The model, while simple in its assumption of a meridionally uniform and static distribution of trace gases and aerosols, captured the large-scale structure and seasonality of Titan's middle atmosphere. The magnitude of the zonal winds, though, was substantially weaker than those inferred from *Voyager 1* and *Cassini* thermal measurements. Likewise, this early model suffered from a relatively low model top (250 km), precluding an analysis of the full vertical extent of Titan's middle atmospheric jet. TitanWRF, a three-dimensional GCM reported by Newman et al., 2011, which utilized a higher model top and modified diffusion scheme, simulated faster zonal winds, though the simulated temperatures of the model exceeded those observed by *Cassini* by several tens of kelvin. The impact of time-varying atmospheric opacity due to seasonal scale changes in Titan's atmospheric aerosol structure was studied by Lebonnois et al., 2012, which included a haze microphysical model coupled to the atmospheric dynamics. Comparable to the simulations from Newman et al., 2011, this model produced zonal winds with a magnitude comparable to that observed, but with an unrealistic middle atmospheric thermal structure.

The Titan Atmospheric Model (TAM; Lora et al., 2015) is a three-dimensional GCM that has recently been updated to improve the realism of the simulated middle atmosphere (~60-600 km) (Lombardo et al., 2023b; Lombardo et al., 2023a), including utilizing an observationally driven database of Titan's atmospheric composition and aerosol opacity (the Seasonally Varying Radiative Species Dataset [SVRS], Lombardo et al., 2023b) to calculate realistic radiative heating rates, as well as parameterizations to enable a higher model top. While the inclusion of the seasonality of the observed radiatively active components of the atmosphere increased the magnitude of the zonal winds by a few tens of m s^{-1}, the simulated jet core achieved a maximum speed of about 180 m s^{-1}, still short of the 240 m s^{-1} inferred from thermal wind measurements in Sharkey et al., 2021. The seasonal cycle of the zonal winds simulated by Lombardo et al., 2023a closely resembles the seasonality inferred from thermal wind measurements; we make use of these simulations.

The zonal jet is typically strongest in the low latitudes (0-30°) of the autumn or winter hemisphere (Shultis et al., 2022). In late winter, the winds strengthen, and the jet core is found at higher latitudes and altitudes. Simultaneously, the low-latitude winds also strengthen, leading to a substantial increase in the average wind speed throughout all of the middle atmosphere. By equinox, the strongest winds are found in the spring mesospheric high latitudes, and the jet core doesn't migrate to the opposite hemisphere until well into that hemisphere's autumn (Lombardo et al., 2023b). By the middle of autumn, the jet core is descending and weakening, leading to the observed mid-winter weakened state of the middle atmospheric jet (Shultis et al., 2022).

4.2 Data collection, reduction, and processing

Adaptive optics imaging of the stellar occultation

On 2022 September 5, Titan occulted a 12.9 K_{mag} star (Figure 4.2). We collected data from 7:51 to 10:21 UTC (second quarter-night) on 2022 September 5 using the NIRC2 instrument on Keck II. The telescope tracked Titan and the AO correction used Titan itself as the guide star. From 08:37:32 to 09:20:01, 245 frames of Titan were collected, each with an exposure time of 4 s and an average cadence of one frame per 9 s. Data were collected in the Kp filter (1.90-2.35 μm) with a frame size of 512 × 512 pixels. The frames spanned the entirety of the occultation (09:02-09:08 UT), as well as a span of time surrounding the occultation where the occulted star was visible beside Titan. Twenty sky frames (each also with an exposure

time of 4 s) were collected, half before and half after the occultation sequence. After the occulted star disappeared from the field of view, we captured narrowband images of Titan (in the Brγ, H2 1-0, and He-IB filters) with integration times of 60, 60, and 30 s, respectively. These wavelength regions probe different regions of Titan's atmosphere and allow monitoring of any transient haze activity occurring during the night of the occultation. We additionally took images of photometric calibration stars HST813-D for the Kp filter (integration time = 0.8 s, coadds = 10) and HD201941 for the narrowband filters (integration time = 0.181 s, coadds = 10).

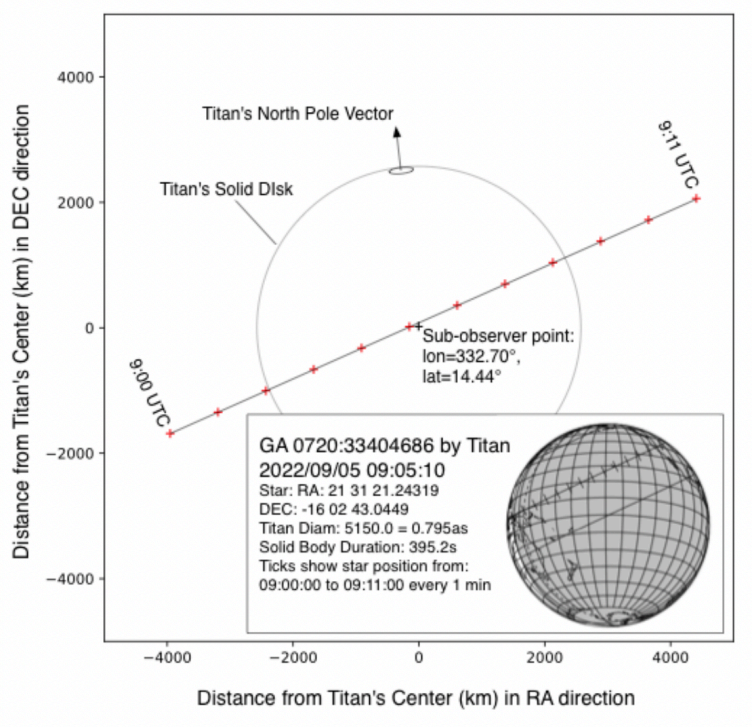


Figure 4.2: Main figure: Path of the star (from the vantage point of Maunakea) as it is occulted by Titan. Red plus signs represent 1-minute increments. The center of the occultation shadow path passes within 50 km of Maunakea, making this site ideal for perceiving the "central flash" (rapidly changing stellar refraction patterns) that occurs near the center of the occultation shadow path. Inset: full shadow path of star 2MASS 21312124-1602427, K_{mag} = 12.9. The hatched line represents the center of the shadow path; solid lines are the outer edges.

Spatially-resolved occultation data were concurrently collected with the NIRI instrument on the Gemini-North telescope, also at a cadence of roughly one frame per 9 s. However, the Gemini images have time stamps that are only accurate to 0.5 s (compared to tens of microseconds for the Keck time stamps). Given the event velocity of 13.8 km s^{-1}, the distribution of light around Titan's limb changes

significantly in 0.5 s. We plan to evaluate whether separate file creation time stamps from the operating system can improve the Gemini timing.

Occultation data reduction and processing

We reduced Keck/NIRC2 data using the `nirc2reduce` Python package (Molter, 2024). Reduction steps included median sky subtraction, application of a flat field, construction of a bad pixel map and subsequent bad pixel removal, cosmic-ray removal, and flux calibration using the photometric standard stars.

In order to better isolate and characterize refracted starlight around Titan's disk, we implemented additional, custom processing steps. We used Richardson-Lucy image deconvolution (Richardson, 1972; Lucy, 1974) to sharpen the data and reduce the effects of Earth's atmosphere on the observed images (Figure 4.3). Deconvolution first required defining a point-spread function (PSF). To find the best PSF for deconvolution, we studied the effectiveness of different PSFs in frames before and after occultation, when the occulted star was in the frame alongside Titan. The PSFs considered were: a frame-to-frame PSF of the star (where the PSF varied by frame), a universal PSF where the sharpest star (as determined by the lowest width of distributed light) was used as PSF for all frames, a frame-to-frame Gaussian, and a universal Gaussian. We ultimately used a universal PSF derived from the frame with the sharpest star, as this gave the sharpest deconvolved disks. For image deconvolution, we used the richardson_lucy function from the skimage.restoration image restoration module by Scikit-Image (Van Der Walt et al., 2014).

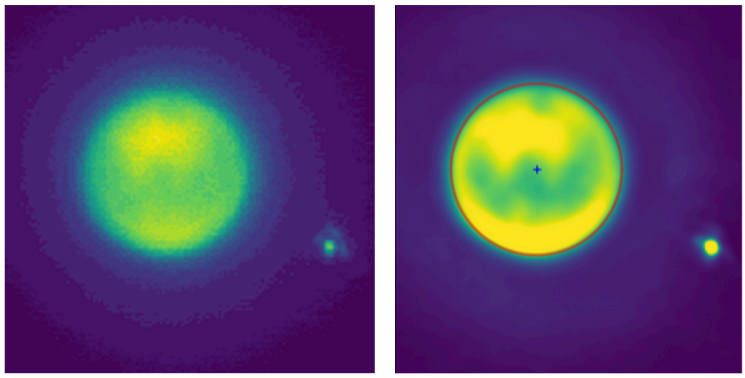


Figure 4.3: Left: reduced data from pre-event. Scattered light around both Titan and the star are caused by Earth's atmosphere. Right: the same frame following Richardson-Lucy deconvolution. Circle center and radius determined by fitting a circle to radial gradient minima around the limb.

Following deconvolution, we stacked all images to minimize the slight drift of Titan across the field of view during observations. Stacking was accomplished by calculating the gradient along radial lines from the center for each frame. Then, a circle was fit to the minimum radial gradient values for all angles around the circle (the minimum – or most negative – radial gradient value corresponds to the sharpest change in flux, a proxy for the edge of the limb). Using the shift2d function from the fft_tools.shift module of the image_registration package by PyPI (Ginsburg, 2023), the images were then aligned so that the (x,y) coordinates of the center of the fitted circles were stacked on top of each other.

To isolate refracted starlight during the occultation, it is necessary to subtract the dominant light coming from Titan's disk in each frame. To achieve this, we determined the median disk emission (calculated from the reduced, deconvolved, and stacked frames) and subtracted it from all of the frames so that only refracted starlight along the limb was visible in each frame. An animation of the occultation post-processing is included in the additional files, and an example figure with individual frames from the occultation is displayed in Figure 4.4.

The forward modeling effort (see Section 4.3– "Forward modeling of a stellar occultation") required the extraction of an additional parameter from the data: the distance in the detector plane between the center of the star and the center of Titan's disk. From the deconvolved frames before and after the occultation, the star was isolated in a 9×9 pixel subframe (x-direction) or an 11×11 pixel subframe (y-direction). These star subframe widths were selected based on which led to the lowest variability in centroid fitting. For calculating the centroid of the star in each frame, we used several different methods of centroid fitting, including two one-dimensional Gaussians, a two-dimensional Gaussian, center of mass, and a quadratic polynomial. Two one-dimensional Gaussians led to centroids with the least variability. The centers of Titan in each frame were calculated as the center coordinates of the circle fitted to the minimized radial gradients in each frame described above. Titan-star offsets were calculated for all pre- and post-occultation frames by taking the difference of the star centroid and the fitted circle center for Titan's disk. Linear fits were applied to both the x- and y- directions (as a function of time) in order to interpolate the x- and y-offsets during the frames when the star was not visible (i.e., being actively occulted by Titan) (Figure 4.5). The Δx and Δy offsets were then converted into ΔR.A. and Δdecl. offsets for occultation frames by

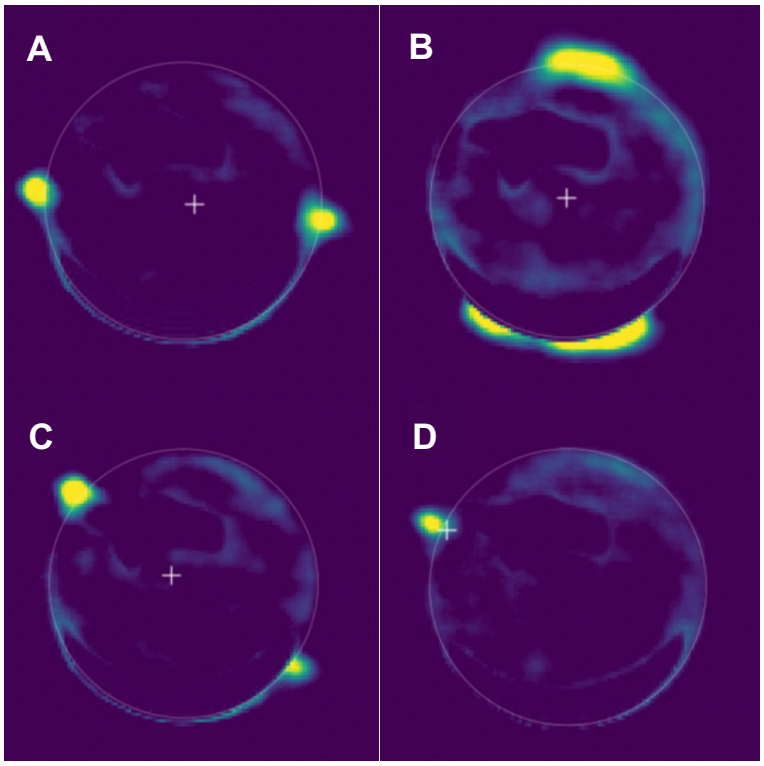


Figure 4.4: Isolated refracted lightspots during the occultation event. Titan's solid body radius is marked with a white circle; the star's interpolated offset relative to Titan's disk is marked in each frame with a white plus sign. Panels A-C are from near the midpoint of the occultation, with Panel B being the most central frame of the occultation that we captured. In the middle panels, multiple refracted lightspots are visible that change position rapidly with the cadence of the images. Panel D is from shortly before egress. The position of the refracted lightspot is aligned with the chord of the occultation.

using the plate scale of the observations and the distance between Titan and Earth (taken from JPL Horizons).

ALMA observations and data reduction

ALMA observations of Titan were obtained on UT 2022 September 6 between 02:29 and 05:48 (less than 24 hr after the occultation observation) using the Band 9 (602-720 GHz; ~0.42-0.5 mm) receivers, covering four lines of the CH_3CN J = 35 – 34 rotational band (between 643.1 and 643.3 GHz) and four lines of the J = 36 – 35 band (between 661.4 and 661.7 GHz). The correlator was set to a spectral resolution of 122 kHz, corresponding to Δv = 55–57 $\mathrm{m\,s^{-1}}$. Weather conditions were very good, with a zenith precipitable water vapor of 0.22–0.32 mm.

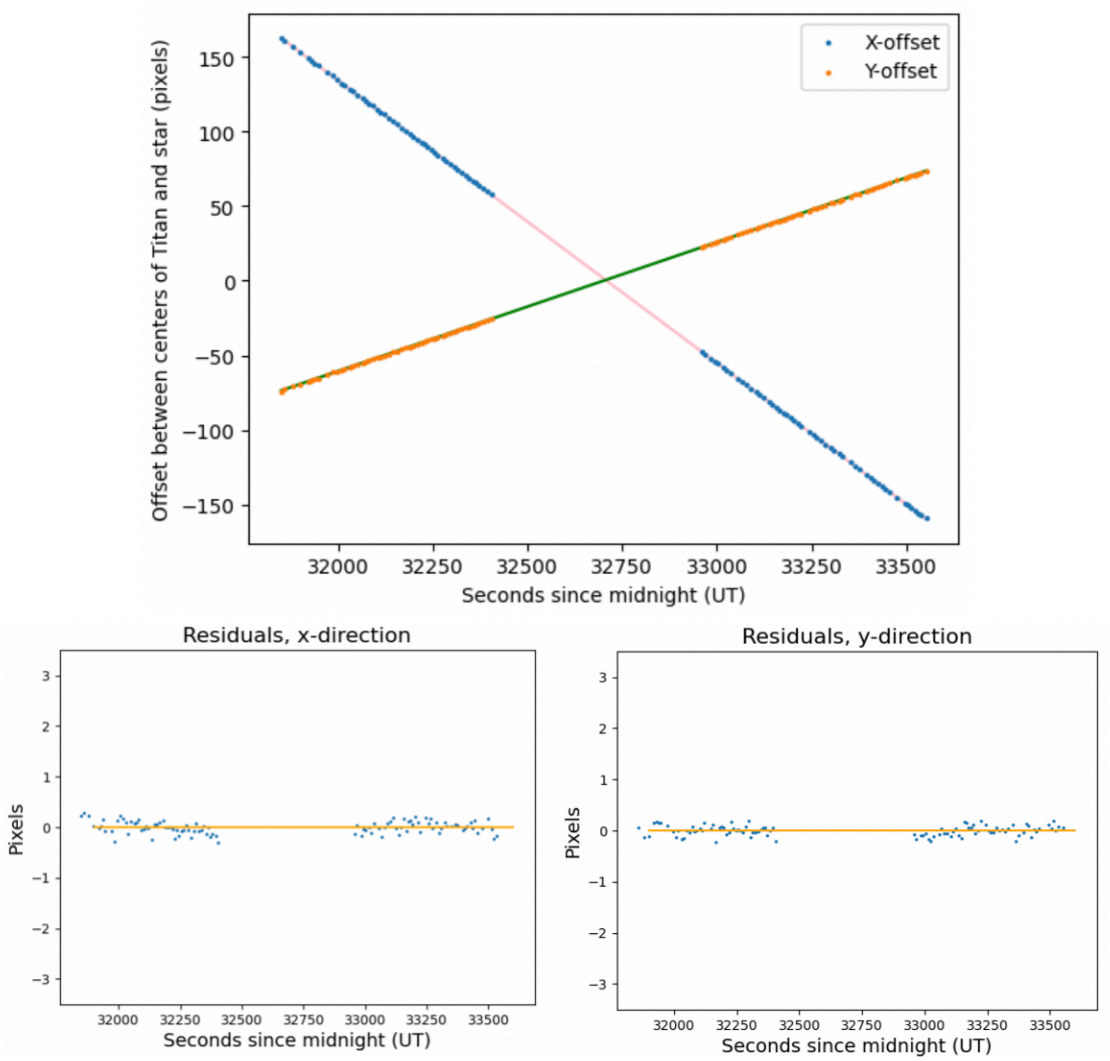


Figure 4.5: Top: linear fits (green and pink lines) to calculate x- and y-offsets between the centers of Titan and the occulted star. Bottom: residuals in the x- (left) and y-directions (right) following the subtraction of the fit.

The interferometric data were flagged and calibrated in the Common Astronomy Software Applications (CASA) package (Jaeger, 2008) using standard scripts supplied by the Joint ALMA Observatory. Additional self-calibration of the phases was performed with respect to the Butler-JPL-Horizons 2012 Titan model included with CASA[1], using separate continuum windows adjacent to the main spectral windows of interest (centered at 649 GHz and 666 GHz, respectively).

[1]https://science.nrao.edu/facilities/alma/aboutALMA/Technology/ALMA_Memo_Series/alma594/memo594.pdf

Prior to imaging, the Titan continuum was subtracted from the interferometric visibility data using a second-order polynomial fit to the line-free (pseudo)continuum regions in each spectral window. The spectral image data were deconvolved (per channel) using the CASA `tclean` Hogböm algorithm with Briggs weighting (robust = 0.5) and a threshold twice the rms noise (σ = 29 mJy at 643 GHz and 38 mJy at 662 GHz). Image restoration was performed for both CH_3CN bands using the smallest common elliptical Gaussian beam, of FWHM $0''.21 \times 0''.18$. For plotting purposes, the data were projected onto a spatial grid in the plane of the sky, according to Titan's geocentric distance of 8.94 au. The spectrally integrated line flux maps and disk-integrated spectra for the two CH_3CN rotational bands are shown in Figure 4.6.

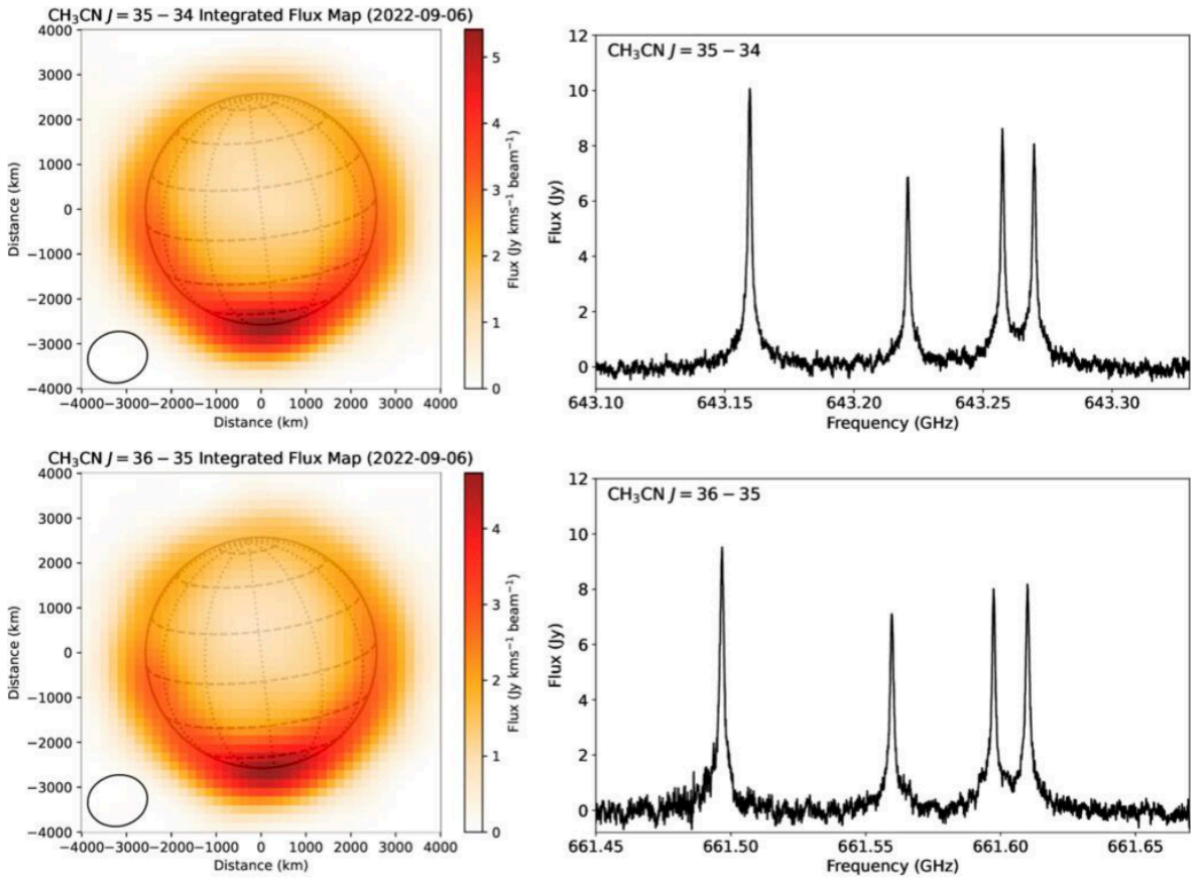


Figure 4.6: Continuum-subtracted ALMA observations of Titan on 2022-09-06, showing the spectrally integrated line flux maps for the CH_3CN $J = 35 - 34$ and $J = 36 - 35$ bands (left panels) and corresponding spectra (right panels), integrated within a $1''.2$-diameter circular aperture centered on Titan. The FWHM of the spatial resolution element (ellipse) is shown in the lower left of the maps.

ALMA wind retrieval

We followed a similar strategy to Cordiner et al., 2020 to retrieve the latitudinal wind velocity profile based on fits to the observed spectral lines to determine their Doppler shifts. The Gaussian line fitting method was updated to use the Moffat function (Moffat, 1969) instead, which was found by Light et al., 2024 to provide a significantly better fit to the CH_3CN lineshapes than Gaussian or Voigt functions, especially in the presence of pressure-broadened Lorentzian line wings. We found that the Moffat function was able to fully reproduce our observed line profiles (within the noise), resulting in a more accurate determination of the line Doppler shift than the conventional Gaussian fitting method.

All eight CH_3CN spectral lines were fitted simultaneously for all pixels in the ALMA images, using a Levenberg-Marquardt least-squares minimization routine written in Python, based on the MPFIT package (Markwardt, 2009). All parameters of the Moffat function were allowed to vary independently for each line, apart from the velocity offset parameter, for which a common (variable) value was used for all lines. The uncertainty on the Doppler shift for each pixel was derived from the diagonal elements of the covariance matrix.

A significant ($\approx +30\ \mathrm{m\,s^{-1}}$) offset in the spectral line Doppler shifts was identified at the center of Titan's disk (and along the direction of its polar axis). This is attributed to an error in the cable routing of the ALMA rubidium maser at the time of our observations, which is likely to have introduced an erroneous and unknown frequency shift in our observations, accompanied by a slight broadening of the spectral lines by a few tens of meters per second (R. Loomis, private communication). The magnitude of the shift was calculated by taking the average of the fitted line-of-sight velocities inside Titan's limb. This "zero point shift" was then subtracted from the individual pixel Doppler shifts for the subsequent data analysis steps. No significant evidence for latitudinal asymmetry in Titan's zonal winds was reported by the detailed studies of Lellouch et al., 2019b and Cordiner et al., 2020. Our ALMA data analysis here therefore also inherently assumes that the zonal winds are symmetric with respect to Titan's polar axis.

To determine the altitudinal sensitivity of our ALMA zonal wind measurements, we used the Non-linear optimal Estimator for MultivariatE spectral analySIS (NEMESIS) to generate a detailed radiative transfer model for the observed CH_3CN emission (Irwin et al., 2008). We followed a similar modeling strategy to Thelen, Nixon, et

al., 2019, updated to incorporate the more recent CH_3CN abundance profile from Nosowitz et al., 2025 for the a priori atmospheric state.

The calibrated ALMA data cubes were re-imaged prior to continuum subtraction, in the same way as described in Section 4.2– "ALMA observations and data reduction". Disk-averaged spectra were then extracted using a circular aperture with a diameter of 1″.5, which includes flux from up to the top of Titan's atmosphere plus twice the standard deviation of the restoring beam's long axis, to account for all the significant emission. Titan's disk (plus atmosphere) was divided into 35 annuli corresponding to emission angles between 0° and 75°, covering the center of Titan up to a tangential altitude of 1050 km (the vertical extent of our model was 1200 km, but emission is negligible above 1000 km). The atmospheric temperature profile was obtained from Thelen, Cordiner, et al., 2020. The observed ALMA data (including the continuum) were scaled by a constant factor of 0.982 to produce a match between the modeled and observed continuum levels. This scaling mitigates errors on the ALMA flux scale (which may be as much as ≈10%, due to uncertainty in the amplitude calibrator flux), as well as accounting for small errors in the assumed (a priori) temperature around the tropopause, which determines the model continuum level. The CH_3CN abundance profile was continuously retrieved at each altitude to obtain a fit to the observed $J = 35 - 34$ spectral line profiles. This abundance profile formed the basis of our "wind contribution function" calculation, which was obtained from the corresponding NEMESIS functional derivatives (dQ/dz) of flux with respect to altitude, as a function of frequency. The dQ/dz values were convolved with the gradient of the (continuum-subtracted) model spectral line profile, to provide weighting according to the frequencies contributing most to the retrieved line Doppler shifts (see, e.g., Lellouch et al., 2019b), which were then averaged and peak-normalized. The resulting, weighted wind contribution function is shown in Figure 4.7. The corresponding average emission altitude is 303 km, with sensitivity to winds primarily in the range ∼ 150-450 km. Due to the similarity of the line opacities and energy levels, this range is also applicable to the $J = 36 - 35$ band.

Due to the effects of beam-smearing, combined with Titan's axial tilt, extraction of the intrinsic zonal wind field requires deconvolution of the Doppler shift data. We therefore followed a similar method to Cordiner et al., 2020 to model the Doppler map and extract a latitudinal wind speed profile using a simplified 3D radiative transfer model. The `atmWindMapGaussFit` code of Cordiner et al., 2020 was

modified to allow a continuously variable wind speed as a function of latitude ($v(l)$), instead of the Gaussian profile previously assumed by those authors. The $v(l)$ profile was generated by joining a set of i points ($v_i(l_i)$, equally spaced in l), by a segmented linear function. This function was then smoothed by a Gaussian function of FWHM equal to the spacing between the points. An exponential taper was applied at the ends of the $v(l)$ profile (with an exponential smoothing scale length of 1°), to ensure a velocity of zero at the poles. Each velocity point v_i was then optimized using MPFIT, to obtain the least-squares solution and associated error estimates.

To maximize the information content in the $v(l)$ retrieval, we experimented in fitting the observations with profiles incorporating different numbers of variable latitudinal points i. Seven latitudinal points (with $\Delta(l) = 30°$ separation) were found to produce a good fit to the observed Doppler map, while still allowing the retrieved profile to be well constrained by the data (i.e., keeping the resulting $v(l)$ errors reasonably small with respect to variations in the retrieved profile). At the equator, this $\Delta(l)$ interval corresponds to a distance of 0″.2 on the sky, which is similar to the spatial resolution of our ALMA data.

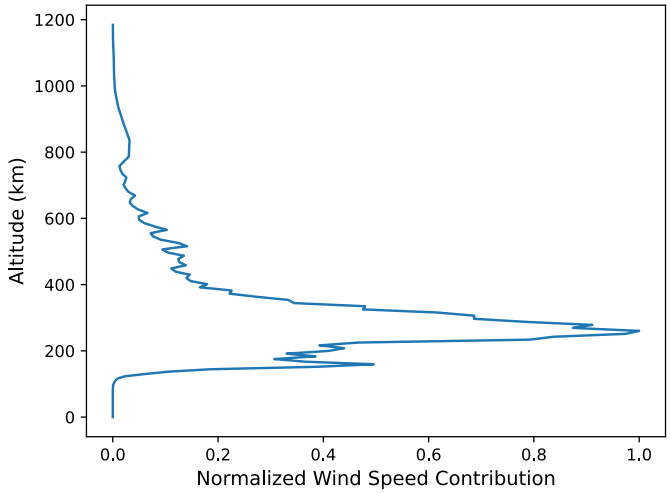


Figure 4.7: Peak-normalized wind contribution function for the observed CH_3CN $J = 35 - 34$ transitions at 643 GHz.

4.3 Forward modeling

Forward modeling of a stellar occultation

Sicardy, 2022 presents a comprehensive overview of occultations (including Titan as a detailed example). Among other things, this review paper shows how central

caustics (concentrations of light rays, see Section 4.1– "Titan's zonal winds via stellar occultations") form in the middle of the shadow. The bending angles of the starlight being refracted around Titan are perpendicular to the contours of constant gas density around the limb. This means that small changes to the shape of the atmosphere lead to large changes in the shape of the central caustic and (in cases where the occulting object is resolved) the distribution of refracted light around the limb. During most of the occultation the refracted light is grouped into two spots, called the "near limb" and the "far limb," referring to the limbs closer to and farther from the star, respectively. These spots appear wherever the sky-plane projection of the lines from the star to the limb are perpendicular to the contours of constant density (isopycnals). The locations of the near- and far-limb spots change as Titan moves across the star, sometimes rapidly near mid-event.

Section 4.3– "Deriving level surface distortions from zonal winds" describes how zonal winds change the isobars as a function of latitude. We use a quantity called Δr, the level surface radius, to describe distortions from a spherical atmosphere. On Titan, the changes to the level surface (Δr) amount to tens of km — small compared to Titan's radius, but since it is the *slopes* of the level surface that control where the near- and far-limb spots appear, the shapes of the isobars on Titan affect the spot locations in easily observable ways. The image sequence taken during the occultation shows the progression of light around Titan's limb during an occultation and lets us compare those distributions to modeled images based on ALMA- or GCM-based zonal wind distributions. Although isobars and isopycnals are not identical, applying the isobar distortions to the bending angle fields over small temperature ranges gives undetectable errors.

Our forward model is constructed based on "ray tracing" — constructing 2D screens of Titan's atmosphere (as would be observed by the telescope), and tracing rays of light as they pass through the screens. We use the process outlined below, beginning with models of Titan's atmosphere and ending up with bending angles as functions of altitude and latitude. To speed up this calculation, we generate a 1D function for bending angle vs. radius. We accommodate the anisotropies due to zonal winds by distorting the radius field as a function of latitude, then calculating a 3D field of bending angles around Titan's limb.

Here is the step-by-step recipe for calculating the bending angles of rays that pass through Titan's atmosphere:

1. Begin with a temperature profile as a function of altitude. In this paper we use the Huygens/HASI profile as our starting reference for Titan's atmosphere (Figure 4.8A; Fulchignoni et al., 2005). While the HASI temperature profile lacks temporal and latitudinal resolution, it offers unparalleled altitudinal resolution and also has the advantage of being the only in situ data of its kind collected in Titan's atmosphere. We also considered scaling the HASI profile by the latitudinal temperature differences simulated in the TAM GCM, but we found the differences in the results to be negligible when compared to using the HASI profile without GCM scaling. We believe that the HASI profile represents the best starting profile for Titan's atmosphere until additional highly altitudinally-resolved data can be collected.

2. Calculate the pressure profile from $T(r)$ using the law of hydrostatic equilibrium and the assumption of a nitrogen atmosphere (Figure 4.8B). There are differential and integral forms of the law of hydrostatic equilibrium; we use an integral form:

$$\ln(P) = -\int \frac{1}{H} dr \tag{4.2}$$

   where r is the radius, P is the pressure, and H is the scale height: $H(r) = \frac{kT(r)}{mg(r)}$. Parameter k is Boltzmann's constant and m is the molecular weight of nitrogen. A boundary condition is also required, such as P at a certain r. Omitting methane leads to an overestimation of roughly 0.5% in bending angles, assuming a constant 1.5% concentration of methane at relevant occultation altitudes (extrapolated from the linearity of methane observed by HASI between 75 and 140 km).

3. Calculate the number density profile, $N(r)$, from $T(r)$ and $P(r)$, using the ideal gas law.

4. Account for zonal winds by distorting the number density field. The conversion of zonal winds to radial distortions is outlined in Section 4.3– "Deriving level surface distortions from zonal winds".

5. Use the distorted number density field to calculate ν, the refractivities. These are mainly proportional to the number density, with a very small dependence on wavelength. We calculate the refractivity through N_2 gas at standard

temperature and pressure, then scale that refractivity by the ratio of the actual number density to Loschmidt's number, the number density at standard temperature and pressure (STP; 273.15 K and 1 atmosphere, respectively):

$$\nu_{STP} = 29.06 \times 10^{-5} \left(1 + \frac{7.7 \times 10^{-3}}{\lambda^2}\right) \tag{4.3}$$

$$\nu(T, P) = \nu_{STP} \left(\frac{N(T, P)}{N_{LOS}}\right), \tag{4.4}$$

where λ is the wavelength in μm and Loschmidt's number (N_{LOS}) is 2.687×10^{19} particles cm^{-3}.

6. Calculate the integrated line-of-sight refractivity for a given chord that traverses through Titan's atmosphere (Figure 4.8C). The most general way to do this is to construct chords that are perpendicular to the sky plane, break up the chords into small steps of length ds, evaluate the refractivity ν at each step, and add up the $\nu\ ds$ products. We use step sizes of 1 km and a chord length of 8000 km, since number densities at distances of 4000 km (and beyond) from Titan's center are negligible. While we considered the effect of Titan's seasonally variable haze, we determined the effect was negligible owing to the high altitudes that are probed by occultations and the wavelength range that the occultation was observed in.

7. Approximate Titan and its atmosphere as 2D screens perpendicular to the observer's line of sight, where each point on the screen has a light-travel time that we calculate by summing $\nu \cdot ds$. The light travel time is proportional to the integrated line-of-sight refractivity. While Titan itself is decidedly 3D, the 2D screen approximation is perfectly acceptable — the bending angles we detect are only about 2 μrad, so that each detectable ray essentially travels straight through Titan's atmosphere.

8. Calculate bending angles from the gradient of the phase delay screen (Figure 4.8D). In general, a wave propagating through a medium experiences bending angles equal to the gradient of the light-travel times along axes perpendicular to the direction of travel. The 2-D sky-plane screen of bending angles lets us simulate resolved images of Titan. Specifically, we trace rays from the star through Titan's atmosphere to the observer. This lets us construct the illumination around Titan's limb at each instant in time. There are typically

spots hovering over the limb at the locations of ingress and egress, but when the star is relatively near Titan's center in the observer plane, the light distribution appears to move around the limb. We convolve the traced light locations with an appropriate PSF to produce an image that we can compare to the AO observations.

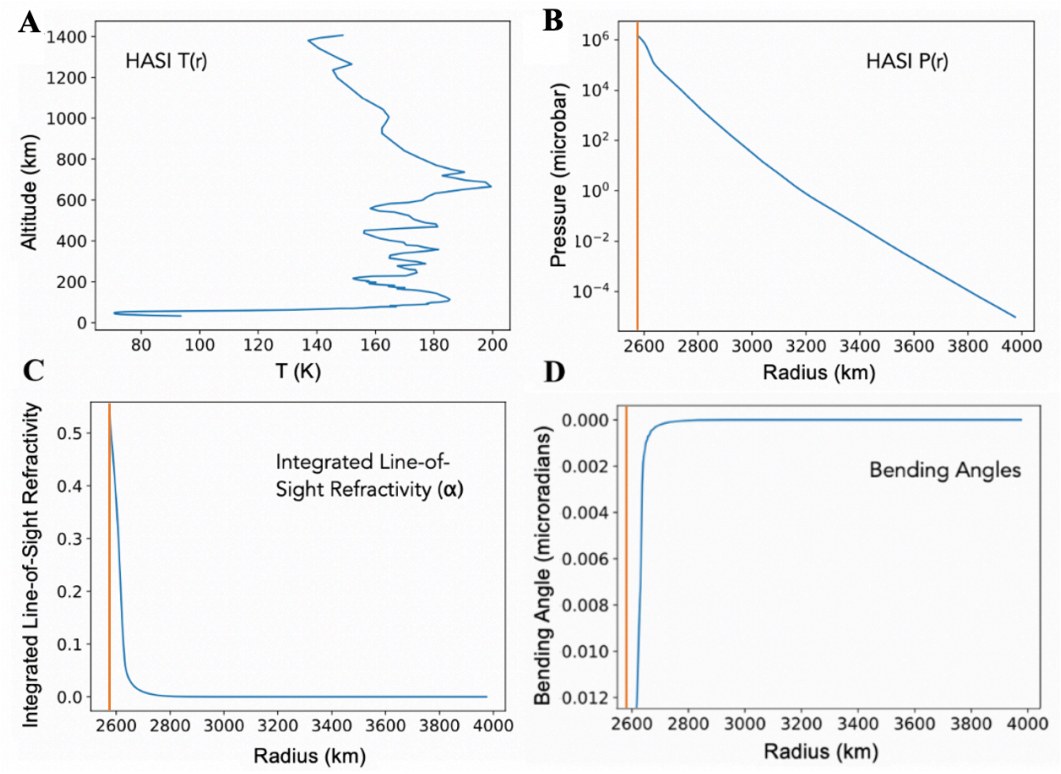


Figure 4.8: A: The atmospheric temperature profile derived by the HASI instrument on board the Huygens probe. B: Pressure is calculated from the temperature profile by leveraging the law of hydrostatic equilibrium and approximating Titan's atmosphere as 100% nitrogen. C: The integrated line-of-sight refractivity is found by stepping across 8000 km chords with step size = 1 km. At each step, refractivity ν is calculated, and the integrated line-of-sight refractivity is the sum of $\nu \cdot ds$ across the chord. D: Bending angles are calculated from the gradient of the phase delay screen. The orange vertical line in Panels B-D denotes Titan's surface.

Variation in radial distortion profiles

The earliest Titan wind occultation study (Hubbard et al., 1993) constrained the zonal wind profiles by requiring them to be symmetric across the equator, ultimately deriving a zonal wind profile with peak speeds at latitudes of 65°N/65°S, lesser peaks at 30°N/30°S, and the lowest speed observed at the equator. Due to the Earth-based

land geography of the 1989 occultation shadowpath, the observations from this occultation were concentrated in chords across Titan's southern hemisphere, but the equatorial symmetry constraint on zonal wind speeds meant that a zonal wind profile was proposed for all latitudes, even those not observed.

About a dozen years later, Bouchez, 2004 captured a double stellar occultation by Titan, obtaining the first spatially-resolved dataset of a Titan occultation. Bouchez, 2004 argued that the equatorially symmetric constraint for Titan zonal wind profiles was unnecessary and that, based on Titan's atmospheric behavior, there is little reason to expect that the wind speeds would be symmetric about the equator throughout all of a Titan year. Subsequent observations and GCM simulations agree with the latter point — most of the time, Titan hosts higher zonal wind speeds in the hemisphere experiencing autumn/winter. We do not constrain the symmetry of the zonal wind profiles and therefore consider Titan model atmospheres with substantially varying wind (and accordingly, distortion) patterns in the northern versus the southern hemispheres. Our forward model does not impose equatorial symmetry; however, we do assume that any given latitude will experience uniform winds throughout (i.e., we assume no longitudinal variations in wind speeds).

Deriving level surface distortions from zonal winds

Hubbard et al., 1993 call Δr the "deviation from spherical structure," and their Figure 34 shows the magnitude of Δr as a function of latitude, ranging from 0 km at the poles to about 35 km at the equator. They express r in terms of Legendre polynomials (their Equations 20 and 23) and calculate Δr by subtracting Titan's polar radius. Bouchez, 2004 derives a similar approximation for the "shape of surfaces of constant pressure," or $r(P, \phi)$, but uses an integral of zonal winds (integrated over latitude) instead of Legendre polynomials (see Eq. 4.7, in which P is pressure and ϕ is colatitude). A key difference between the two expressions for level surfaces is that Hubbard et al., 1993 require that Δr be symmetric about the equator, but Bouchez, 2004 does not. Both require that the Δr contours be perpendicular to the radius at the equator.

Bouchez, 2004 refers to the surfaces of constant pressure "as an altitude correction to the pressure structure of Titan's atmosphere, due to the presence of zonal winds." It may seem strange that these corrections only amount to a few tens of kilometers, yet they can produce significant changes in the locations of the near- and far-limb spots during an occultation, as well as major changes in the shape of the central flash

caustic in the middle of the shadow that Titan casts in the observer's plane. There is a reason that small distortions are so observable during occultations: it is because incoming rays are bent in a direction that is perpendicular to contours of constant density. Even small changes in Δr can produce big changes in the orientation of isopycnal contours. This is especially apparent in central flash features, as depicted in the comparison for a simple oblate planet and a case based on a Titan-like distorted atmosphere (Fig. 4.1) (Sicardy, 2022).

In order to incorporate a zonal wind profile into the description of Titan's atmospheric density structure, we follow the methodology conducted by Bouchez, 2004 (Equations 4.16-4.26). We first apply radial distortions to a model Titan atmosphere (in this case, one derived from the HASI profile). To account for zonal winds, we begin by expressing Titan's atmospheric rotation as the sum of the satellite's rotation and the rotation due to zonal winds:

$$\omega(r, \phi) = \omega_s + \frac{V_w(r, \phi)}{r sin\phi}, \tag{4.5}$$

where V_w refers to zonal winds and ω_s refers to the satellite's angular rotation.

In hydrostatic equilibrium, the sum of the gravitational and centrifugal accelerations times the mass density of the gas is balanced by the pressure gradient. As gravitational acceleration vastly exceeds the radial term of centrifugal acceleration for zonal winds, we can disregard the centrifugal acceleration component when considering the partial derivative of pressure with respect to radius and express the relationship between radius, pressure, and colatitude as:

$$-g \left(\frac{\partial r}{\partial P}\right)_\phi \left(\frac{\partial P}{r \partial \phi}\right)_r = \omega^2 r sin(\phi) cos(\phi). \tag{4.6}$$

Rearranging Equation 4.6, we get the partial differential equation describing shapes of constant pressure, which can then be integrated to calculate radius as a function of colatitude. Radius r and gravitational acceleration g can be removed from the integral when the surfaces are nearly spherical, leading to Equation 4.7 for radius as a function of colatitude in the presence of distorting zonal winds, with a reference altitude $r(P, \phi_0)$, in our case corresponding to the peak altitude from the ALMA contribution function. This equation is then applied in Step #4 above.

$$r(P, \phi) \approx r\,(P, \phi_0) \left(1 - \frac{r\,(P, \phi_0)^3}{GM} \int_{\phi_0}^{\phi} \omega\,(P, \phi')^2 \sin\phi' \, \cos\phi' d\phi'\right). \tag{4.7}$$

Quantifying refracted lightspot patterns

This paper compares the *observed* light distribution around Titan's limb to *simulated* distributions that would be observed if Titan's atmosphere had a particular 3D density structure. This paper is exclusively a forward modeling effort: we generate images of Titan during the occultation from GCM simulation snapshots of Titan or from atmospheres corresponding to the zonal winds observed by ALMA on 2022 September 6, and then we compare the synthetic limb light distributions to the observed distributions from Keck.

In general, concentrations of light on the limb appear where the projected line from the occulted star to the limb is perpendicular to contours of constant density. At the beginning of the occultation when the star has just been obscured by Titan, the lightspot appears along the limb at the location of ingress. The inverse is observed just prior to egress: the refracted lightspot is present at the point of egress (where the occultation chord and the edge of Titan's disk intersect). In the frames where the star was relatively close to the center of Titan's disk, refracted light patterns changed rapidly in an occultation-specific phenomenon known as a "central flash." Characterization of the comparatively faint refracted lightspots required extensive processing to isolate them from Earth's atmospheric effects and the dominant light from Titan's disk. The deconvolution, stacking, and disk subtraction are described in detail in Section 4.2– "Occultation data reduction and processing". Examples of resulting isolated refracted lightspots are visible in Figure 4.4.

The final product of a simulated occultation using the forward model described in Section 4.3– "Forward modeling of a stellar occultation", and a model atmosphere can be compared to our data frame by frame. Quantitative comparisons were carried out by plotting the summed distribution of light around the limb in both data and model images as a function of θ, with $\theta = 0°$ in the positive x-direction (Figure 4.9).

The duration of the occultation was just over 6 minutes — at the NIRC2 cadence of one frame per 9 s, we collected 46 frames covering the entirety of the occultation. Due to the faintness of the star and variable interference from Earth's atmosphere, not all occultation data frames were usable. We identified an "ingress lightspot" (appearing along the limb near the point of star ingress) in 22 of the 46 frames (mostly in the first half of the occultation) and an "egress lightspot" (appearing along the limb near the point of star egress) in 18 of the 46 frames (mostly in the second half of the occultation). Ten of the 46 frames had both near- and far-limb spots visible; these spanned the middle of the occultation. The ability of the model

to match the data was quantified by finding the sum of squared errors (SSE) between data and model θ values for the ingress spot and the egress spot in data frames where the lightspots could be isolated. θ values for data and model were determined with Gaussian fitting (Matthew Newville et al., 2024).

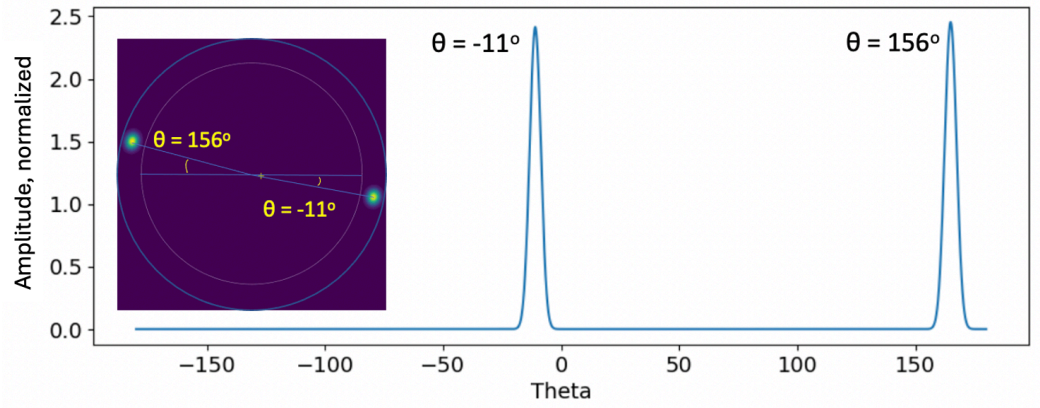


Figure 4.9: Quantitative comparison of data and model can be achieved by treating Titan's disk as a circle and expressing the sum of the distribution of light around its limb as a function of angle θ. This figure demonstrates this for a model frame near the center of the occultation. Both near- and far-limb spots are visible (inset), and when the sum of the light distribution around the limb is plotted, the peaks of the lightspots are found to be at $\theta = 156°$ and $\theta = -11°$.

Forward model input from GCM zonal wind profiles

We use a range of GCM simulation snapshots and the near-concurrent ALMA zonal wind data for our forward model atmosphere profile sample space. As outlined in Section 4.3 – "Forward modeling of a stellar occultation", a 2D temperature profile can be converted to a 2D density profile, which allows calculation of refractivities and ultimately bending angles for refracted starlight.

We used 36 snapshots of 2D zonal wind profiles over a Titan year derived from simulations with TAM. The limited vertical resolution in TAM 2D density profiles means that the resulting refractivity profiles lack the necessary resolution across occultation-relevant altitudes. Instead of interpolating across the GCM 2D density profiles and using these profiles to construct our refractivity screens and bending angles, we chose to apply the radial distortions derived from zonal wind profiles in each GCM snapshot (distortion calculations outlined in Section 4.3– "Deriving level surface distortions from zonal winds") to a refractivity profile calculated from the HASI temperature profile. Radial distortions across the range of altitudes in the

TAM GCM were calculated as per Eq. 4.7 and the refractivity profile from HASI was stretched accordingly. We use the integral form of hydrostatic equilibrium in our forward model exploring modifications to surfaces of level pressure exerted by zonal winds. The wind profiles extracted from the TAM simulations are depicted in Figure 4.10 for a reference altitude (307 km). While 36 snapshots are displayed, we note that the shape of the zonal wind distribution does not change in every snapshot. Changes are most readily observed around the equinoxes ($L_s = 350^\circ$ to $L_s = 40^\circ$ and $L_s = 170^\circ$ to $L_s = 220^\circ$); between equinoxes, the change between snapshots is primarily in the magnitude of the zonal wind speeds. The observed occultation occurred around $L_s = 160^\circ$, a few Earth years (0.06 Titan years) before Titan's northern autumnal equinox in 2025.

The radial distortions corresponding to the GCM snapshot zonal wind speeds are depicted in Figure 4.11. While zonal wind profiles underlie the observed radial distortions, it is the radial distortions that ultimately affect the pattern of the refractivity screens and, by extension, bending angles. Latitudinally symmetric GCM profile snapshots (e.g., at $L_s = 10^\circ$ and $L_s = 190^\circ$) lead to latitudinally symmetric distortion profiles, although the majority of profiles are asymmetric about the equator. In addition to the 36 GCM zonal wind profiles here, we ran the forward model with both doubled and halved zonal wind speeds from each of the GCM snapshots to determine the effect of increased and decreased atmospheric distortion on the correspondence between the data and the model.

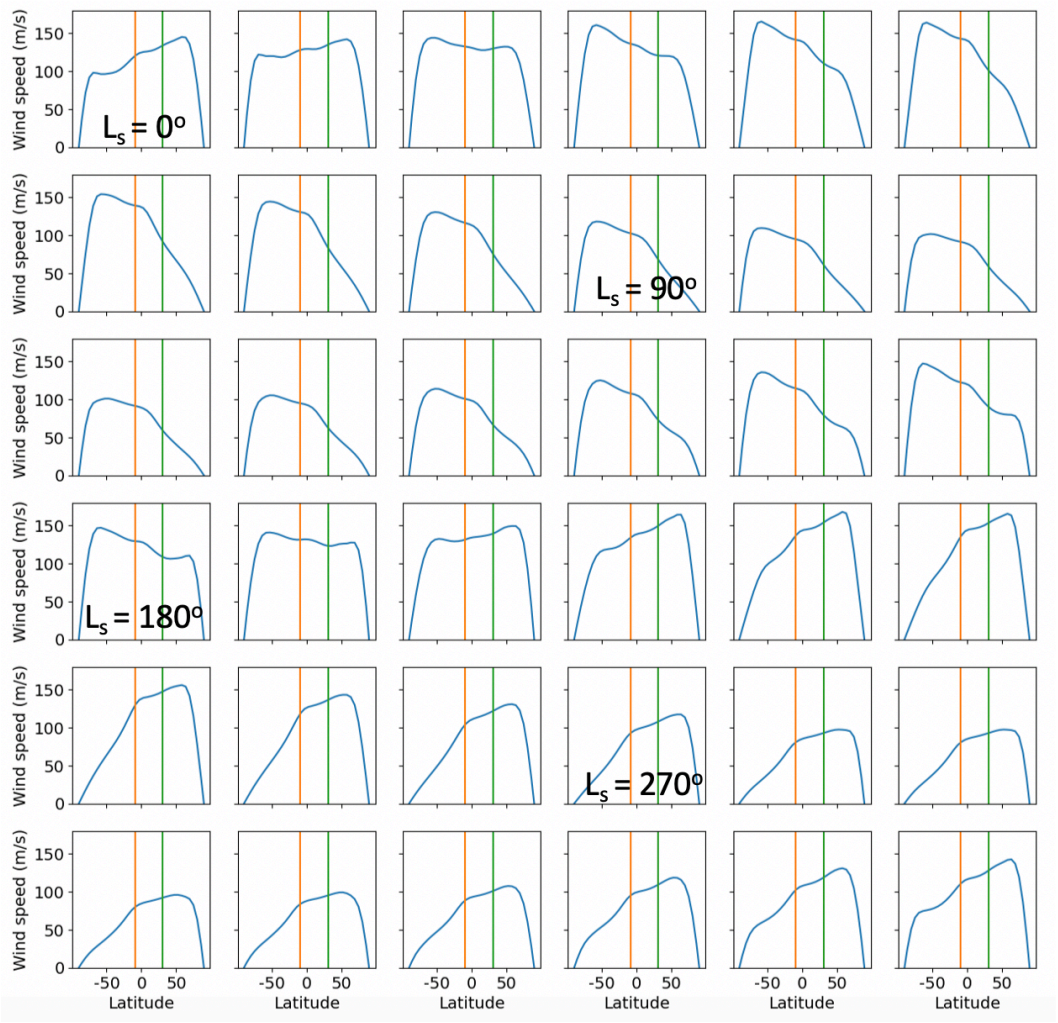


Figure 4.10: Snapshots of simulated zonal wind profiles from TAM at an altitude z = 307 km. L_s values of 0°, 90°, 180°, and 270° correspond to northern vernal equinox, summer solstice, autumnal equinox, and winter solstice, respectively. Wind trends are most dynamic around the two equinoxes. The orange line represents the latitude of ingress (−9°) and the green line represents latitude of egress (31°).

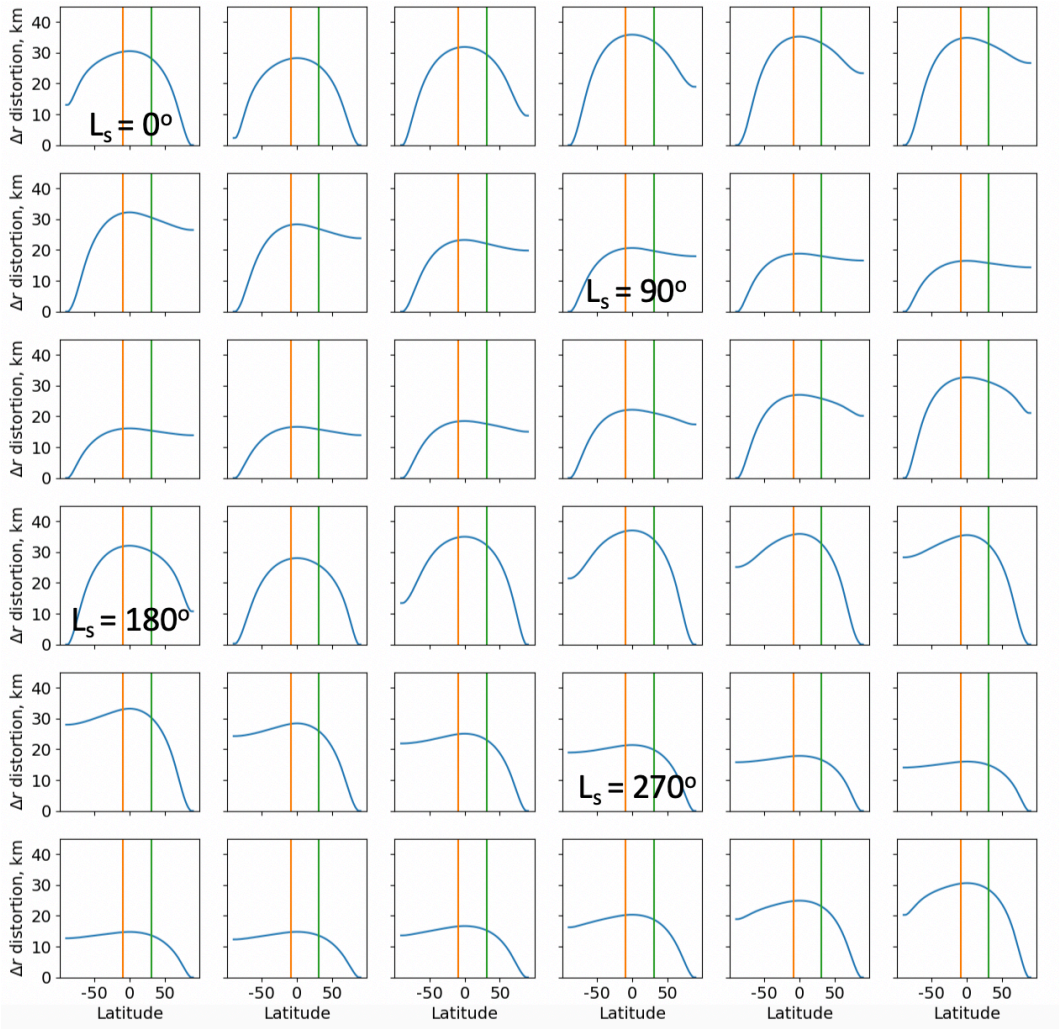


Figure 4.11: The radial distortions (contours of level pressure) corresponding to the 36 zonal wind snapshots in Figure 4.10. The orange line represents the latitude of ingress (−9°) and the green line represents latitude of egress (31°).

4.4 Results

Retrieved zonal wind field using ALMA

The final Doppler map (averaged over all eight CH_3CN lines) from our ALMA observations is shown in Figure 4.12, along with the 1σ uncertainty map for each pixel. The data have been masked within a circular aperture of radius 3600 km for display purposes. The resulting best-fitting latitudinal wind profile is shown in Figure 4.13. This wind profile corresponds to the CH_3CN contribution function depicted in Figure 4.7.

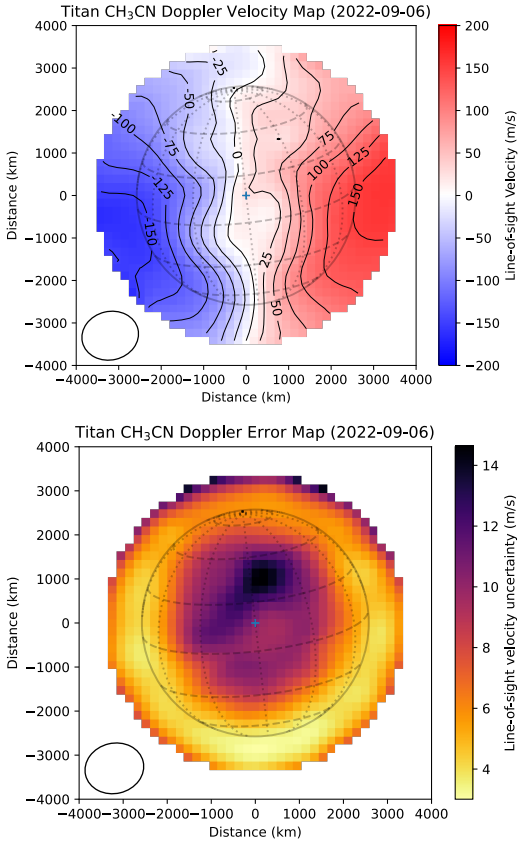


Figure 4.12: Left: the color map shows line-of-sight CH_3CN Doppler shifts, averaged across all observed transitions, overlaid on a Titan wireframe grid at the epoch of our ALMA observations. Velocity contours (labeled in units of $\mathrm{m\,s^{-1}}$) are also overlaid. Right: error map showing 1σ statistical uncertainties on the Doppler shift for each pixel. The spatial resolution (elliptical beam FWHM) is indicated in the lower left corner.

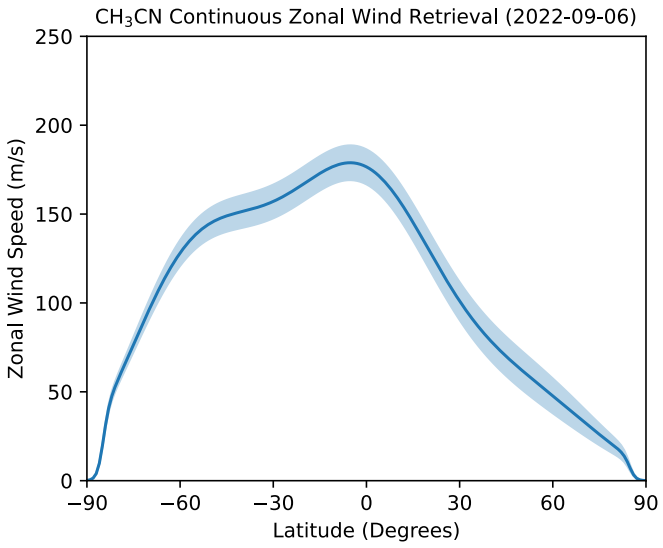


Figure 4.13: Zonal wind velocity profile ($v(l)$) and 1σ error envelope retrieved from our ALMA CH_3CN observations on 2022-09-06, using a continuously variable parameterization with latitudinal sampling of 30°.

Occultation forward model with GCM and ALMA input atmospheres: comparison to data

Data versus model: overall

Of the input zonal wind profiles surveyed (36 GCM snapshots and one ALMA profile), the overall best match to the occultation data was for the input GCM atmosphere corresponding to $L_s = 120°$, closely followed by those corresponding to $L_s = 110°$, $L_s = 130°$, and $L_s = 100°$. $L_s = 120°$ is 40° — or roughly half of a Titan season — from the time of the occultation ($L_s 160°$), and both profiles are from Titan's northern summer. The profiles for $L_s = 120°$ and $L_s = 160°$ are similar in shape and vary only in peak zonal wind magnitude. The degree to which the occultation simulations generated by various input zonal wind profiles matched the data was measured by calculating SSE values for data versus model as described in Section 4.3– "Quantifying refracted lightspot patterns" (Table 4.1; full table of SSE values can be found in Table C.1 in the Supplemental Information). We note that the zonal wind profiles from these four GCM snapshot simulations are nearly identical (Figure 4.10) and that variation between the matches for these profiles was low. The data-model comparison is shown in Figure 4.14.

We considered how increasing or decreasing the GCM wind speed profiles by a factor of two (and thus accordingly increasing or decreasing the distortions of

Combined	SSE	Ingress	SSE	Egress	SSE
$L_s 120°$	570.5	ALMA	42.6	$L_s 120°$	496.7
$L_s 110°$	573.2	$L_s 10°$	52.8	$L_s 110°$	499.9
$L_s 130°$	576.7	$L_s 190°$	53.8	$L_s 130°$	504.3
$L_s 100°$	584.1	$L_s 70°$	56.5	$L_s 100°$	512.6

Table 4.1: Sum of squared errors table of the closest model-data matches for both ingress and egress spots combined, ingress spots alone, and egress spots alone. Only the original 37 input profiles (36 GCM snapshots and one ALMA profile) are included. See Table C.1 in the Supplemental Information for all SSE values for original magnitude profiles.

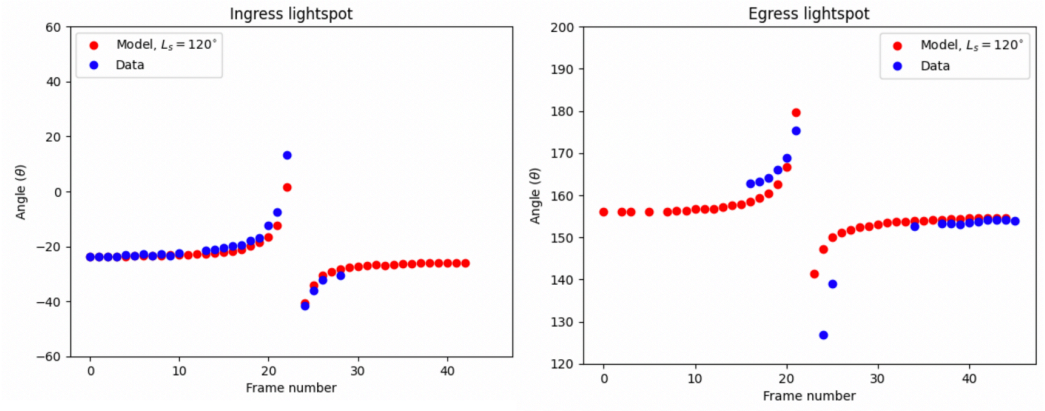


Figure 4.14: Best-match distributions of the angles of the refracted lightspots visible during occultation on the ingress and egress sides of Titan's disk. Data are depicted in blue and the model simulations with a starting atmosphere from the TAM simulation at $L_s = 120°$ are depicted in red.

surfaces of level pressure, as described in Section 4.3– "Deriving level surface distortions from zonal winds") would affect the matches. When evaluated across all residuals (ingress and egress lightspots, all frames), it was apparent that doubled wind speeds led to poorer matches across all simulations. An example poor match to a doubled GCM profile is depicted in Figure 4.15. We note that worse matches are not necessarily universally worse; rather, the comparison between model and data for the ingress lightspot in the first half of the occultation (Figure 4.15, frames 1-23 of left panel) represent a better match than the best overall match depicted in Figure 4.14. However, the trends for the egress lightspot and the latter frames for the egress lightspot denote a marked departure from the trends observed in the data, and the overall matches of the doubled zonal wind profiles from the GCM simulations perform more poorly than those of the nondoubled GCM-simulated

zonal wind profiles. Best matches for the expanded set of forward model input zonal wind profiles are presented in Table 4.2 (all SSE values listed in Tables C.2 and C.3 in the Supplemental Information).

Combined	SSE	Ingress	SSE	Egress	SSE
0.5 $\times L_s$110°	512.8	2 $\times L_s$270°	26.0	0.5 $\times L_s$110°	428.1
0.5 $\times L_s$130°	514.4	2 $\times L_s$240°	29.0	0.5 $\times L_s$130°	430.5
0.5 $\times L_s$80°	516.4	2 $\times L_s$340°	30.3	0.5 $\times L_s$120°	433.6
0.5 $\times L_s$120°	518.0	2 $\times L_s$250°	30.8	0.5 $\times L_s$80°	436.3

Table 4.2: Sum of squared errors table of the closest model-data matches for both ingress and egress spots combined, ingress spots alone, and egress spots alone. Input profiles include the original 36 GCM snapshots and one ALMA profile (that are shown above), and the same 37 profiles with both halved and doubled magnitudes (total of 111 input profiles). See Supplemental Information, Tables C.2 and C.3 for all SSE values for halved and doubled magnitude profiles.

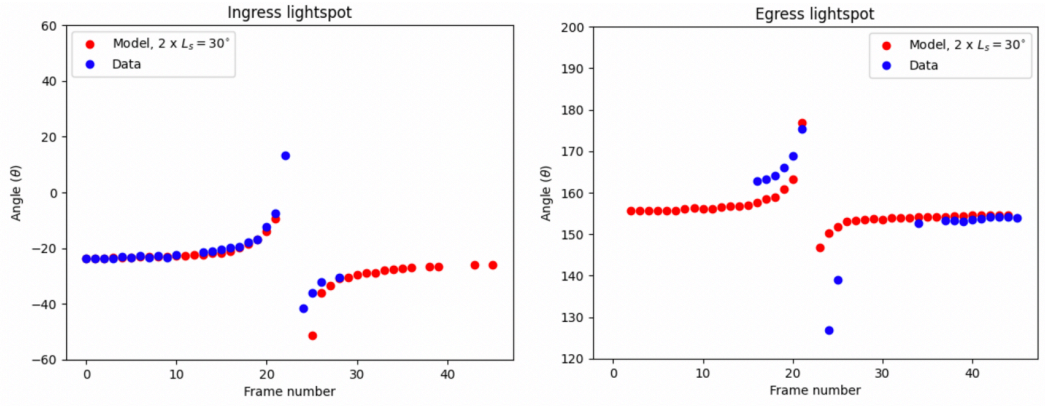


Figure 4.15: Distributions of the angles of the refracted lightspots visible during occultation on the ingress and egress side of Titan's disk. Data are depicted in blue and the model simulations (with an atmosphere corresponding to double the GCM wind speeds) at $L_s = 30°$ are depicted in red.

Halving the wind speed magnitudes from the GCM led to slightly improved matches, although the differences in matches compared to the original magnitudes were far smaller than those observed between doubled and original magnitudes. Halving the wind speed profiles did not improve the matches for the ingress spot, but generally led to better matches for the egress spot in many cases (e.g., Figure 4.16). In the set of simulations with halved magnitudes, $L_s = 120°$ was no longer the best match – there were three L_s values that produced closer matches to the data ($L_s = 110°$, $L_s = 130°$, and $L_s = 80°$) (Table 4.2).

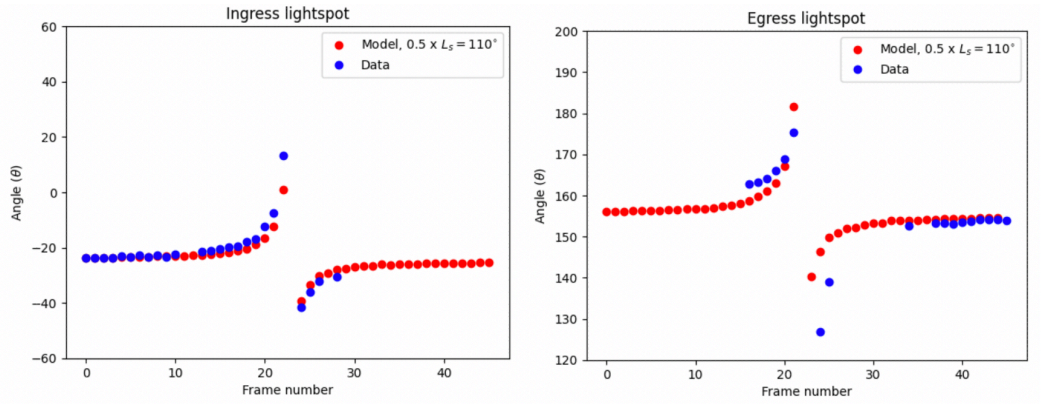


Figure 4.16: Distributions of the angles of the refracted lightspots visible during occultation on the ingress and egress side of Titan's disk. Data are depicted in blue, and the model simulations (with an atmosphere corresponding to half the GCM wind speeds) at $L_s = 120°$ are depicted in red.

Due to Titan's north pole angle on the night of the observations ($\theta = 6°.522$) and the trajectory of the occulted star, the latitudes of ingress and egress were significantly different from each other ($-9°.2$ at ingress and $31°.2$ at egress). We note that the match between data and model is significantly better for the ingress lightspot than it is for the egress lightspot and that different atmospheric profiles emerge as the best match when each lightspot is considered individually. The latitude of ingress ($-9°.2$) is closer to the equator than that of egress ($31°.2$), and the asymmetry of the matches suggest that the GCM zonal wind profiles more closely match the data nearer to the equator. We note that the radial distortion profile is constrained by a slope of zero at the equator and monotonically decreases from equator to pole on both sides. This meant that for the forward models tested the slopes for latitudes near the equator were nearer to zero and less variant than those farther from the equator. The monotonic and equatorial constraints on the radial distortion profiles come from the fact that atmospheric zonal flow will cause centrifugal acceleration directed outward radially, parallel to the equatorial plane. This force is accordingly balanced by an equator-pointing positive pressure gradient. Thus, surfaces of constant pressure from equator to both poles slope downward monotonically (Bouchez, 2004).

After determining the combined best match, we probed each individual lightspot to see what distinct trends appeared at ingress and egress.

Data versus model: Ingress lightspot

Of the original input zonal wind profiles surveyed (36 GCM snapshots and one ALMA profile), the model that best matches the data for the ingress lightspot was the ALMA input atmosphere, followed by $L_s = 10°$ and $L_s = 190°$, the two zonal wind profiles corresponding to the most symmetric radial distortions (Figure 4.11). Data-model matches are shown in Figure 4.17 and SSE values are in Table 4.1.

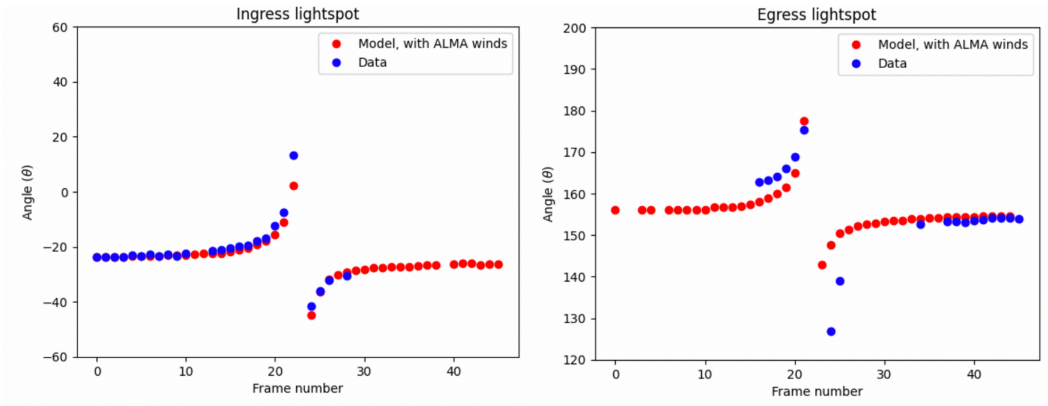


Figure 4.17: Distributions of the angles of the refracted lightspots visible during occultation on the ingress and egress sides of Titan's disk. Data are depicted in blue, and the model simulations are depicted in red. Model simulations correspond to a starting zonal wind profile derived from the ALMA data.

Although doubling the wind speeds did not lead to improved matches overall, several of the doubled zonal wind profiles from the GCM simulations did lead to a better match for the ingress lightspot. Doubling the zonal wind profile from the GCM simulation at $L_s = 270°$ led to the closest match of all starting atmospheric profiles tried, exceeding even the ALMA starting profile in quality of the match. While the best match for the combined ingress and egress lightspot favored zonal wind profiles with lower peak speeds, this restriction was not present when the ingress spot was considered alone.

Data versus model: Egress lightspot

The egress lightspot trends match those of the best match for the two lightspots combined. The best match for the egress lightspot is found at $L_s = 120°$, with $L_s = 100 - 110°$ and $L_s = 130 - 140°$ close behind. The match is visualized on the right side of Figure 4.14. All of these GCM simulated zonal wind profiles are similar in shape and magnitude, with their peak zonal winds being low compared

to other snapshots in the course of a Titan year. Doubling the zonal wind profiles led to substantially poorer matches, suggesting that there is some dependence of the match of the egress lightspot on the peak zonal wind (favoring lower values).

4.5 Discussion

On the better model match to the ingress than egress data

We propose the GCM zonal wind simulations for $L_s = 120°$ as the overall closest match among the GCM simulations for the observed occultation. The GCM zonal wind profile simulated for $L_s = 120°$ has the same basic shape as $L_s = 110°$ and $L_s = 130°$. The primary difference is that $L_s = 120°$ has the lowest peak zonal wind speeds within that time period of Titan's year, with the highest speeds reaching just under 100 m s^{-1}. When forward models were run with halved wind speeds, we determined that these half-magnitude simulations match the data slightly better overall compared to the original magnitudes. In both original magnitude and half-magnitude cases, the best-matching profiles had the same shape (peak winds at southern latitudes). The correlation between data-model match and peak wind speed magnitude was only observed in the case of the original magnitude simulations.

The best match was driven by the degree of data-model overlap observed for the egress lightspot (at latitude of 31°), which yielded higher residuals (i.e., poorer fits) than those observed for the ingress lightspot. It is additionally possible that a zonal wind profile that varies distinctly from all simulated GCM profiles would provide a better match to the data.

It is noteworthy that the improved match with lower peak zonal wind speed observed for the egress lightspot is not observed for the ingress lightspot. The best match for the ingress lightspot was observed with the ALMA data with a peak wind speed just under 200 m s^{-1}, higher than nearly all of the zonal wind profiles simulated by the GCM. Furthermore, when the GCM zonal wind speeds were doubled and the resulting profiles were inputted into the forward model, we found that some of these profiles emerged as better matches even than the ALMA data, and the ones that were the best matches had high peak wind speeds and radial distortions.

Level Surface Contours and the Mid-Event Frame: Evidence for a Southern Stratospheric Jet

The 2022 September 5 occultation was special because the Maunakea observatories were situated very close to the central chord. Images taken when the star is behind the center of Titan's disk are very important owing to the geometry of refracted

rays around the entire limb. We discuss that geometry now in the context of zonal winds, the corresponding level surfaces in the atmosphere (Δr), and what we can learn about the Δr contours from the distribution of light around the limb.

We start with the fact that the bending angle is proportional to the gradient of the line-of-sight integrated density field. This means that rays from a distant star will bend in a direction that is perpendicular to contours of constant density. If Titan were completely spherical, the occultation shadow in the observers' plane would have a sharp bright spot in the middle from all of the rays that pass through a certain annulus above Titan's limb (the annulus where the bending angle is equal to $Radius_{Titan}/Distance_{Earth-Titan}$, or $\sim 2\mu rad$). Observers at the center of the shadow would see a ring of refracted starlight around Titan's entire circular disk, because from their point of view, the projected radial lines from the star to the isopycnal contours are perpendicular around Titan's entire limb (Fig. 4.18). That is the value of an AO-capable site near the central chord — observers get to see where level surface contours are perpendicular to radial lines around Titan's entire disk. When the star is *not* directly behind the center of Titan's disk (as is the case for most or all of an occultation), there will be two regions around the limb where the perpendicular conditions hold.

What if the star is directly behind Titan's disk but Titan's projected atmosphere is *not* circular? In this case the arcs of refracted light show exactly where the isopycnal lines are perpendicular to the radial lines from the star. A rough interpretation of Panel B in Figure 4.4 is that there is a small perpendicular region near the north pole plus two broader regions around the south pole (Fig. 4.19). The implication is that Titan's atmosphere is shaped like an egg, with the pointy end near the north pole, a pattern that is consistent with stronger winds in the southern hemisphere. The near- and far-limb spots move dramatically in the few frames on either side of mid-event: these frames also constrain regions where the projected line from the star must be perpendicular to isopycnal lines. A high-cadence series of images near mid-event can map out the slopes of the Δr surface over most of Titan's limb. In theory, the slopes could be integrated to get the Δr surface itself, from which a profile of zonal winds could then be recovered. The NIRC2 data rate was one frame every 9 s, which was limited in part by the speed of the network in saving frames to disk. Still, the distribution of light around the limb in the five or six mid-event frames will be useful in constraining zonal winds, especially near the poles. We note that neither

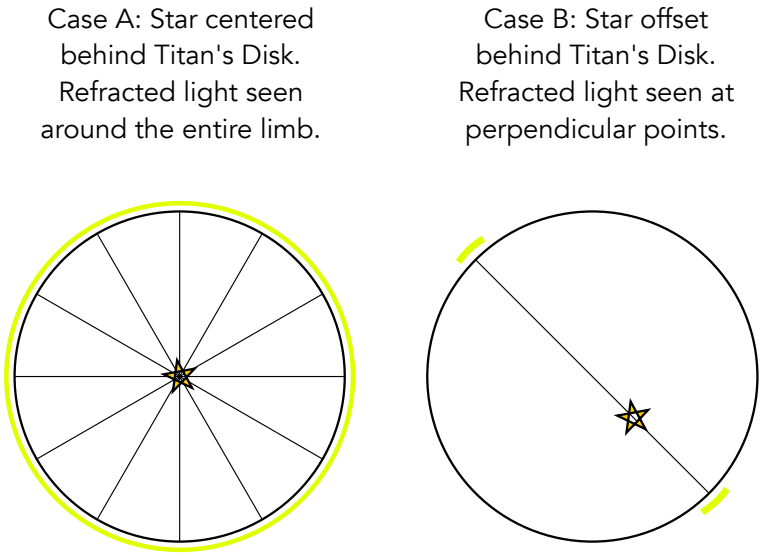


Figure 4.18: Limb light distributions for a circular Titan. Case A (left panel) shows Titan as seen by an observer at mid-event with the star directly behind Titan's disk. If Titan's atmosphere is circularly symmetric, there will be a ring of light around the entire limb because the projected lines from the star to the limb are perpendicular to the isopycnal lines all around the disk. In Case B, the star is offset from the center, and there are only two regions where the projected lines from the star are perpendicular to the isopycnal lines.

the ALMA zonal wind profile nor any of the GCM profiles produce refracted light distributions like Panel B of Fig. 4.4.

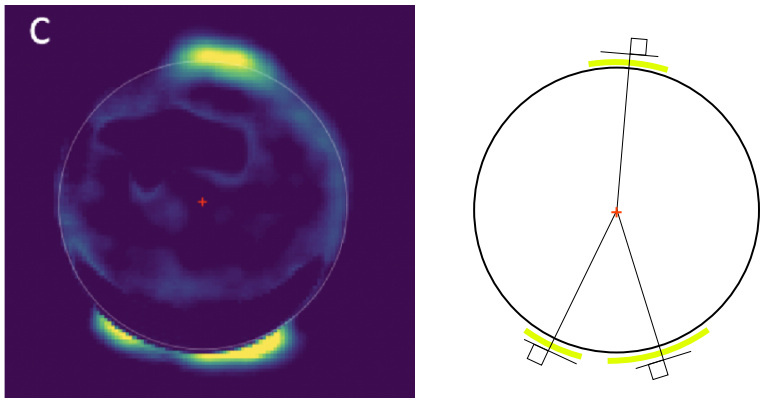


Figure 4.19: The left panel shows the resolved image of Titan taken closest to mid-event, when the star is nearly directly behind Titan's disk. The right panel is a diagram to show regions where the Δr level surface is perpendicular to the radial lines from star.

Comparison between GCM, occultation, and ALMA zonal winds

Stellar occultations, ALMA CH_3CN Doppler shifts, and TAM GCM simulations probe overlapping altitudes in Titan's atmosphere: occultations are sensitive to roughly 180-500 km, CH_3CN Doppler shift data are most sensitive to 200-400 km, and TAM GCM simulations provide predictions of wind speeds up to 650 km altitude. Overall, the GCM snapshots with higher wind speeds at southern latitudes seem to provide the best match, indicating that the GCM predictions for the solar longitude corresponding to our observations are reasonable. We additionally find that lowering the peak wind speed of the GCM profiles led to slightly better data-model matches, although the profiles that best match the ingress spot were different from those that best match the egress spot. The forward model resulting from the ALMA wind profile matches the data for the ingress spot better than any of the GCM model simulations, although its match to the egress spot was poorer. The shape of the derived ALMA wind profile did not closely match any of the GCM wind profiles for the surrounding L_s values, which had peak wind speeds at latitudes farther from the equator. We note that the implementations of ALMA and GCM profiles in our forward model varied slightly owing to GCM simulations being altitudinally resolved while ALMA-retrieved wind speeds are averaged over an altitude contribution function (Figure 4.7). Thus, a forward model implementation with a GCM starting profile incorporates wind speeds that vary with altitude, which may account for some of the differences observed when employing the two different types of starting profiles.

We considered results from three distinctly different methods of studying zonal winds: computational simulations from General Circulation Models, characterization of radial distortion profiles and, accordingly, zonal wind profiles via the behavior of refracted starlight, and zonal winds derived from ALMA Doppler shifts of specific molecules in Titan's atmosphere. The GCM affords the ability to define and refine input parameters, specify latitudes, and simulate profiles across an entire Titan year. However, as the simulations consist of free-running numerical simulations, they do not necessarily probe the real system like the other two techniques discussed here.

Zonal wind profiles from ALMA data of Doppler shifts of a specific molecule probe a large range of altitudes in Titan's atmosphere. Spatial resolution is driven by the configuration of the ALMA dishes on the night of the observation and CH_3CN (the molecule probed in the results presented here) has a contribution function that

reaches higher altitudes than either the TAM simulations or stellar occultations, albeit at limited sensitivities above 400 km (Figure 4.7). As the thermospheric equatorial jet proposed by Lellouch et al., 2019b has been shown to extend down into the mesosphere (Cordiner et al., 2020), it is possible that the jet has a small influence on the overall ALMA wind profile, which would be less prominent in the occultation data and GCM simulations owing to their lower maximum altitudes. As the ALMA wind profile is not vertically resolved, isolating the contribution of the equatorial jet from the contributions of winds at lower altitudes that contribute more heavily to the CH_3CN profile is not possible.

Stellar occultation observations with AO-equipped telescopes present a unique chance to directly image refracted starlight as it moves around Titan's limb. The combination of starting GCM-derived wind profiles and the HASI temperature profile allowed vertical resolution to be maximized across the sensitive range. However, the process of comparing refracted lightspots to potential atmospheres that could generate such patterns is cumbersome and computationally expensive, making inversion with ray-tracing time-intensive. Development of faster pipelines has not been a priority due to the rarity of observable occultations and data sets; the 2022 Titan occultation is only the second one to be observed with AO and the first one in more than 20 yr. With this data set, an additional recent Titan occultation data set, and an upcoming 2026 Titan occultation, we are hopeful for increased attention toward this field in the coming years.

4.6 Conclusions

We present observations of a stellar occultation by Titan obtained with Keck on 2022 September 5, together with ALMA data of the satellite one day later. We use a forward model to simulate the occultation, and to compare the stellar occultation data to the ALMA profile and to 36 GCM profiles spanning an entire Titan year, as well as the same set of 37 profiles with both doubled and halved zonal wind speeds. We find that overall the GCM profile corresponding to a solar longitude of 120° (roughly 40° before the time of the occultation) matches the data best, with similarly shaped profiles with neighboring L_s values following close behind (Table 4.1). The zonal wind profile (and corresponding radial distortion profile) for L_s = 120° is not substantially different from the neighboring L_s values, and it has a low peak zonal wind and peak radial distortion value compared to many of the other L_s values from the GCM simulations. The peak zonal wind is found in the southern hemisphere, which is consistent with GCM predictions given Titan's season at the time of the

occultation. The findings of this paper may aid future studies of Titan's climate, chemistry, and long-term atmospheric evolution, as well as constrain and inform findings of the upcoming *Dragonfly* mission.

There was a notable disparity between the matches of the ingress lightspot and the egress lightspot to the data, with the best model match to the ingress lightspot data being substantially better than that of the egress lightspot. The latitudes of ingress and egress vary significantly ($-9°$ versus $31°$). It seems that the data better constrain zonal winds (and accordingly, radial distortions) at the ingress latitude. We also note that assuming longitudinal symmetry excludes possible localized events that could be happening in the atmosphere regions probed by ingress and egress, such as planetary-scale waves. When the ingress lightspot and egress lightspot are considered individually, different starting atmospheric profiles match best — the best match for the egress lightspot favors lower peak wind speeds, while the ingress lightspot data were best matched by the ALMA starting atmosphere and several doubled GCM zonal wind profiles (i.e., no favoring of low wind speeds as is observed for the egress lightspot). The strength of the match between the ingress lightspot observations and the atmospheric model derived from ALMA interferometry supports the complementarity of (optical) occultation and (radio) Doppler mapping techniques for zonal wind investigations.

Finally, the mid-event frame shows wider arcs on both the north and south limbs in a pattern that we were unable to reproduce with any of our forward models. We are looking forward to enriching the results of this paper with a refined inversion technique, analyzing a second occultation dataset gathered in 2022, and gathering additional data from the upcoming 2026 South America occultation.

Separately, the impending autumnal equinox suggests a critical time of rapid change for the zonal wind structure of Titan's atmosphere. We are fortunate to have one additional Titan stellar occultation of a bright (G_{mag} = 10.62) star approaching in September 2026. The center of the shadowpath will cross over southern Argentina and Chile, and we will employ a "picket fence" line of portable telescopes, with chords crossing near the central flash of the occultation. The Very Large Telescope (VLT) is also within the shadowpath, and we hope to leverage the combination of the VLT and the portable telescopes to gain a comprehensive profile of Titan in the time immediately following northern autumnal equinox.

4.7 Acknowledgements

We would like to thank the staff astronomers and telescope operators at W. M. Keck Observatory for assisting with the operations both leading up to the observation night and during the event itself. TCM, EFY, and MAC were supported by a grant from the NASA ROSES Solar System Observations program. MAC and CAN were supported by a grant from the NASA ROSES Solar System Observations program.

This paper makes use of the following ALMA data: ADS/JAO.ALMA#2021.A.00034.S. ALMA is a partnership of ESO (representing its member states), NSF (USA) and NINS (Japan), together with NRC (Canada), NSTC and ASIAA (Taiwan), and KASI (Republic of Korea), in cooperation with the Republic of Chile. The Joint ALMA Observatory is operated by ESO, AUI/NRAO and NAOJ.

References

Achterberg, Richard K (2023). "Temporal Evolution of Titan's Stratospheric Temperatures and Trace Gases from a Two-dimensional Retrieval of Cassini Composite Infrared Spectrometer Data". In: *The Planetary Science Journal* 4.8, p. 140.

Achterberg, Richard K., Barney J. Conrath, et al. (Mar. 2008). "Titan's middle-atmospheric temperatures and dynamics observed by the Cassini Composite Infrared Spectrometer". In: *Icarus* 194.1, pp. 263–277. ISSN: 0019-1035. DOI: 10.1016/j.icarus.2007.09.029. URL: https://www.sciencedirect.com/science/article/pii/S0019103507004976.

Achterberg, Richard K., Peter J. Gierasch, et al. (Jan. 2011). "Temporal variations of Titan's middle-atmospheric temperatures from 2004 to 2009 observed by Cassini/CIRS". In: *Icarus* 211.1, pp. 686–698. ISSN: 0019-1035. DOI: 10.1016/j.icarus.2010.08.009. URL: https://www.sciencedirect.com/science/article/pii/S0019103510003155.

Bird, Michael K. et al. (2005). "The vertical profile of winds on Titan". In: *Nature* 438.7069, pp. 800–802.

Bouchez, Antonin Henri (2004). "Seasonal trends in Titan's atmosphere: Haze, wind, and clouds". ISBN: 9780496723560 Publication Title: ProQuest Dissertations and Theses. Ph.D. United States – California: California Institute of Technology. URL: https://www.proquest.com/docview/305203060/abstract/7887C087627C4A4EPQ/1.

Brown, Robert H., Jean-Pierre Lebreton, and J. Hunter Waite, eds. (2010). *Titan from Cassini-Huygens*. Dordrecht: Springer Netherlands. ISBN: 978-1-4020-9214-5 978-1-4020-9215-2. DOI: 10.1007/978-1-4020-9215-2. URL: http://link.springer.com/10.1007/978-1-4020-9215-2.

Clark, Roger N. et al. (2010). "Detection and mapping of hydrocarbon deposits on Titan". In: *Journal of Geophysical Research: Planets* 115.E10. _eprint: https://onlinelibrary.wiley.com/doi/p ISSN: 2156-2202. DOI: 10.1029/2009JE003369. URL: https://onlinelibrary.wiley.com/doi/abs/10.1029/2009JE003369.

Cordiner, Martin A. et al. (Nov. 2020). "Detection of Dynamical Instability in Titan's Thermospheric Jet". In: *The Astrophysical Journal* 904. ADS Bibcode: 2020ApJ...904L..12C, p. L12. ISSN: 0004-637X. DOI: 10.3847/2041-8213/abc688. URL: https://ui.adsabs.harvard.edu/abs/2020ApJ...904L..12C.

Flasar, F. Michael and R. Achterberg (Nov. 2008). "The structure and dynamics of Titan's middle atmosphere". In: *Philosophical Transactions of the Royal Society A: Mathematical, Physical and Engineering Sciences* 367.1889. Publisher: Royal Society, pp. 649–664. DOI: 10.1098/rsta.2008.0242. URL: https://royalsocietypublishing.org/doi/full/10.1098/rsta.2008.0242.

Flasar, F. Michael, Richard K Achterberg, et al. (2005). "Titan's atmospheric temperatures, winds, and composition". In: *science* 308.5724, pp. 975–978.

Fulchignoni, Marcello et al. (Dec. 2005). "In situ measurements of the physical characteristics of Titan's environment". In: *Nature* 438.7069. Publisher: Nature Publishing Group, pp. 785–791. ISSN: 1476-4687. DOI: 10.1038/nature04314. URL: https://www.nature.com/articles/nature04314.

Ginsburg, Adam (Sept. 2023). *image-registration: Package for registering images with extended emission*. URL: https://image-registration.readthedocs.io/en/latest/.

Hörst, Sarah M. (2017). "Titan's atmosphere and climate". In: *Journal of Geophysical Research: Planets* 122.3, pp. 432–482. ISSN: 2169-9100. DOI: 10.1002/2016JE005240. URL: https://onlinelibrary.wiley.com/doi/abs/10.1002/2016JE005240.

Hourdin, Frédéric et al. (Oct. 1995). "Numerical Simulation of the General Circulation of the Atmosphere of Titan". In: *Icarus* 117.2, pp. 358–374. ISSN: 0019-1035. DOI: 10.1006/icar.1995.1162. URL: https://www.sciencedirect.com/science/article/pii/S0019103585711621.

Hubbard, William B. et al. (Mar. 1993). "The occultation of 28 SGR by Titan." In: *Astronomy and Astrophysics* 269. ADS Bibcode: 1993A&A...269..541H, pp. 541–563. ISSN: 0004-6361. URL: https://ui.adsabs.harvard.edu/abs/1993A&A...269..541H.

Irwin, Patrick G. J. et al. (Apr. 2008). "The NEMESIS planetary atmosphere radiative transfer and retrieval tool". In: *J. Quant. Spectrosc. Radiat. Transfer* 109, pp. 1136–1150. DOI: 10.1016/j.jqsrt.2007.11.006.

Jaeger, Shannon (Aug. 2008). "The Common Astronomy Software Application (CASA)". In: *Astronomical Data Analysis Software and Systems XVII*. Ed. by R. W. Argyle, P. S. Bunclark, and J. R. Lewis. Vol. 394. Astronomical Society of the Pacific Conference Series, p. 623.

Lebonnois, Sébastien et al. (2012). "Titan global climate model: A new 3-dimensional version of the IPSL Titan GCM". In: *Icarus* 218.1, pp. 707–722.

Lellouch, E. et al. (Apr. 2019a). "An intense thermospheric jet on Titan". In: *Nature Astronomy* 3, pp. 614–619. DOI: 10.1038/s41550-019-0749-4. arXiv: 1903.12116 [astro-ph.EP].

Lellouch, Emmanuel et al. (2019b). "An intense thermospheric jet on Titan". In: *Nature Astronomy* 3.7, pp. 614–619.

Light, Siobhan et al. (2024). "Measurements of Titan's Stratospheric Winds during the 2009 Equinox with the eSMA". In: *The Planetary Science Journal* 5.4, p. 98.

Lombardo, Nicholas A. and J. M. Lora (2023a). "The Heat and Momentum Budgets of Titan's Middle Atmosphere". In: *Journal of Geophysical Research: Planets* 128.12. _eprint: https://onlinelibrary.wiley.com/doi/pdf/10.1029/2023JE008061, e2023JE008061. ISSN: 2169-9100. DOI: 10.1029/2023JE008061. URL: https://onlinelibrary.wiley.com/doi/abs/10.1029/2023JE008061.

Lombardo, Nicholas A. and Juan M. Lora (Jan. 2023b). "Influence of observed seasonally varying composition on Titan's stratospheric circulation". In: *Icarus* 390. ADS Bibcode: 2023Icar..39015291L, p. 115291. ISSN: 0019-1035. DOI: 10.1016/j.icarus.2022.115291. URL: https://ui.adsabs.harvard.edu/abs/2023Icar..39015291L.

Lora, Juan M., Jonathan I. Lunine, and Joellen L. Russell (Apr. 2015). "GCM simulations of Titan's middle and lower atmosphere and comparison to observations". In: *Icarus* 250, pp. 516–528. ISSN: 0019-1035. DOI: 10.1016/j.icarus.2014.12.030. URL: https://www.sciencedirect.com/science/article/pii/S0019103514007210.

Lucy, L. B. (June 1974). "An iterative technique for the rectification of observed distributions". In: *The Astronomical Journal* 79, p. 745. DOI: 10.1086/111605.

MacKenzie, Shannon M. et al. (June 2021). "Titan: Earth-like on the Outside, Ocean World on the Inside". In: *The Planetary Science Journal* 2.3. Publisher: IOP Publishing, p. 112. ISSN: 2632-3338. DOI: 10.3847/PSJ/abf7c9. URL: https://iopscience.iop.org/article/10.3847/PSJ/abf7c9/meta.

Markwardt, Craig B. (2009). "Non-linear least squares fitting in IDL with MPFIT". In: *arXiv preprint arXiv:0902.2850*.

Matthew Newville, Till Stensitzki, and Renee Otten (2024). *Built-in Fitting Models in the models module — Non-Linear Least-Squares Minimization and Curve-Fitting for Python*. URL: https://lmfit.github.io/lmfit-py/builtin_models.html.

Moffat, Anthony F. J. (1969). "A theoretical investigation of focal stellar images in the photographic emulsion and application to photographic photometry". In: *Astronomy and Astrophysics, Vol. 3, p. 455 (1969)* 3, p. 455.

Molter, Ned (Sept. 2024). *emolter/nirc2_reduce*. original-date: 2017-11-13T22:13:31Z. URL: https://github.com/emolter/nirc2_reduce.

Moreno, Ramiro, A. Marten, and T. Hidayat (July 2005). "Interferometric measurements of zonal winds on Titan". In: *Astronomy & Astrophysics* 437.1. Number: 1 Publisher: EDP Sciences, pp. 319–328. ISSN: 0004-6361, 1432-0746. DOI: 10.1051/0004-6361:20042117. URL: https://www.aanda.org/articles/aa/abs/2005/25/aa2117-04/aa2117-04.html.

Newman, Claire E. et al. (June 2011). "Stratospheric superrotation in the TitanWRF model". In: *Icarus* 213.2, pp. 636–654. ISSN: 0019-1035. DOI: 10.1016/j.icarus.2011.03.025. URL: https://www.sciencedirect.com/science/article/pii/S0019103511001163.

Nixon, Conor A. (Mar. 2024). "The Composition and Chemistry of Titan's Atmosphere". In: *ACS Earth and Space Chemistry* 8.3. Publisher: American Chemical Society, pp. 406–456. DOI: 10.1021/acsearthspacechem.2c00041. URL: https://doi.org/10.1021/acsearthspacechem.2c00041.

Nosowitz, Jonathon et al. (May 2025). "Improved Carbon and Nitrogen Isotopic Ratios for CH3CN in Titan's Atmosphere Using ALMA". In: *The Planetary Science Journal* 6.5. Publisher: The American Astronomical Society, p. 107. DOI: 10.3847/PSJ/adc390. URL: https://dx.doi.org/10.3847/PSJ/adc390.

Richardson, William Hadley (Jan. 1972). "Bayesian-Based Iterative Method of Image Restoration*". In: *J. Opt. Soc. Am.* 62.1, pp. 55–59. DOI: 10.1364/JOSA.62.000055. URL: https://opg.optica.org/abstract.cfm?URI=josa-62-1-55.

Sharkey, Jason et al. (2021). "Potential vorticity structure of Titan's polar vortices from Cassini CIRS observations". In: *Icarus* 354, p. 114030.

Shultis, Jacob et al. (2022). "Winter weakening of Titan's stratospheric polar vortices". In: *The Planetary Science Journal* 3.4, p. 73.

Sicardy, Bruno (2022). "Study of atmospheres in the solar system, from stellar occultation or planetary transit". fr. In: *Comptes Rendus. Physique* 23.S1, pp. 213–241. ISSN: 1878-1535. DOI: 10.5802/crphys.109. URL: https://comptes-rendus.academie-sciences.fr/physique/articles/10.5802/crphys.109/.

Sicardy, Bruno et al. (2006). "The two Titan stellar occultations of 14 November 2003". In: *Journal of Geophysical Research: Planets* 111.E11. ISSN: 2156-2202. DOI: 10.1029/2005JE002624. URL: https://onlinelibrary.wiley.com/doi/abs/10.1029/2005JE002624.

Soderblom, Laurence A. et al. (Nov. 2007). "Correlations between Cassini VIMS spectra and RADAR SAR images: Implications for Titan's surface composition and the character of the Huygens Probe Landing Site". In: *Planetary and Space Science*. Titan as seen from Huygens 55.13, pp. 2025–2036. ISSN: 0032-0633. DOI: 10.1016/j.pss.2007.04.014. URL: https://www.sciencedirect.com/science/article/pii/S0032063307001304.

Teanby, Nicholas A., P. G. J. Irwin, R. de Kok, et al. (Feb. 2007). "Vertical profiles of HCN, HC3N, and C2H2 in Titan's atmosphere derived from Cassini/CIRS data". In: *Icarus* 186.2, pp. 364–384. ISSN: 0019-1035. DOI: 10.1016/j.icarus.2006.09.024. URL: https://www.sciencedirect.com/science/article/pii/S0019103506003459.

Teanby, Nicholas A., P. G. J. Irwin, Conor A. Nixon, et al. (Nov. 2012). "Active upper-atmosphere chemistry and dynamics from polar circulation reversal on Titan". In: *Nature* 491.7426. Publisher: Nature Publishing Group, pp. 732–735. ISSN: 1476-4687. DOI: 10.1038/nature11611. URL: https://www.nature.com/articles/nature11611.

Teanby, Nicholas A., R. de Kok, et al. (2008). "Titan's winter polar vortex structure revealed by chemical tracers". In: *Journal of Geophysical Research: Planets* 113.E12. _eprint: https://onlinelibrary.wiley.com/doi/pdf/10.1029/2008JE003218. ISSN: 2156-2202. DOI: 10.1029/2008JE003218. URL: https://onlinelibrary.wiley.com/doi/abs/10.1029/2008JE003218.

Thelen, Alexander E, C. A. Nixon, et al. (2019). "Abundance measurements of Titan's stratospheric HCN, HC_3N, C_3H_4, and CH_3CN from ALMA observations". In: *Icarus* 319, pp. 417–432.

Thelen, Alexander E., Martin A. Cordiner, et al. (Nov. 2020). "Detection of CH_3C_3N in Titan's Atmosphere". In: *The Astrophysical Journal Letters* 903.1, L22, p. L22. DOI: 10.3847/2041-8213/abc1e1. arXiv: 2010.08654 [astro-ph.EP].

Van Der Walt, Stéfan et al. (June 2014). "scikit-image: image processing in Python". In: *PeerJ* 2, e453. ISSN: 2167-8359. DOI: 10.7717/peerj.453. URL: https://peerj.com/articles/453.

Willacy, Karen et al. (July 2022). "Vertical Distribution of Cyclopropenylidene and Propadiene in the Atmosphere of Titan". In: *The Astrophysical Journal* 933.2. Publisher: The American Astronomical Society, p. 230. ISSN: 0004-637X. DOI: 10.3847/1538-4357/ac6b9d. URL: https://dx.doi.org/10.3847/1538-4357/ac6b9d.

Zalucha, A. et al. (Dec. 2007). "The 2003 November 14 occultation by Titan of TYC 1343-1865-1: II. Analysis of light curves". In: *Icarus* 192.2, pp. 503–518. ISSN: 0019-1035. DOI: 10.1016/j.icarus.2007.08.008. URL: https://www.sciencedirect.com/science/article/pii/S0019103507003545.

Chapter 5

CONCLUSION AND FUTURE DIRECTIONS

This work presents three distinct astrobiological findings oriented toward understanding the origins of life on Earth and the complex organic inventory present on the Saturnian satellite Titan.

Chapter 2 considers reactions of simple organics (alpha keto acids) and chemical gardens (hydrothermal vent analogs). The catalytic properties of the mixed compositions of chemical gardens (amorphous silica, iron oxyhydroxide minerals, and iron hydroxide minerals) under various conditions are assessed. Non-saline reactions containing glyoxylic acid and ammonia led to the formation of glycine, the simplest amino acid. Production of maloyl formate (a precursor to alpha keto glutarate/AKG, a key metabolic intermediate) was observed in the presence of both glyoxylic acid and pyruvic acid and in the absence of heat, an exciting result that suggests many more avenues for follow-up experiments. The formation of prebiotically-relevant molecules in a controlled laboratory setting (simplified chemical garden analogs) suggests a pathway for abiotic synthesis of these same molecules in an early Earth setting. It is critical to be aware of the simplifications of the laboratory analogs and to note that highly saline conditions (such as the Enceladus analog) led to diminished product formation. Thus, the key findings of this study are unfortunately not likely to be as applicable to Enceladus, although it is worth noting that the salinity used to approximate an Enceladus ocean was based on a model and not necessarily the actual ocean composition found at Enceladus. Additional studies could increase complexity, probe a spectrum of salinity, or consider additional reactants in order to further characterize the potential for hydrothermal vent-mediated origins of life at the sea floor. These findings further the search for how life originated on Earth by demonstrating plausible pathways for synthesis of key prebiotic molecules in a laboratory setting approximating the early Earth sea floor.

Chapter 3 presents a novel characterization of propyne ice, a photochemically produced organic species in Titan's atmosphere. It presents the first published Raman data of propyne ice in the amorphous and crystalline phases, offers complementary infrared spectroscopy data to work published by Hudson et al., 2021, and explores physical parameters of the unit cell via X-ray diffraction. The amorphous-

to-crystalline temperatures in the Raman versus the Infrared spectral data had a discrepancy of roughly 30 Kelvin. We attributed this discrepancy to the rapid deposition rate of the Raman system, as rapid deposition rate has long been known to influence transition temperature (Malherbe et al., 1951). Propyne is just one molecule in a complex system of photochemically produced, interacting organics. The work presented here is a critical baseline for future work studying how the organics in Titan's atmosphere interact with each other, travel through the atmosphere, and deposit upon and interact with Titan's surface. Understanding pure propyne enables a more informed analysis of the vast amount of data left behind by *Cassini* (particularly in characterizing the stratospheric ice clouds that motivated this work initially). In just under a decade, the rotorcraft *Dragonfly* will land on Titan's surface, conducting detailed measurements of its organic inventory. Should solid propyne be found on its surface, this foundational work will be complementary to *Dragonfly*'s findings. Although *Dragonfly* does not have a Raman or infrared spectrometer on board, these data will still provide valuable context. Additionally, a Titan orbiter is included in the decadal survey (*Origins, Worlds, and Life* 2022) as a potential future mission — although such a mission would be many years away, the findings in this work would complement and elevate Titan orbiter data.

Chapter 4 presents a comparison of zonal winds in Titan's middle atmosphere via stellar occultations, ALMA Doppler shifts, and General Circulation Models (GCMs). It is a forward modeling effort, determining whether various predicted GCM simulations and a near-concurrent night of ALMA data match the winds probed by a one-time stellar occultation. The best match was still quite far from the observed data, highlighting the potential limitations of GCMs. While GCMs allow us to probe an unparalleled range of latitudes, times, and altitudes, they are simulations. They can be compared to and informed by data, but they are not themselves data. Thus, it is worth noting that the poor match between data and simulation could be simply because the GCMs are not properly or fully modeling some aspect of Titan's atmosphere. The work also compared ALMA Doppler shift data findings to the stellar occultation data. The match was close for the point of ingress (the beginning of the occultation), but the point of egress did not match as well. The discrepancy may be due to the contribution function and single vertical profile to which ALMA is sensitive. The sensitivity of the resulting wind profile is dependent on the distribution of the probed molecule within Titan's atmosphere, and variation due to latitude cannot be incorporated. While these limitations should be acknowledged, this work presents a best-match middle atmosphere wind profile with

stronger winds observed in the southern hemisphere. This finding broadly agrees with trends observed in the occultation data. Understanding middle atmosphere winds is highly relevant for transport of organics on Titan, which are photochemically produced high in the atmosphere and pass through the middle atmosphere as they drift lower and eventually deposit on the surface. Understanding middle atmosphere wind speeds at equatorial latitudes (where *Dragonfly* will land) will provide valuable context for the spacecraft's study of surface organics.

The three distinct chapters presented here each offer a story. But as with any research project, the questions answered within each chapter raised countless more — ideas for follow-up experiments, observations, and studies. Below is a combination of works in progress, planned works, and wishlist items that hopefully one day will be studied:

5.1 Chemical gardens as analogs for prebiotic chemistry on ocean worlds:

- **Variation of pyruvic acid/glyoxylic acid ratio in CG experiments.** Some of the most interesting and exciting chemistry observed was seen in the samples containing both pyruvic acid and glyoxylic acid. The peak signature of maloyl formate was observed (Figure 2.4). Although we were not able to confirm with certainty that maloyl formate was indeed formed, it is highly likely due to the distinctive character of maloyl formate and the fact that maloyl formate has been observed as a product in reactions containing pyruvic acid and glyoxylic acid before (Stubbs et al., 2020). Maloyl formate is a particularly exciting product as it is a precursor to alpha keto glutarate, a key metabolic molecule. We did not observe any alpha keto glutarate formation in our reactions, but it has been suggested that proceeding beyond maloyl formate to alpha keto glutarate formation requires an excess of glyoxylic acid. Thus, an immediate future step would be to repeat the reactions and increase the glyoxylic acid/pyruvic acid ratio above 1 to see how it affects maloyl formate abundance and whether it leads to the formation of alpha keto glutarate.

- **Conduct heated reactions with stirring.** The heated reactions for this work were carried out in a hot water bath, meaning that there was no possibility for the reactions to be stirred. The reactions conducted reaction under heated conditions displayed several distinct variations from the aerobic/anaerobic room temperature conditions that were both stirred: the VNIR peaks were smoother and no maloyl formate formation was observed. The solid product

at the end of each set of reactions also varied greatly for the heated reaction: it was discrete chunks of material instead of the fine power that resulted from weeks of continuous stirring. So while we can hypothesize that the product differences between heated and non-heated are a result of the presence or absence of heat, the presence or absence of stirring can not be discounted either. Additional experiments would allow a better separation of the effects of heat versus room-temperature and of stirring versus not stirring.

- **Grow chemical gardens under anaerobic and/or heated conditions.** The chemical gardens in all of our reactions were grown on the benchtop — in aerobic, room temperature conditions. An interesting future avenue would be to grow the chemical gardens under heated and anaerobic conditions such that the chemical garden growth condition matches the condition that each reaction is carried out under. Particularly, growing chemical gardens in an anaerobic chamber would be an interesting avenue to pursue: a week on the benchtop led to substantial oxidation and darkening of the chemical garden (see Figure 2.1) which would be entirely cirucmvented if the chemical gardens were grown in the anaerobic chamber.

- **Doing reactions under heated, anaerobic conditions.** We considered benchtop (room temperature/aerobic), anaerobic (room temperature), or heated (aerobic). Each of these corresponded to a different aspect relevant to the origin of life. However, one notably missing condition was carrying out reactions under anaerobic, heated conditions. It would be particularly interesting to trace the formation of maloyl formate (which was observed anaerobically but not at heat). It would also be valuable to study whether the characteristic signatures observed in the heated and anaerobic reactions are additive in the case of both conditions being imposed at once, or if a different set of product signatures emerges.

- **Grow "Enceladuslike" chemical gardens, or ones in different solutions.** The chemical gardens in this work were constructed with two ingredients: dilute sodium silicate and ferrous chloride. The dilution of sodium silicate was carried out with Milli-Q (ultra pure) water. To approximate Earth seawater or an ocean elsewhere in the Solar System, the Milli-Q water could be substituted with a saline solution approximating Earth's ocean, or a solution approximating the conditions and components predicted in Enceladus' subsurface ocean (Glein et al., 2020). Growing these chemical gardens in

Enceladuslike conditions has already been preliminarily explored (Cardoso et al., 2019); an interesting next step would be using these in the reactions conducted in Enceladuslike conditions.

- **Conduct experiments under high pressure.** All experiments conducted were done at atmospheric (1 atm) pressure. However, hydrothermal vents do not occur on the surface: they are on the ocean floor under much higher pressure (hundreds of atmospheres). This difference in pressure between experimental analog and actual hydrothermal vent could potentially alter the reactions and products formed. By collaborating with a laboratory capable of running reactions at high pressure, we would be able to further characterize these reactions at high pressure and better understand how the chemistry might proceed at the ocean floor.

- **Incorporation of phosphate into chemical garden experiments.** Phosphate is a key biogenic molecule. There are potential pathways for it to have existed on early Earth (e.g. Ritson et al., 2020), and it was recently discovered at Enceladus (Postberg et al., 2023). Some preliminary work has been done in iron-silicate-phosphate chemical gardens to consider how the quantity and ratio of phosphate compared to other components affects the morphology of the chemical gardens (Barge et al., 2012). However, little work has been done yet to study the chemical reactivity of iron-silicate-phosphate chemical gardens. Replicating a subset of these experiments with phosphate-containing chemical gardens could lead to novel prebiotically-relevant products while adding another layer of complexity that is relevant to early Earth and Enceladus.

5.2 Propyne: Determination of Physical Properties and Unit Cell Parameters under Titan-Relevant Conditions

- **Full characterization of propyne at ambient pressure:** Before we started collecting the data that is in the published work currently presented in this thesis, many days were spent in the lab puzzling over the propyne spectra that were yielded by using a non-vacuum cryostage (i.e., at ambient pressure, an analog for Titan's surface). In fact, Morgan and I collected a total of 100 spectra of pure propyne, roughly 60 of which were conducted with the ambient pressure stage. We only put two spectra (and 0 at ambient pressure) in the final paper, a dismal effort to publication ratio. We simply could not get a consistent spectrum for propyne under ambient pressure, with the H-C≡C region (600-

700 cm^{-1}) having a large amount of variability. Even when deposition styles were the same (as in the bottom five traces)- the spectral peaks were variant in amplitude and distribution. The arbitrary appearance and disappearance of the so-nicknamed "mystery peak" (675 cm^{-1}) was of particular interest and frustration to us, and we ultimately switched to a vacuum pressure stage in the interest of seeing if we could get more consistent data. With the vacuum stage, we were able to characterize the mystery peak as resulting from amorphous phase propyne. However, propyne and its spectra under ambient pressure remains a wide open field with many more questions and characterizations to pursue. These are of particular interest and relevance for Titan's surface as organics are expected to deposit and form co-crystals (Cable, Runčevski, et al., 2021).

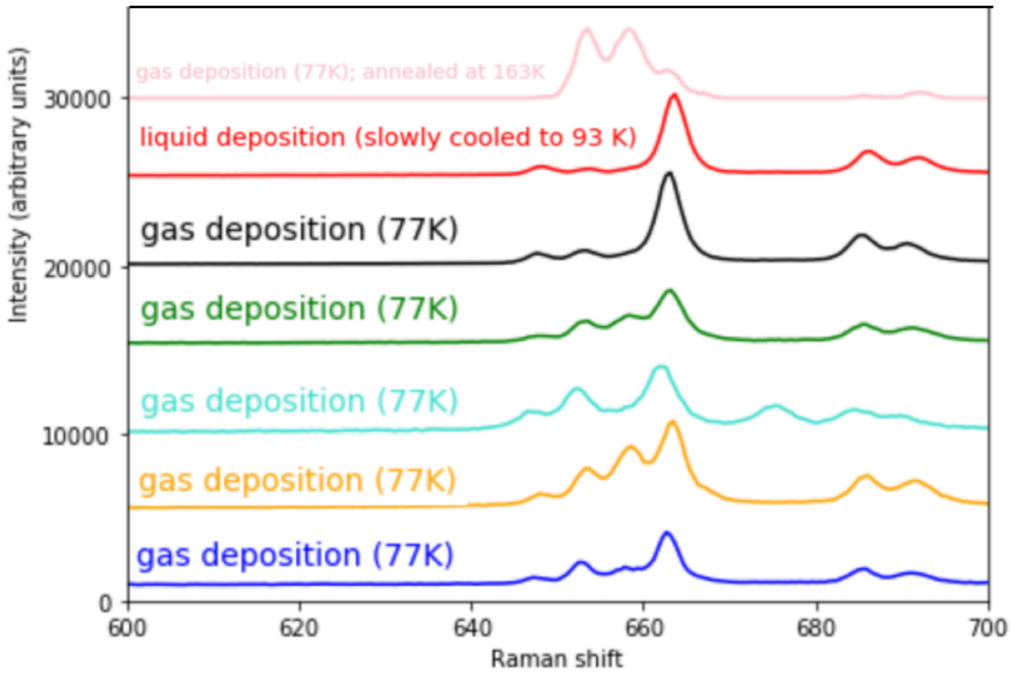


Figure 5.1: The many flavors of the H-C≡C region of propyne under ambient pressure.

- **Exploration of a potential propyne-methane co-crystal and other co-crystals involving propyne.** The behavior of and interactions between the various organic compounds in Titan's atmosphere and surface deposits are of particularly interest to the scientific community with the impending *Dragonfly* mission. Co-crystals have been observed to form between various organics

in Titan-relevant conditions (e.g., Cable, Vu, Maynard-Casely, et al., 2018; Cable, Vu, Malaska, et al., 2019; Cable, Vu, Malaska, et al., 2020; Czaplinski et al., 2020), but there have not yet been any published co-crystals with propyne. Tentative evidence was discovered for a co-crystal between propyne and methane at ambient pressure; shifts were observed in both the CH_3 s-stretch region (around 2900 cm^{-1}) and the H-C≡ stretch region (around 3275 cm^{-1}). The shifts and tentative co-crystal existence were short-lived: within 40 seconds, the peaks had shifted back to what would be expected from an additive combination of propyne and methane. A propyne-methane co-crystal would be particularly interesting due to methane's presence in surface lakes. Even a transient co-crystal interaction between organically deposited propyne and the methane lakes would be an important aspect of the overall characterization of organic-laden lake shorelines in Titan's polar regions.

- **Raman spectroscopy with an ultra-tunable deposition rate.** The temperature of amorphous-to-crystalline transformation for solid propyne was markedly different for infrared spectroscopy (70-75K) versus Raman spectroscopy (105-107K). The discrepancy was hypothesized to be due to the elevated and uncontrollable deposition rate of the Raman spectroscopy system. Future experimentation to augment the infrared characterization would ideally use a Raman cryostage that is capable of slow and steady deposition to confirm the transition temperature observed with infrared spectroscopy.

- **Structural characterization of co-condensed organics relevant to Titan's stratospheric clouds.** The work for this chapter was born out of a project dedicated to a deeper understanding of Titan's stratospheric ice clouds observed by the Composite Infrared Spectrometer (CIRS) onboard *Cassini*. The CIRS spectra have been partially reproduced in lab (e.g., Ugelow et al., 2020); however, the best-matched combination of organics in lab still do not entirely reproduce the spectra measured by CIRS. It is possible that the clouds are either a binary combination that has not been studied yet or even potentially a ternary mixture. Studying additional co-condensed combinations of two and three organic species in lab may yield better matches to the CIRS data and thus shed light on the cloud compositions observed by the CIRS instrument.

- **Computational modeling of crystalline propyne to predict vibrational spectra.** Density functional theory (DFT) and related computational methods could be employed to model candidate crystal structures of propyne and

generate predicted Raman and infrared spectra. Comparing these theoretical spectra with experimental data would help confirm vibrational mode assignments, constrain the likely crystalline phases present under Titan-relevant conditions, and provide a framework for interpreting spectral variability such as the "mystery peak" highlighted earlier. These calculations would allow for a direct connection between X-ray diffraction and vibrational spectroscopy, strengthening the link between structure and spectroscopy.

5.3 Zonal winds in Titan's middle atmosphere from a stellar occultation observed with Keck adaptive optics

- **Legendre parameterization and fitting of non-spherical distortions; mapping back to zonal wind space.** The work presented here is an adequate first analysis that analyzes the degree to which various forward models match the data. However, it is clear that even the closest match still varies substantially from the data. A parameterization and inversion would allow a full sample space to be searched instead of just a pre-selected series of input profiles. An inversion is best conducted in distortion space, as this is more directly related to the refracted lightspots that are displayed, and spherical distortions have more constraints than zonal wind profiles. Following the work of Bouchez, 2004, we parameterize $f(b, \theta)$ (the deviation from sphericity for a colatitude θ and reference altitude b, where $r(P, \theta) = b[1 + f(b, \phi)]$), as a sum of Legendre polynomials P_l:

$$f(b, \phi) = \sum_{l=0}^{N} f_l(b) P_l(cos\phi). \tag{5.1}$$

Various constraints can be imposed upon several of the Legendre polynomial terms to ensure that the physical requirements of the system are met. The parameterization and fitting is currently in progress — with parallelization and optimization of the sky plane from which backward ray-tracing is conducted, the time for a singular occultation model to run has gone from ~33 minutes to ~70 seconds. At the moment, an MCMC structure is being conducted with which to contain this faster model. Ultimately, an MCMC will be run to search the Legendre polynomial parameter space to find the non-spherical distortion profile that best fits the data. From there, a simple inversion of Equation 4.7 yields zonal winds as a function of radial distortion.

- **Reanalysis of archival data using the *Huygens*/HASI descent temperature profile.** Prior to the descent of the *Huygens* atmospheric probe, temperature models for Titan's atmosphere were coarse with wide error margins. The unparalleled data collected during the *HASI* descent has given a high resolution atmosphere profile for Titan. Reanalyzing occultation data from before the *Huygens* probe would allow more accurate data analysis and potentially closer fits to the data, leading to an enhanced understanding of Titan's atmospheric dynamics at various points in its year.

- **A second Titan late northern summer occultation.** Following the September 2022 occultation, another occultation occurred which was captured by the Very Large Telescope (VLT) in Chile. Although the center of the shadow path did not pass as near to the observatory, the star was brighter and the data clearly captured the refracted lightspots. These data offer a unique opportunity to probe a data set very near in time to the data presented in this thesis and determine whether the best-fit zonal wind profiles are in agreement with each other. As these occultations are only two Earth months apart (a negligible fraction of a Titan year), discrepant zonal wind profiles would indicate very rapid atmospheric change and help us better understand and characterize the dynamic period around equinox.

- **Argentina-Chile occultation, 2026.** In September 2026, Titan will occult a bright star; the center of the shadowpath will cross southern Argentina and Chile. We will travel to South America to deploy portable telescopes near the center of the shadowpath and capture occultation light curves. Furthermore, the VLT is once again in the shadow path of the occultation. Pending clear skies, we will be able to combine both spatially-resolved VLT data and light curves from near the center of the event. These data will represent the first data collected of a stellar occultation occurring shortly after Titan's equinox. As equinox is expected to usher in a time of rapid atmospheric change, these data will allow us to directly probe the transient post-equinox era and profile the winds of Titan in-transition.

- **Instrument sampling method upgrades.** The data collected for the occultation was impeded by the low sampling rate of the NIRC2 instrument on Keck II. This past summer, I spent five weeks at Keck Observatory working on site to determine methods for faster sampling with less overhead. I determined that Up-the-Ramp sampling — a method which resets less frequently than

the normally used Correlated Double Sampling — could be implemented to reduce readout time. As NIRC2 transitions to the new SCALES instrument, this is hopefully a method that occultation observers will be able to use to reduce readout time between exposures. As an occultation occurs in on the order of seconds to minutes, having as many data points as possible is critical in order to best inform data-to-model comparisons and inversions.

References

Barge, Laura M. et al. (Feb. 2012). "Characterization of Iron – Phosphate – Silicate Chemical Garden Structures". In: *Langmuir* 28.8. Publisher: American Chemical Society, pp. 3714–3721. ISSN: 0743-7463. DOI: 10.1021/la203727g. URL: https://doi.org/10.1021/la203727g.

Bouchez, Antonin Henri (2004). "Seasonal trends in Titan's atmosphere: Haze, wind, and clouds". ISBN: 9780496723560 Publication Title: ProQuest Dissertations and Theses. Ph.D. United States – California: California Institute of Technology. URL: https://www.proquest.com/docview/305203060/abstract/7887C087627C4A4EPQ/1.

Cable, Morgan L., Tomče Runčevski, et al. (Aug. 2021). "Titan in a Test Tube: Organic Co-crystals and Implications for Titan Mineralogy". In: *Accounts of Chemical Research* 54.15. Publisher: American Chemical Society, pp. 3050–3059. ISSN: 0001-4842. DOI: 10.1021/acs.accounts.1c00250. URL: https://doi.org/10.1021/acs.accounts.1c00250.

Cable, Morgan L., Tuan H. Vu, Michael J. Malaska, et al. (Dec. 2019). "A Co-Crystal between Acetylene and Butane: A Potentially Ubiquitous Molecular Mineral on Titan". In: *ACS Earth and Space Chemistry* 3, pp. 2808–2815. DOI: 10.1021/acsearthspacechem.9b00275. URL: https://ui.adsabs.harvard.edu/abs/2019ESC.....3.2808C.

– (Aug. 2020). "Properties and Behavior of the Acetonitrile–Acetylene Co-Crystal under Titan Surface Conditions". In: *ACS Earth and Space Chemistry* 4.8. Publisher: American Chemical Society, pp. 1375–1385. DOI: 10.1021/acsearthspacechem.0c00129. URL: https://doi.org/10.1021/acsearthspacechem.0c00129.

Cable, Morgan L., Tuan H. Vu, Helen E. Maynard-Casely, et al. (Apr. 2018). "The Acetylene-Ammonia Co-crystal on Titan". In: *ACS Earth and Space Chemistry* 2.4. Publisher: American Chemical Society, pp. 366–375. DOI: 10.1021/acsearthspacechem.7b00135.

Cardoso, Silvana S. S., Julyan H. E. Cartwright, and C. Ignacio Sainz-Díaz (Feb. 2019). "Carbonate-hydroxide chemical-garden tubes in the soda ocean of Enceladus: Abiotic membranes and microtubular forms of calcium carbonate". In: *Icarus* 319, pp. 337–348. ISSN: 0019-1035. DOI: 10.1016/j.icarus.2018.

09.020. URL: https://www.sciencedirect.com/science/article/pii/S0019103518302896.

Czaplinski, Ellen et al. (Dec. 2020). "Experimental Investigation of the Acetylene–Benzene Cocrystal on Titan". In: *The Planetary Science Journal* 1.3. Publisher: IOP Publishing, p. 76. ISSN: 2632-3338. DOI: 10.3847/PSJ/abbf57. URL: https://iopscience.iop.org/article/10.3847/PSJ/abbf57/meta.

Glein, Christopher R. and J. Hunter Waite (Feb. 2020). "The Carbonate Geochemistry of Enceladus' Ocean". In: *Geophysical Research Letters* 47, e85885. ISSN: 0094-8276. DOI: 10.1029/2019GL085885. URL: https://ui.adsabs.harvard.edu/abs/2020GeoRL..4785885G.

Hudson, Reggie L. et al. (Jan. 2021). "Infrared spectra and optical constants of astronomical ices: III. Propane, propylene, and propyne". In: *Icarus* 354, p. 114033. ISSN: 0019-1035. DOI: 10.1016/j.icarus.2020.114033. URL: https://www.sciencedirect.com/science/article/pii/S0019103520303924.

Malherbe, F. E. and H. J. Bernstein (Dec. 1951). "Infrared Spectra of Rapidly Solidified Vapors". In: *The Journal of Chemical Physics* 19.12. Publisher: American Institute of Physics, pp. 1607–1608. ISSN: 0021-9606. DOI: 10.1063/1.1748132. URL: https://aip.scitation.org/doi/10.1063/1.1748132 (visited on 01/16/2023).

Origins, Worlds, and Life (2022). *Origins, Worlds, and Life: A Decadal Strategy for Planetary Science and Astrobiology 2023-2032*. Washington, D.C.: National Academies Press. ISBN: 978-0-309-47578-5. DOI: 10.17226/26522. URL: https://www.nap.edu/catalog/26522.

Postberg, Frank et al. (June 2023). "Detection of phosphates originating from Enceladus's ocean". In: *Nature* 618.7965. Publisher: Nature Publishing Group, pp. 489–493. ISSN: 1476-4687. DOI: 10.1038/s41586-023-05987-9. URL: https://www.nature.com/articles/s41586-023-05987-9 (visited on 09/01/2025).

Ritson, Dougal J., Stephen J. Mojzsis, and John D. Sutherland (May 2020). "Supply of phosphate to early Earth by photogeochemistry after meteoritic weathering". In: *Nature Geoscience* 13.5. Publisher: Nature Publishing Group, pp. 344–348. ISSN: 1752-0908. DOI: 10.1038/s41561-020-0556-7. URL: https://www.nature.com/articles/s41561-020-0556-7 (visited on 09/01/2025).

Stubbs, R. Trent et al. (Nov. 2020). "A plausible metal-free ancestral analogue of the Krebs cycle composed entirely of α-ketoacids." In: *Nature chemistry* 12.11, pp. 1016–1022. ISSN: 1755-4330. DOI: 10.1038/s41557-020-00560-7. URL: https://www.ncbi.nlm.nih.gov/pmc/articles/PMC8570912/.

Ugelow, Melissa and Carrie Anderson (Aug. 2020). *Investigating the Chemical Composition of the CIRS-Observed 160 cm^{-1} Ice Cloud in Titan's Stratosphere*. Tech. rep. EPSC2020-423. Conference Name: EPSC2020. Copernicus Meetings. DOI:

10.5194/epsc2020-423. URL: https://meetingorganizer.copernicus.org/EPSC2020/EPSC2020-423.html (visited on 07/12/2025).

Appendix A

CHEMICAL GARDENS SUPPLEMENTAL INFORMATION

A.1 Figures and Tables

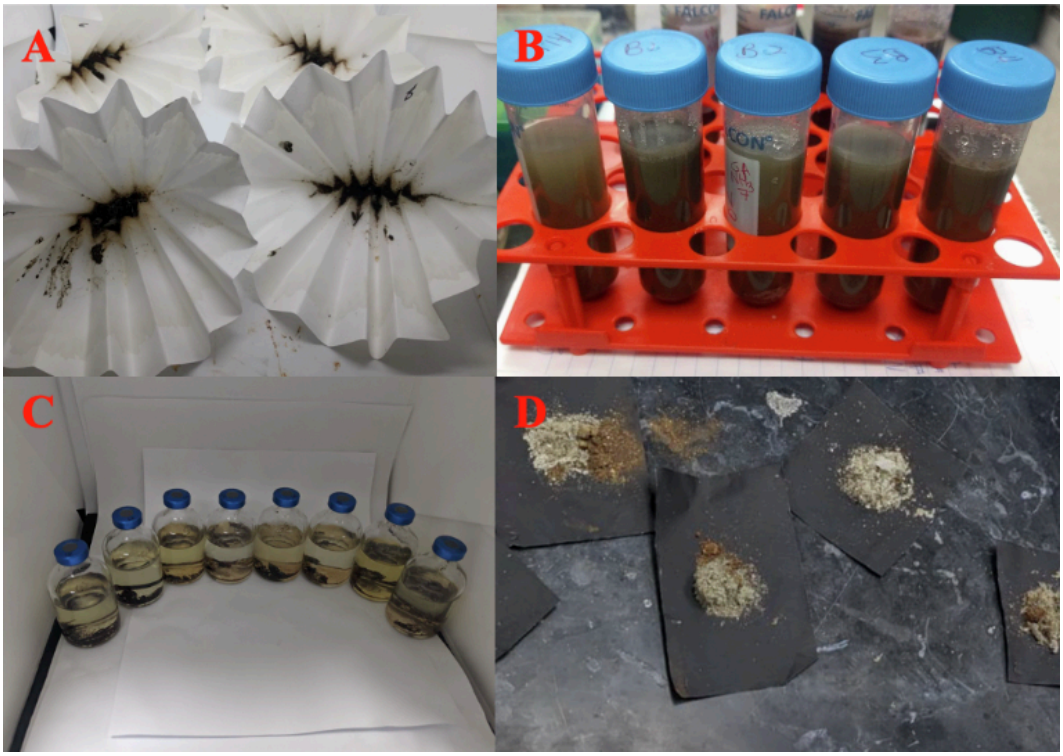


Figure A.1: Photos of chemical gardens in various stages. (A): filtering after growth. (B): stirred into a reaction. (C): in a reaction without being stirred (heated condition). (D): freeze-dried mineral remaining after the reaction used for VNIR analysis.

Pyruvate 10 mM	Glyoxylate 10 mM	Ammonia 20 mM	pH	Encel. salts
x		x	10	
x		x	7	
x			10	
x			7	
	x	x	10	
	x	x	7	
	x		10	
	x		7	
x	x	x	10	
x	x	x	7	
x			7	*
x		x	7	*
	x		7	*
	x	x	7	*
x		x	7	**
	x	x	7	**

Table A.1: Experimental and control reactions conducted. Conditions in every row correspond to reactions conducted both without and with a chemical garden (control). Both control and experimental reactions in each row were conducted in all three experimental conditions: benchtop, heated/aerobic, and anaerobic. (*) concentrations are approximating those of Enceladus from (Glein et al., 2020) (0.2 M NaCl and 0.07 M $NaHCO_3$); (**) concentrations refer to the same set of Enceladuslike conditions but with increased (doubled) carbonate.

Compound	Peak
Glyoxylate	5.057 (singlet)
Glycolate	3.93 (singlet)
Glycine	3.54 (singlet; pH-varied)
Formate*	8.45 (singlet)
Glycolic acid decomposition	4.23 (singlet)
Glycolic acid oligomer	3.81 (singlet)
Pyruvate	2.361 (singlet)
Lactate	1.3 (doublet); 4.1 (quadruplet)
Alanine	1.47 (doublet); 3.77 (quadruplet)
Acetate*	1.91 (singlet)
Pyruvate hydrate	1.36 (singlet)
Pyruvic acid decomposition	3.23 (quadruplet)

Table A.2: Peaks for compounds of interest. *: Acetic acid and formic acid have NMR peaks at 2.1 ppm and 8.26 ppm, respectively. Due to the low pKa of these acids and the experimental conditions we use, these products are not formed in high quantities. References for peaks: glyoxylate: (Cui et al., 2008), glycolate, glycine, formate, pyruvate, lactate, and alanine: (Wishart et al., 2009), glycolic acid decomposition and glycolic acid oligomer: (Weber et al., 2021), acetate: (*Sodium acetate - Optional[1H NMR] - Chemical Shifts - SpectraBase* 2024)

.

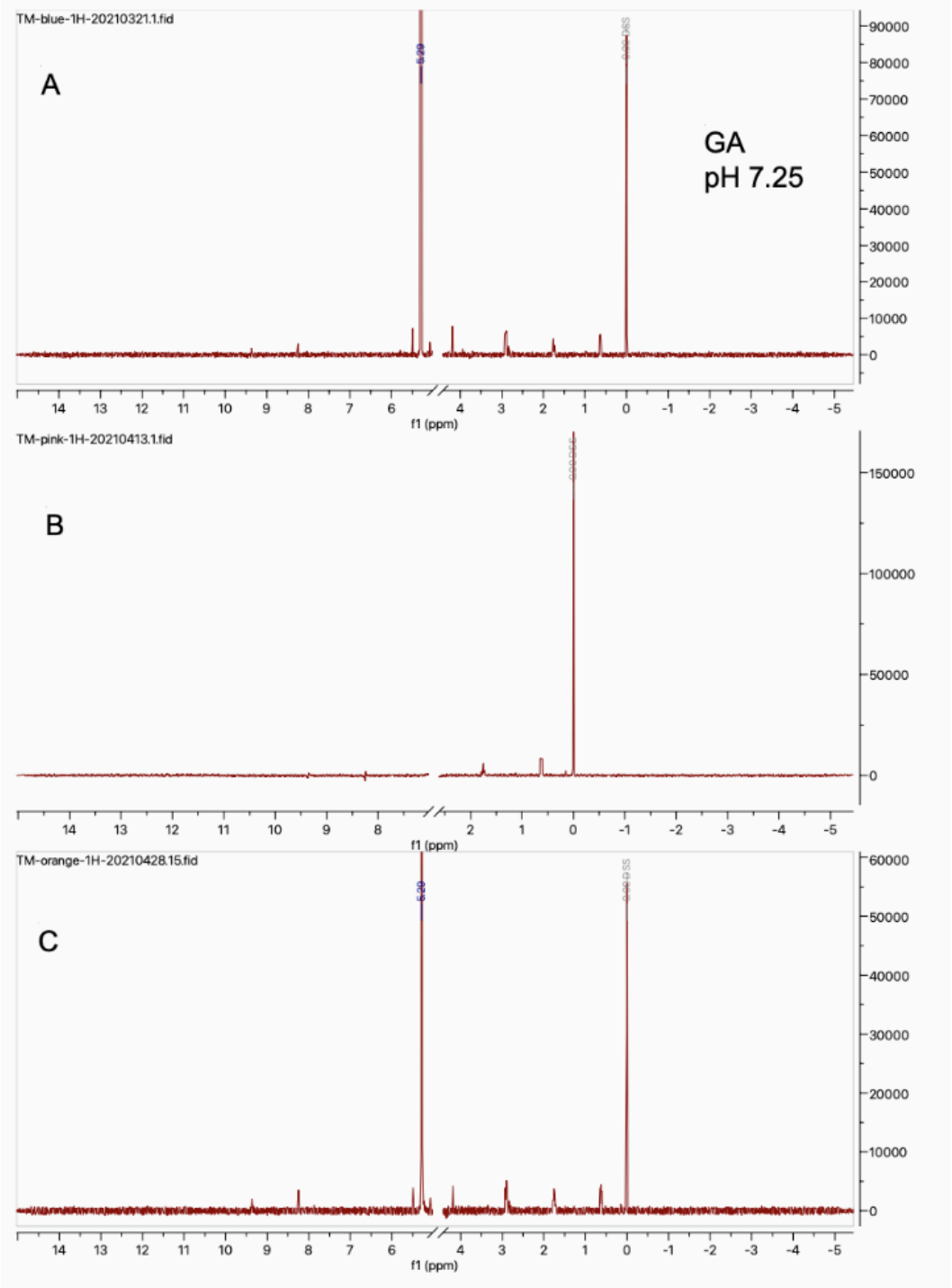


Figure A.2: Control ^{1}H nuclear magnetic resonance (NMR) spectra; glyoxylate (GA) reaction under benchtop/aerobic conditions, pH 7.25. A: t = 0 weeks, B: t = 1 week, C: t = 2 weeks.

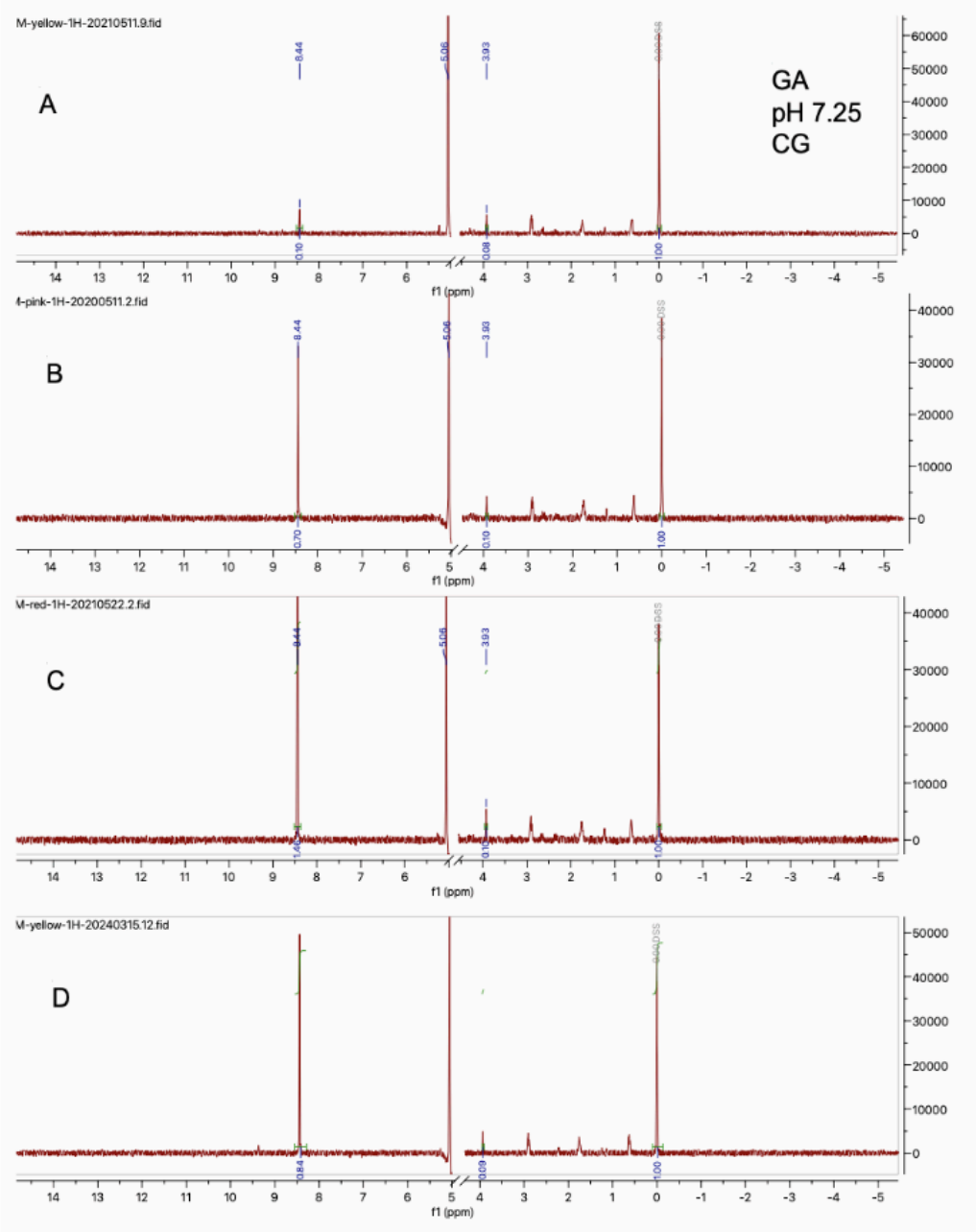


Figure A.3: NMR spectra; glyoxylate and chemical garden reaction under bench-top/aerobic conditions, pH 7.25. A: t = 0 weeks, B: t = 1 week, C: t = 2 weeks, D: t = 3 weeks.

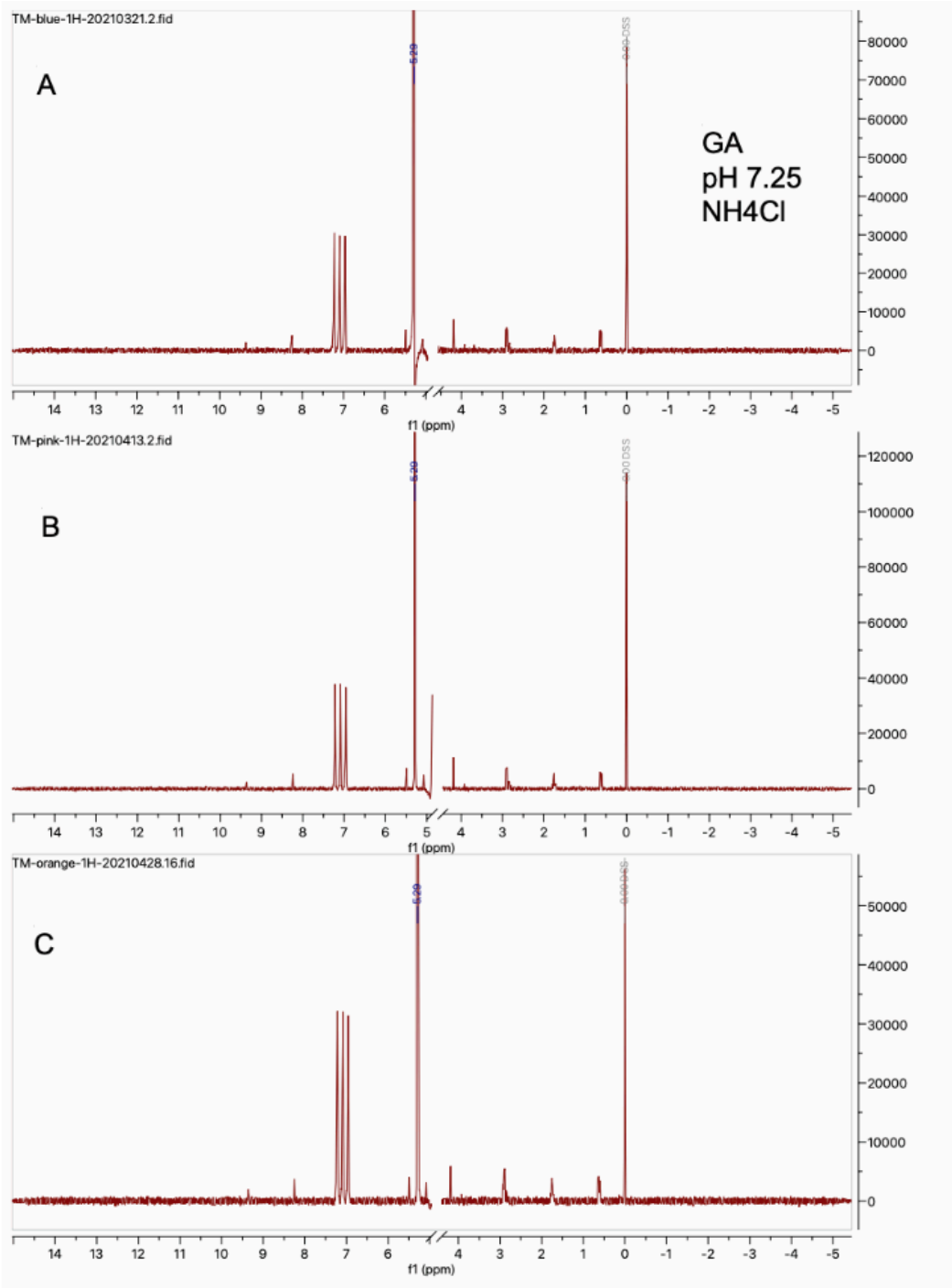


Figure A.4: Control NMR spectra; glyoxylate and ammonium chloride reaction under benchtop/aerobic conditions, pH 7.25. A: t = 0 weeks, B: t = 1 week, C: t = 2 weeks.

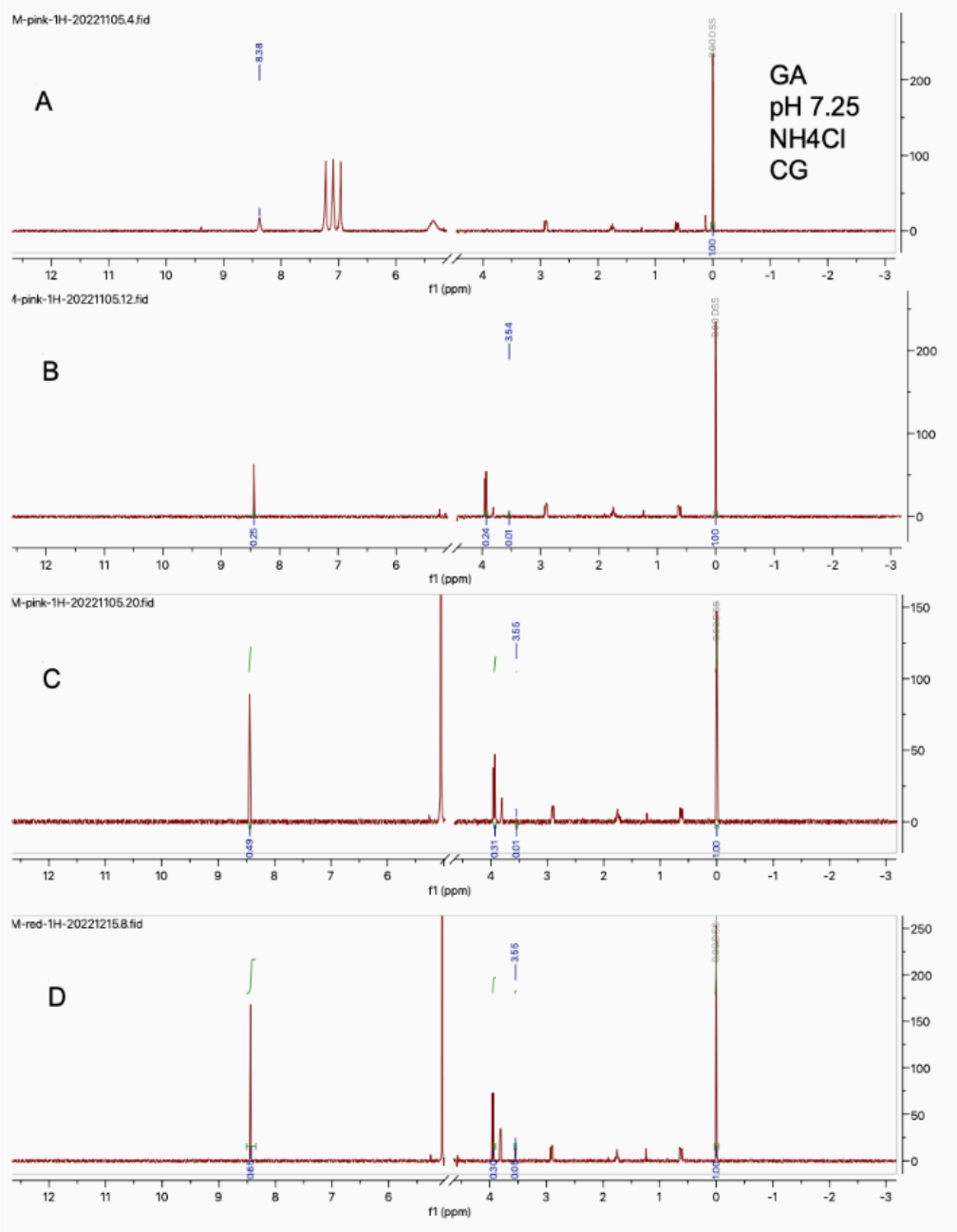


Figure A.5: NMR spectra; glyoxylate, ammonium chloride, and chemical garden reaction under benchtop/aerobic conditions, pH 7.25. A: t = 0 weeks, B: t = 1 week, C: t = 2 weeks, D: t = 3 weeks.

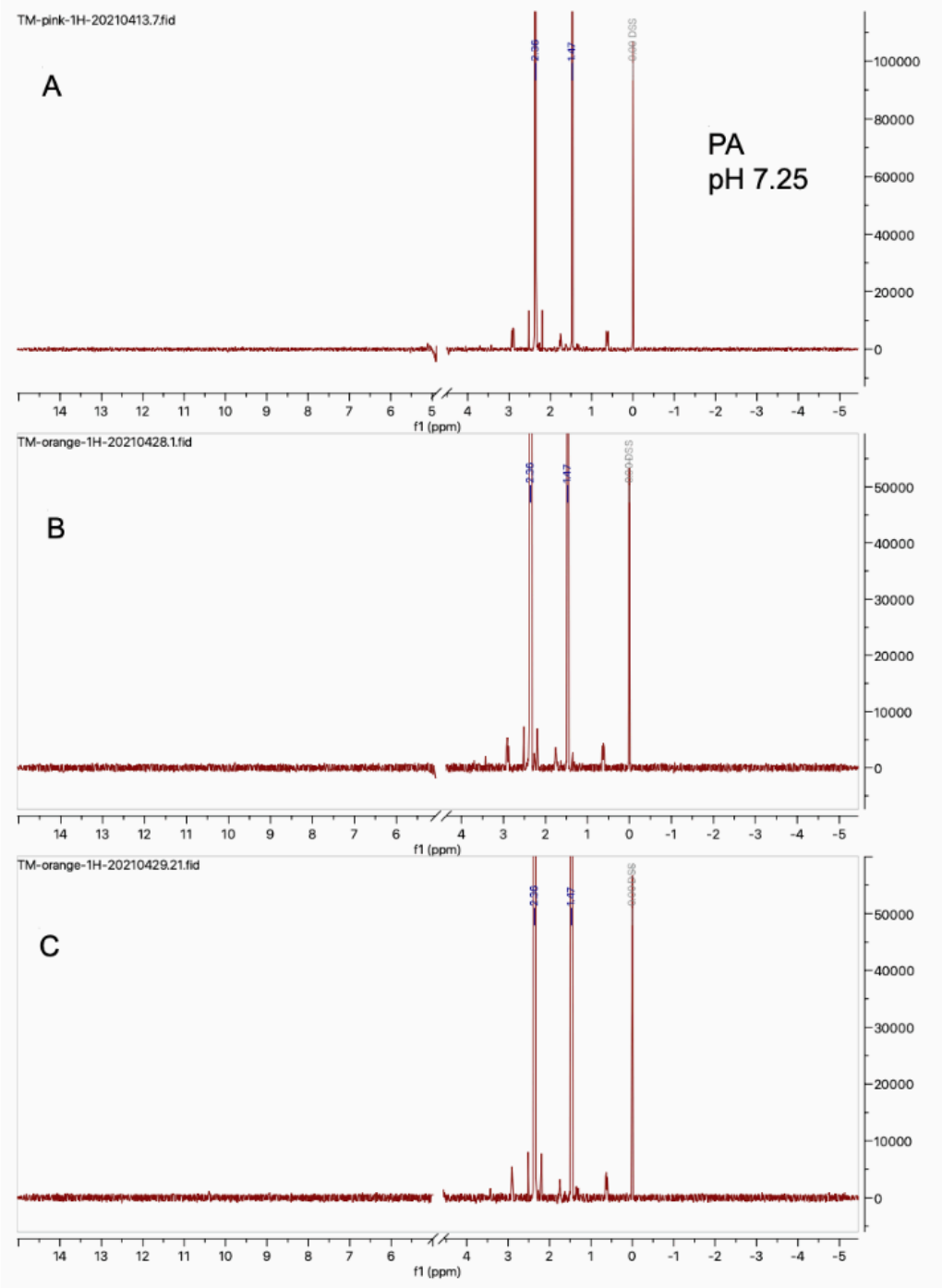


Figure A.6: Control NMR spectra; pyruvate reaction under benchtop/aerobic conditions, pH 7.25. A: t = 0 weeks, B: t = 1 week, C: t = 2 weeks.

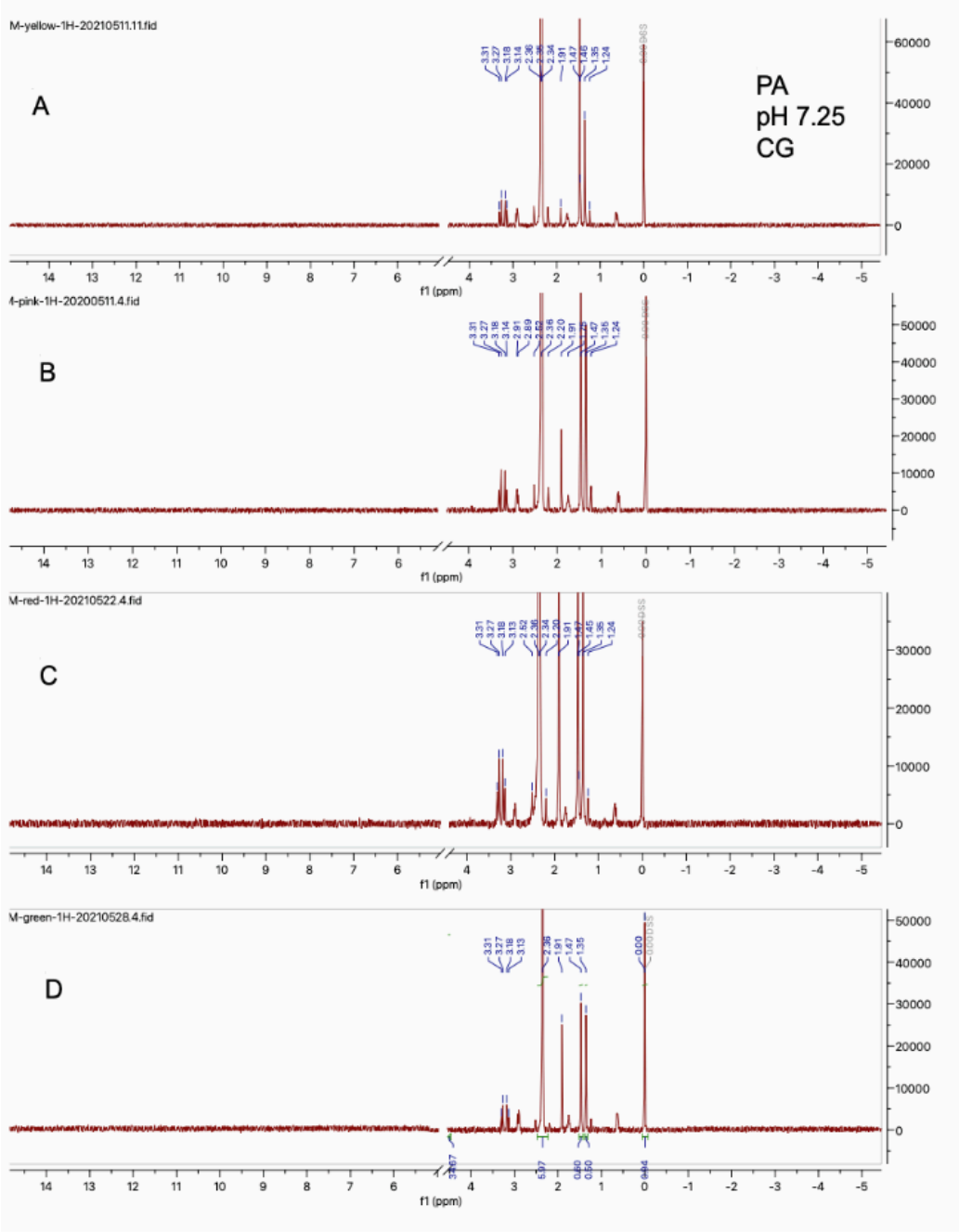


Figure A.7: NMR spectra; pyruvate and chemical garden reaction under bench-top/aerobic conditions, pH 7.25. A: t = 0 weeks, B: t = 1 week, C: t = 2 weeks, D: t = 3 weeks.

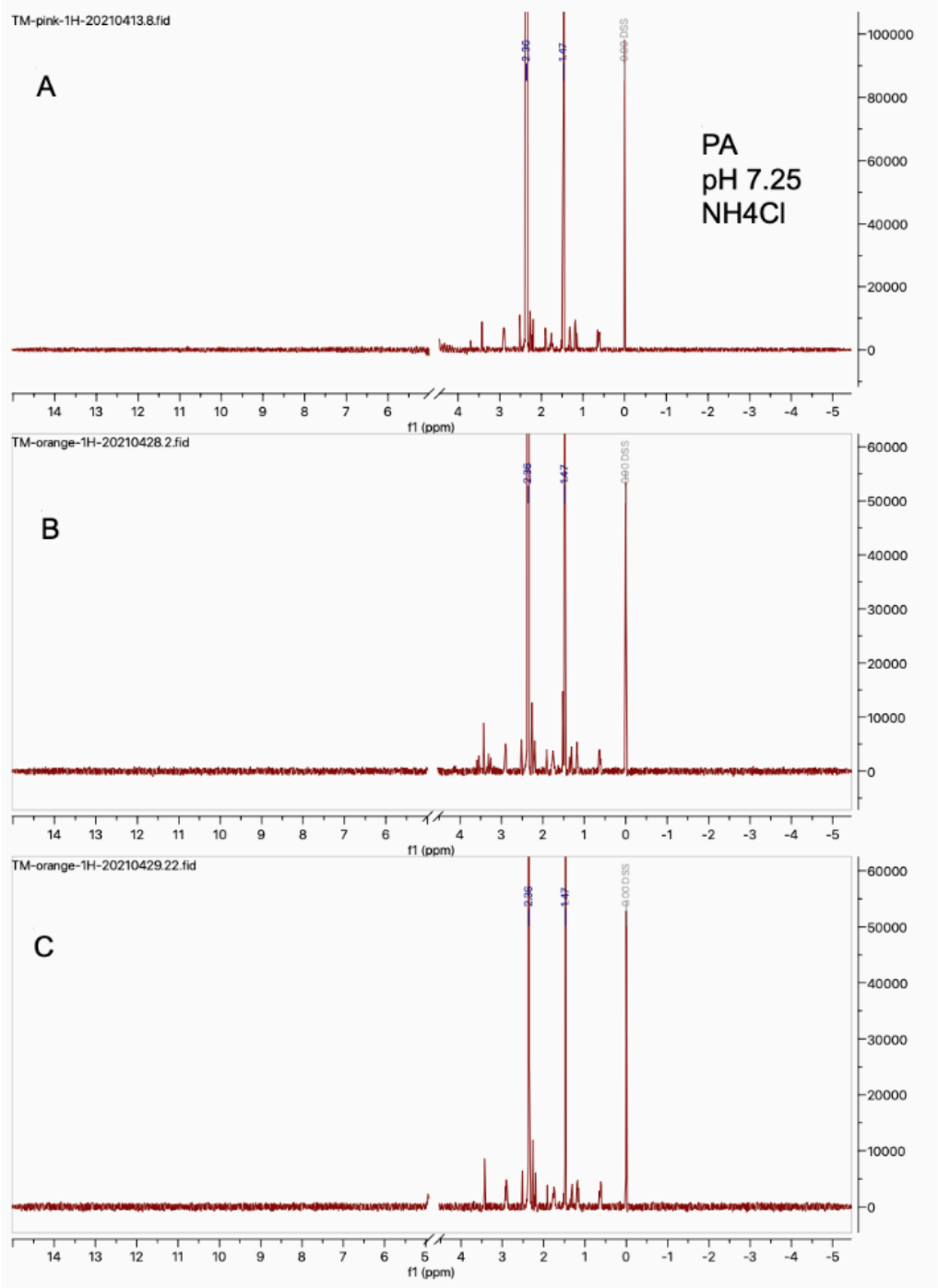


Figure A.8: Control NMR spectra; pyruvate and ammonium chloride reaction under benchtop/aerobic conditions, pH 7.25. A: t = 0 weeks, B: t = 1 week, C: t = 2 weeks.

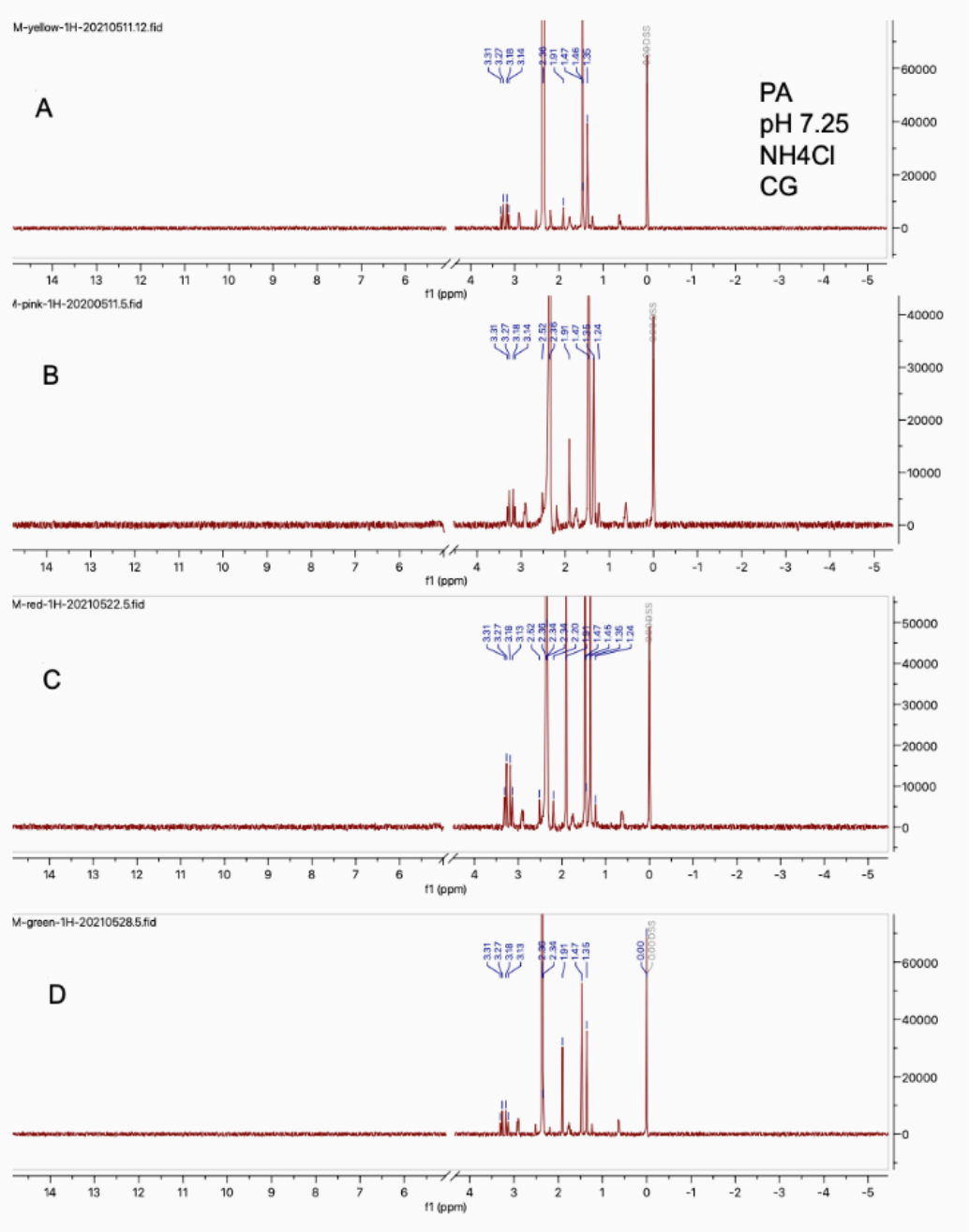


Figure A.9: NMR spectra; pyruvate, ammonium chloride and chemical garden reaction under benchtop/aerobic conditions, pH 7.25. A: t = 0 weeks, B: t = 1 week, C: t = 2 weeks, D: t = 3 weeks.

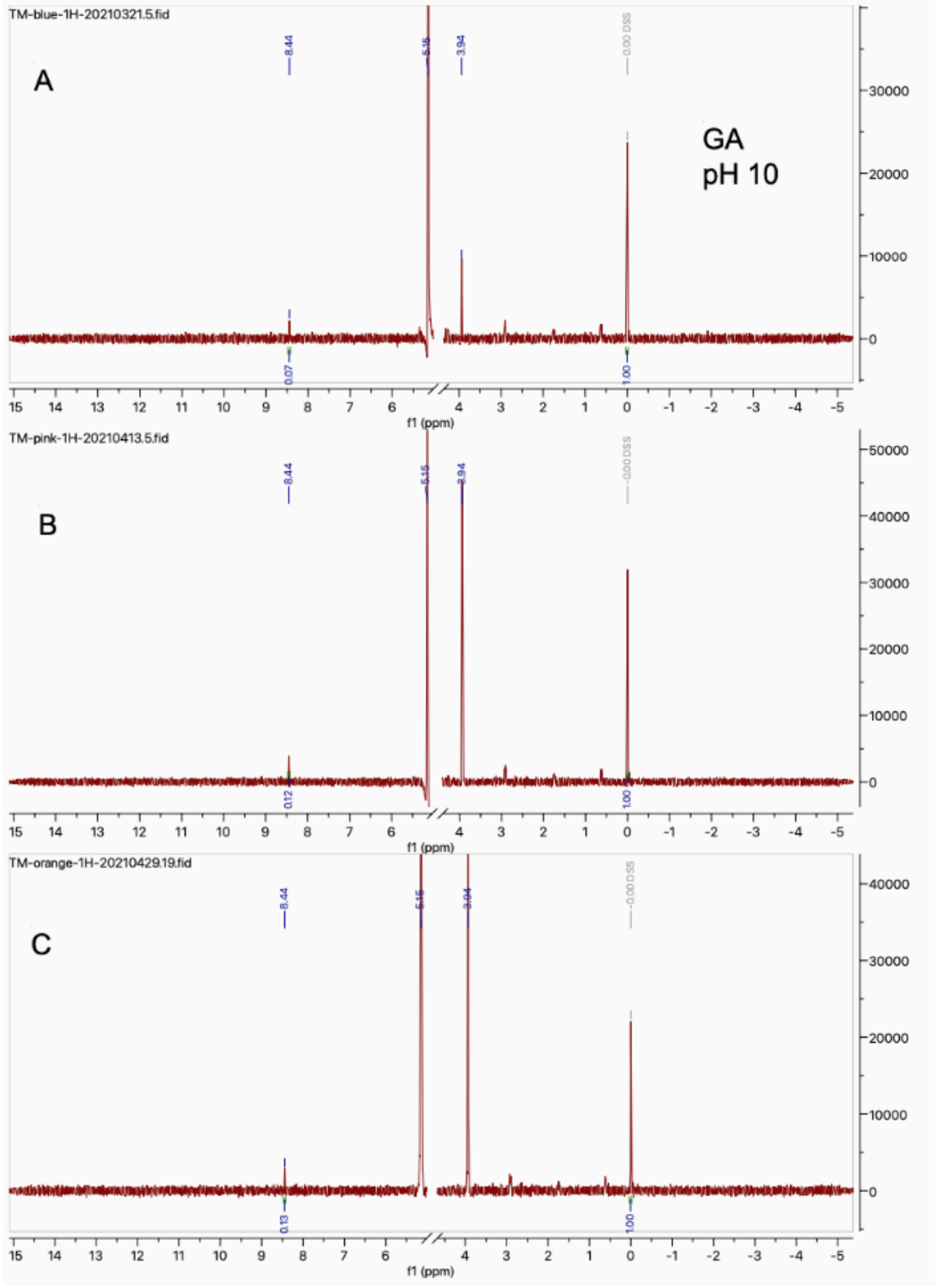


Figure A.10: Control NMR spectra; glyoxylate reaction under benchtop/aerobic conditions, pH 10. A: t = 0 weeks, B: t = 1 week, C: t = 2 weeks.

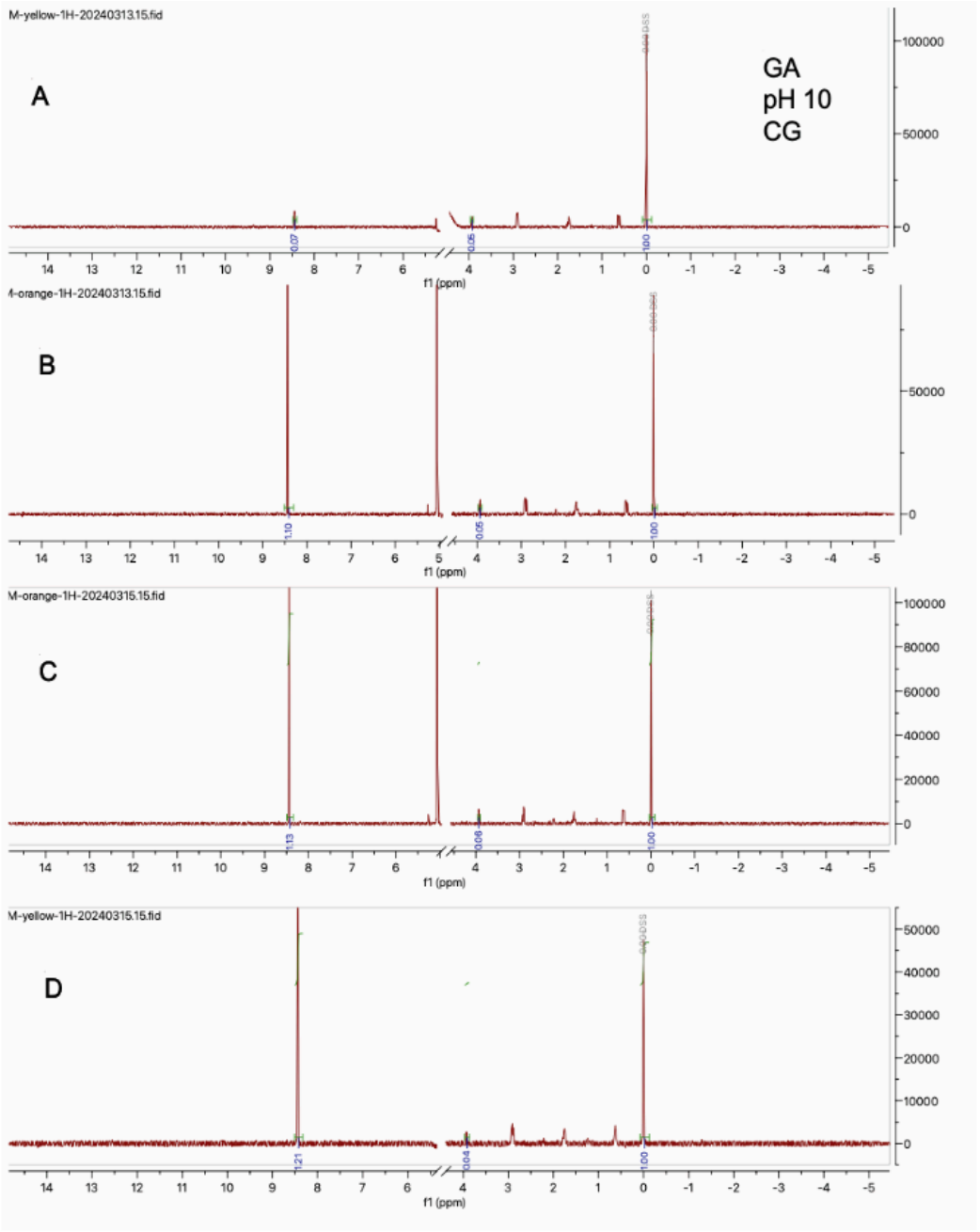


Figure A.11: NMR spectra; glyoxylate and chemical garden reaction under bench-top/aerobic conditions, pH 10. A: t = 0 weeks, B: t = 1 week, C: t = 2 weeks, D: t = 3 weeks.

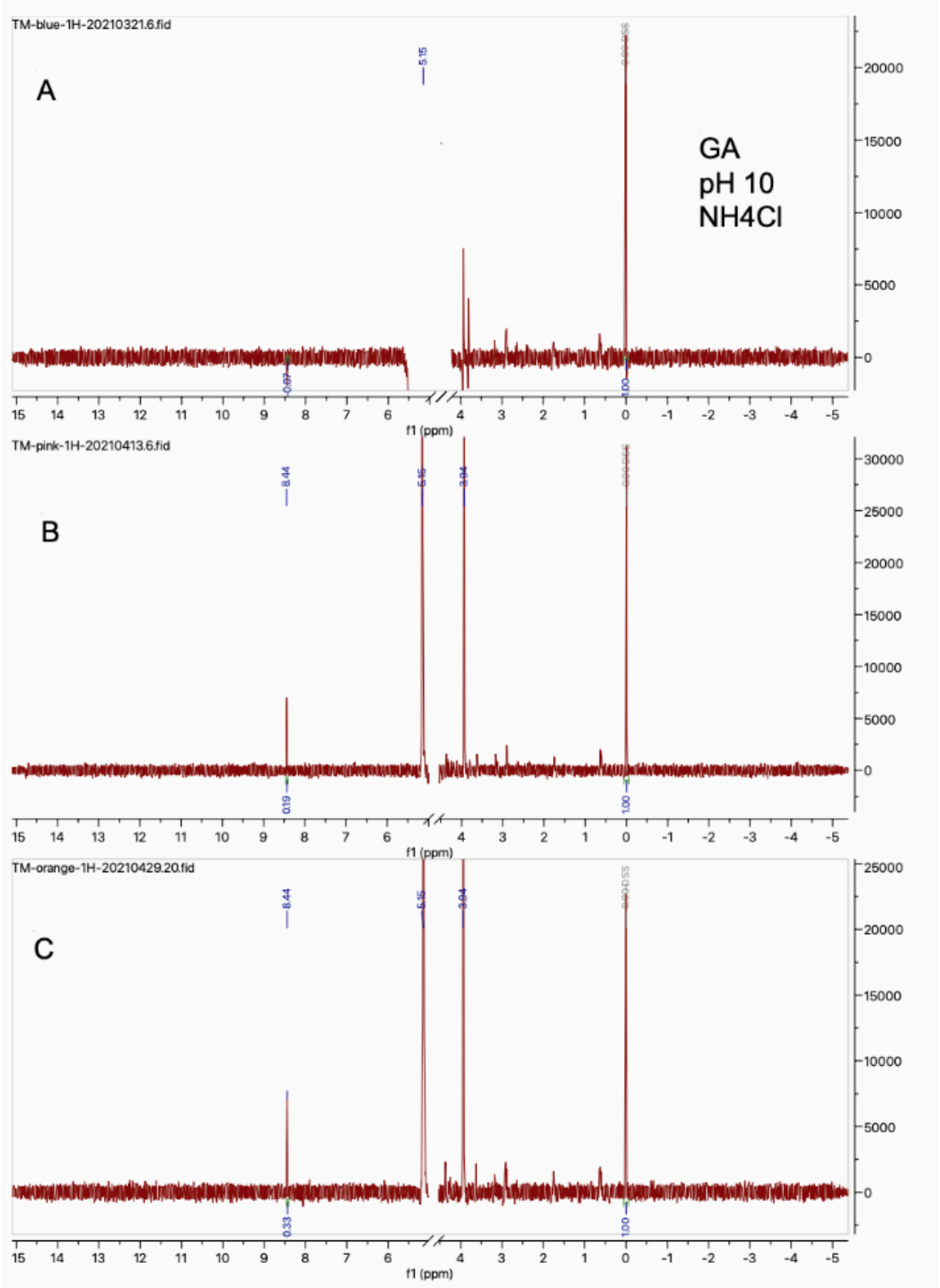


Figure A.12: Control NMR spectra; glyoxylate and ammonium chloride reaction under benchtop/aerobic conditions, pH 10. A: t = 0 weeks, B: t = 1 week, C: t = 2 weeks.

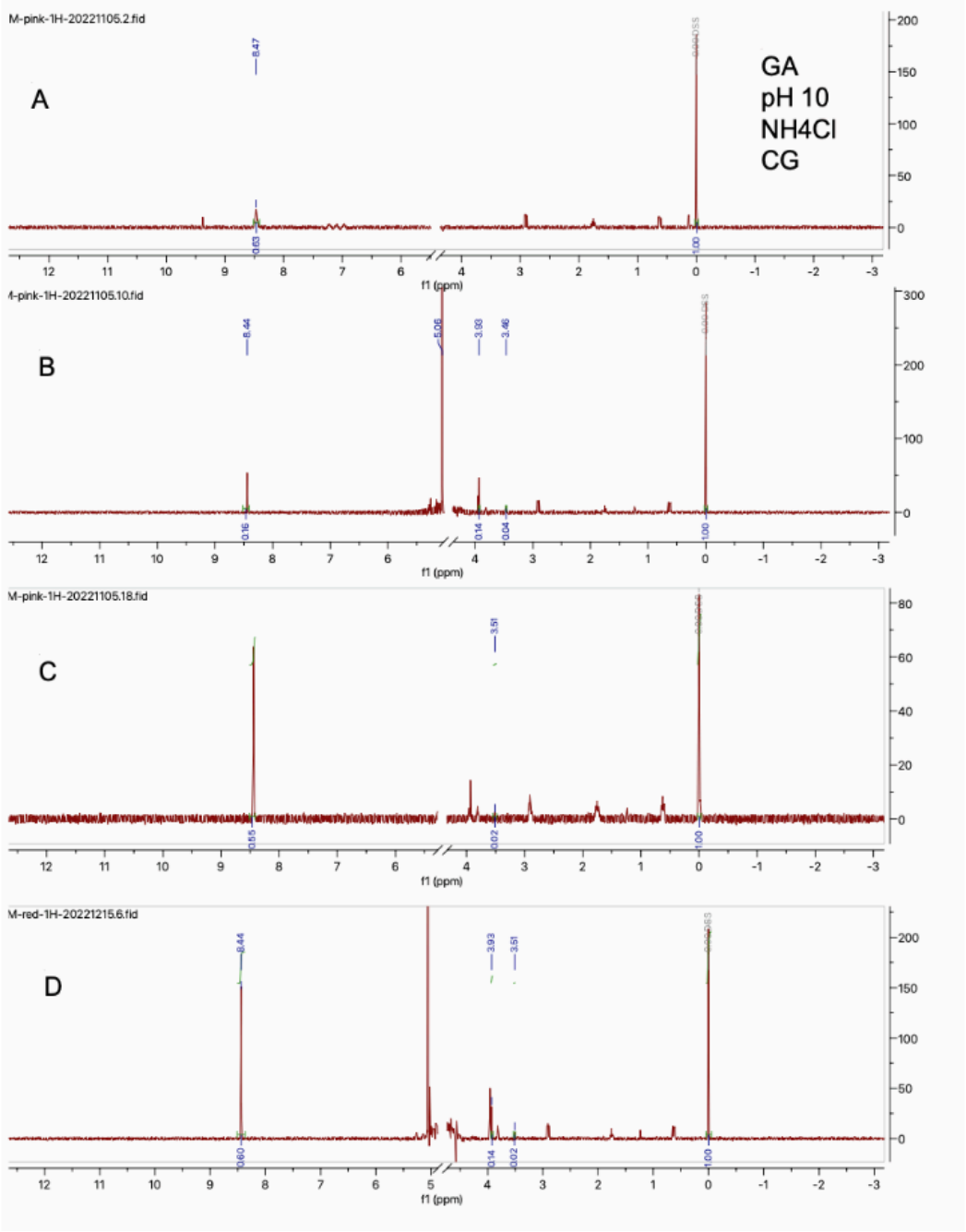


Figure A.13: NMR spectra; glyoxylate, ammonium chloride, and chemical garden reaction under benchtop/aerobic conditions, pH 10. A: t = 0 weeks, B: t = 1 week, C: t = 2 weeks, D: t = 3 weeks.

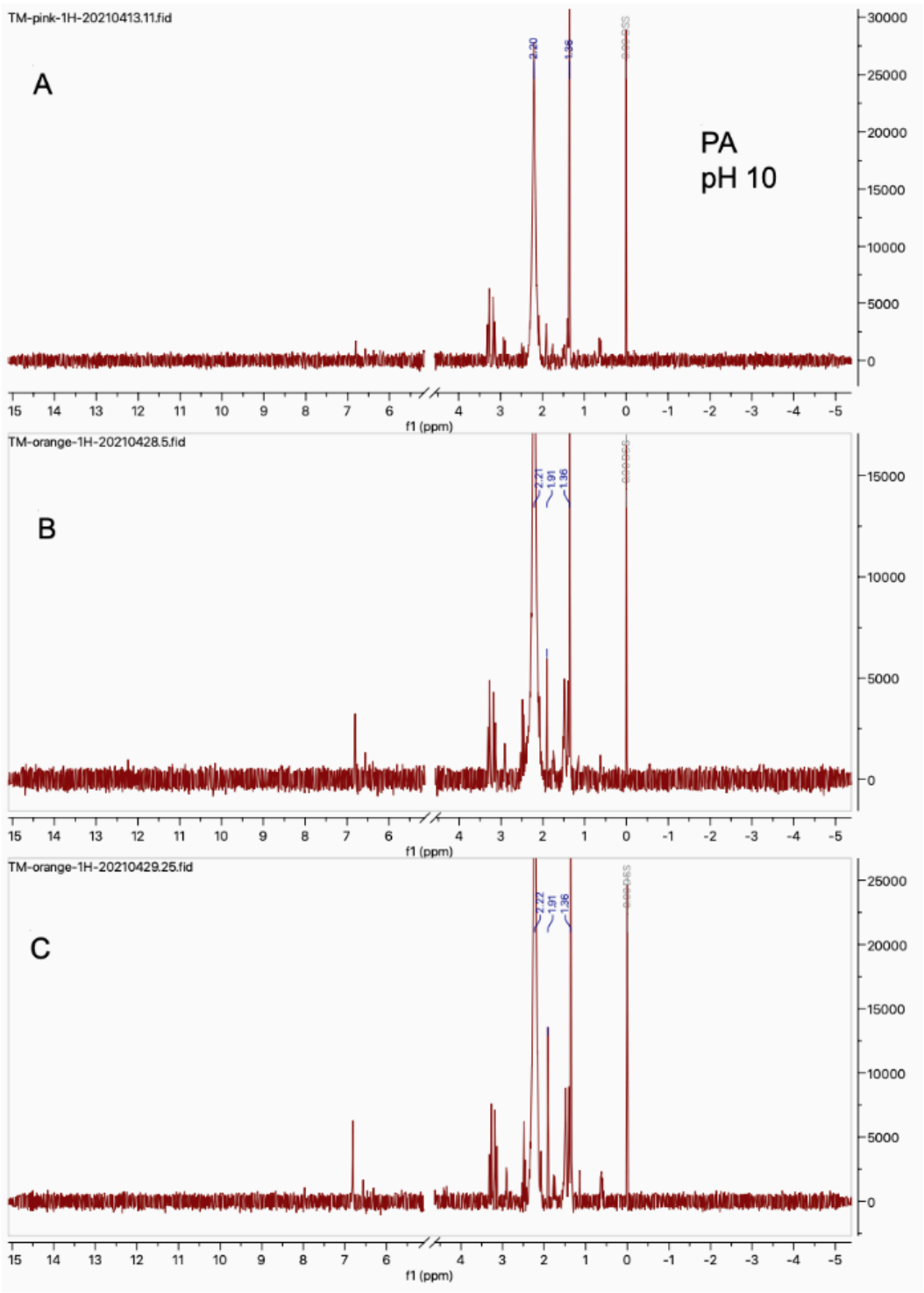


Figure A.14: Control NMR spectra; pyruvate reaction under benchtop/aerobic conditions, pH 10. A: t = 0 weeks, B: t = 1 week, C: t = 2 weeks.

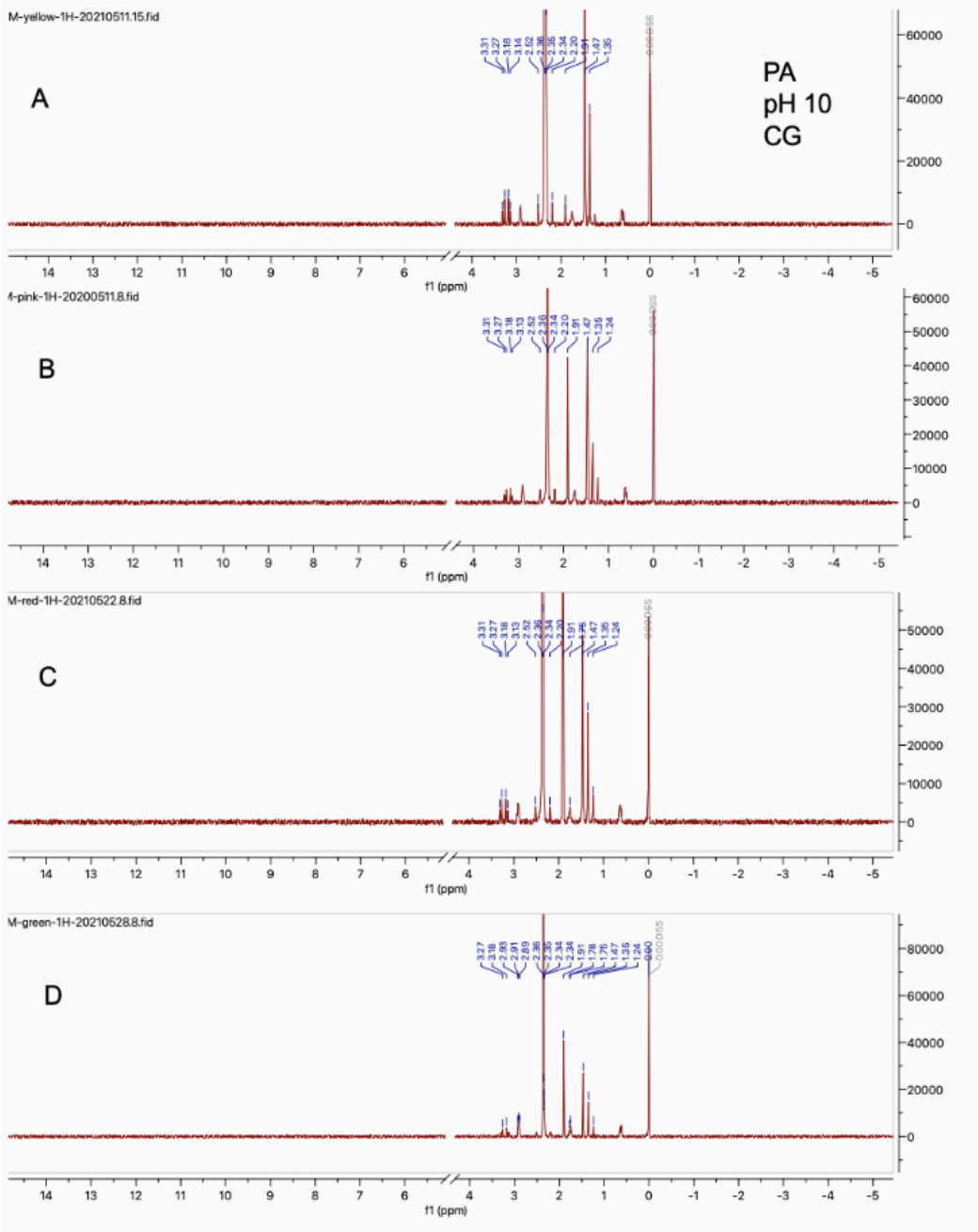


Figure A.15: NMR spectra; pyruvate and chemical garden reaction under bench-top/aerobic conditions, pH 10. A: t = 0 weeks, B: t = 1 week, C: t = 2 weeks, D: t = 3 weeks.

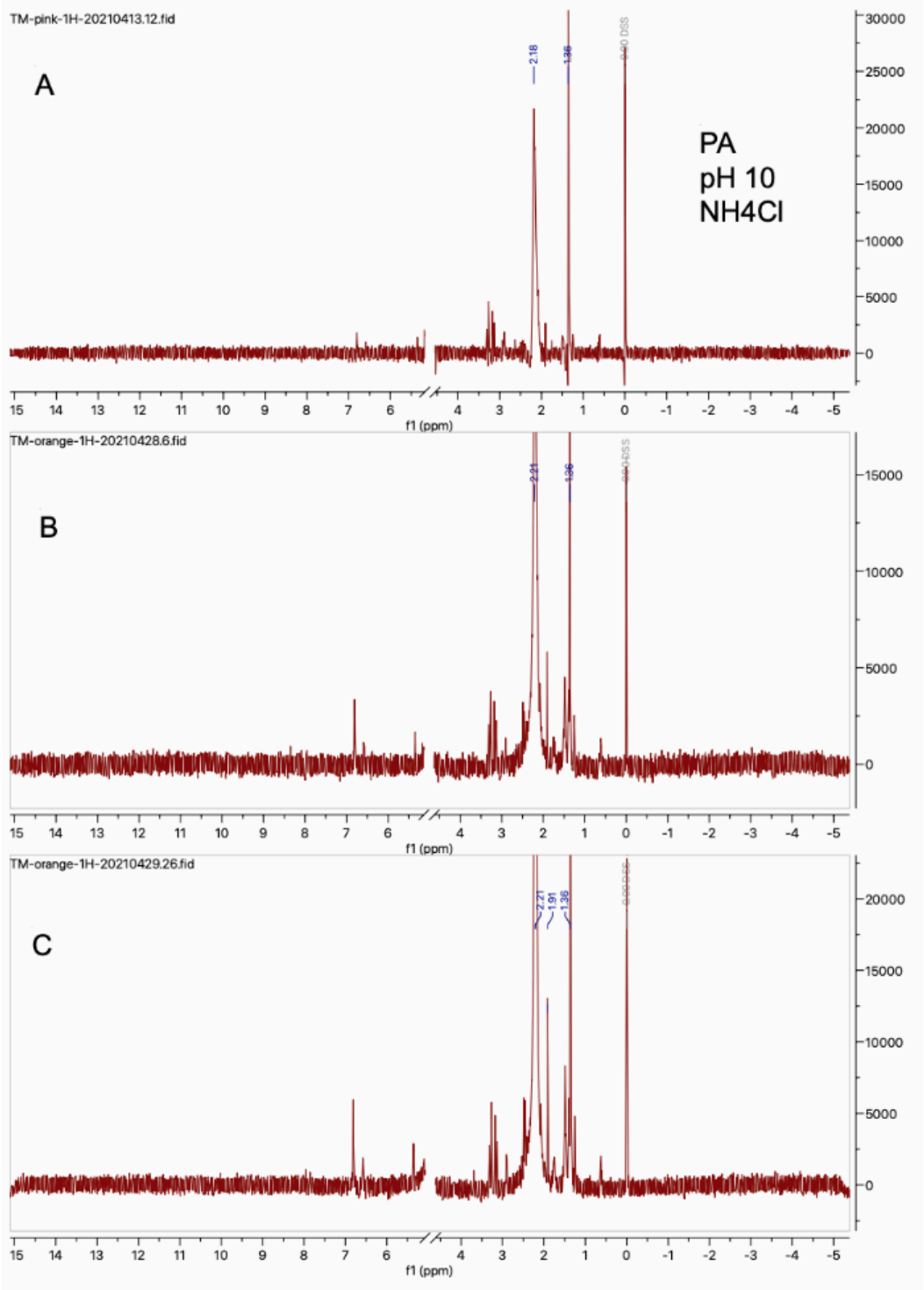


Figure A.16: Control NMR spectra; pyruvate and ammonium chloride reaction under benchtop/aerobic conditions, pH 10. A: t = 0 weeks, B: t = 1 week, C: t = 2 weeks.

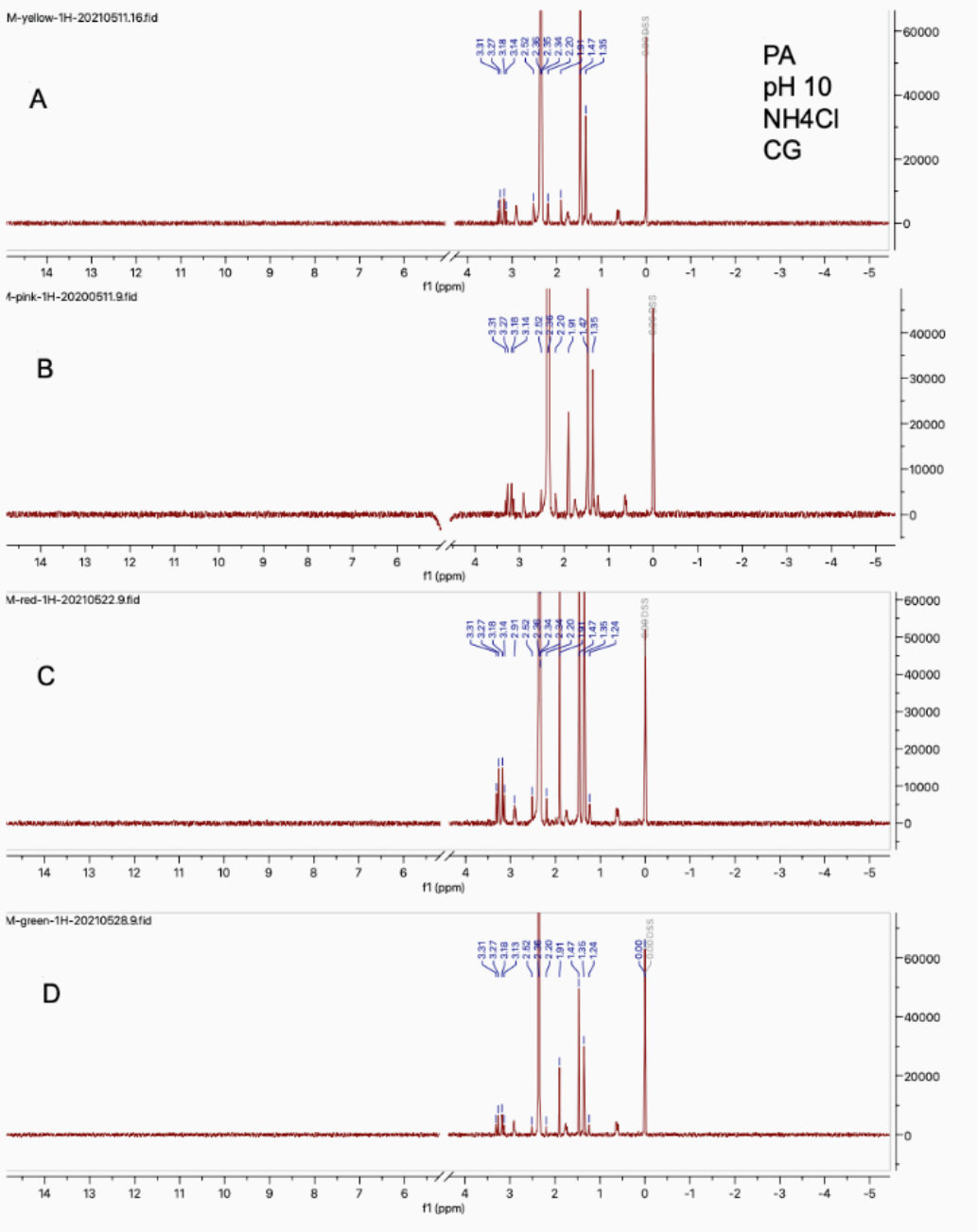


Figure A.17: NMR spectra; pyruvate, ammonium chloride, and chemical garden reaction under benchtop/aerobic conditions, pH 10. A: t = 0 weeks, B: t = 1 week, C: t = 2 weeks, D: t = 3 weeks.

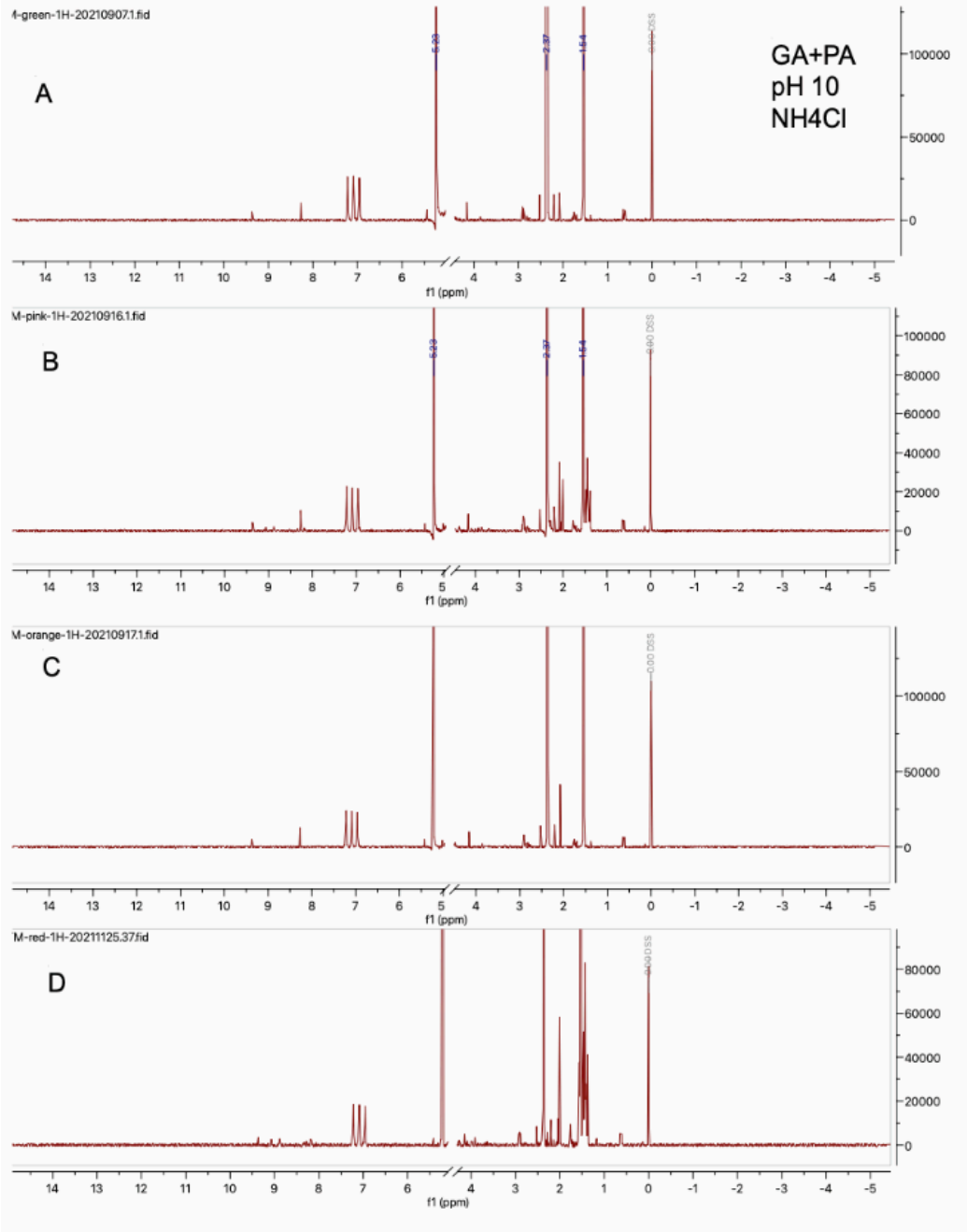


Figure A.18: Control NMR spectra; pyruvate, glyoxylate, and ammonium chloride reaction under benchtop/aerobic conditions, pH 10. A: t = 0 weeks, B: t = 1 week, C: t = 2 weeks, D: t = 3 weeks.

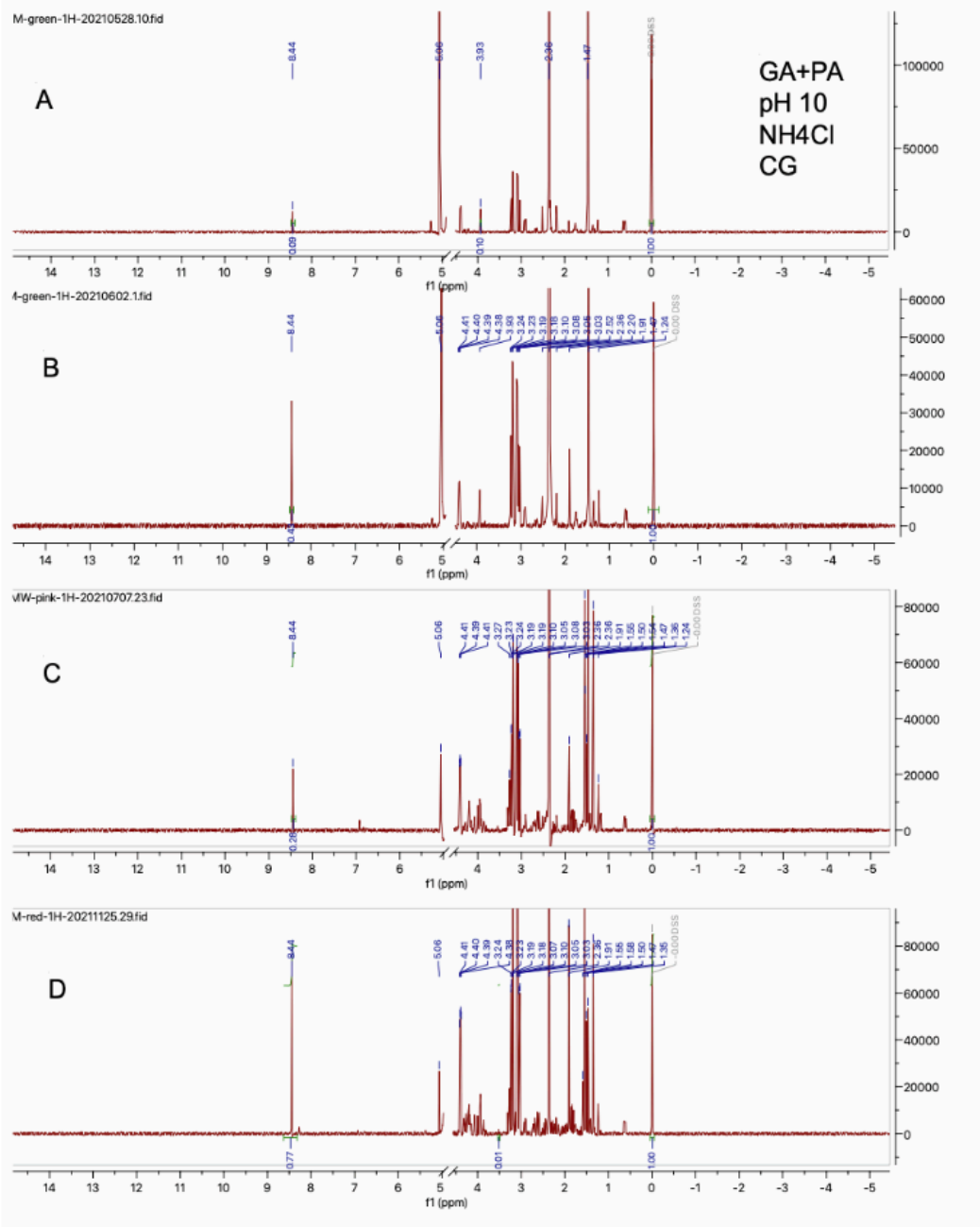


Figure A.19: NMR spectra; pyruvate, glyoxylate, ammonium chloride, and chemical garden reaction under benchtop/aerobic conditions, pH 10. A: t = 0 weeks, B: t = 1 week, C: t = 2 weeks, D: t = 3 weeks.

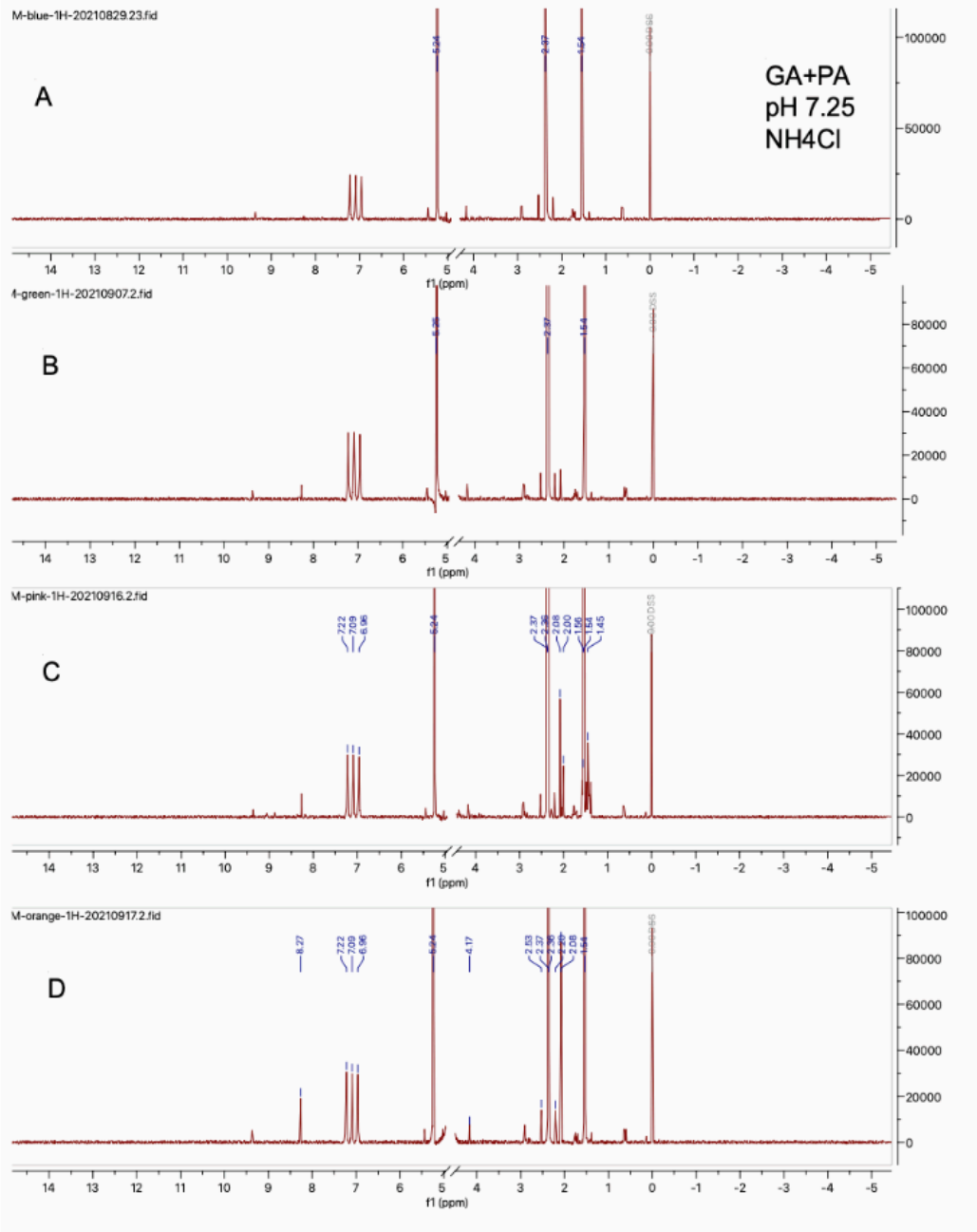


Figure A.20: Control NMR spectra; pyruvate, glyoxylate, and ammonium chloride reaction under benchtop/aerobic conditions, pH 7.25. A: t = 0 weeks, B: t = 1 week, C: t = 2 weeks, D: t = 3 weeks.

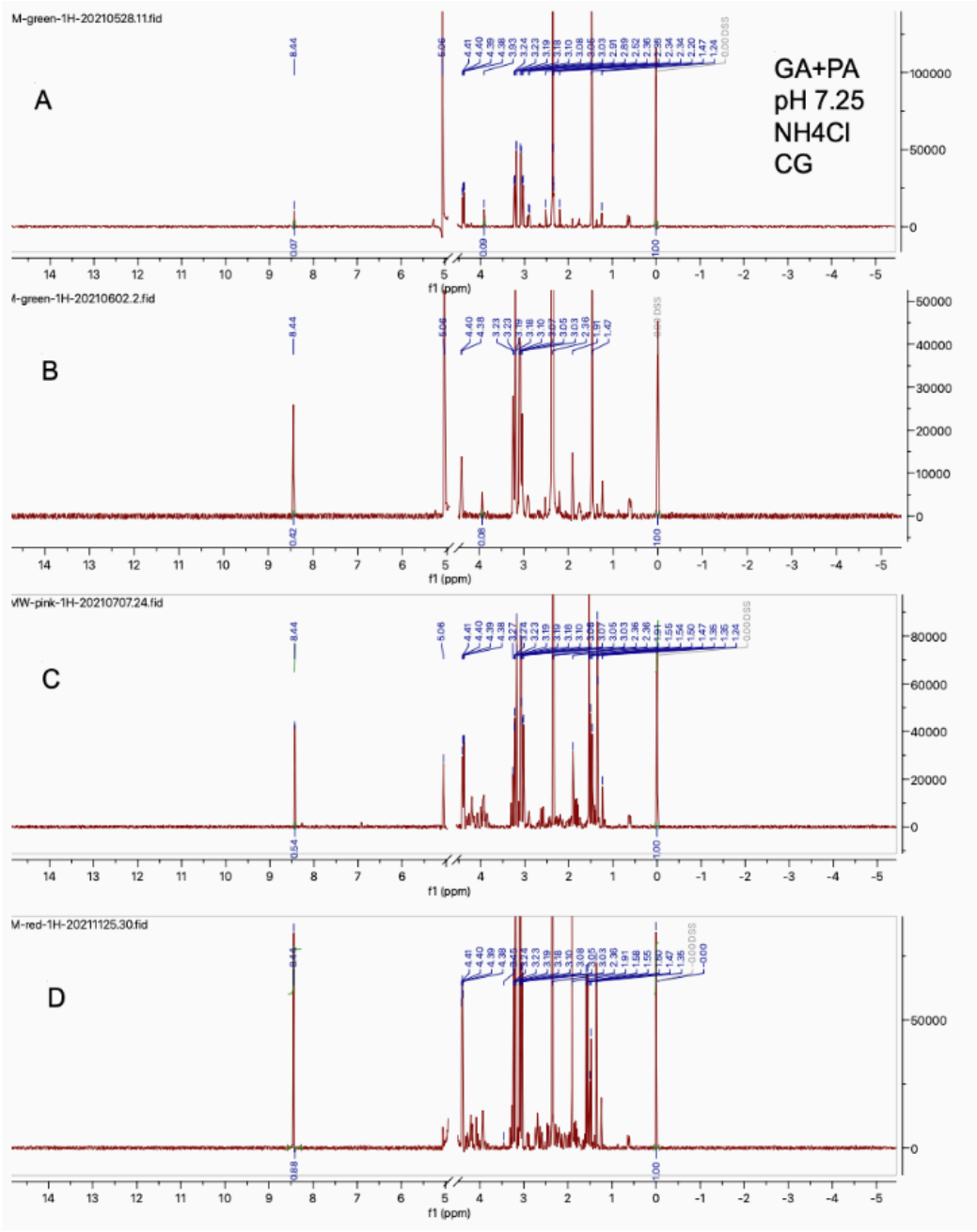


Figure A.21: NMR spectra; pyruvate, glyoxylate, ammonium chloride, and chemical garden reaction under benchtop/aerobic conditions, pH 7.25. A: t = 0 weeks, B: t = 1 week, C: t = 2 weeks, D: t = 3 weeks.

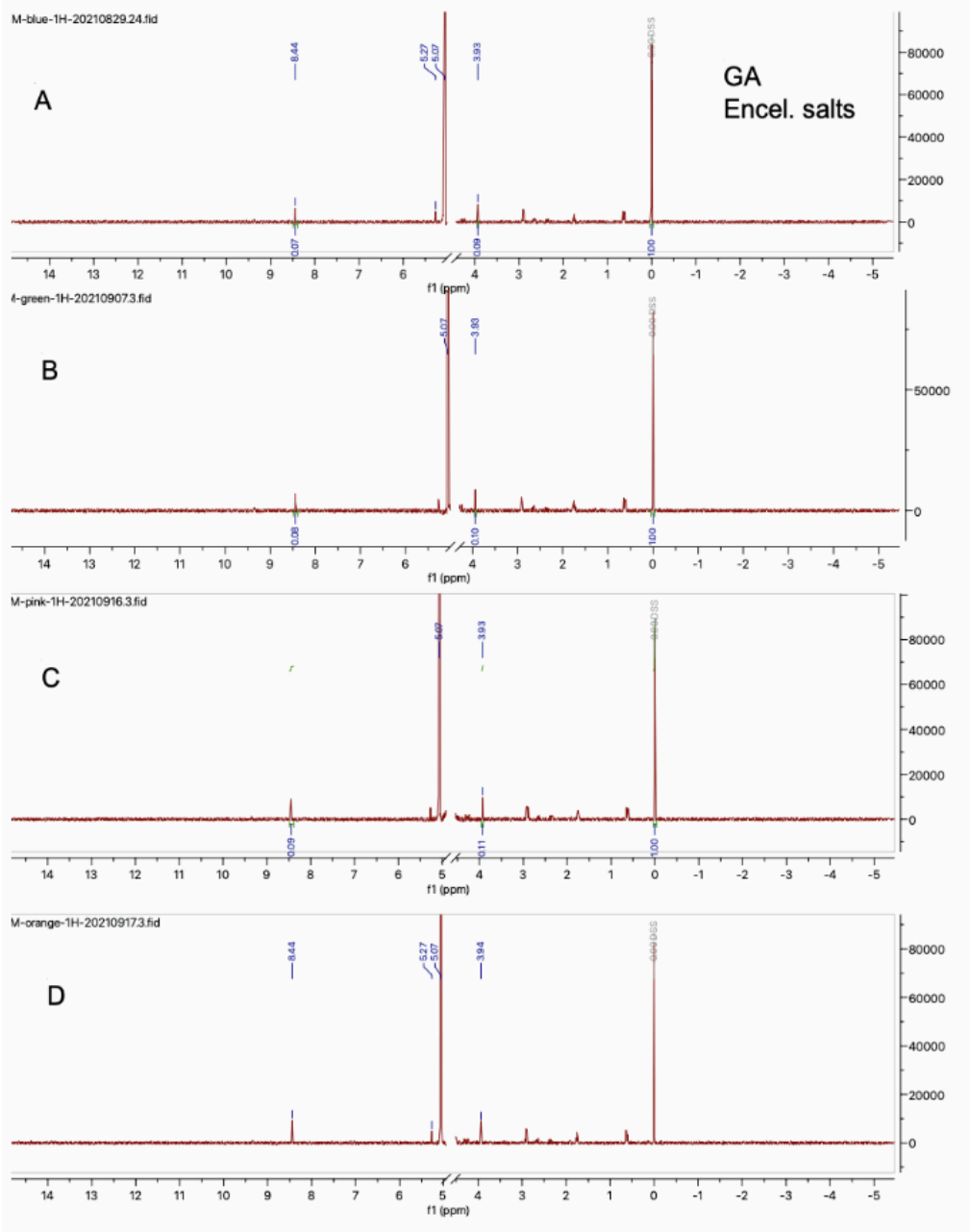


Figure A.22: Control NMR spectra; glyoxylate, sodium chloride, and sodium carbonate reaction under benchtop/aerobic conditions. A: t = 0 weeks, B: t = 1 week, C: t = 2 weeks, D: t = 3 weeks.

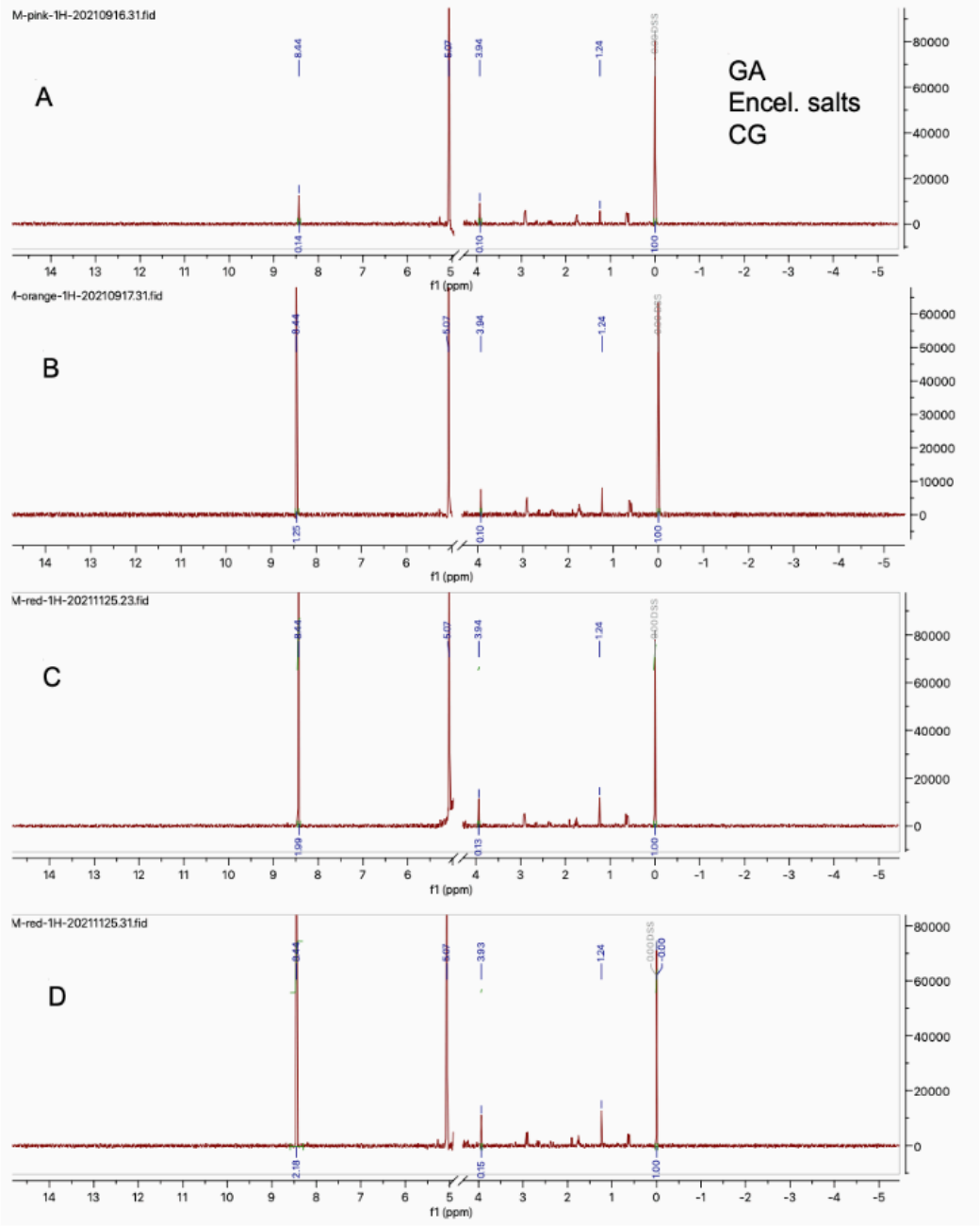


Figure A.23: NMR spectra; glyoxylate, sodium chloride, sodium carbonate, and chemical garden reaction under benchtop/aerobic conditions. A: t = 0 weeks, B: t = 1 week, C: t = 2 weeks, D: t = 3 weeks.

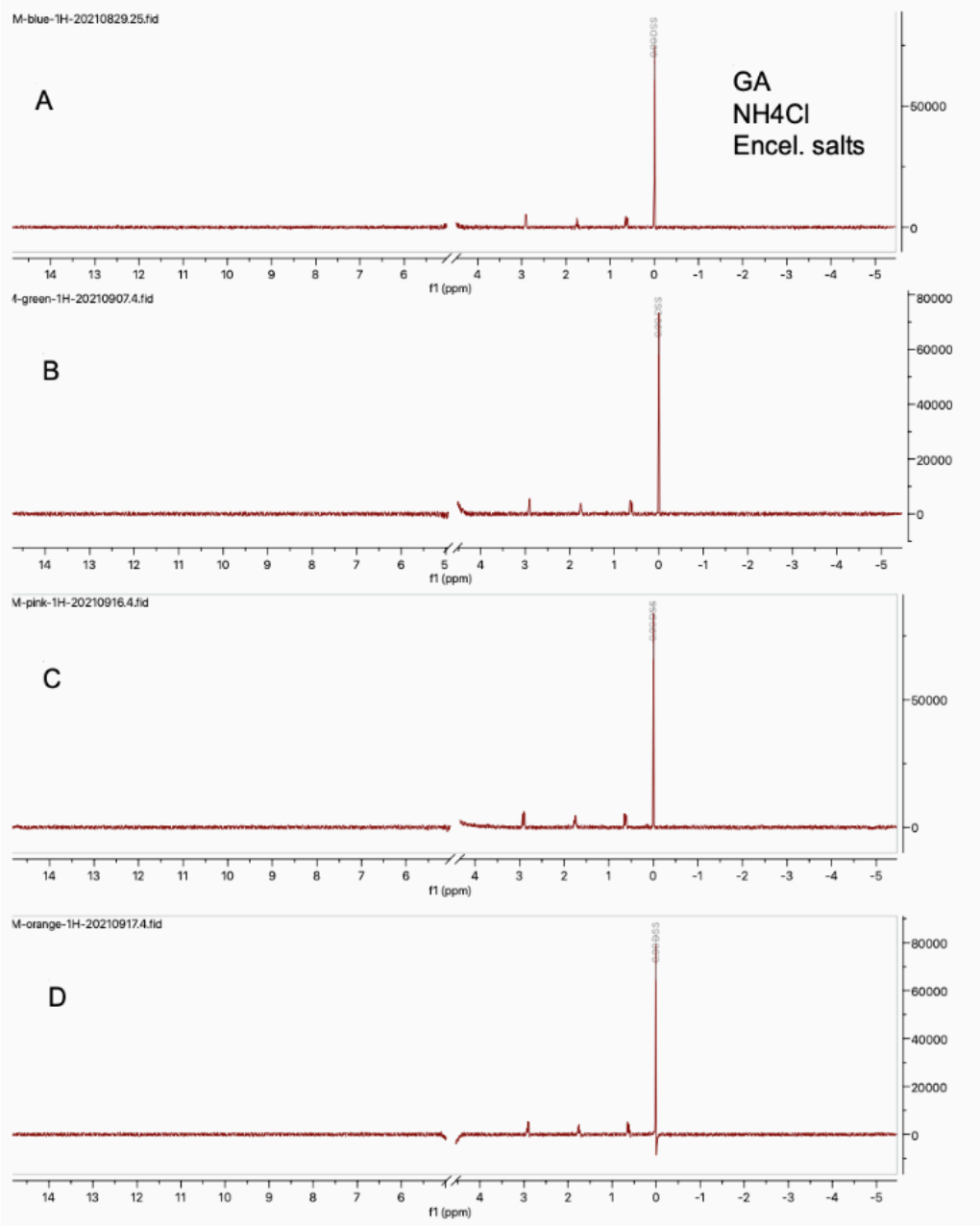


Figure A.24: Control NMR spectra; glyoxylate, sodium chloride, sodium carbonate, and ammonium chloride reaction under benchtop/aerobic conditions. A: t = 0 weeks, B: t = 1 week, C: t = 2 weeks, D: t = 3 weeks.

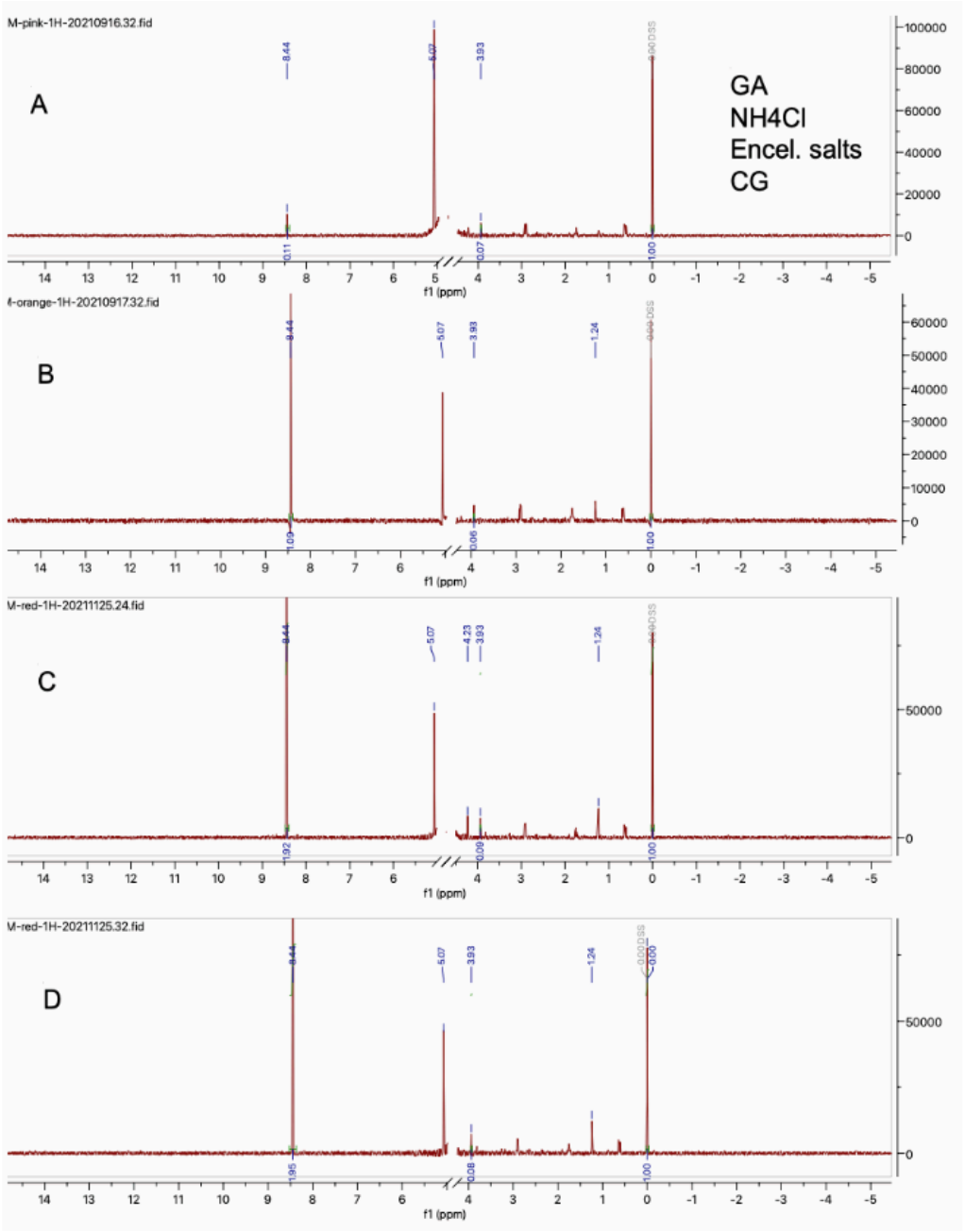


Figure A.25: NMR spectra; glyoxylate, sodium chloride, sodium carbonate, ammonium chloride, and chemical garden reaction under benchtop/aerobic conditions. A: t = 0 weeks, B: t = 1 week, C: t = 2 weeks, D: t = 3 weeks.

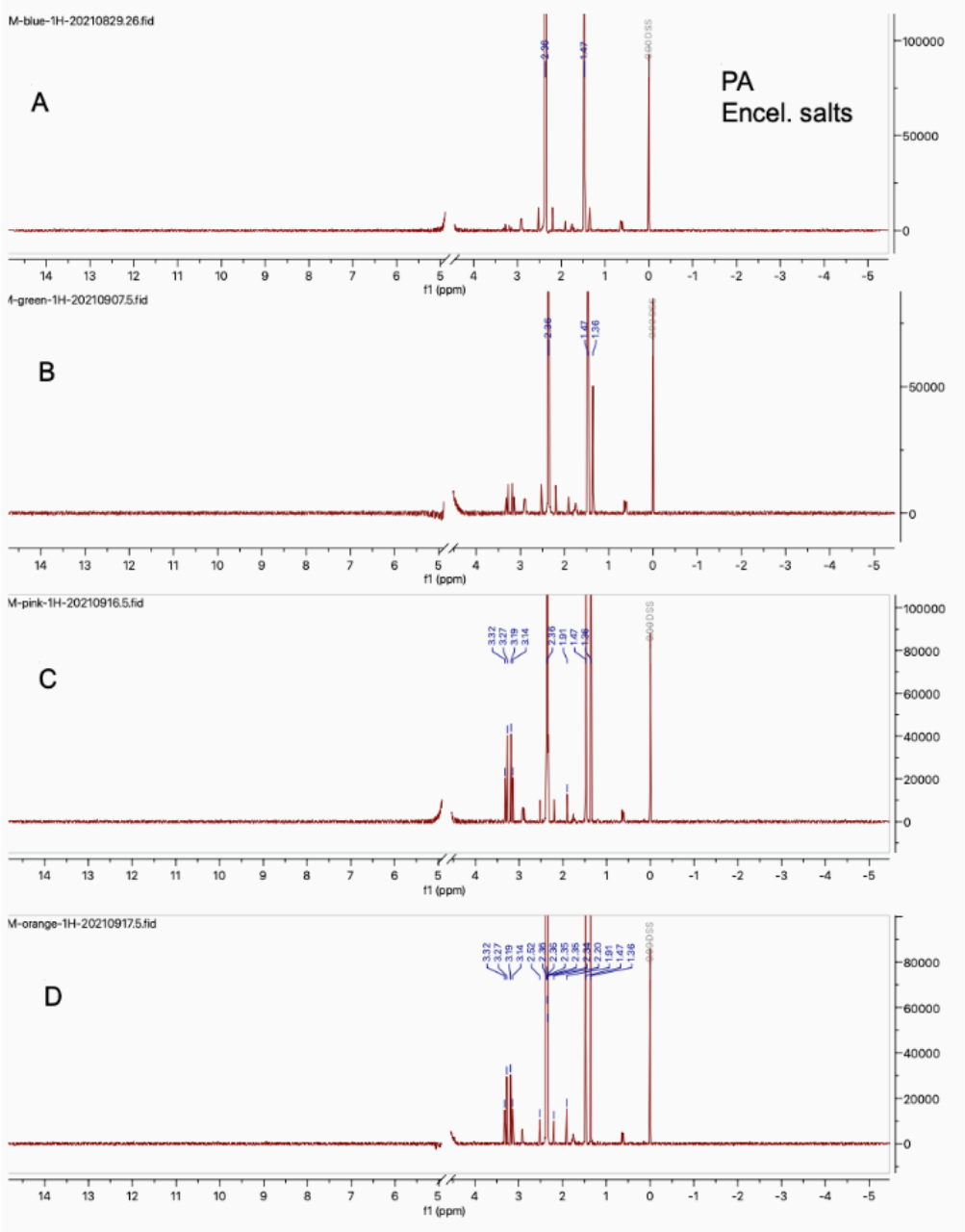


Figure A.26: Control NMR spectra; pyruvate, sodium chloride, and sodium carbonate reaction under benchtop/aerobic conditions. A: t = 0 weeks, B: t = 1 week, C: t = 2 weeks, D: t = 3 weeks.

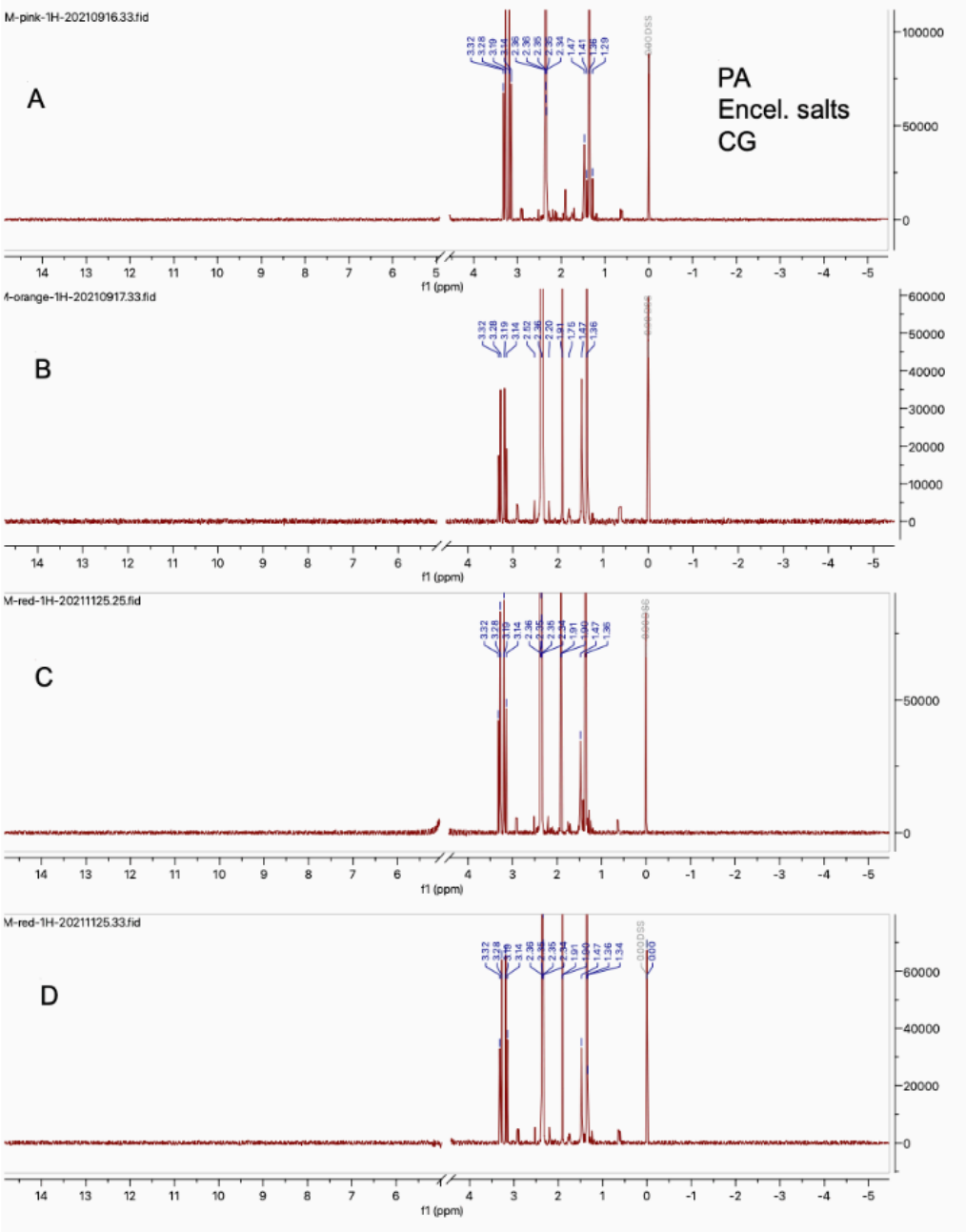


Figure A.27: NMR spectra; pyruvate, sodium chloride, sodium carbonate, and chemical garden reaction under benchtop/aerobic conditions. A: t = 0 weeks, B: t = 1 week, C: t = 2 weeks, D: t = 3 weeks.

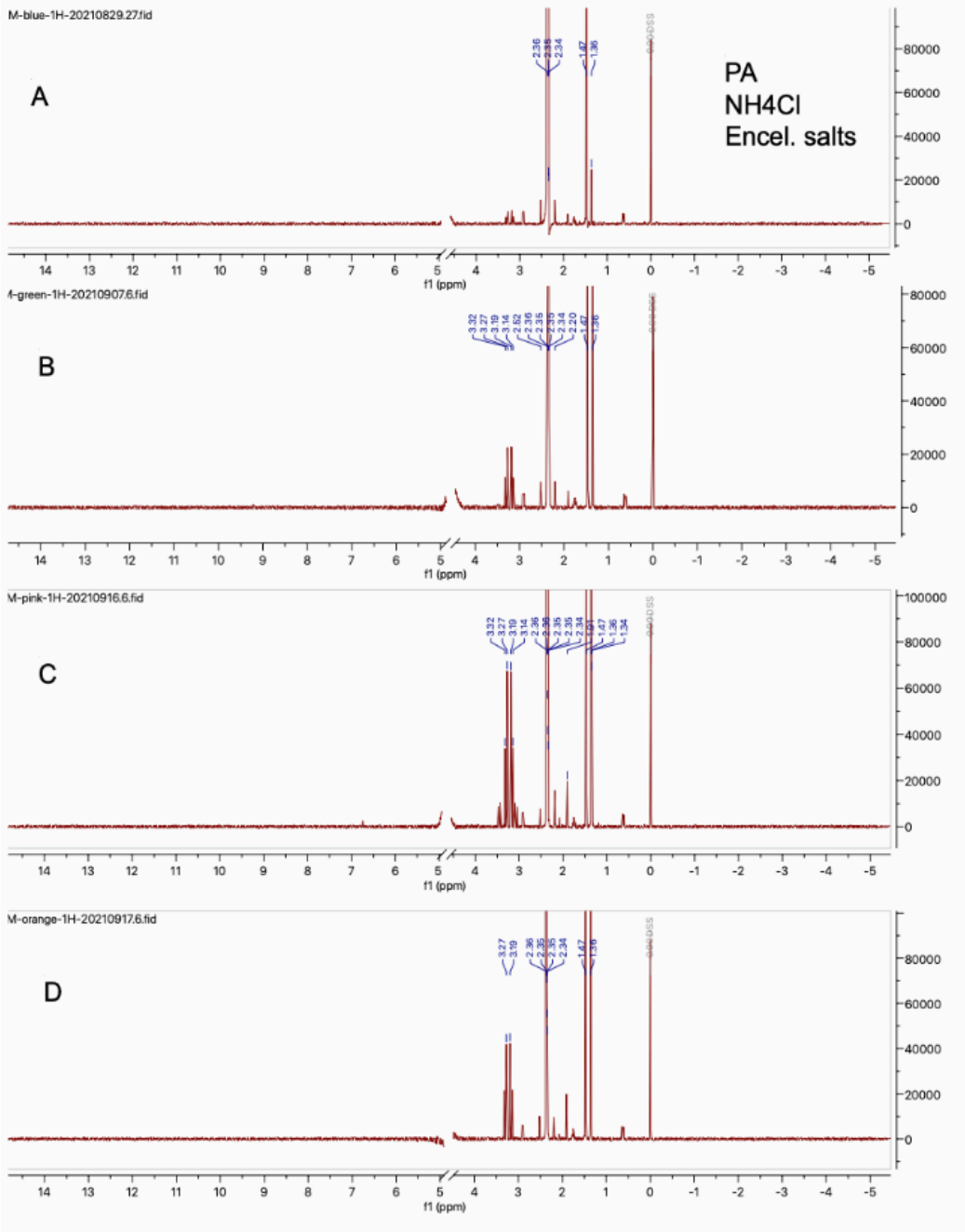


Figure A.28: Control NMR spectra; pyruvate, sodium chloride, sodium carbonate, and ammonium chloride reaction under benchtop/aerobic conditions. A: t = 0 weeks, B: t = 1 week, C: t = 2 weeks, D: t = 3 weeks.

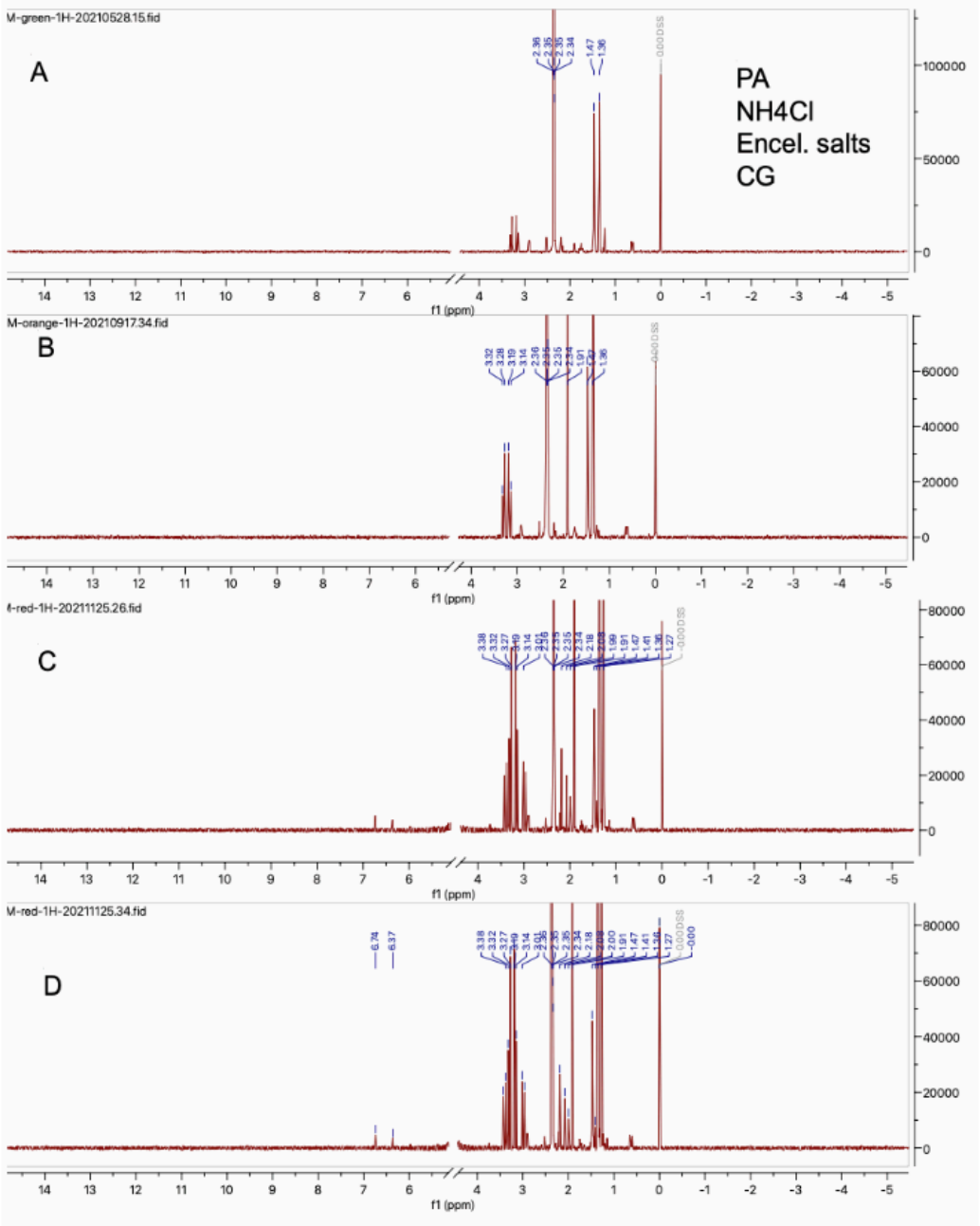


Figure A.29: NMR spectra; pyruvate, sodium chloride, sodium carbonate, ammonium chloride, and chemical garden reaction under benchtop/aerobic conditions. A: t = 0 weeks, B: t = 1 week, C: t = 2 weeks, D: t = 3 weeks.

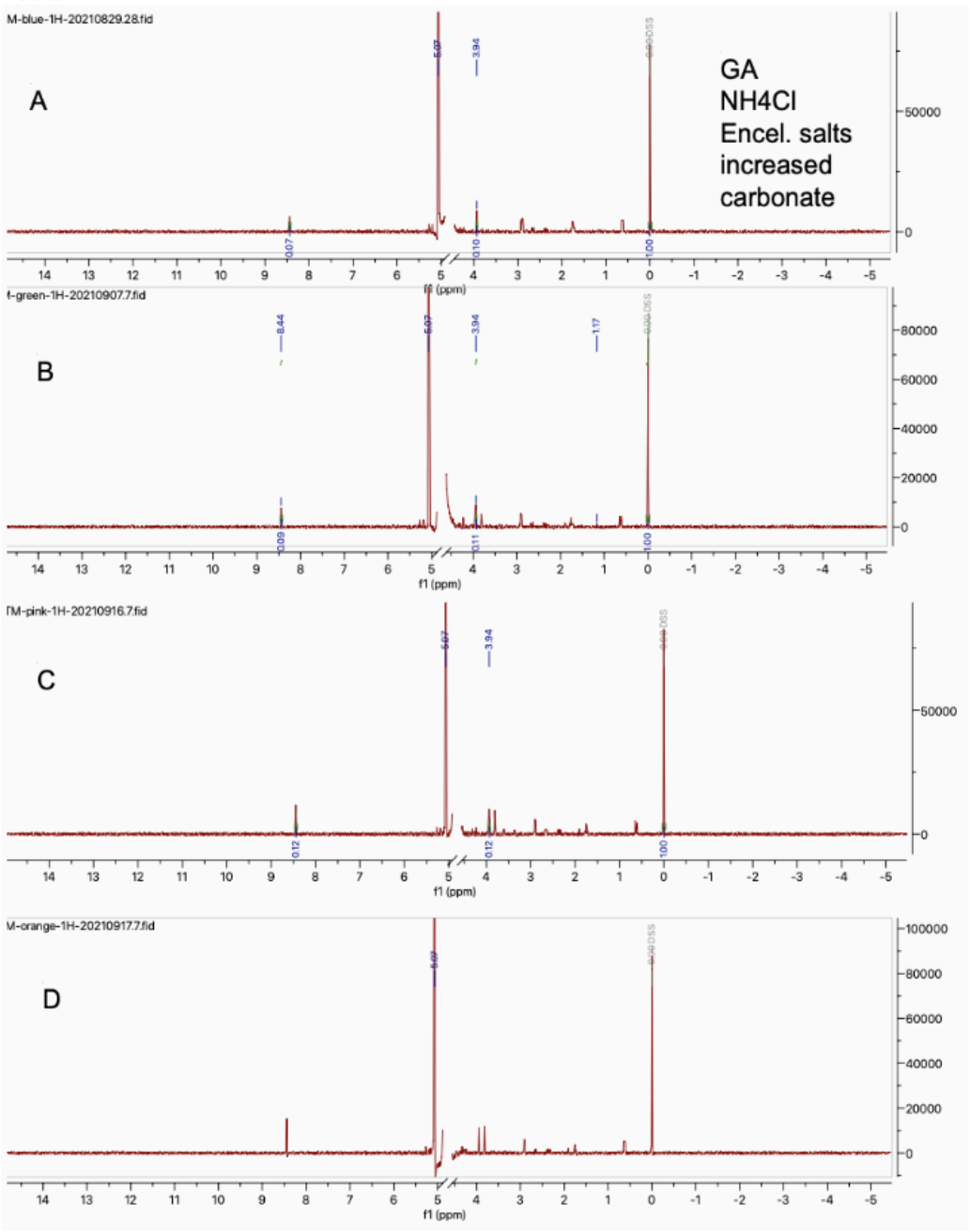


Figure A.30: Control NMR spectra; glyoxylate, sodium chloride, increased sodium carbonate, and ammonium chloride reaction under benchtop/aerobic conditions. A: t = 0 weeks, B: t = 1 week, C: t = 2 weeks, D: t = 3 weeks.

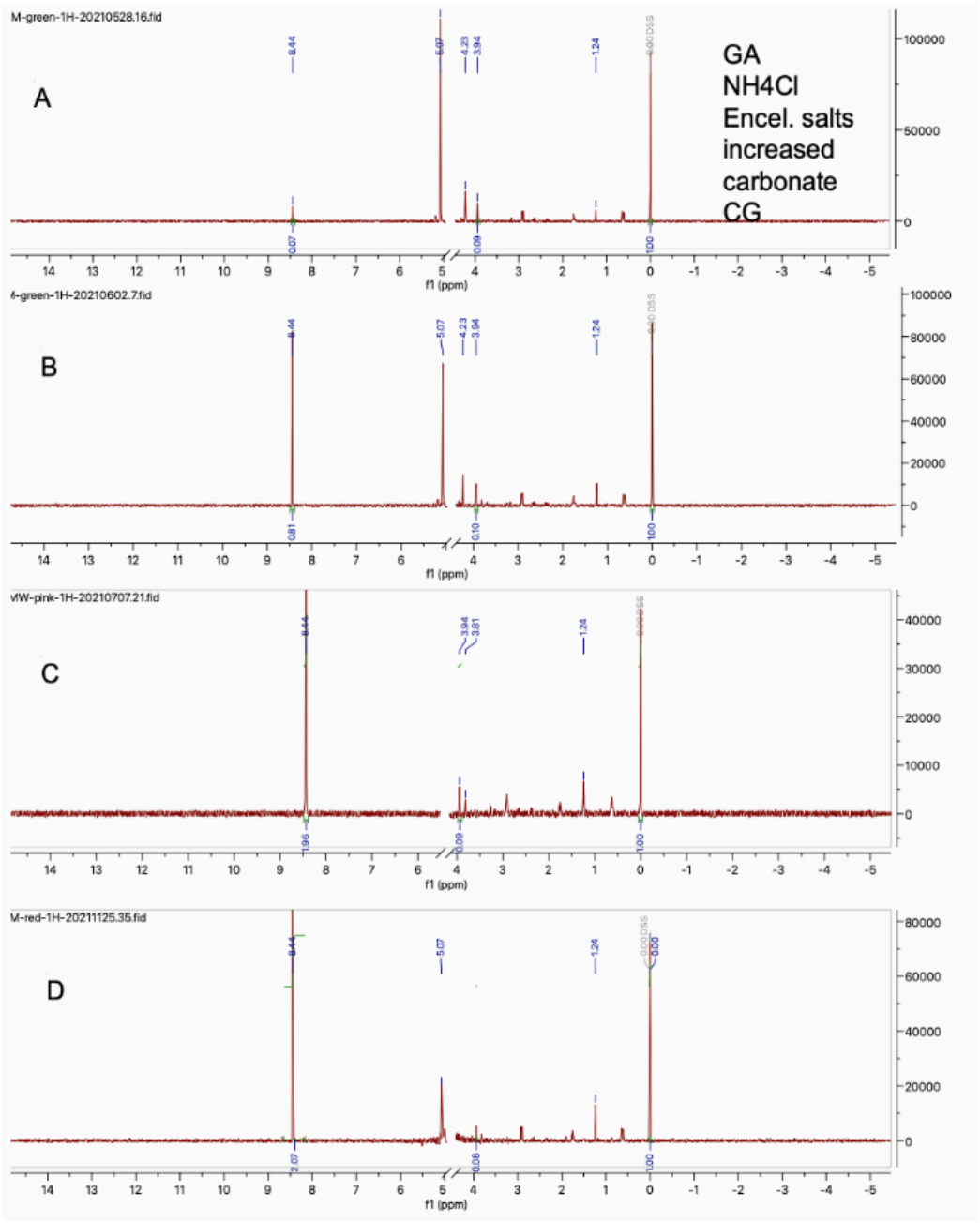


Figure A.31: NMR spectra; glyoxylate, sodium chloride, increased sodium carbonate, ammonium chloride, and chemical garden reaction under benchtop/aerobic conditions. A: t = 0 weeks, B: t = 1 week, C: t = 2 weeks, D: t = 3 weeks.

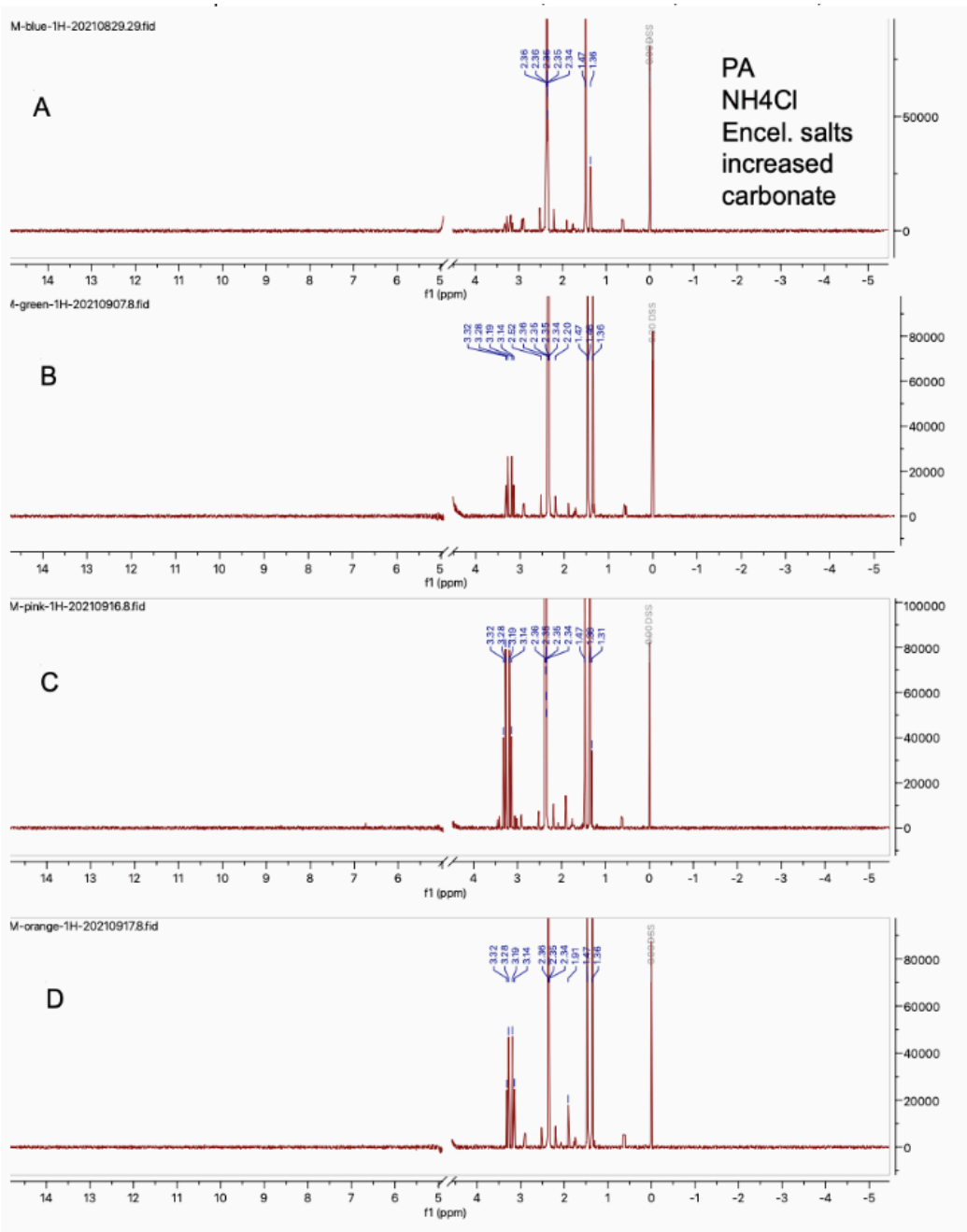


Figure A.32: Control NMR spectra; pyruvate, sodium chloride, increased sodium carbonate, and ammonium chloride reaction under benchtop/aerobic conditions. A: t = 0 weeks, B: t = 1 week, C: t = 2 weeks, D: t = 3 weeks.

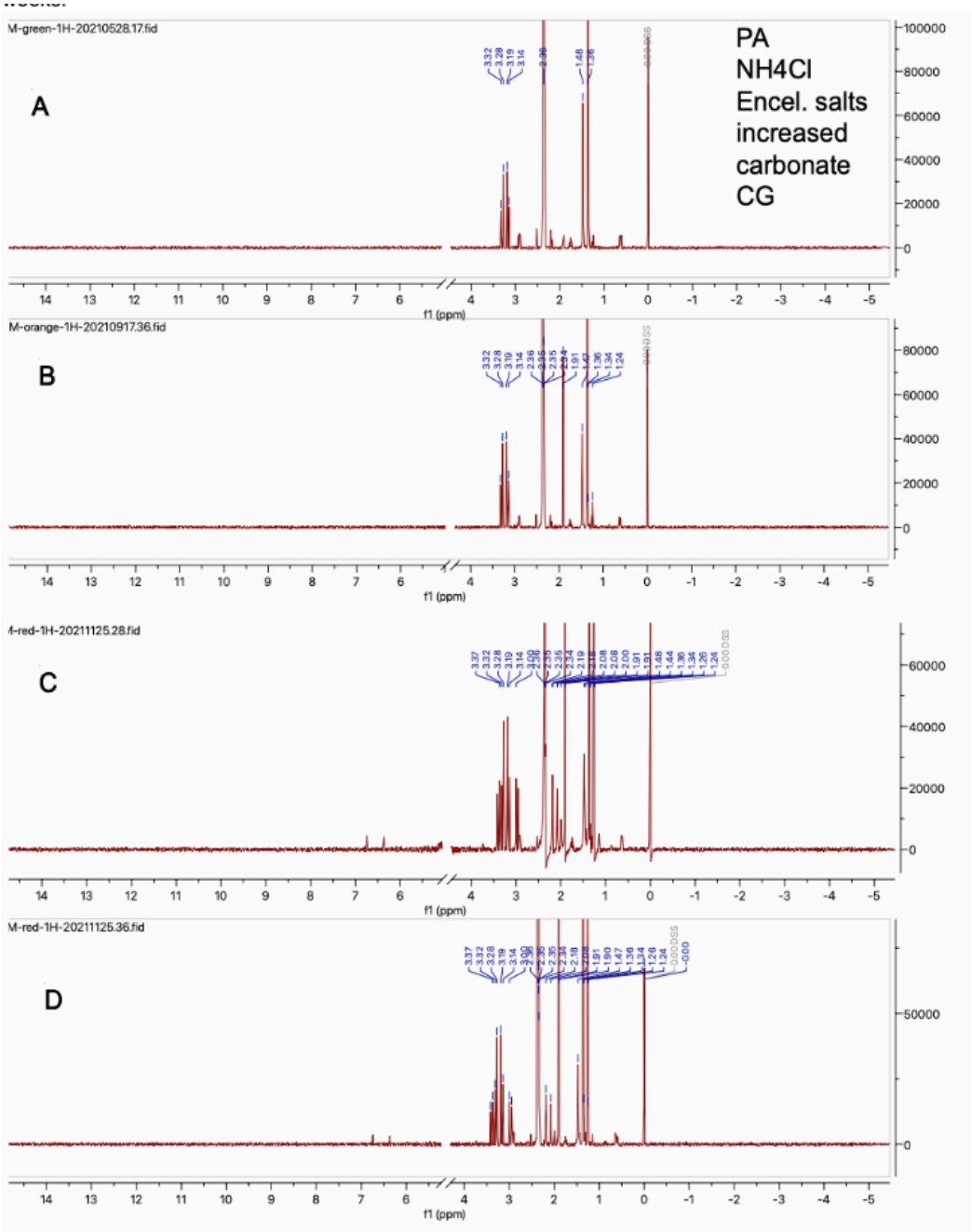


Figure A.33: NMR spectra; pyruvate, sodium chloride, increased sodium carbonate, ammonium chloride, and chemical garden reaction under benchtop/aerobic conditions. A: t = 0 weeks, B: t = 1 week, C: t = 2 weeks, D: t = 3 weeks.

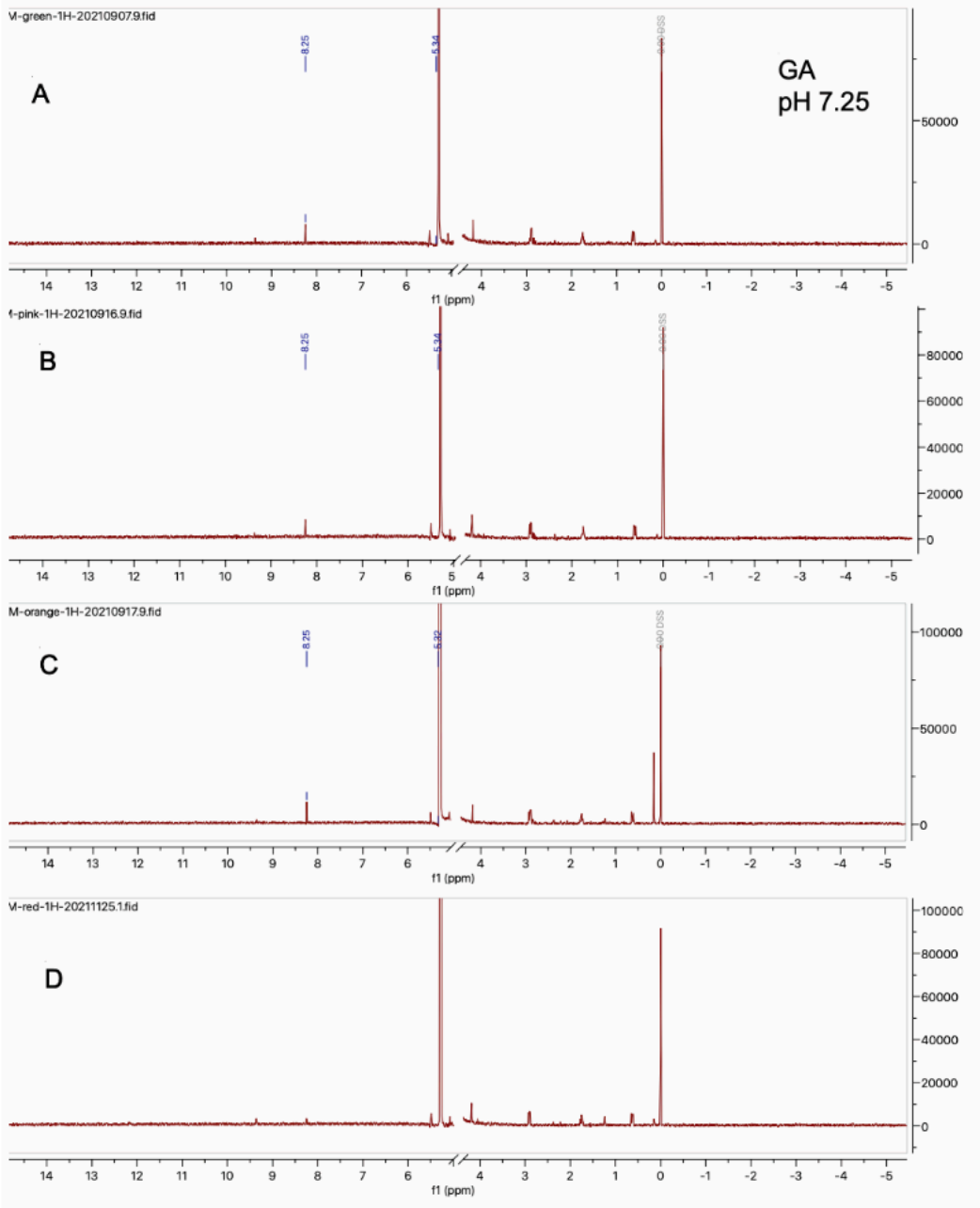


Figure A.34: Control NMR spectra; glyoxylate reaction under heated conditions, pH 7.25. A: t = 0 weeks, B: t = 1 week, C: t = 2 weeks, D: t = 3 weeks.

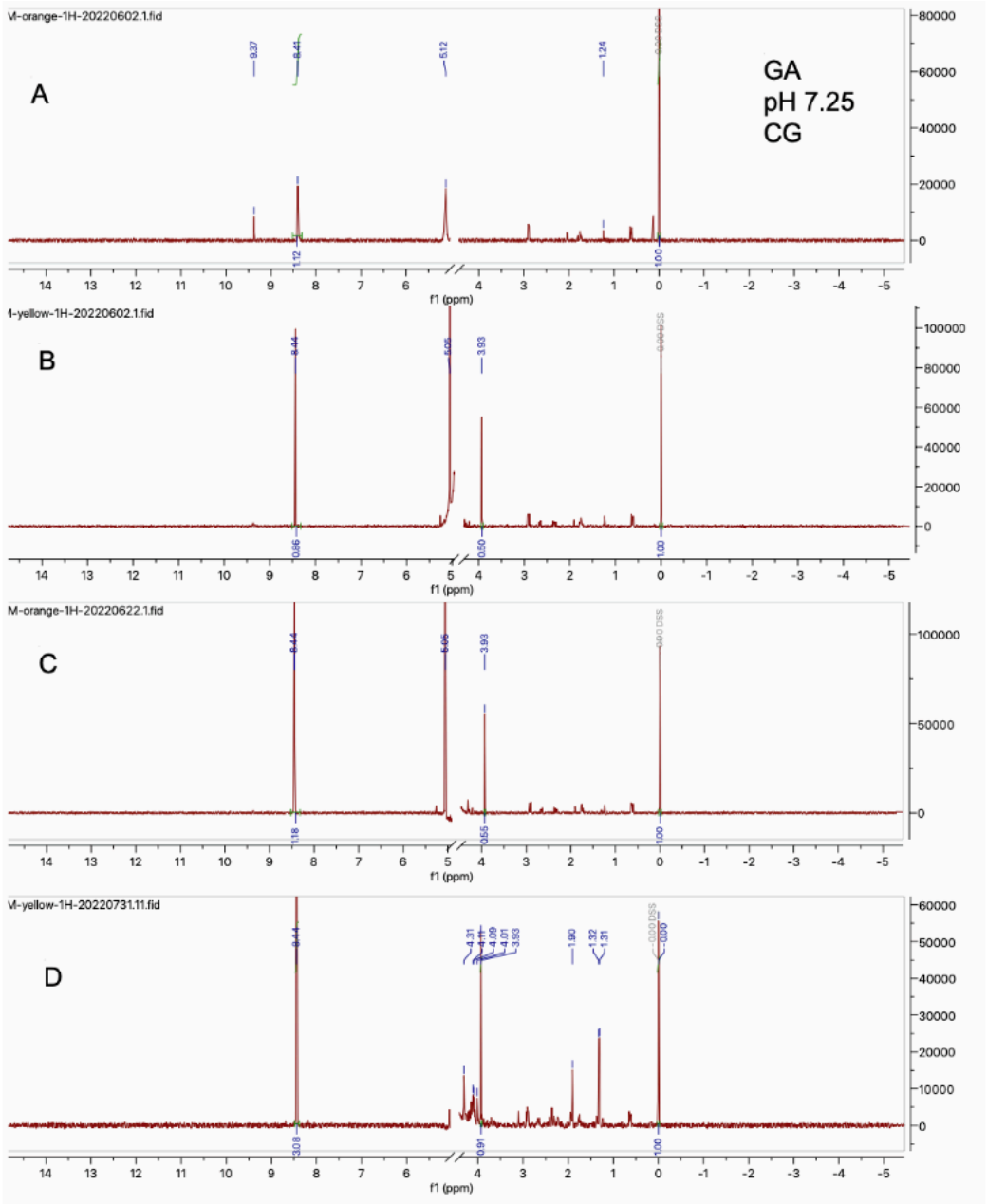


Figure A.35: NMR spectra; glyoxylate and chemical garden reaction under heated conditions, pH 7.25. A: t = 0 weeks, B: t = 1 week, C: t = 2 weeks, D: t = 3 weeks.

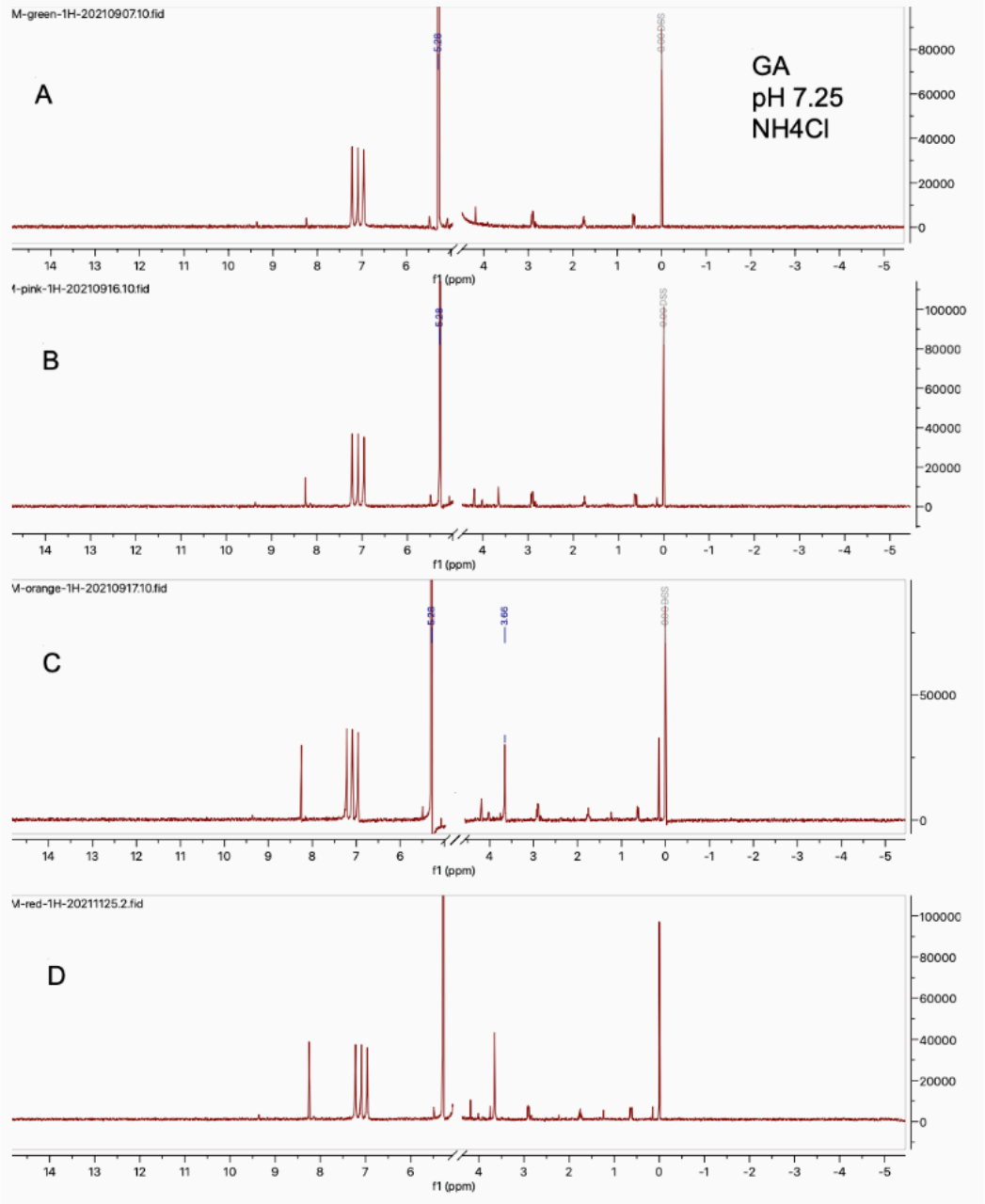


Figure A.36: Control NMR spectra; glyoxylate and ammonium chloride reaction under heated conditions, pH 7.25. A: t = 0 weeks, B: t = 1 week, C: t = 2 weeks, D: t = 3 weeks.

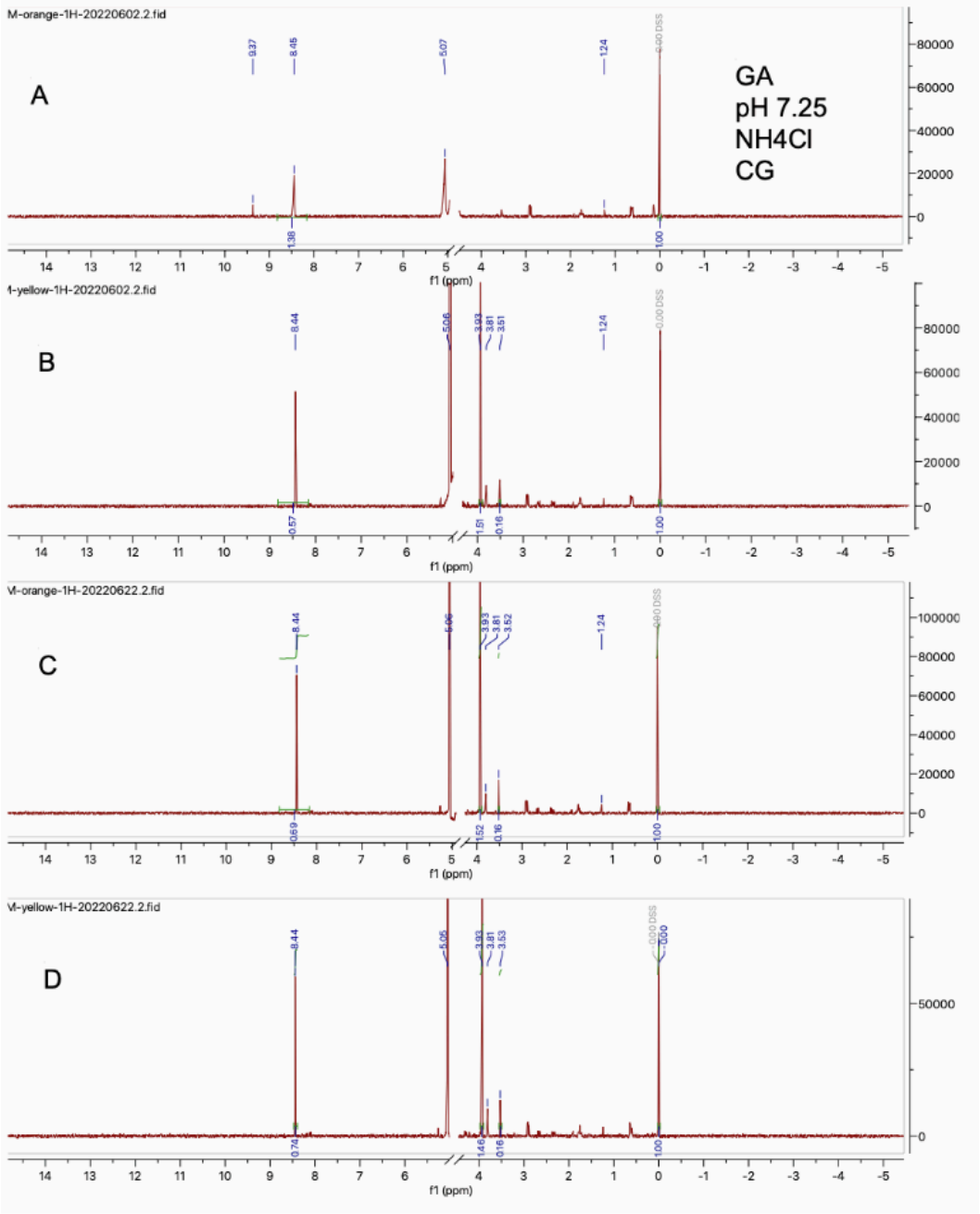


Figure A.37: NMR spectra; glyoxylate, ammonium chloride, and chemical garden reaction under heated conditions, pH 7.25. A: t = 0 weeks, B: t = 1 week, C: t = 2 weeks, D: t = 3 weeks.

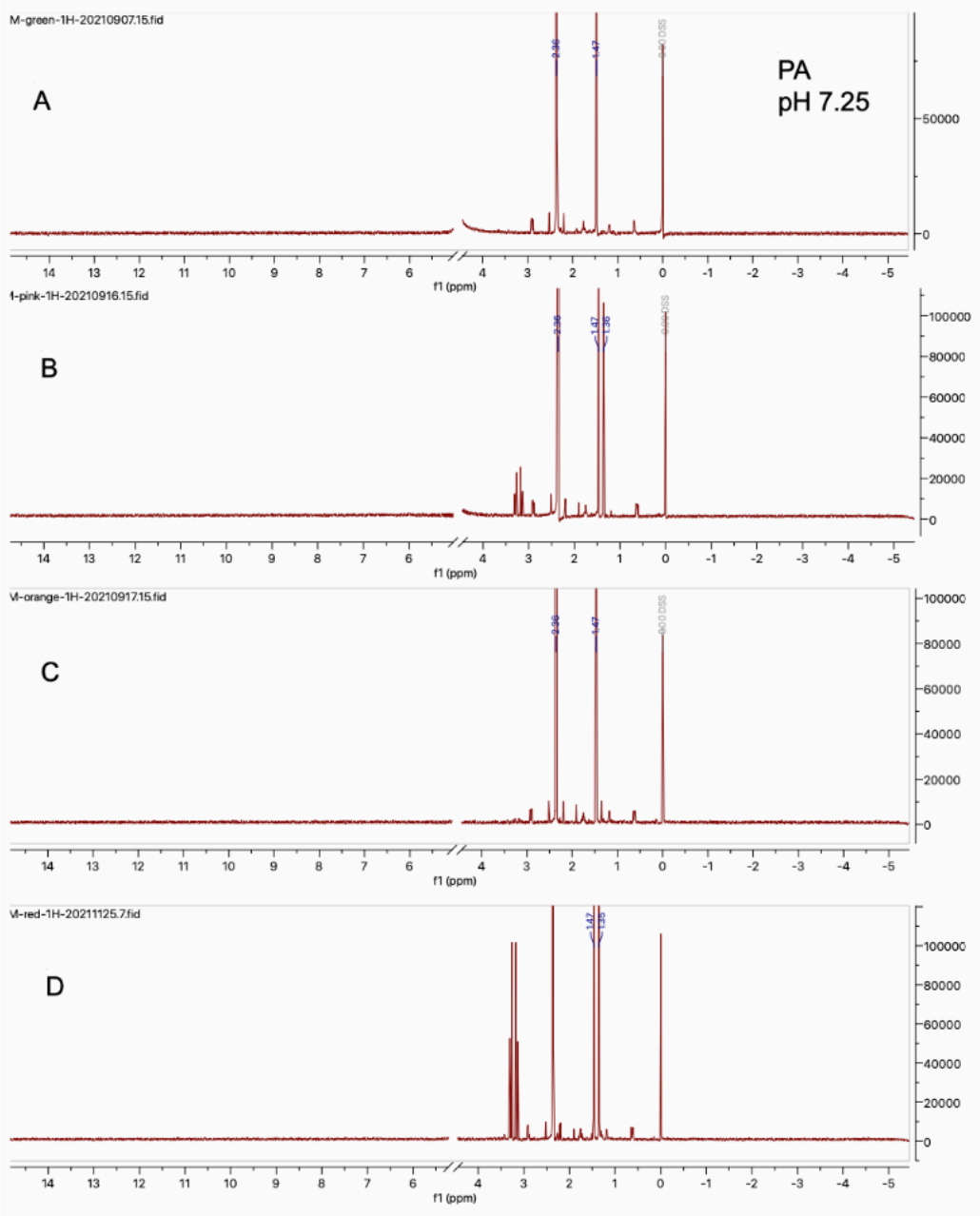


Figure A.38: Control NMR spectra; pyruvate reaction under heated conditions, pH 7.25. A: t = 0 weeks, B: t = 1 week, C: t = 2 weeks, D: t = 3 weeks.

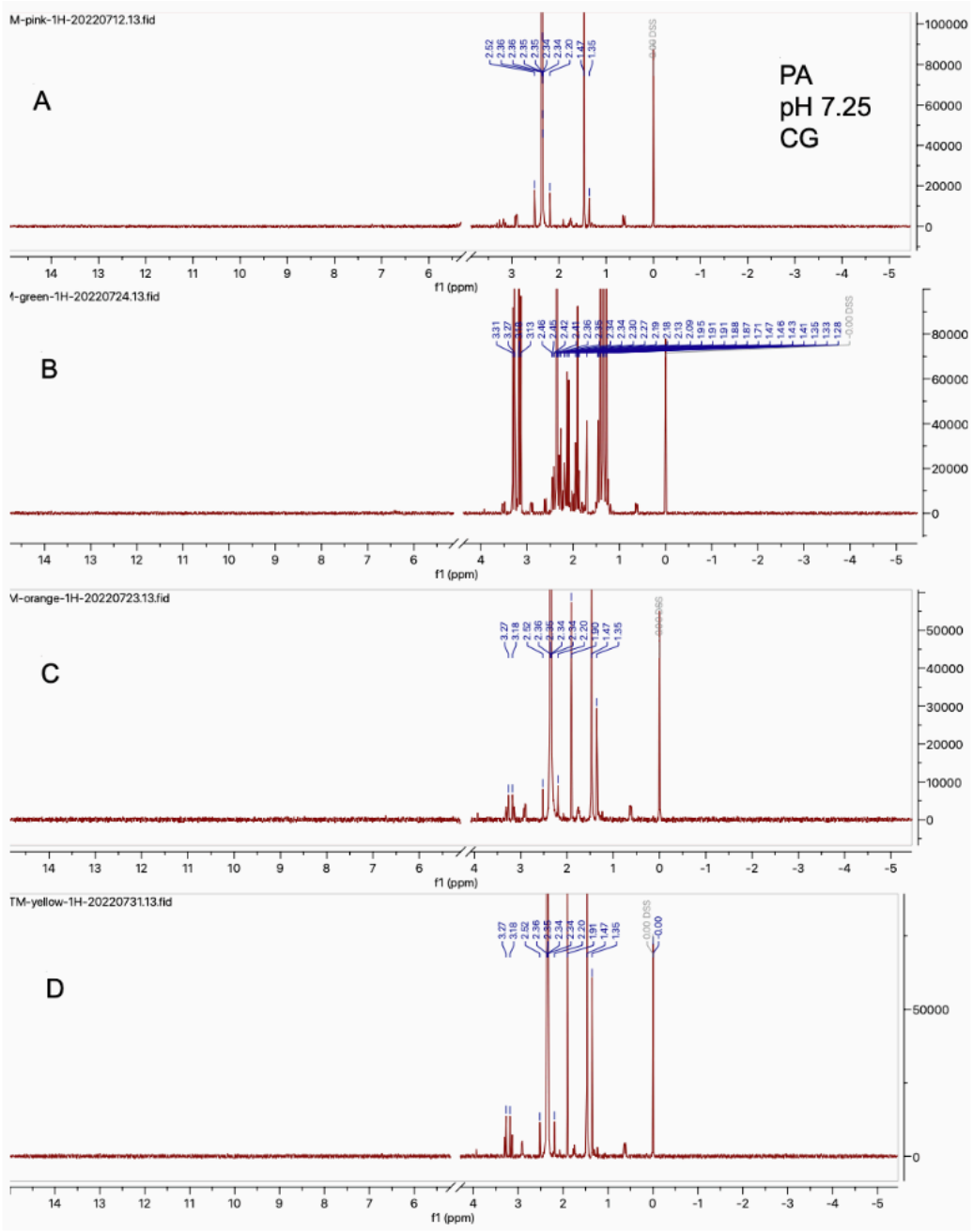


Figure A.39: NMR spectra; pyruvate and chemical garden reaction under heated conditions, pH 7.25. A: t = 0 weeks, B: t = 1 week, C: t = 2 weeks, D: t = 3 weeks.

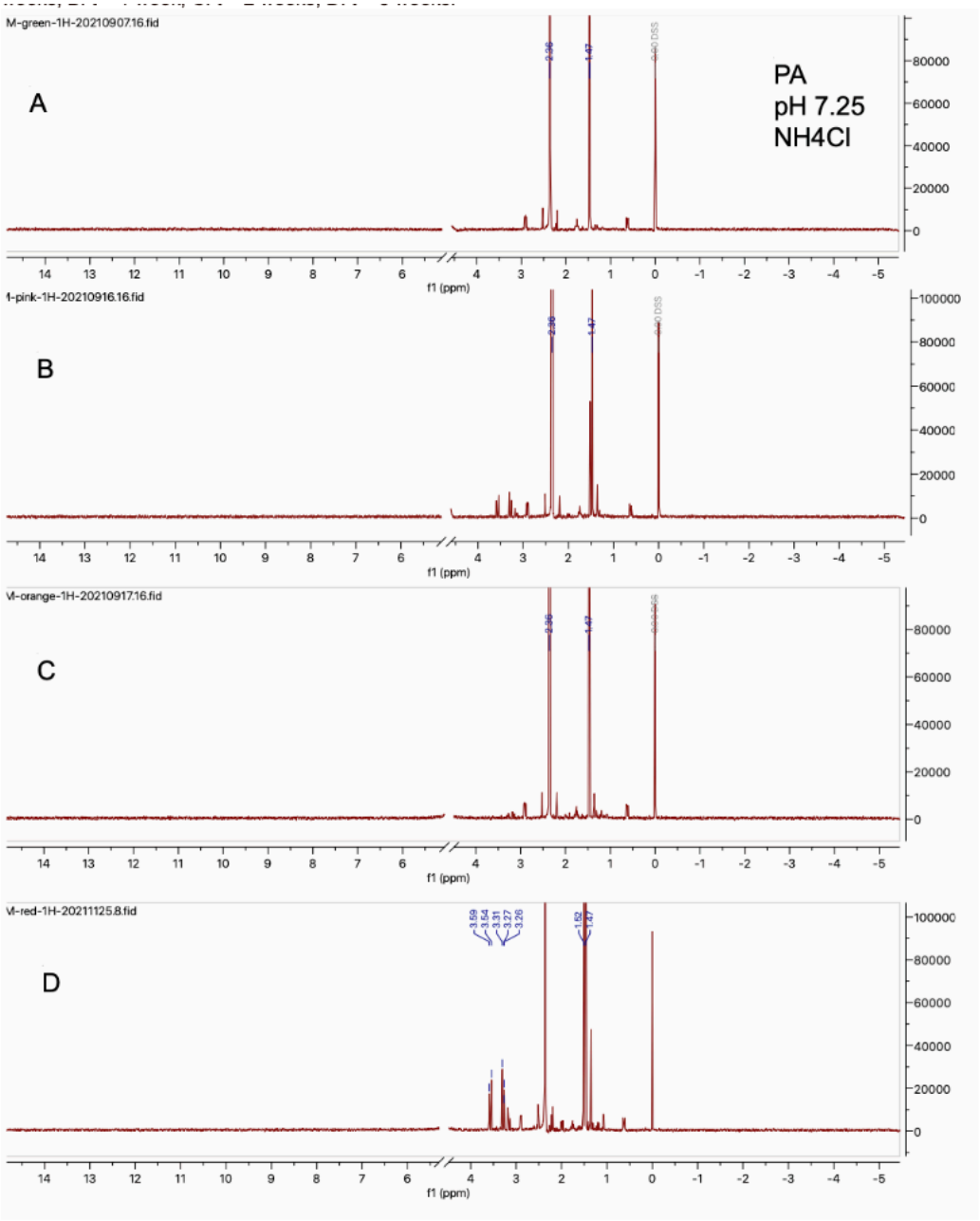


Figure A.40: Control NMR spectra; pyruvate and ammonium chloride reaction under heated conditions, pH 7.25. A: t = 0 weeks, B: t = 1 week, C: t = 2 weeks, D: t = 3 weeks.

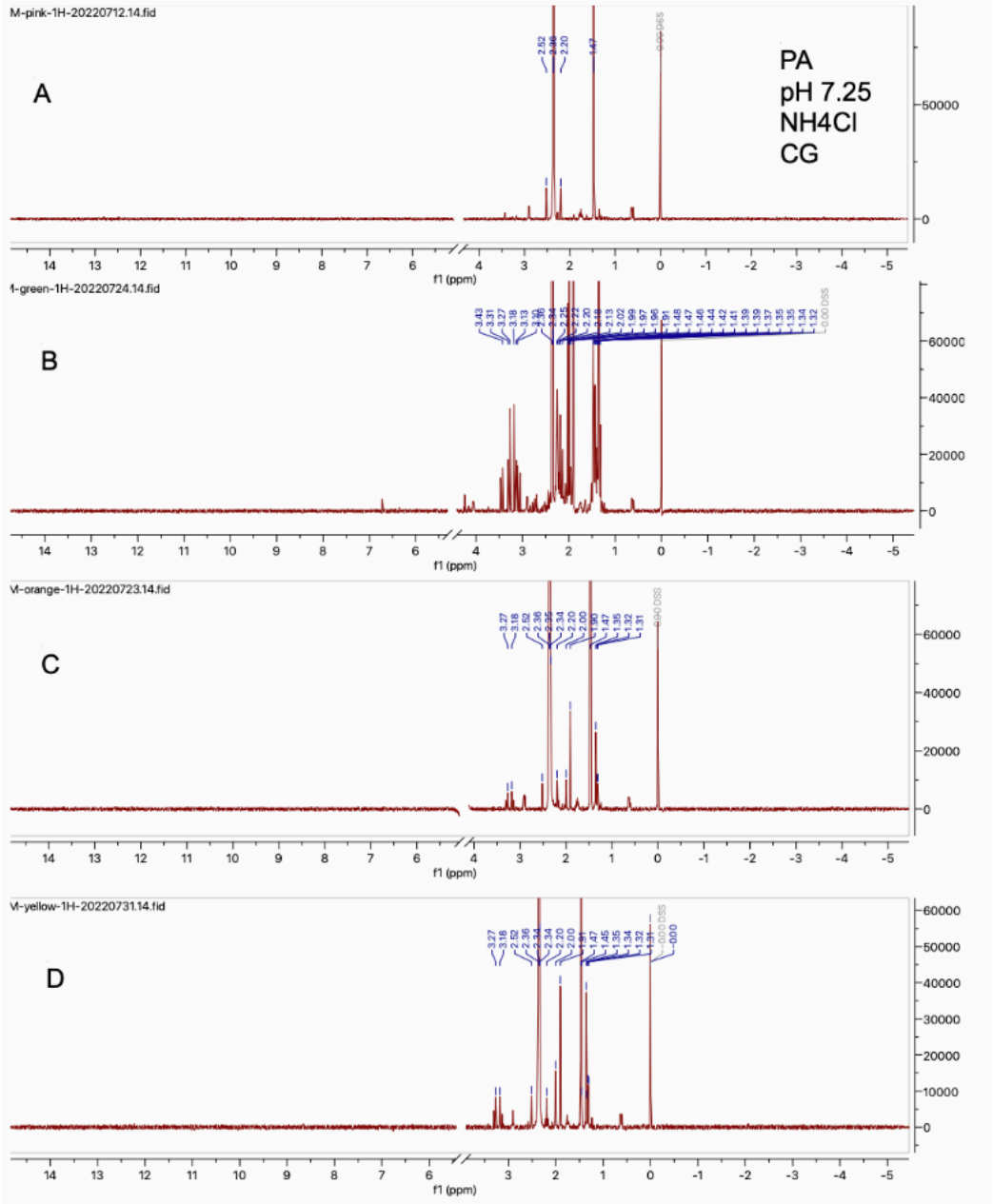


Figure A.41: NMR spectra; pyruvate, ammonium chloride and chemical garden reaction under heated conditions, pH 7.25. A: t = 0 weeks, B: t = 1 week, C: t = 2 weeks, D: t = 3 weeks.

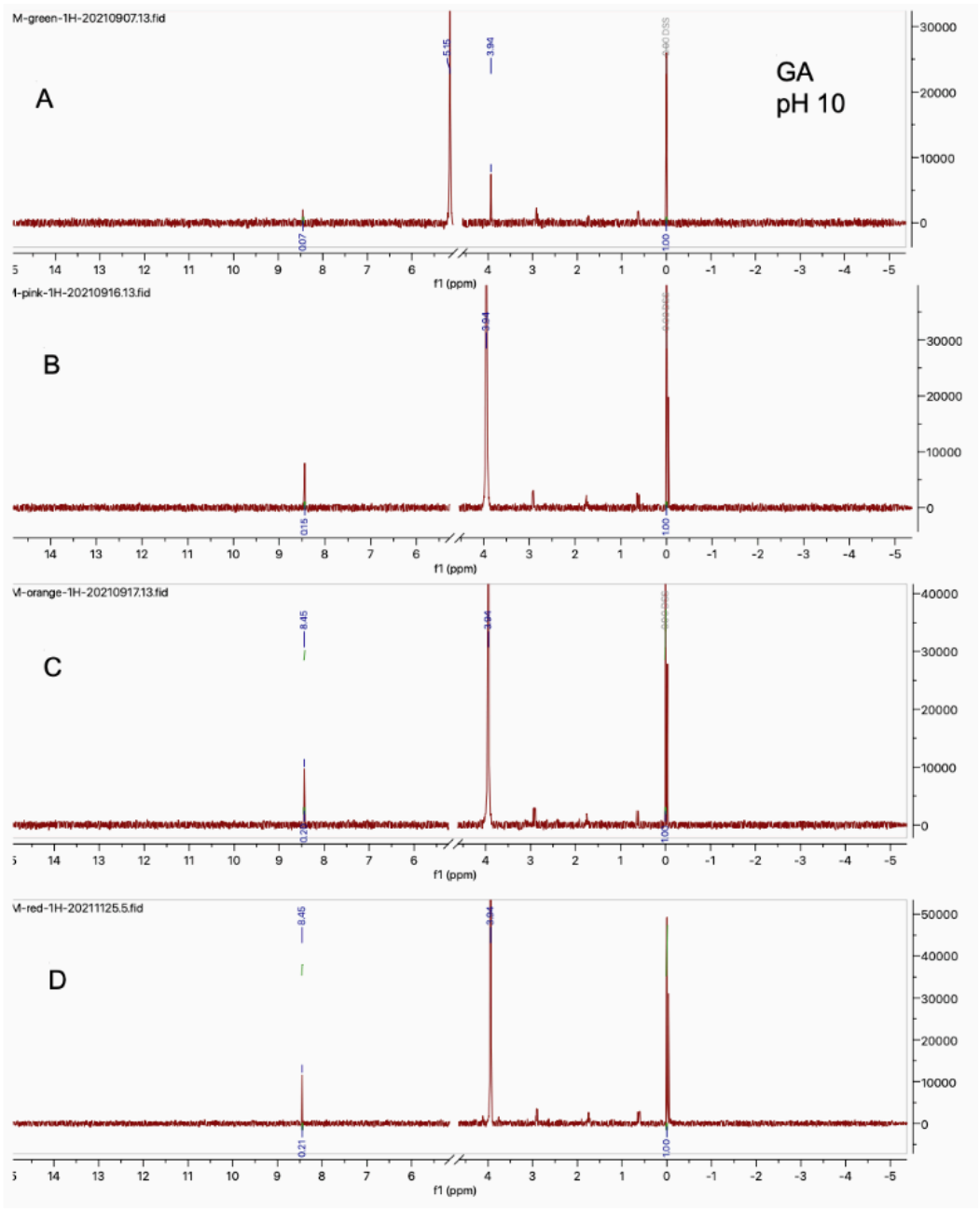


Figure A.42: Control NMR spectra; glyoxylate reaction under heated conditions, pH 10. A: t = 0 weeks, B: t = 1 week, C: t = 2 weeks, D: t = 3 weeks.

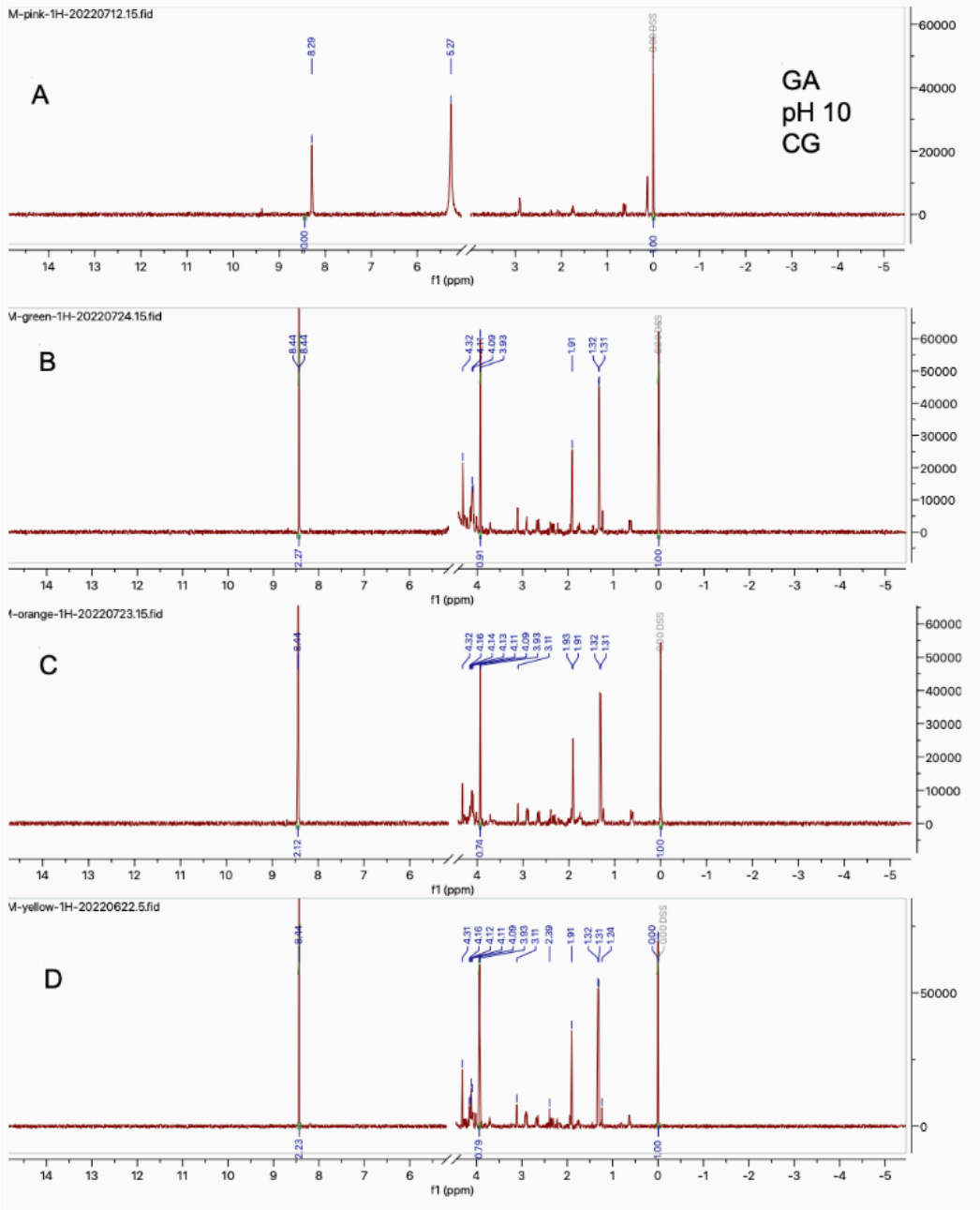


Figure A.43: NMR spectra; glyoxylate and chemical garden reaction under heated conditions, pH 10. A: t = 0 weeks, B: t = 1 week, C: t = 2 weeks, D: t = 3 weeks.

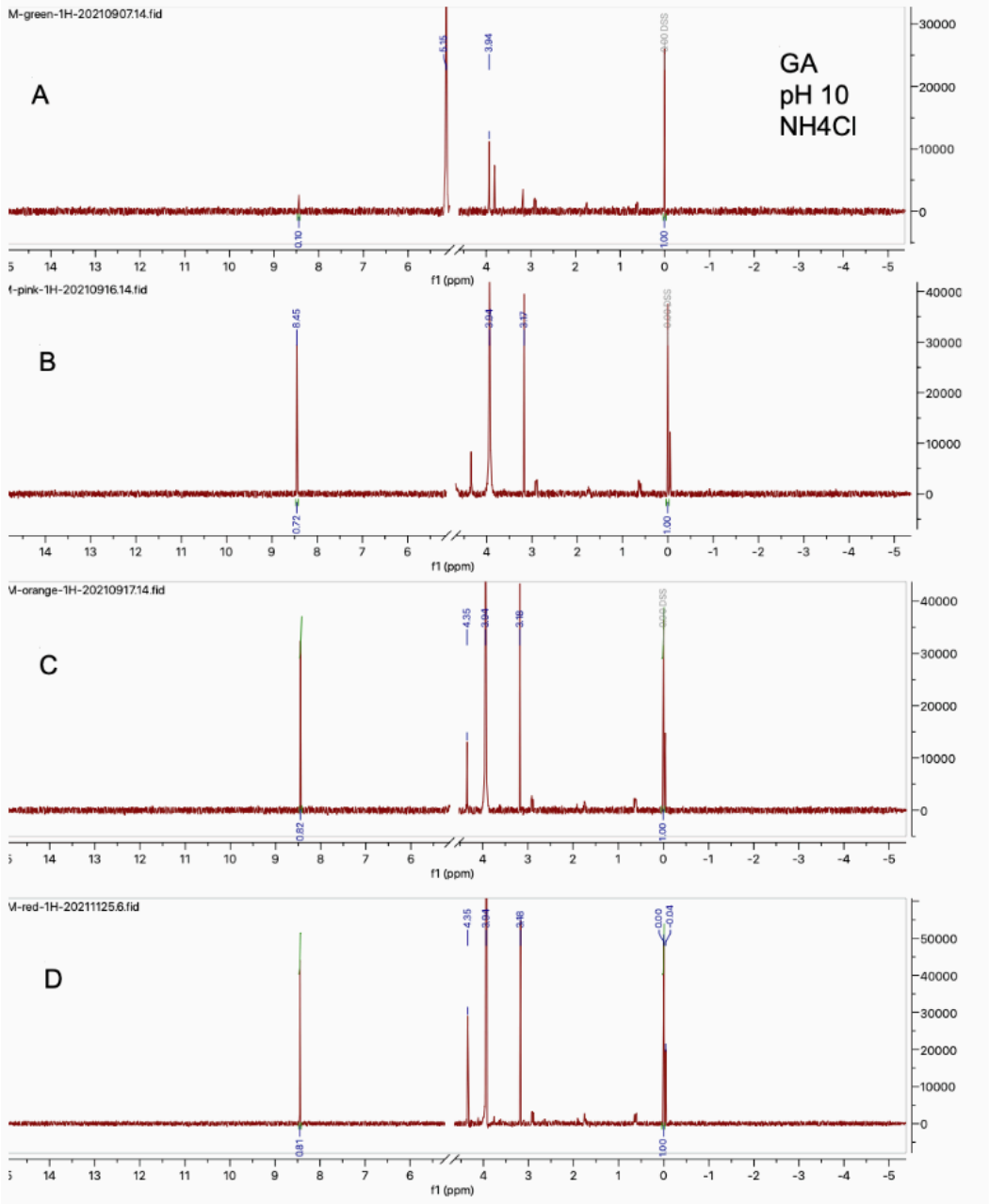


Figure A.44: Control NMR spectra; glyoxylate and ammonium chloride reaction under heated conditions, pH 10. A: t = 0 weeks, B: t = 1 week, C: t = 2 weeks, D: t = 3 weeks.

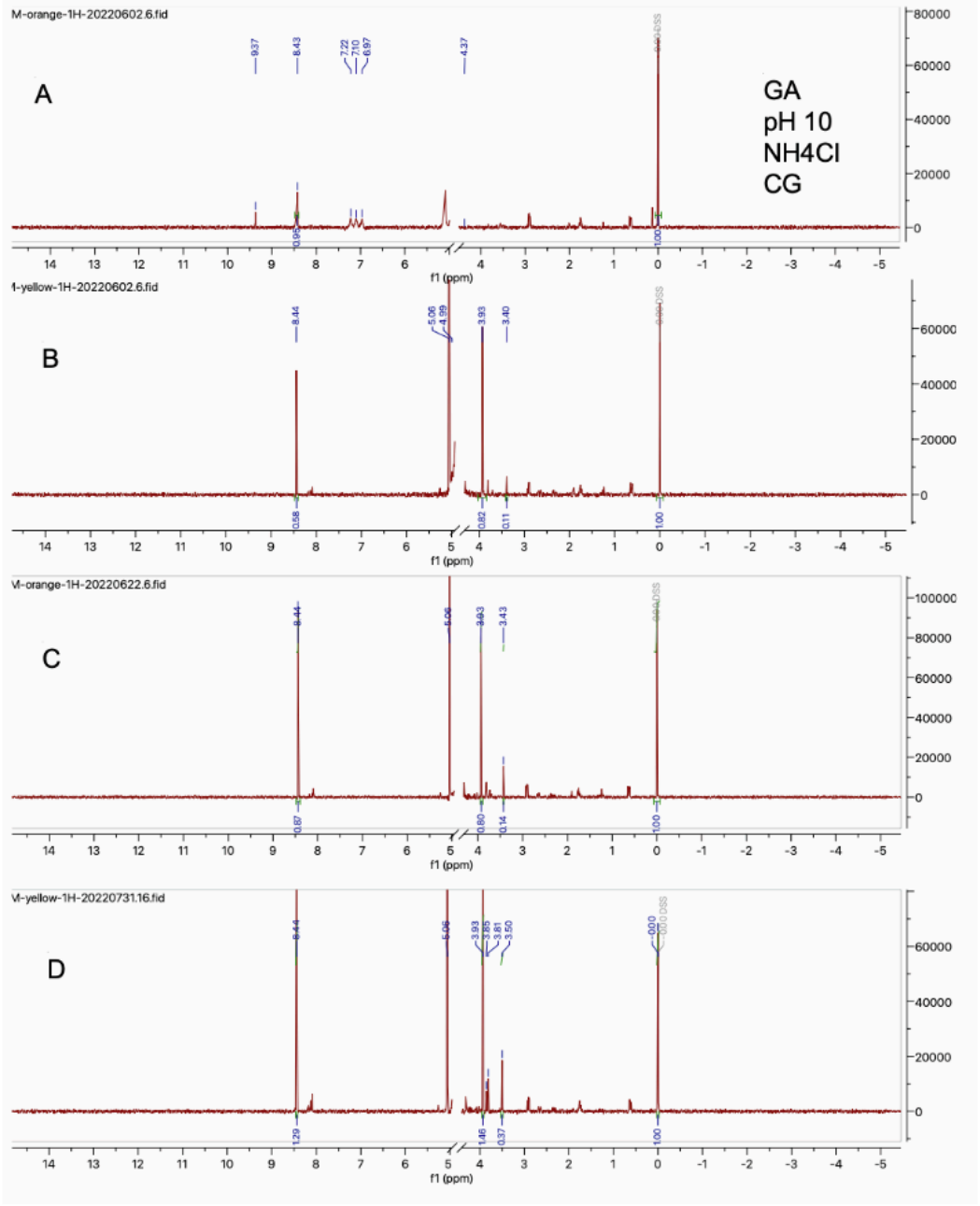


Figure A.45: NMR spectra; glyoxylate, ammonium chloride, and chemical garden reaction under heated conditions, pH 10. A: t = 0 weeks, B: t = 1 week, C: t = 2 weeks, D: t = 3 weeks.

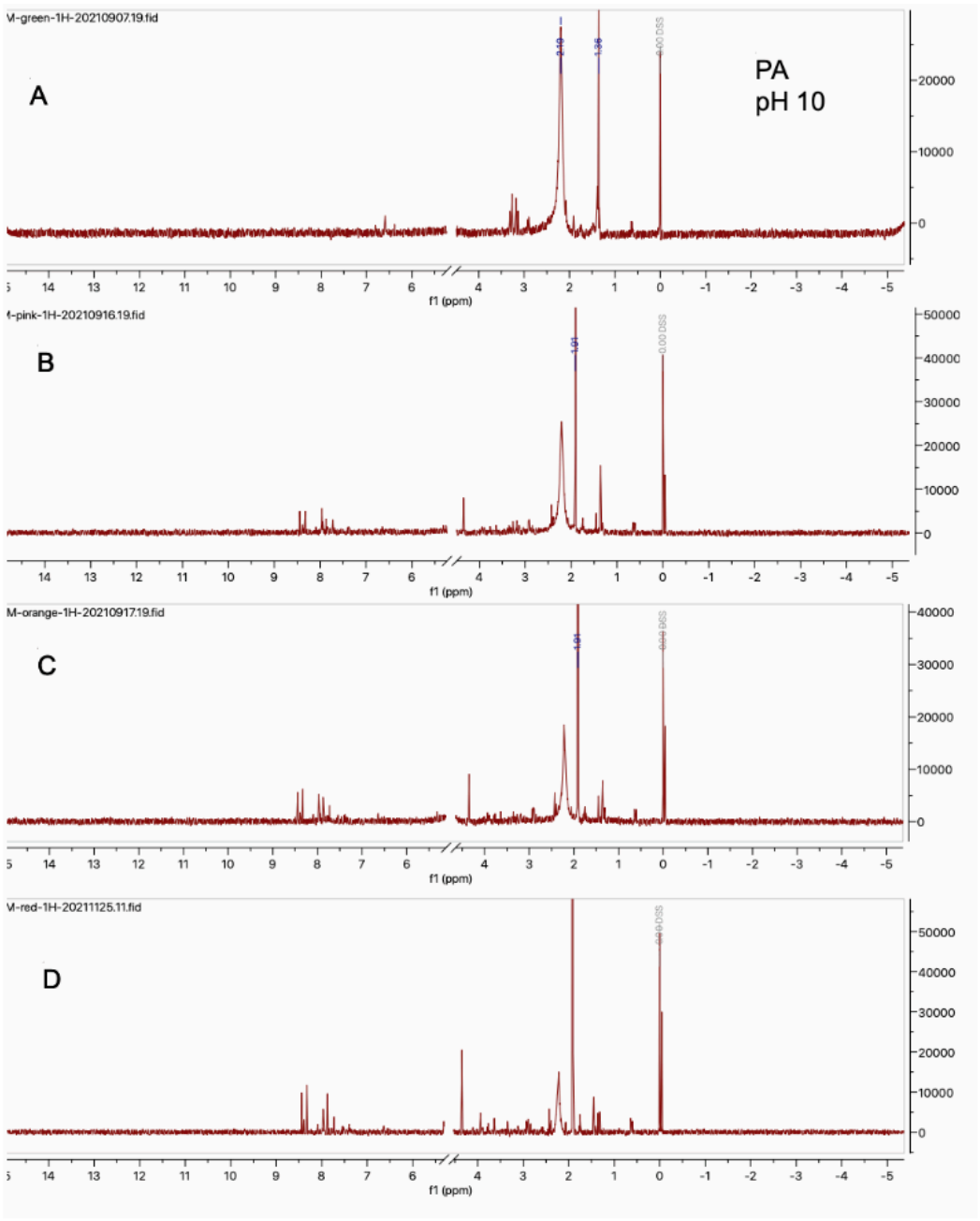


Figure A.46: Control NMR spectra; pyruvate reaction under heated conditions, pH 10. A: t = 0 weeks, B: t = 1 week, C: t = 2 weeks, D: t = 3 weeks.

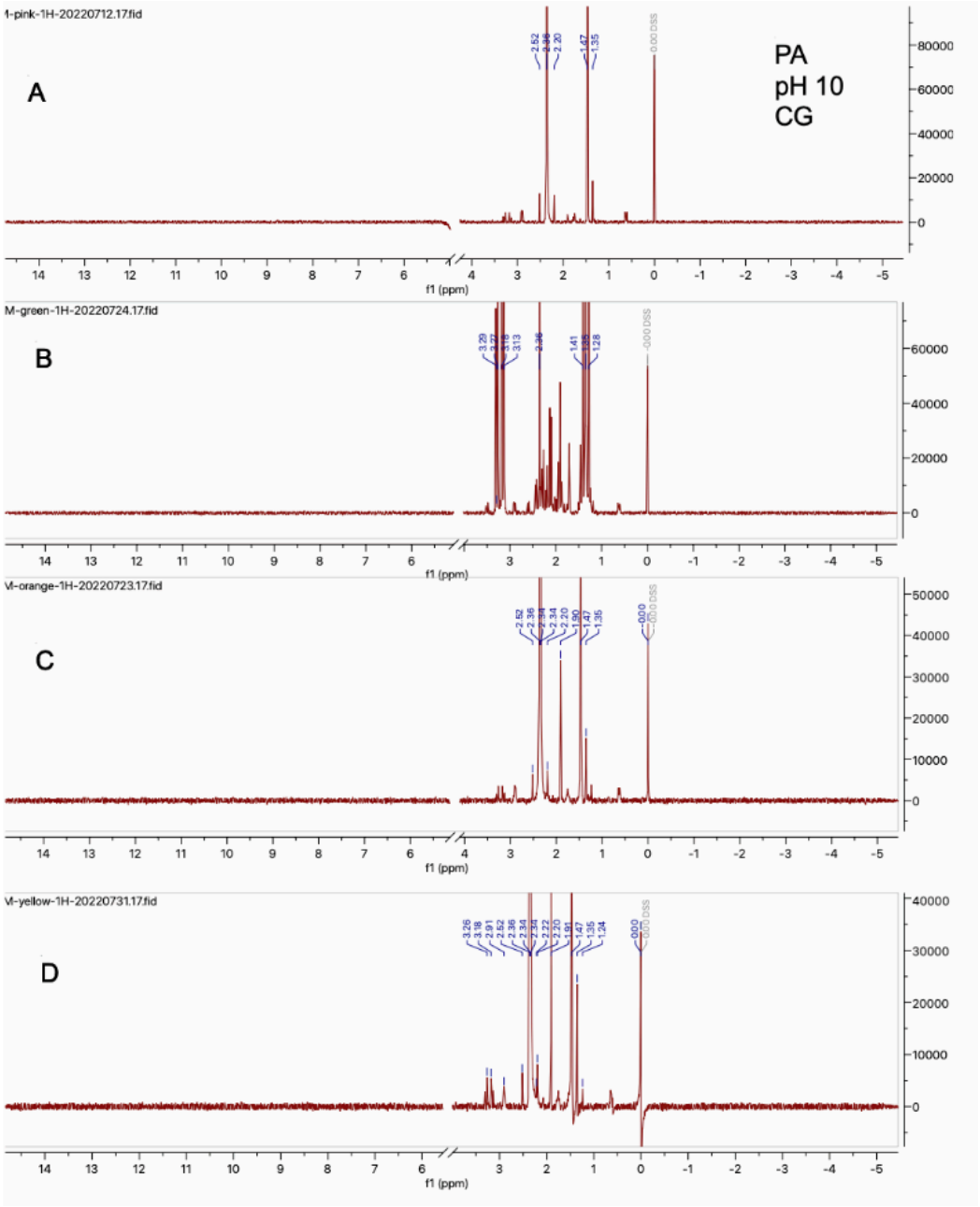


Figure A.47: NMR spectra; pyruvate and chemical garden reaction under heated conditions, pH 10. A: t = 0 weeks, B: t = 1 week, C: t = 2 weeks, D: t = 3 weeks.

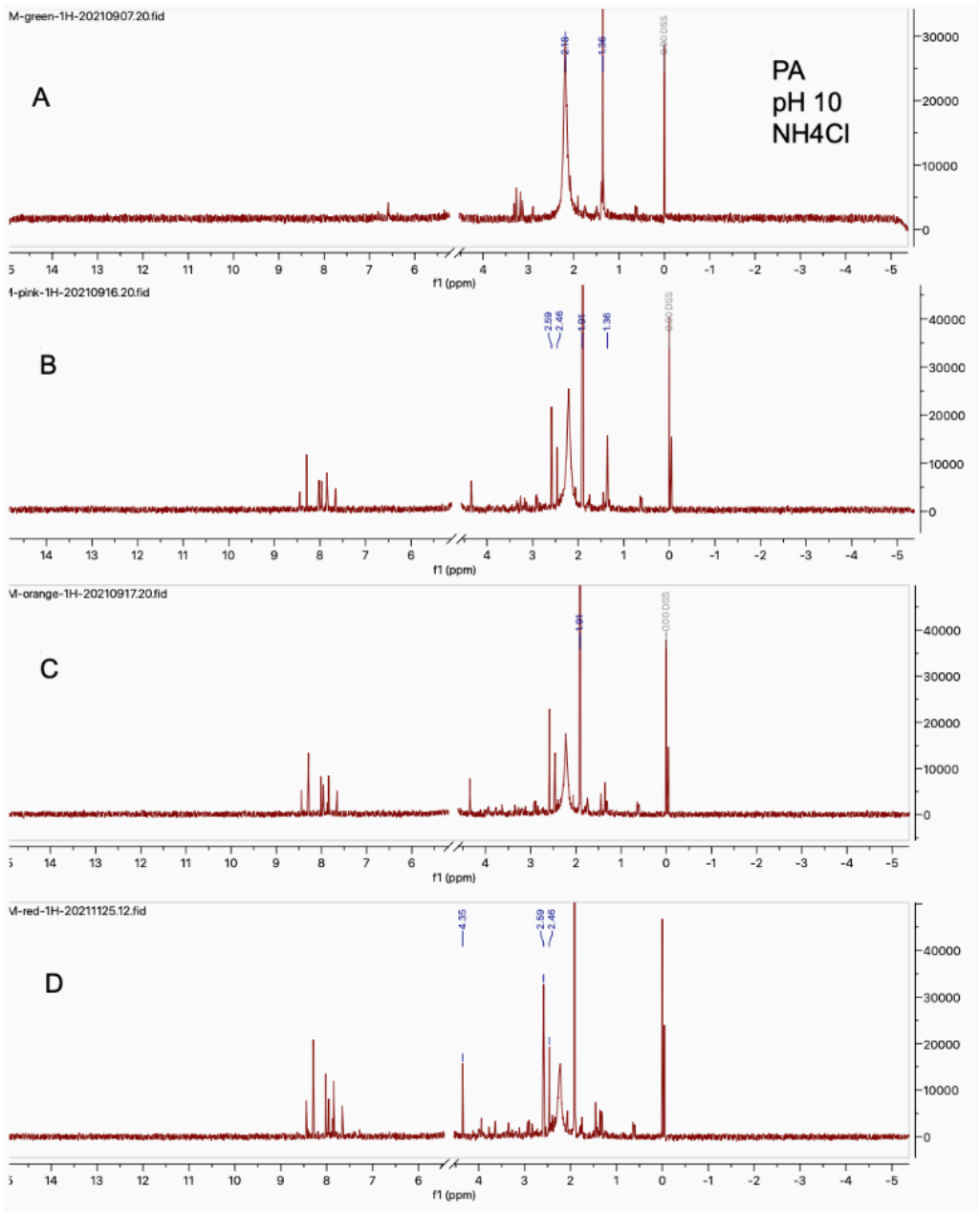


Figure A.48: Control NMR spectra; pyruvate and ammonium chloride reaction under heated conditions, pH 10. A: t = 0 weeks, B: t = 1 week, C: t = 2 weeks, D: t = 3 weeks.

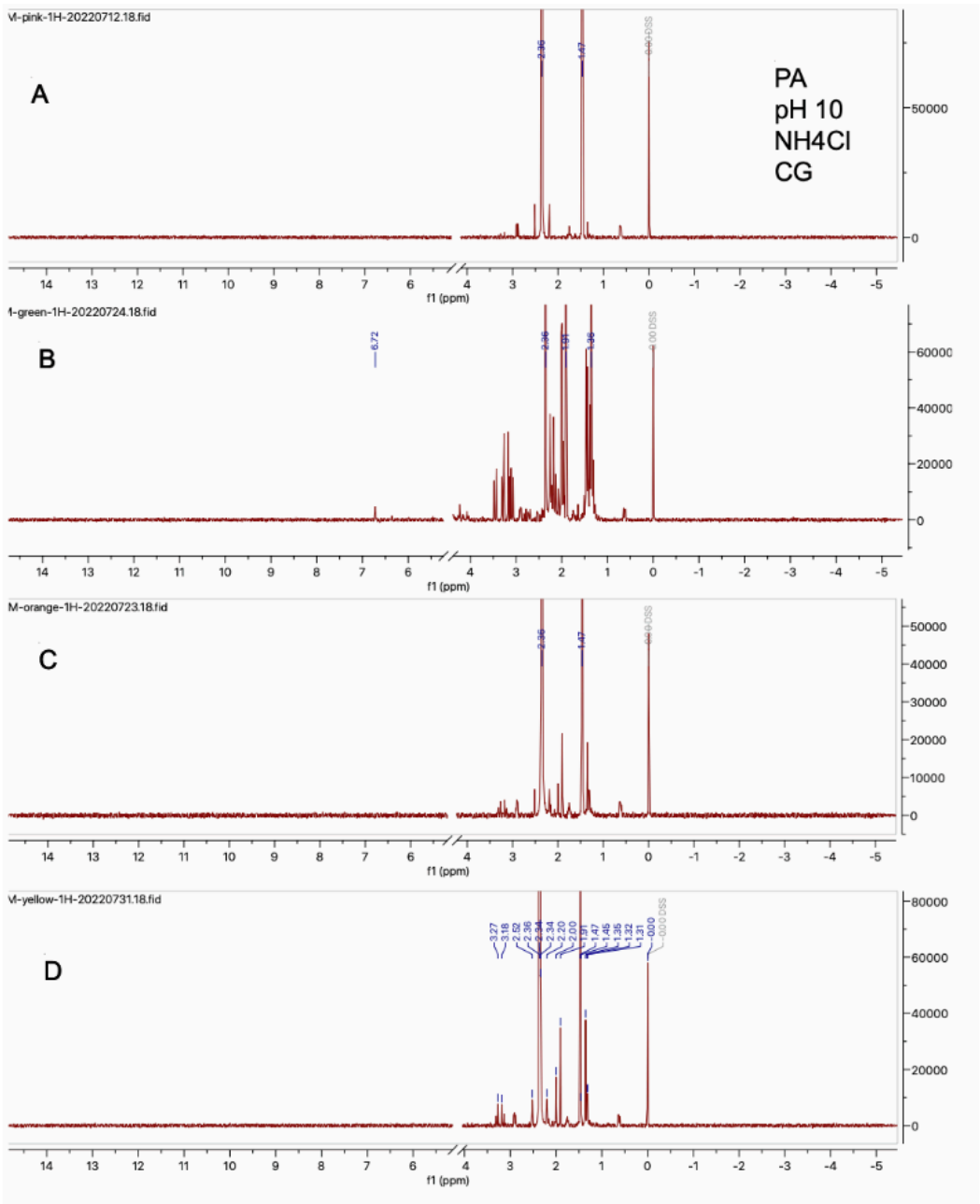


Figure A.49: NMR spectra; pyruvate, ammonium chloride, and chemical garden reaction under heated conditions, pH 10. A: t = 0 weeks, B: t = 1 week, C: t = 2 weeks, D: t = 3 weeks.

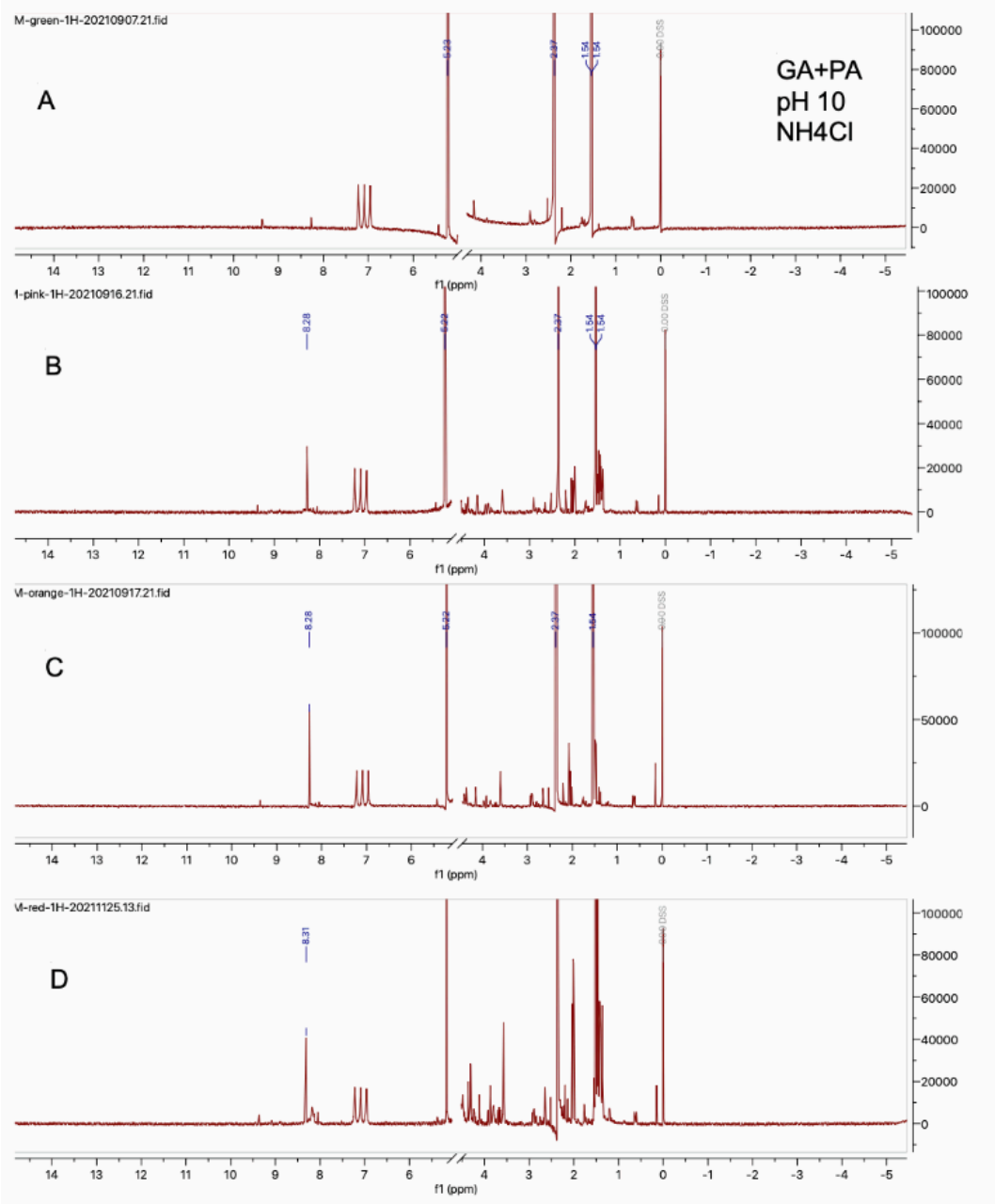


Figure A.50: Control NMR spectra; pyruvate, glyoxylate, and ammonium chloride reaction under heated conditions, pH 10. A: t = 0 weeks, B: t = 1 week, C: t = 2 weeks, D: t = 3 weeks.

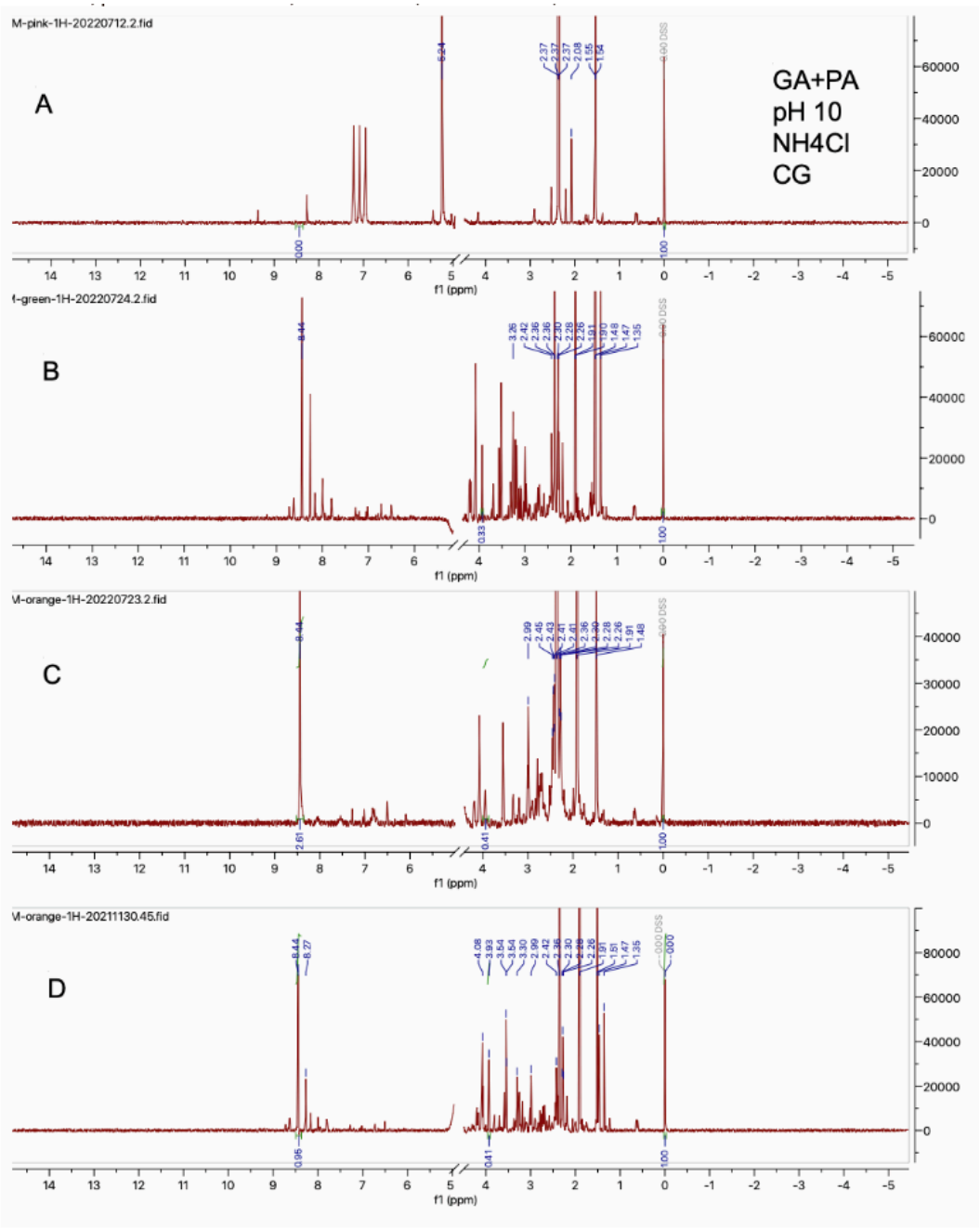


Figure A.51: NMR spectra; pyruvate, glyoxylate, ammonium chloride, and chemical garden reaction under heated conditions, pH 10. A: t = 0 weeks, B: t = 1 week, C: t = 2 weeks, D: t = 3 weeks.

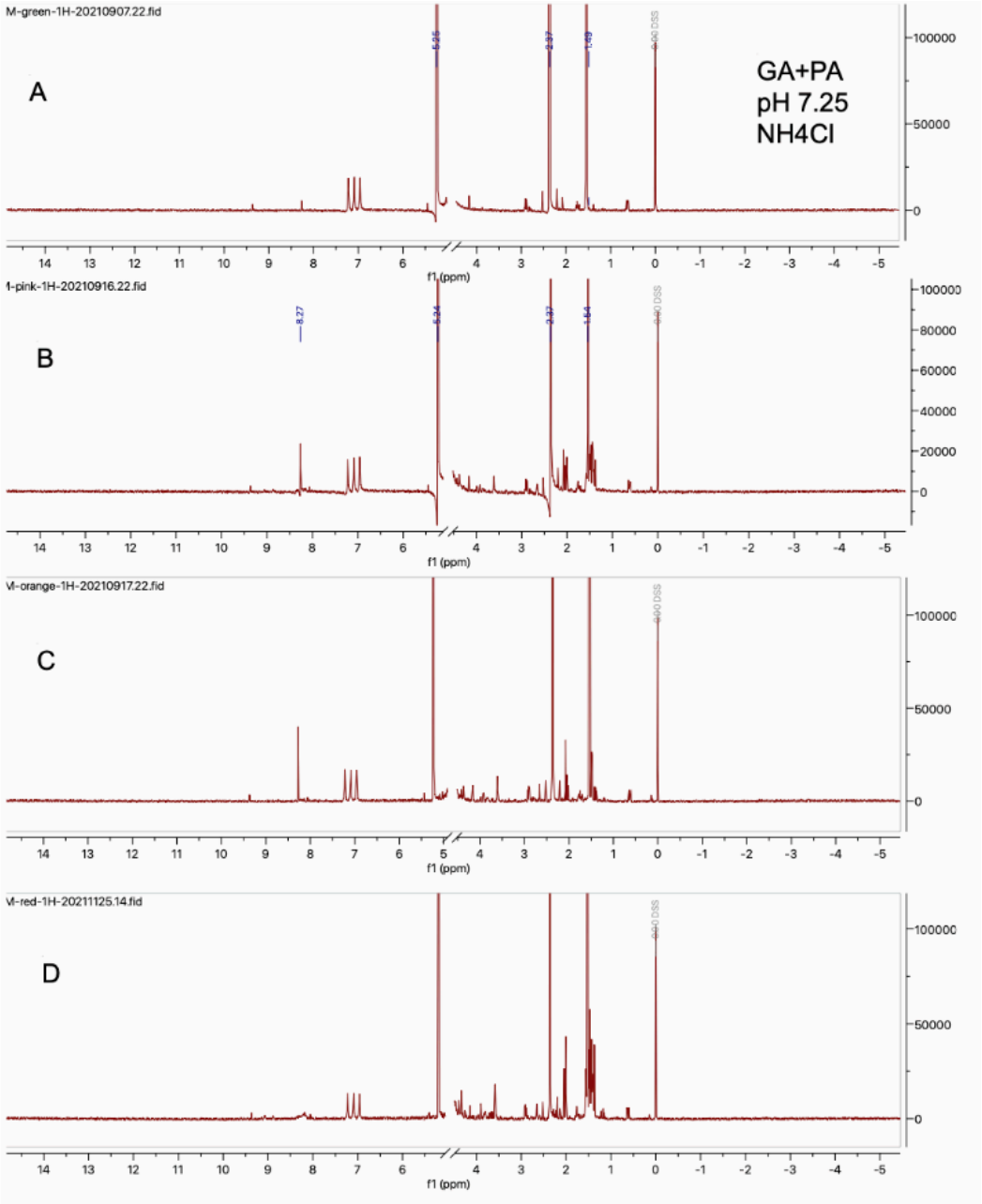


Figure A.52: Control NMR spectra; pyruvate, glyoxylate, and ammonium chloride reaction under heated conditions, pH 7.25. A: t = 0 weeks, B: t = 1 week, C: t = 2 weeks, D: t = 3 weeks.

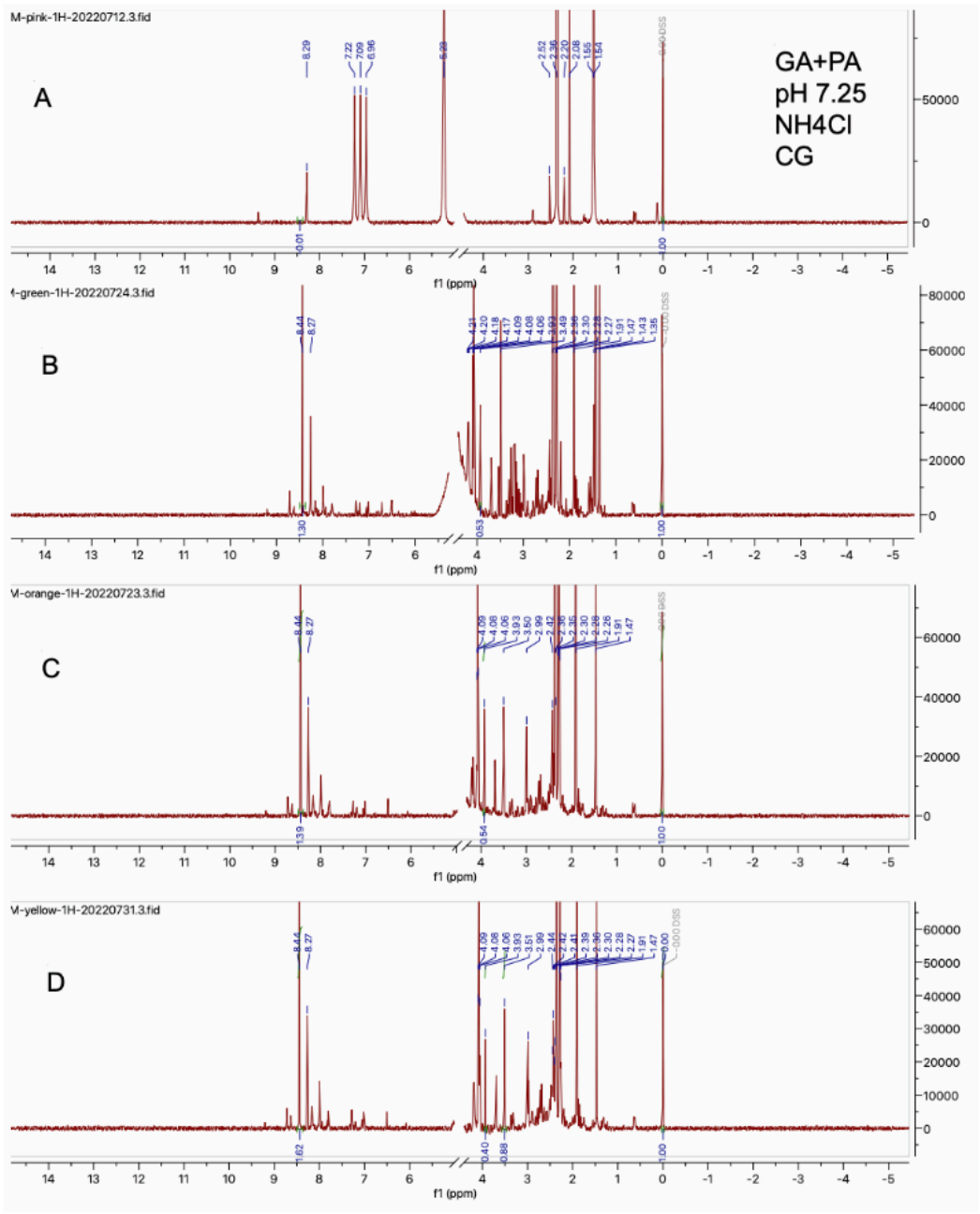


Figure A.53: NMR spectra; pyruvate, glyoxylate, ammonium chloride, and chemical garden reaction under heated conditions, pH 7.25. A: t = 0 weeks, B: t = 1 week, C: t = 2 weeks, D: t = 3 weeks.

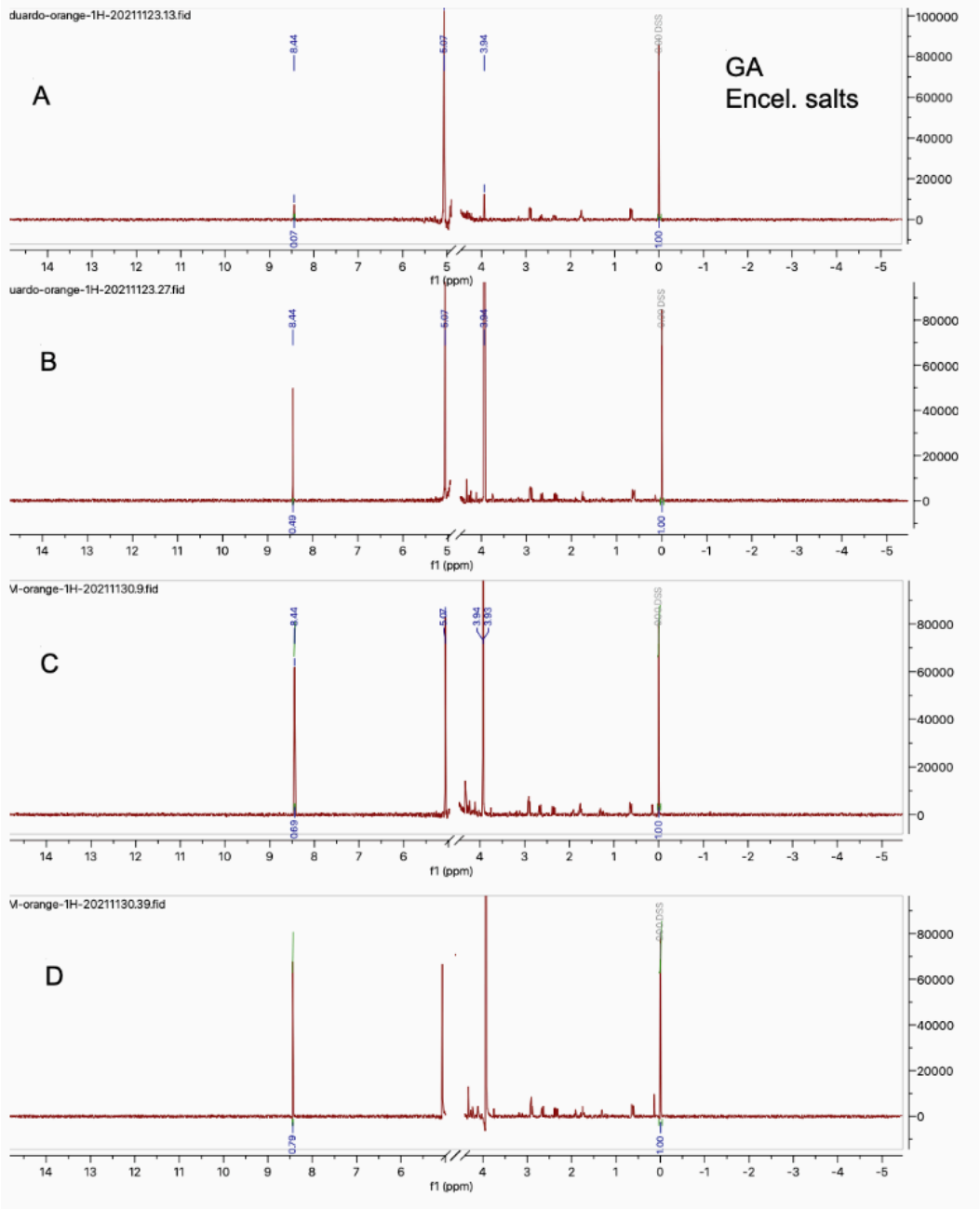


Figure A.54: Control NMR spectra; glyoxylate, sodium chloride, and sodium carbonate reaction under heated conditions. A: t = 0 weeks, B: t = 1 week, C: t = 2 weeks, D: t = 3 weeks.

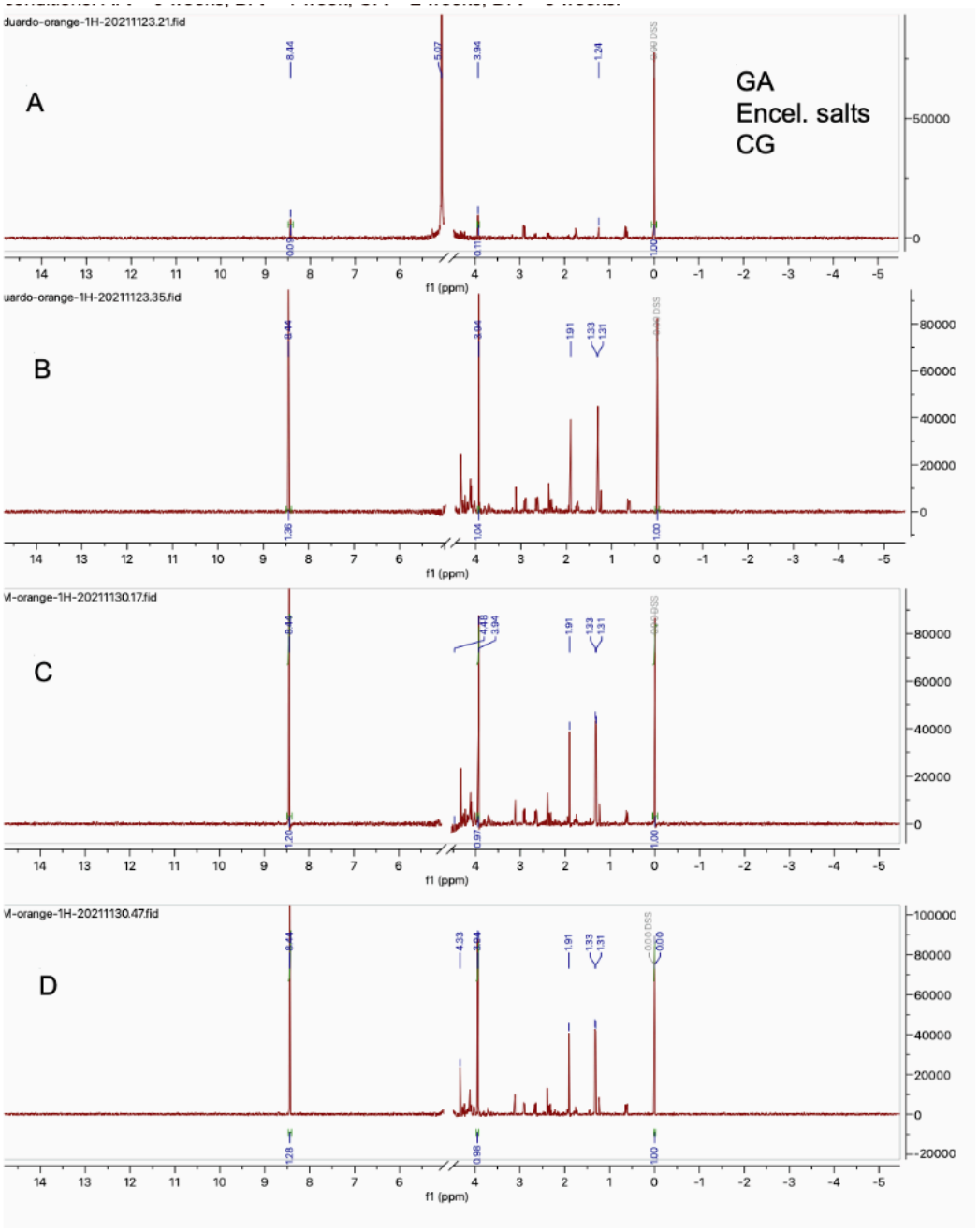


Figure A.55: NMR spectra; glyoxylate, sodium chloride, sodium carbonate, and chemical garden reaction under heated conditions. A: t = 0 weeks, B: t = 1 week, C: t = 2 weeks, D: t = 3 weeks.

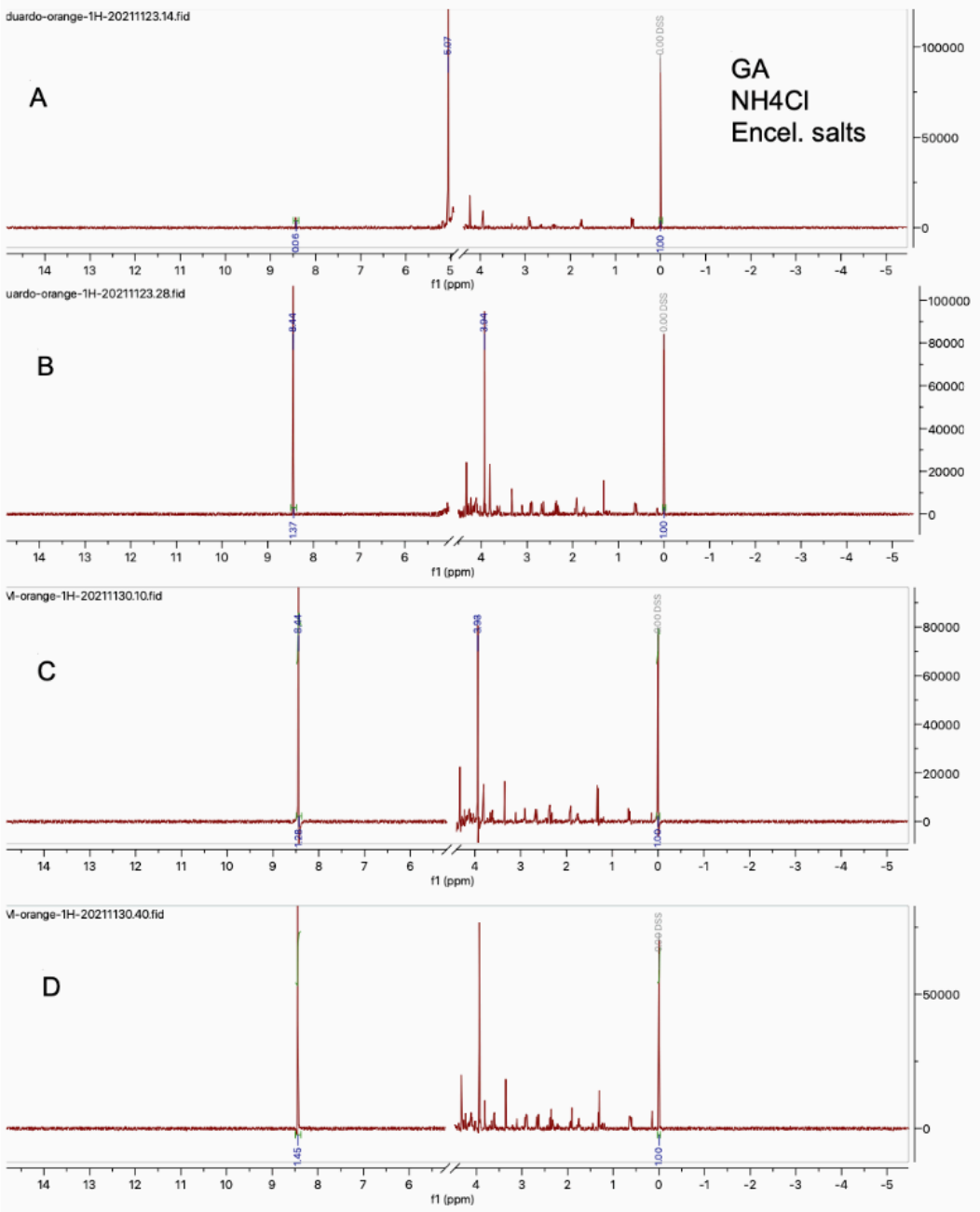


Figure A.56: Control NMR spectra; glyoxylate, sodium chloride, sodium carbonate, and ammonium chloride reaction under heated conditions. A: t = 0 weeks, B: t = 1 week, C: t = 2 weeks, D: t = 3 weeks.

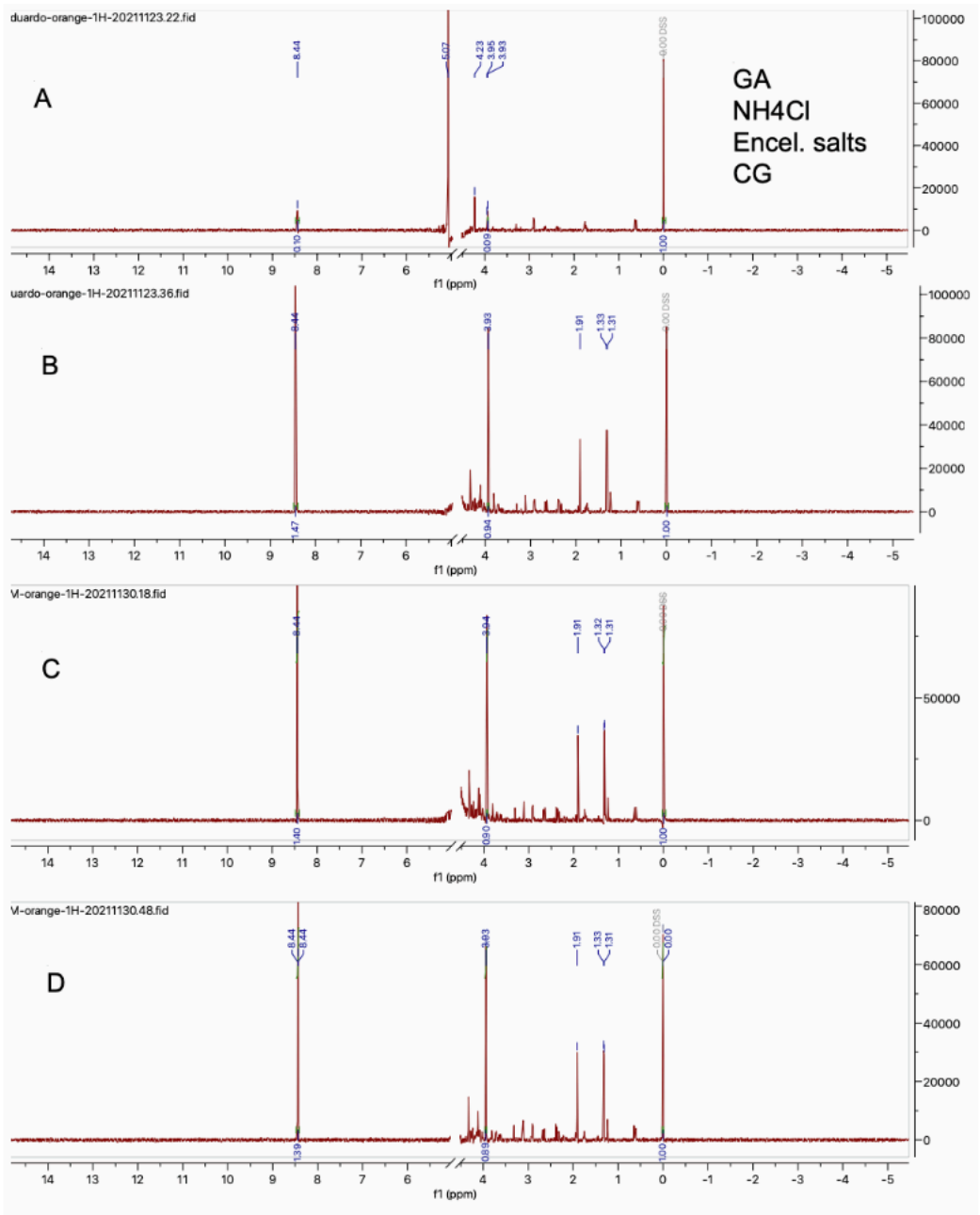


Figure A.57: NMR spectra; glyoxylate, sodium chloride, sodium carbonate, ammonium chloride, and chemical garden reaction under heated conditions. A: t = 0 weeks, B: t = 1 week, C: t = 2 weeks, D: t = 3 weeks.

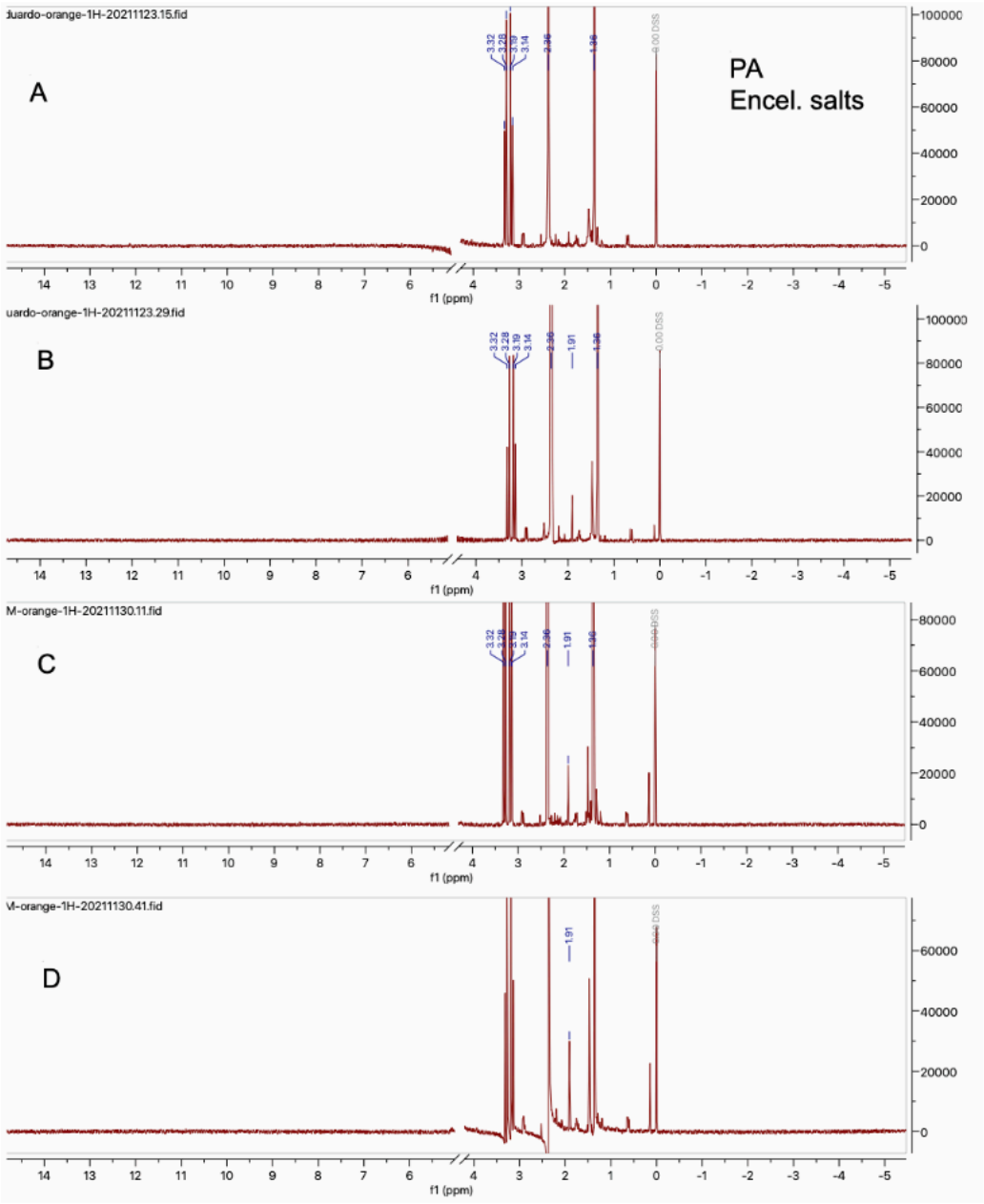


Figure A.58: Control NMR spectra; pyruvate, sodium chloride, and sodium carbonate reaction under heated conditions. A: t = 0 weeks, B: t = 1 week, C: t = 2 weeks, D: t = 3 weeks.

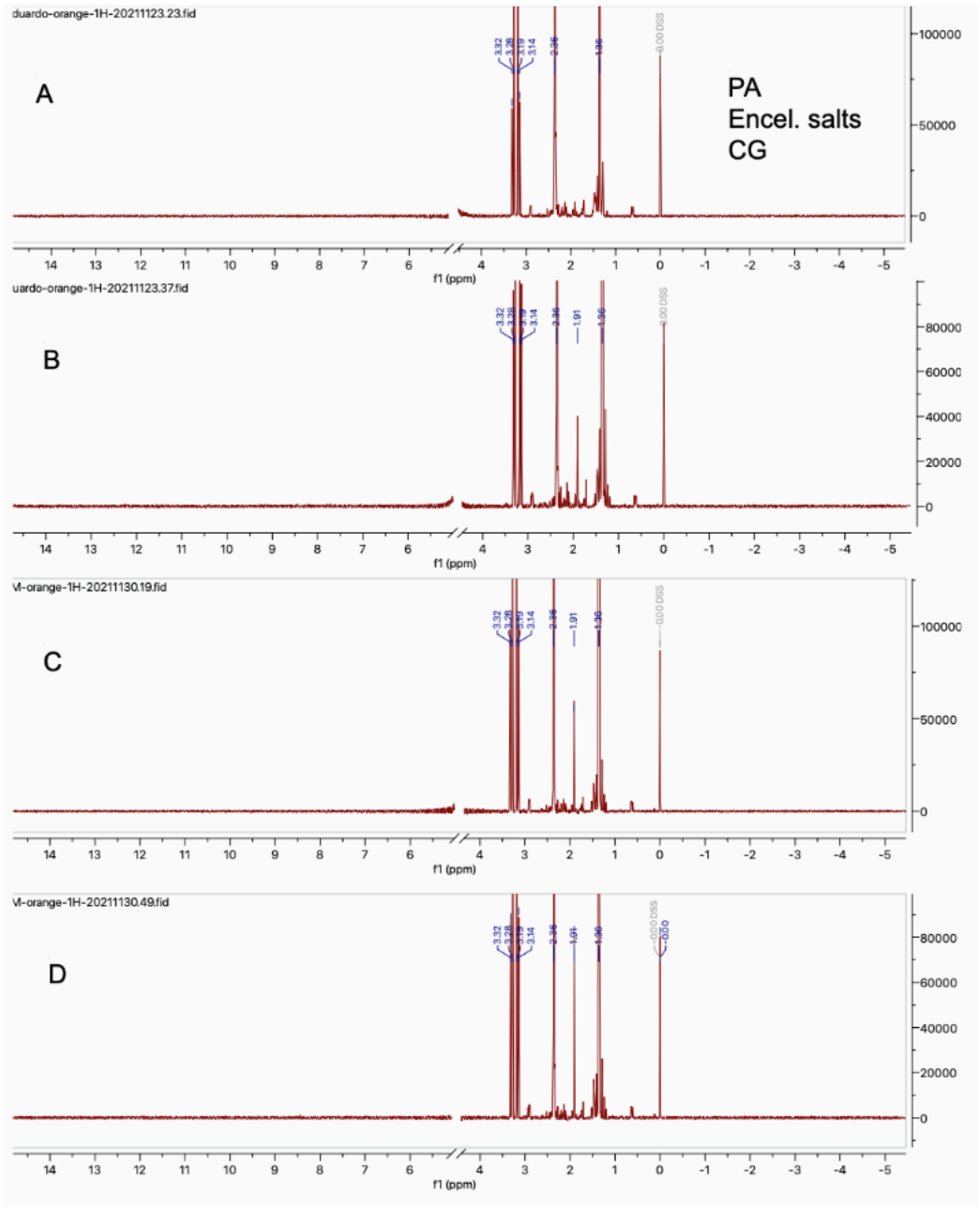


Figure A.59: NMR spectra; pyruvate, sodium chloride, sodium carbonate, and chemical garden reaction under heated conditions. A: t = 0 weeks, B: t = 1 week, C: t = 2 weeks, D: t = 3 weeks.

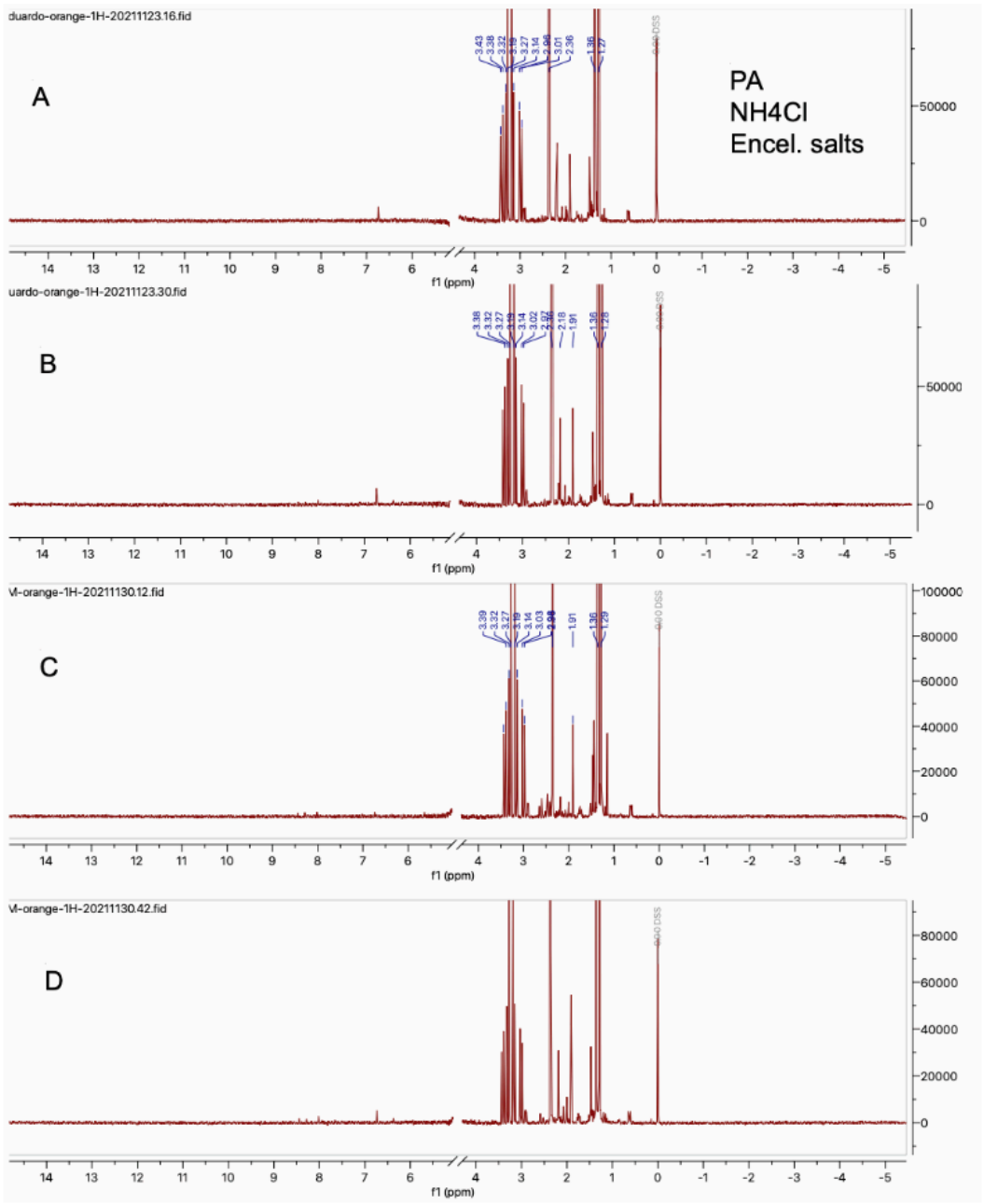


Figure A.60: Control NMR spectra, pyruvate, sodium chloride, sodium carbonate, and ammonium chloride reaction under heated conditions. A: t = 0 weeks, B: t = 1 week, C: t = 2 weeks, D: t = 3 weeks.

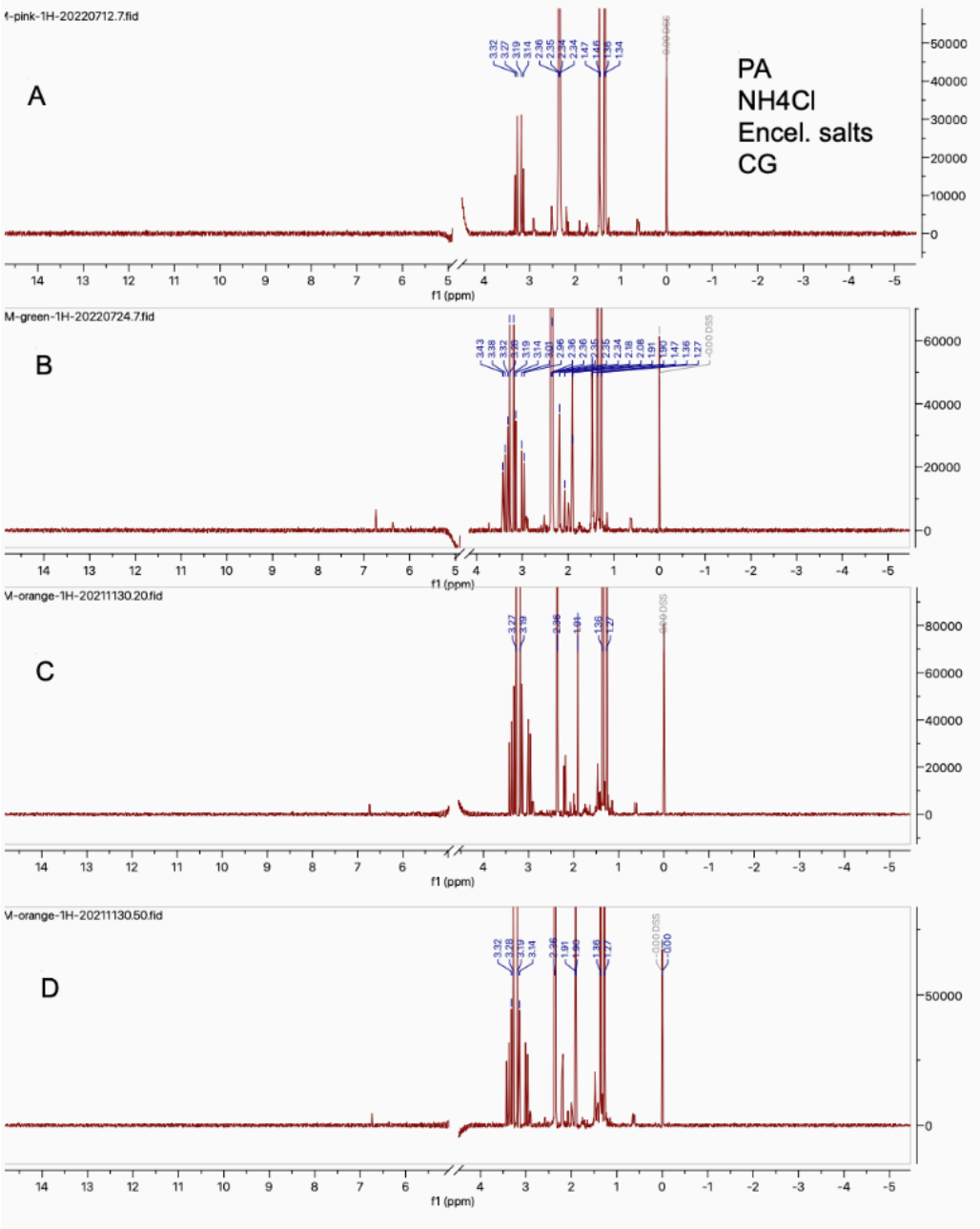


Figure A.61: NMR spectra; pyruvate, sodium chloride, sodium carbonate, ammonium chloride, and chemical garden reaction under heated conditions. A: t = 0 weeks, B: t = 1 week, C: t = 2 weeks, D: t = 3 weeks.

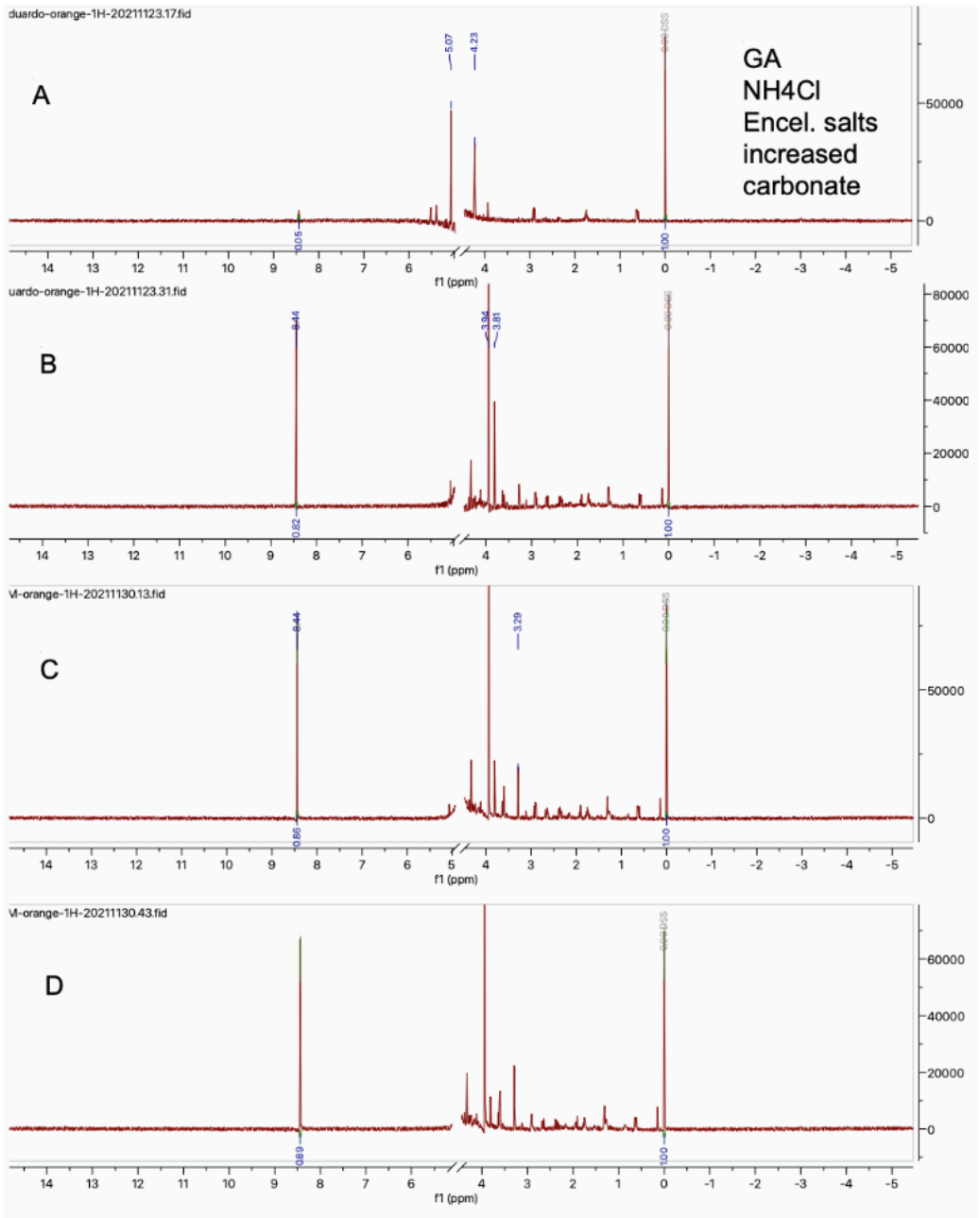


Figure A.62: Control NMR spectra; glyoxylate, sodium chloride, increased sodium carbonate, and ammonium chloride reaction under heated conditions. A: t = 0 weeks, B: t = 1 week, C: t = 2 weeks, D: t = 3 weeks.

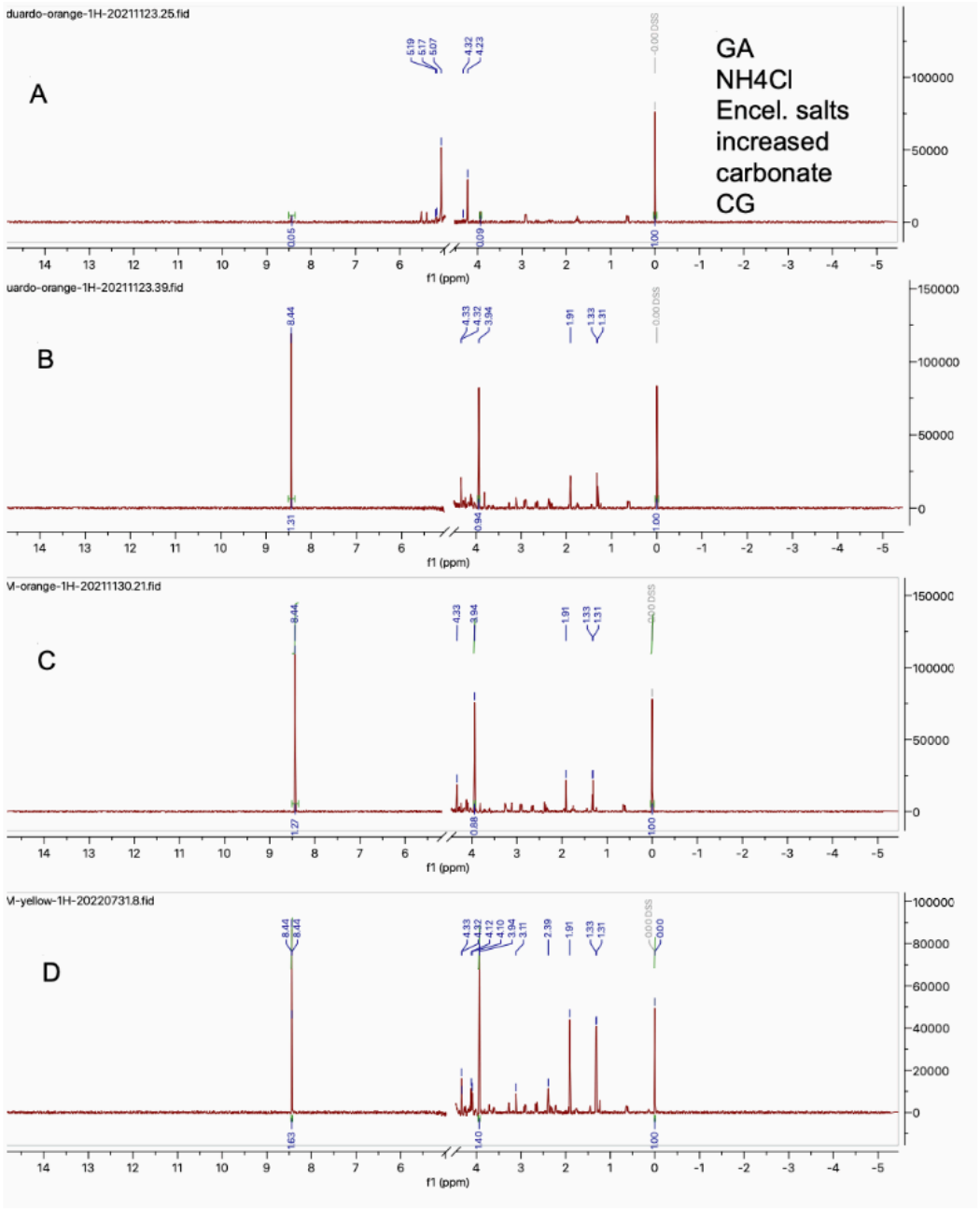


Figure A.63: NMR spectra; glyoxylate, sodium chloride, increased sodium carbonate, ammonium chloride, and chemical garden reaction under heated conditions. A: t = 0 weeks, B: t = 1 week, C: t = 2 weeks, D: t = 3 weeks.

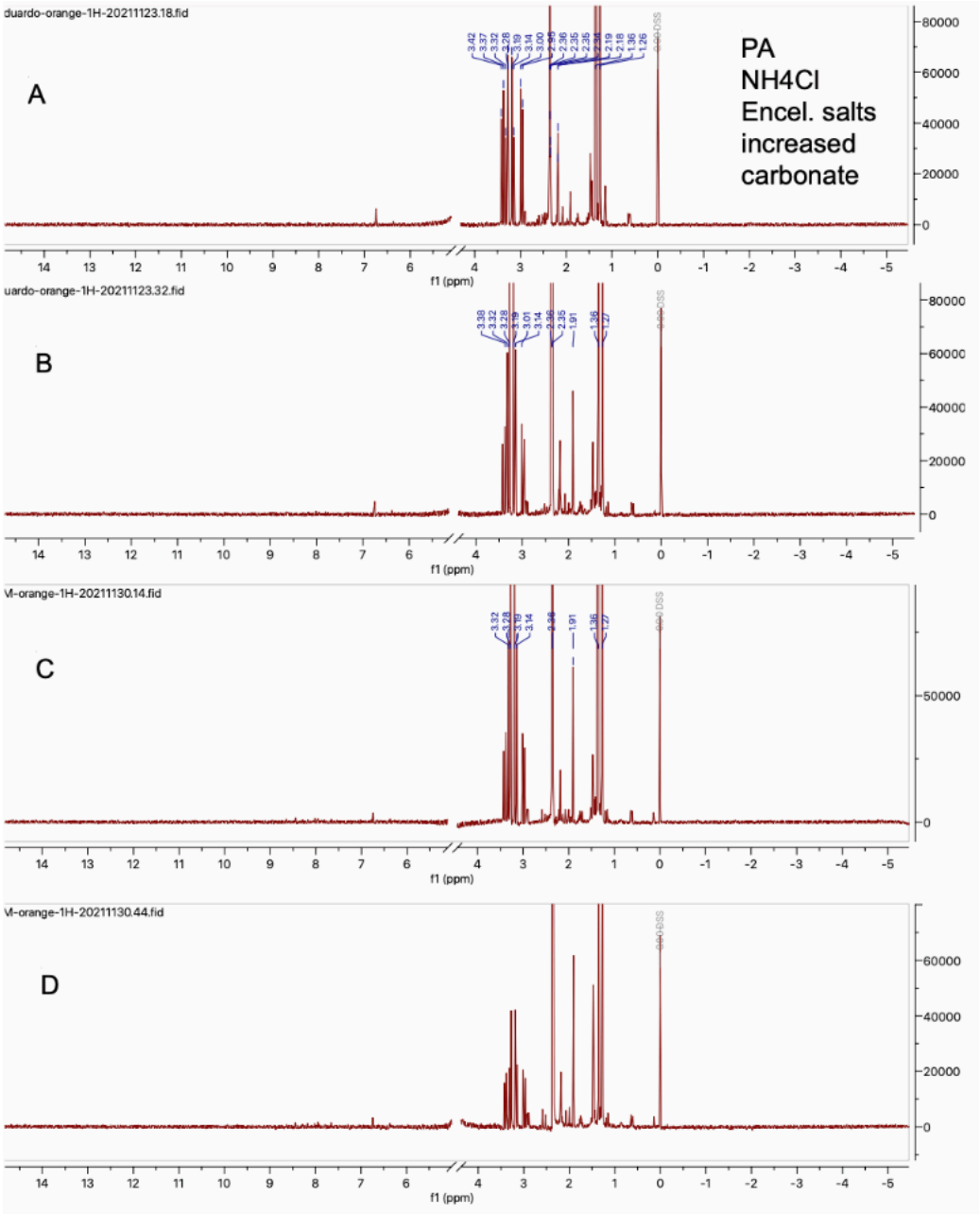


Figure A.64: Control NMR spectra; pyruvate, sodium chloride, increased sodium carbonate, and ammonium chloride reaction under heated conditions. A: t = 0 weeks, B: t = 1 week, C: t = 2 weeks, D: t = 3 weeks.

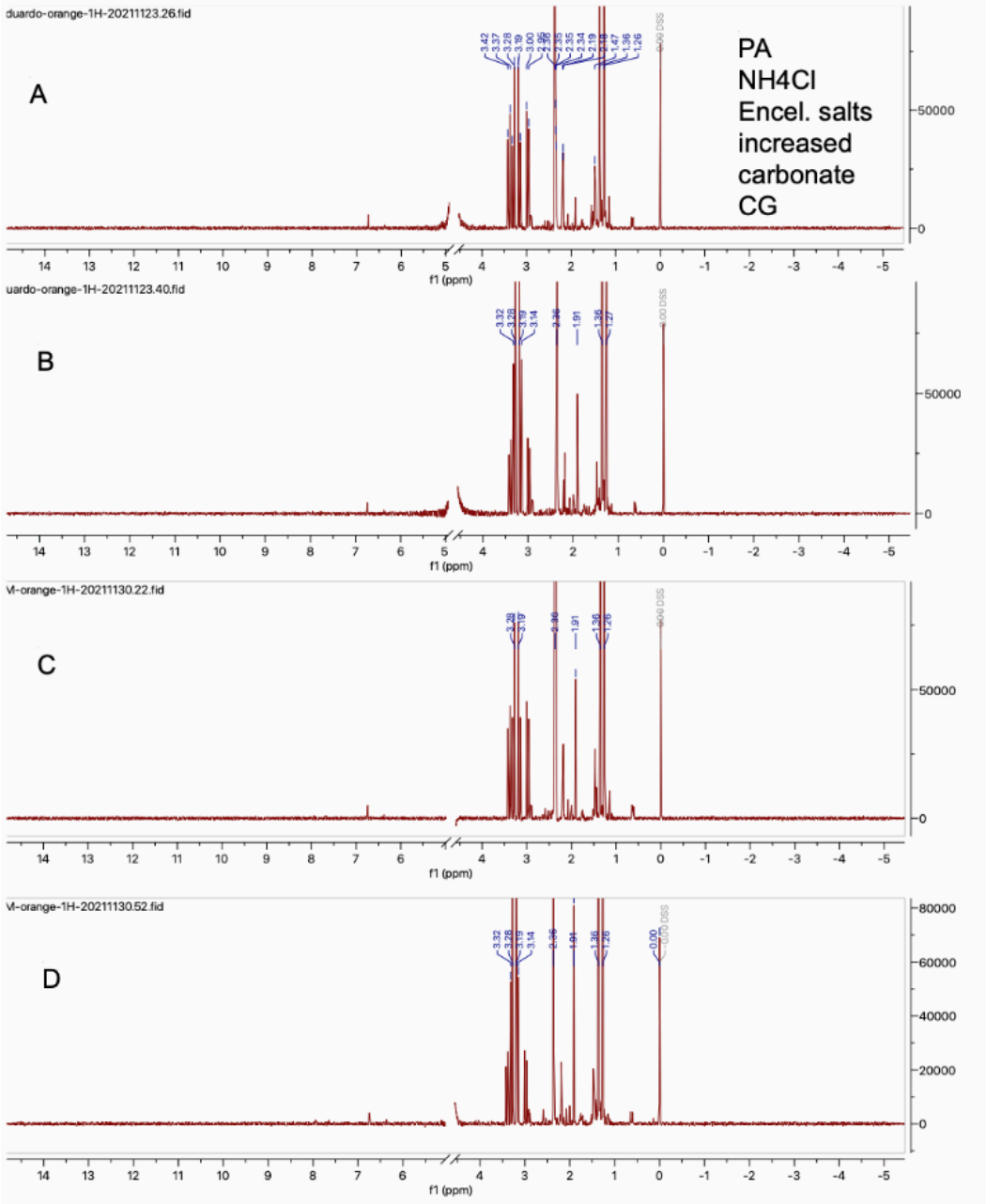


Figure A.65: NMR spectra; pyruvate, sodium chloride, increased sodium carbonate, ammonium chloride, and chemical garden reaction under heated conditions. A: t = 0 weeks, B: t = 1 week, C: t = 2 weeks, D: t = 3 weeks.

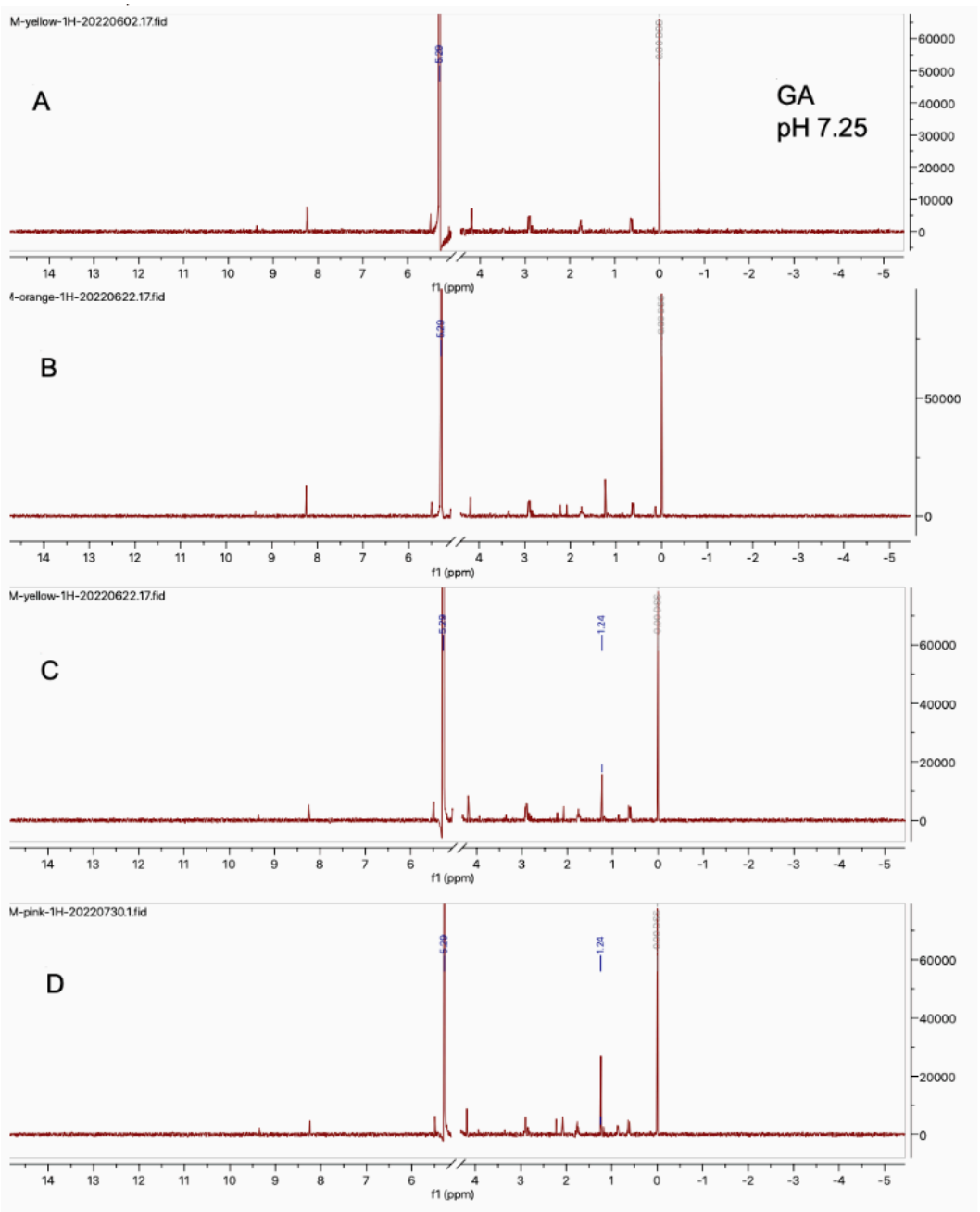


Figure A.66: Control NMR spectra; glyoxylate reaction under anaerobic conditions, pH 7.25. A: t = 0 weeks, B: t = 1 week, C: t = 2 weeks, D: t = 3 weeks.

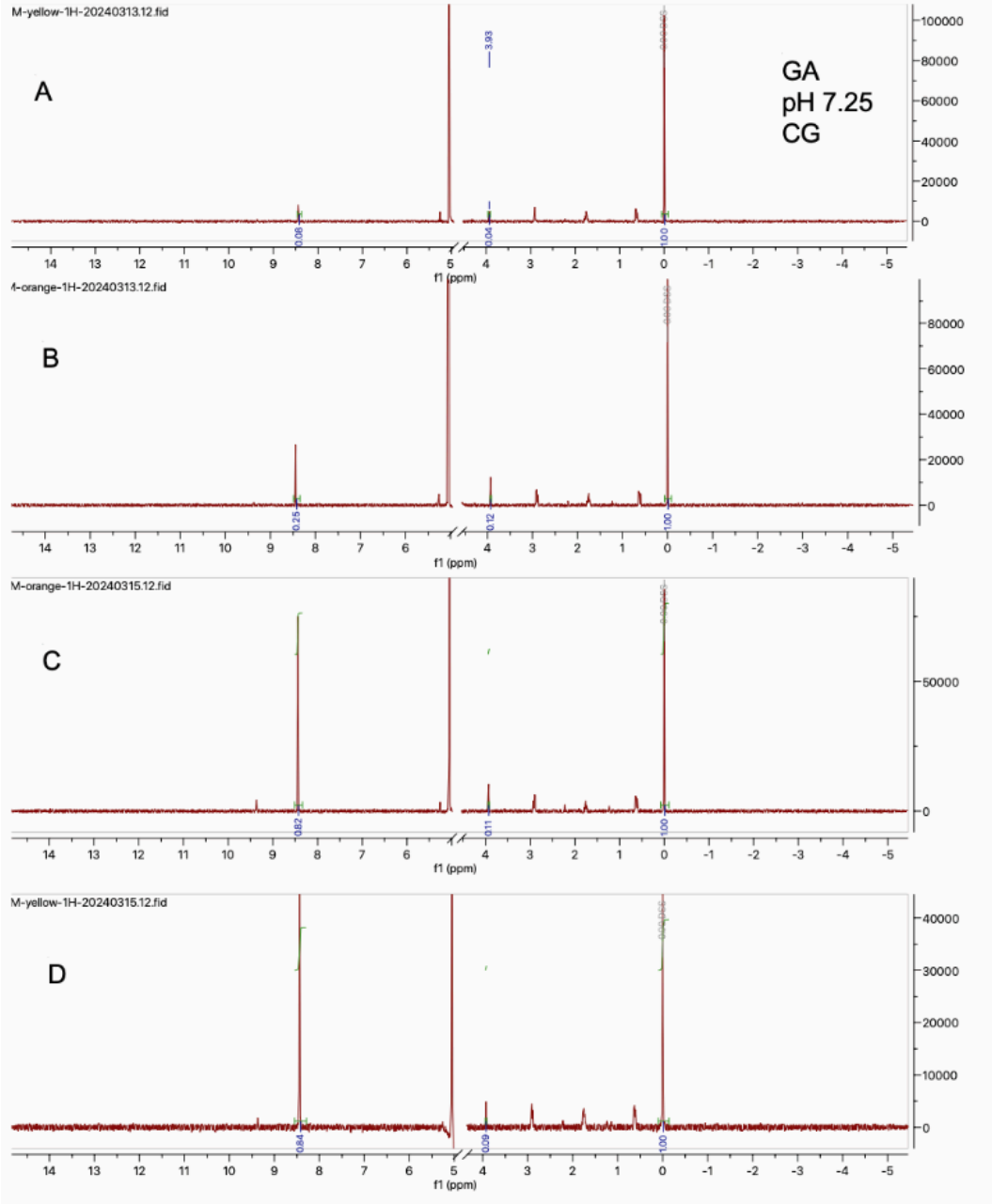


Figure A.67: NMR spectra; glyoxylate and chemical garden reaction under anaerobic conditions, pH 7.25. A: t = 0 weeks, B: t = 1 week, C: t = 2 weeks, D: t = 3 weeks.

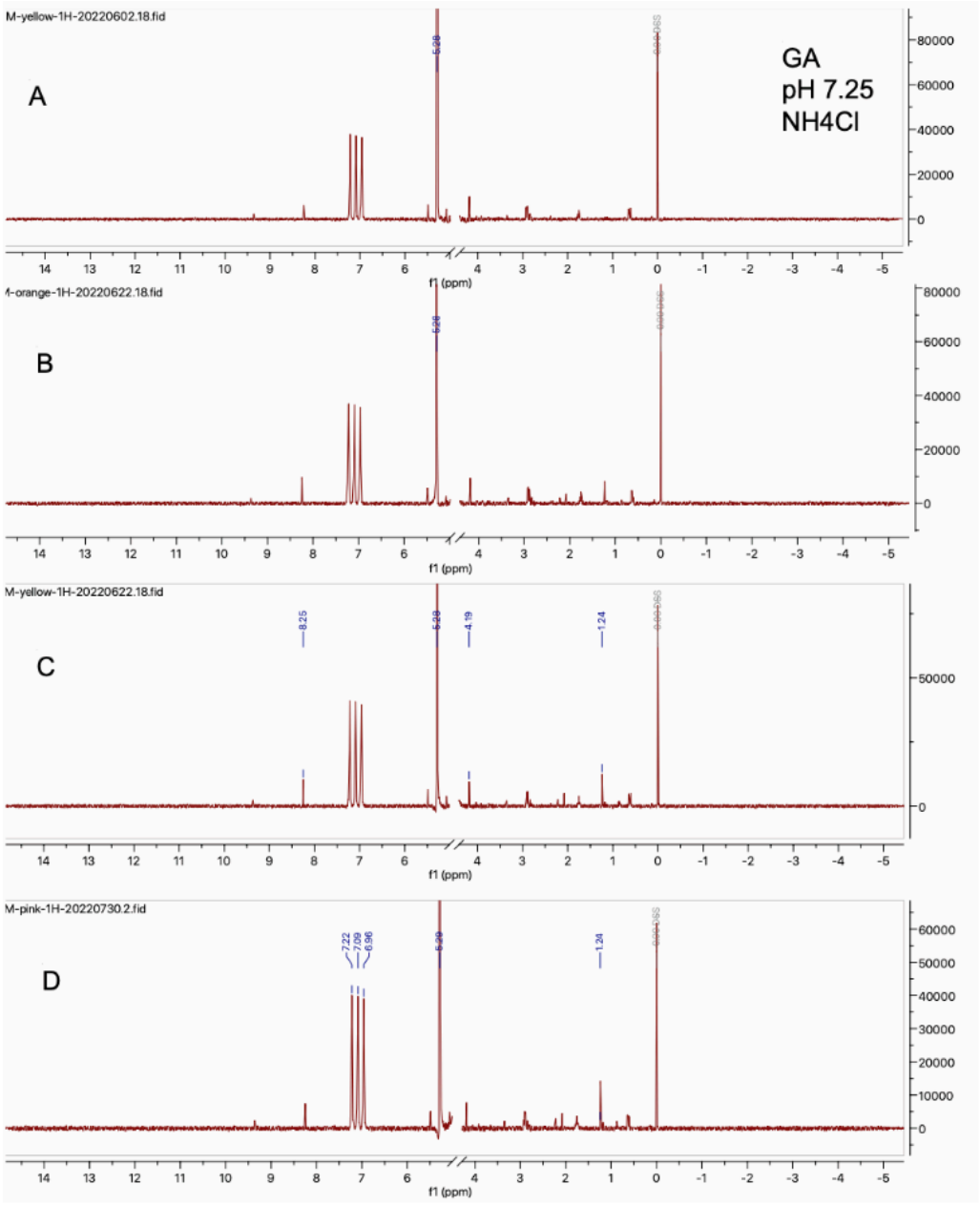


Figure A.68: Control NMR spectra; glyoxylate and ammonium chloride reaction under anaerobic conditions, pH 7.25. A: t = 0 weeks, B: t = 1 week, C: t = 2 weeks, D: t = 3 weeks.

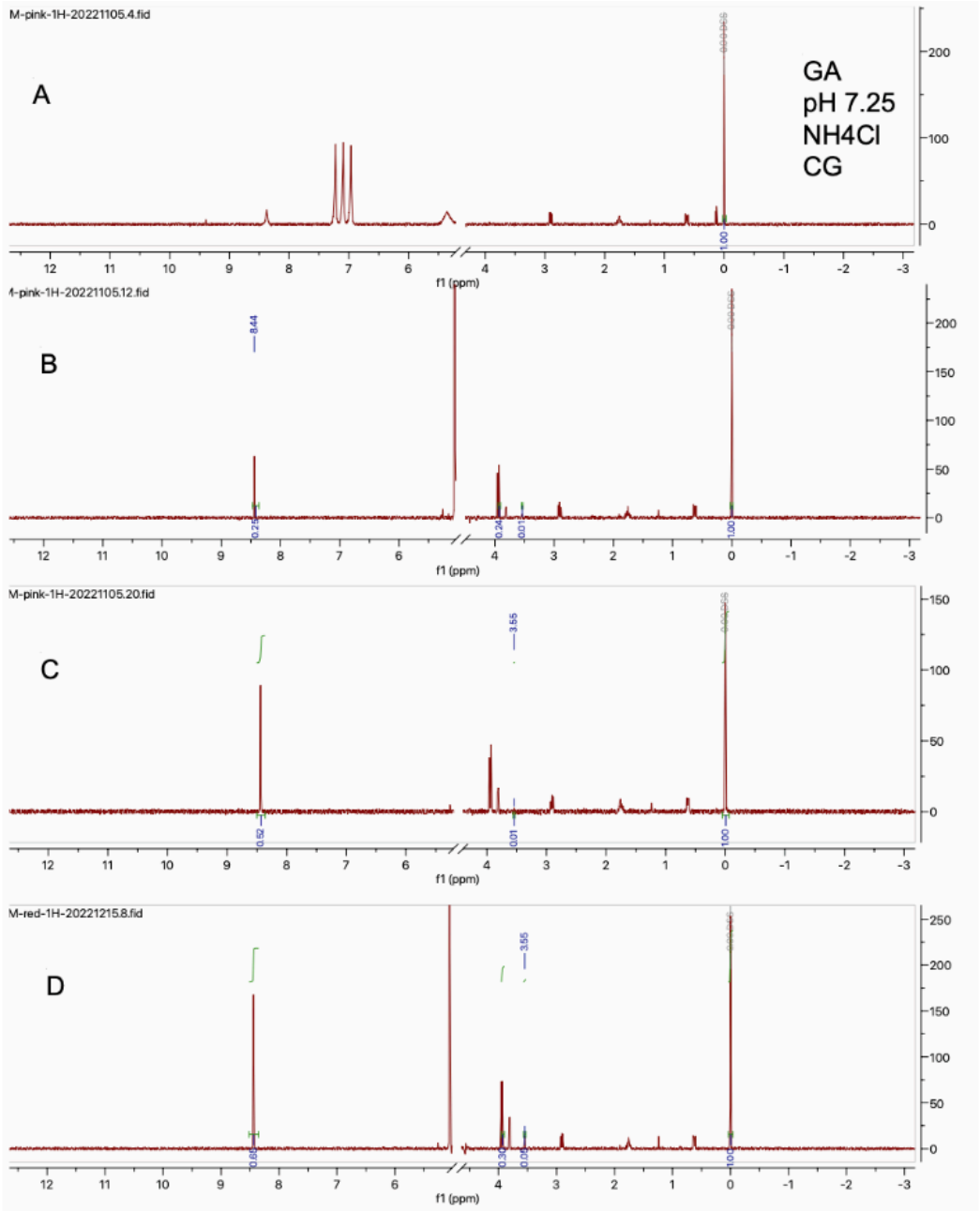


Figure A.69: NMR spectra; glyoxylate, ammonium chloride, and chemical garden reaction under anaerobic conditions, pH 7.25. A: t = 0 weeks, B: t = 1 week, C: t = 2 weeks, D: t = 3 weeks.

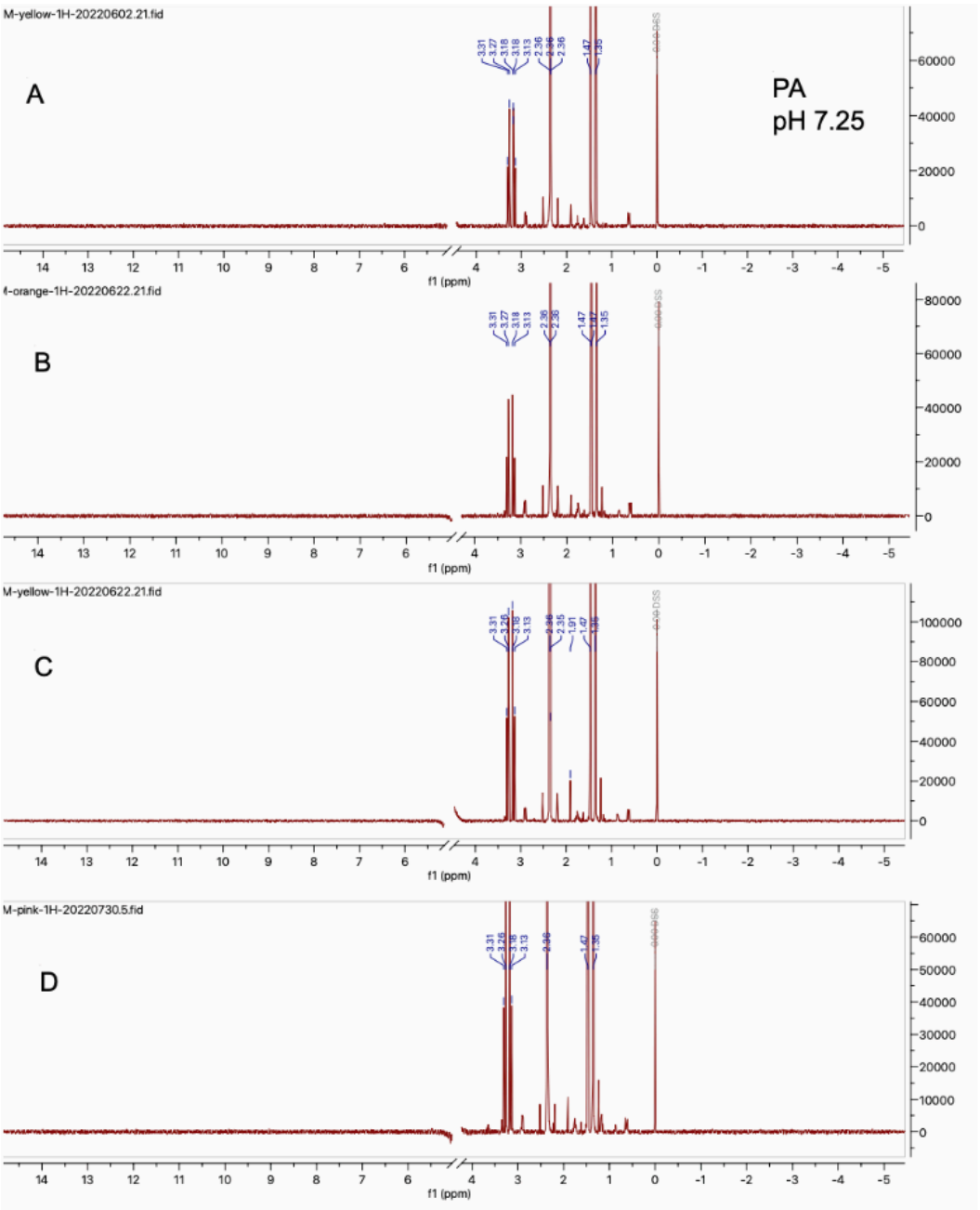


Figure A.70: Control NMR spectra; pyruvate reaction under anaerobic conditions, pH 7.25. A: t = 0 weeks, B: t = 1 week, C: t = 2 weeks, D: t = 3 weeks.

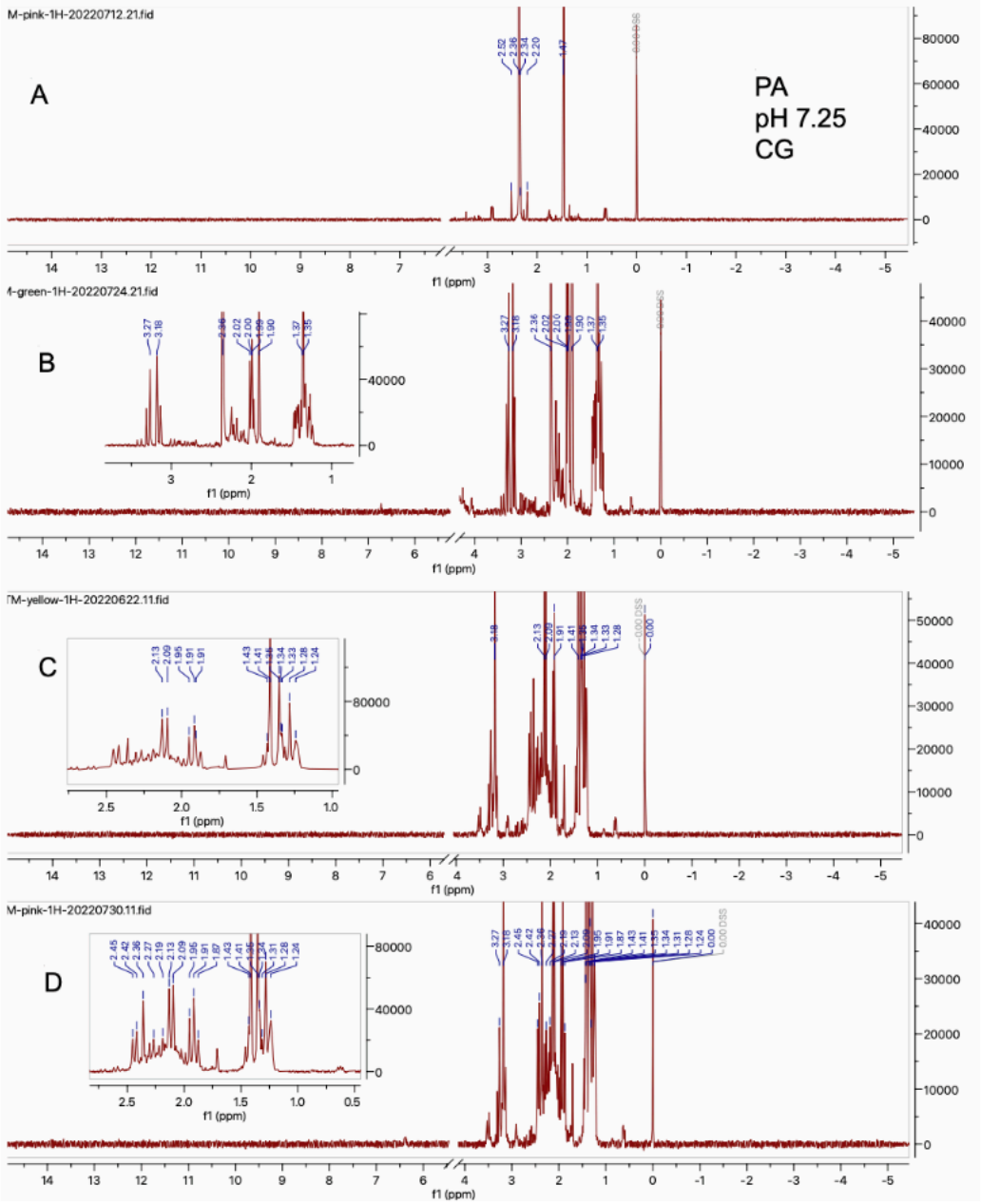


Figure A.71: NMR spectra; pyruvate and chemical garden reaction under anaerobic conditions, pH 7.25. A: t = 0 weeks, B: t = 1 week, C: t = 2 weeks, D: t = 3 weeks.

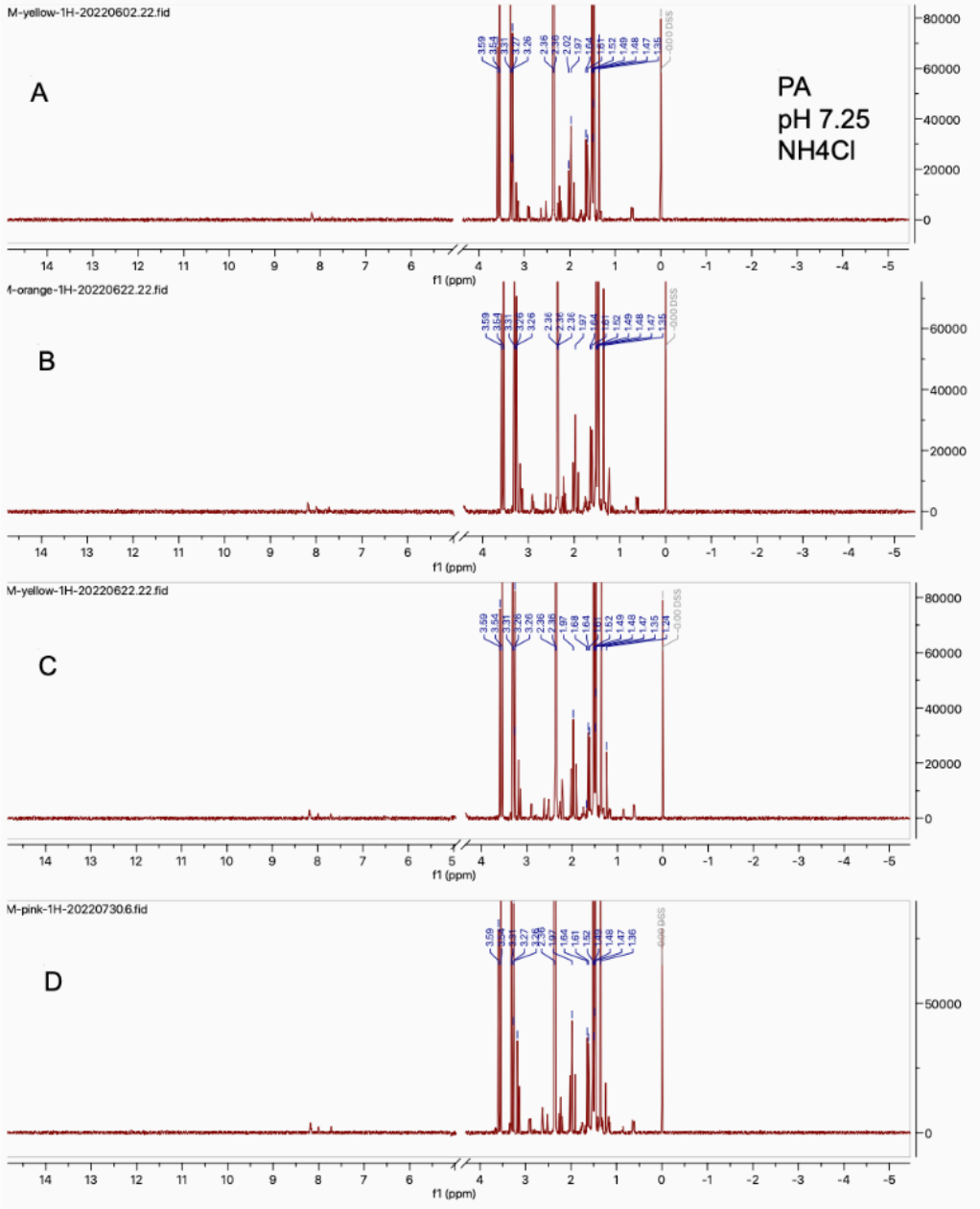


Figure A.72: Control NMR spectra; pyruvate and ammonium chloride reaction under anaerobic conditions, pH 7.25. A: t = 0 weeks, B: t = 1 week, C: t = 2 weeks, D: t = 3 weeks.

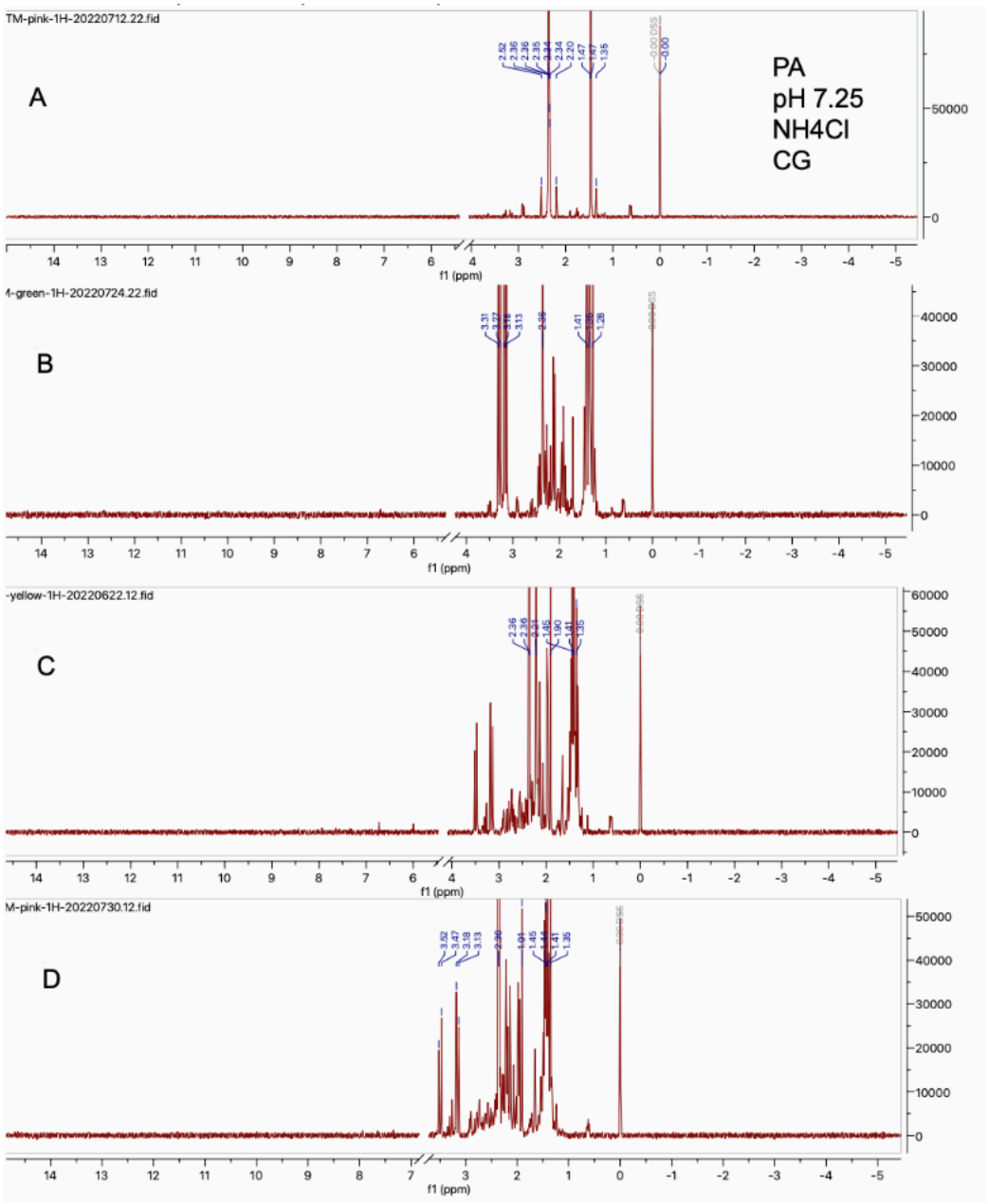


Figure A.73: NMR spectra; pyruvate, ammonium chloride and chemical garden reaction under anaerobic conditions, pH 7.25. A: t = 0 weeks, B: t = 1 week, C: t = 2 weeks, D: t = 3 weeks.

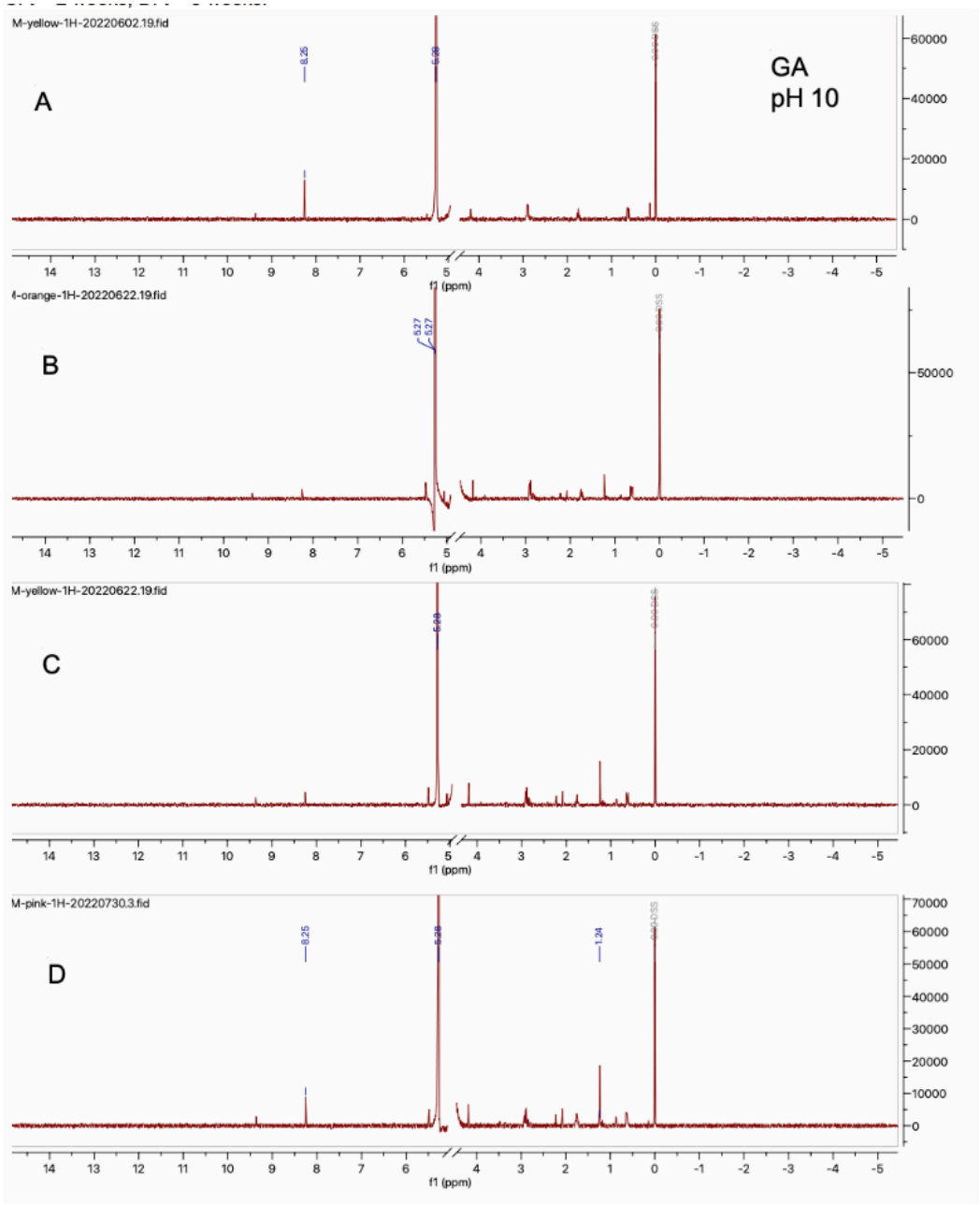


Figure A.74: Control NMR spectra; glyoxylate reaction under anaerobic conditions, pH 10. A: t = 0 weeks, B: t = 1 week, C: t = 2 weeks, D: t = 3 weeks.

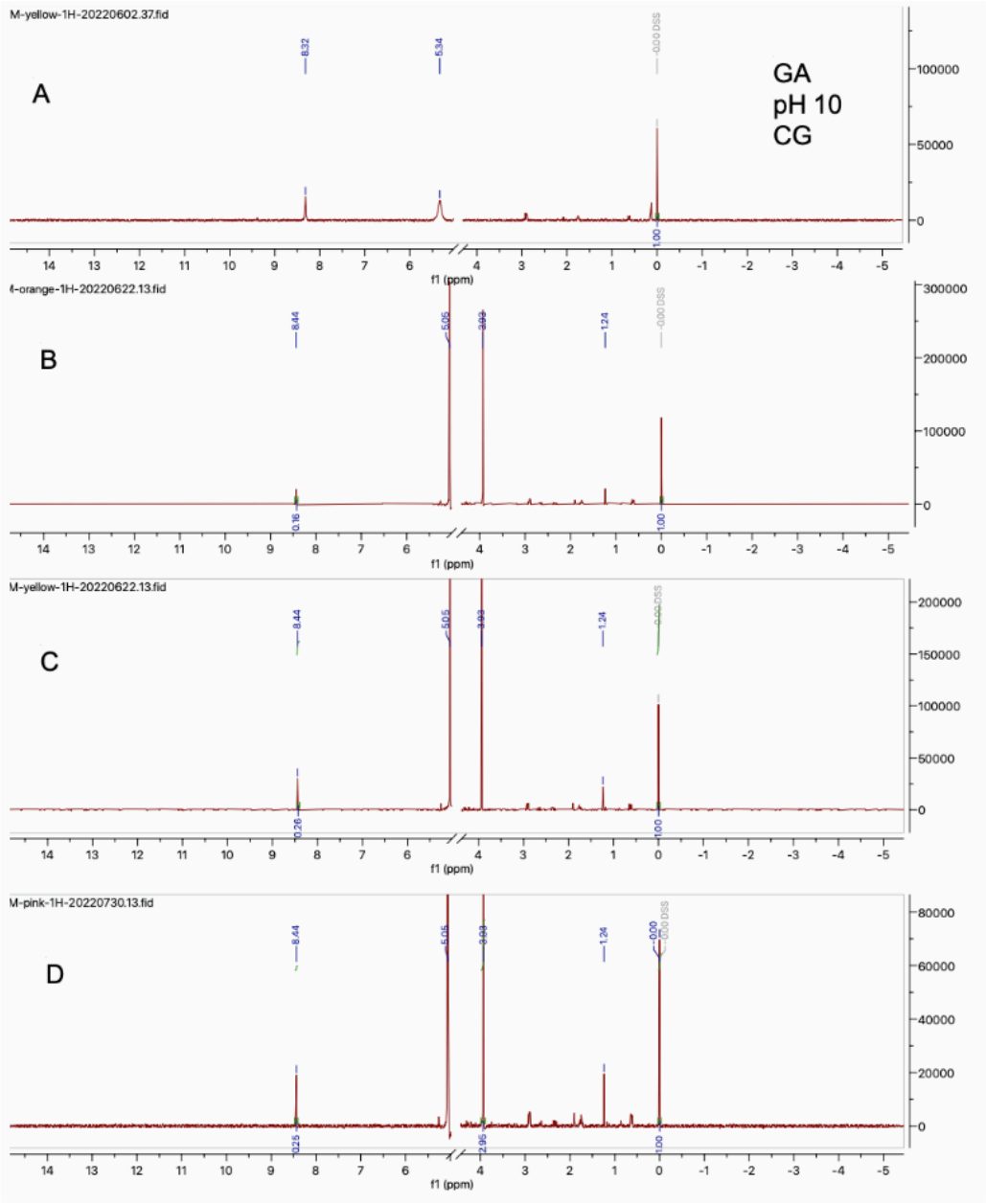


Figure A.75: NMR spectra; glyoxylate and chemical garden reaction under anaerobic conditions, pH 10. A: t = 0 weeks, B: t = 1 week, C: t = 2 weeks, D: t = 3 weeks.

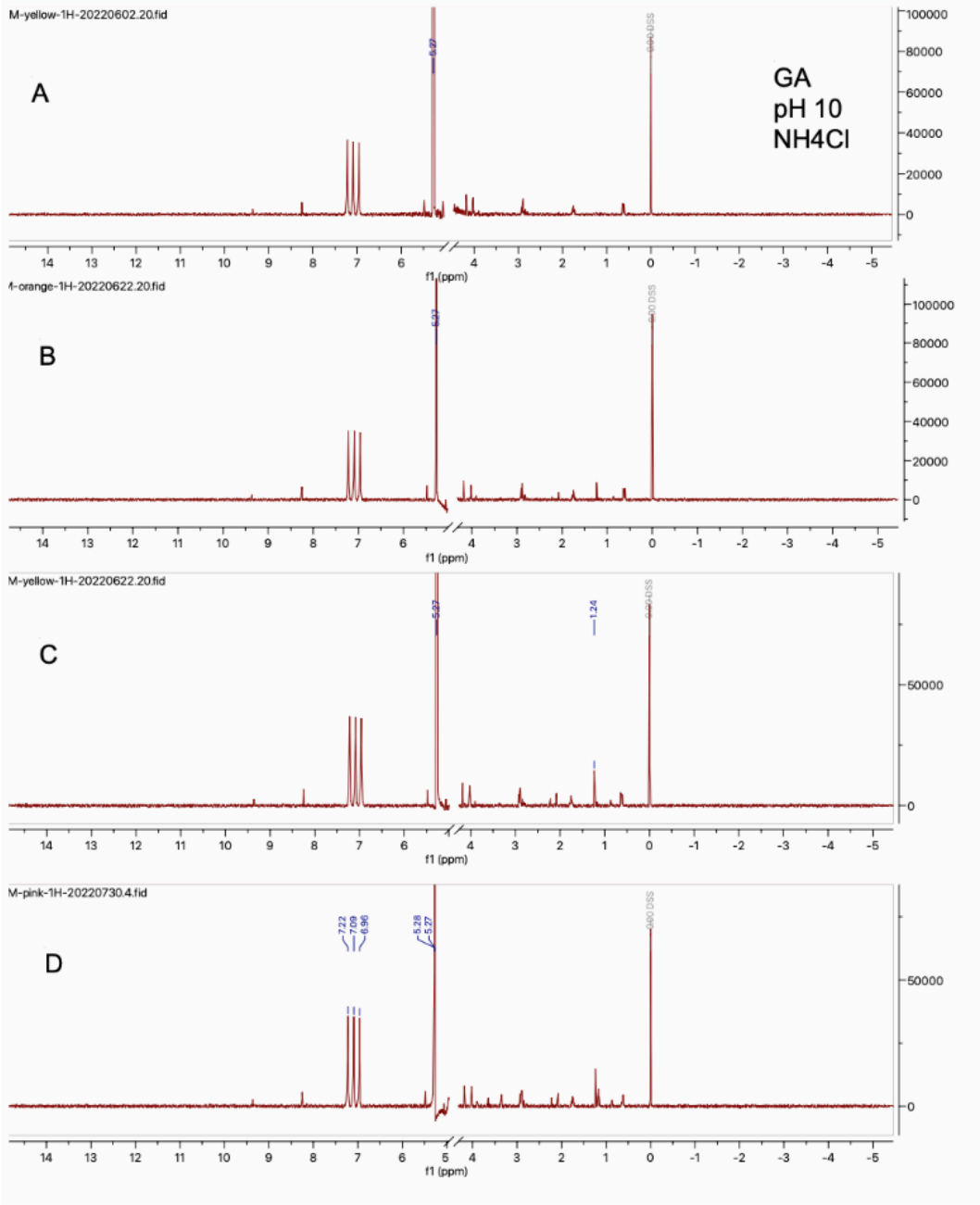


Figure A.76: Control NMR spectra; glyoxylate and ammonium chloride reaction under anaerobic conditions, pH 10. A: t = 0 weeks, B: t = 1 week, C: t = 2 weeks, D: t = 3 weeks.

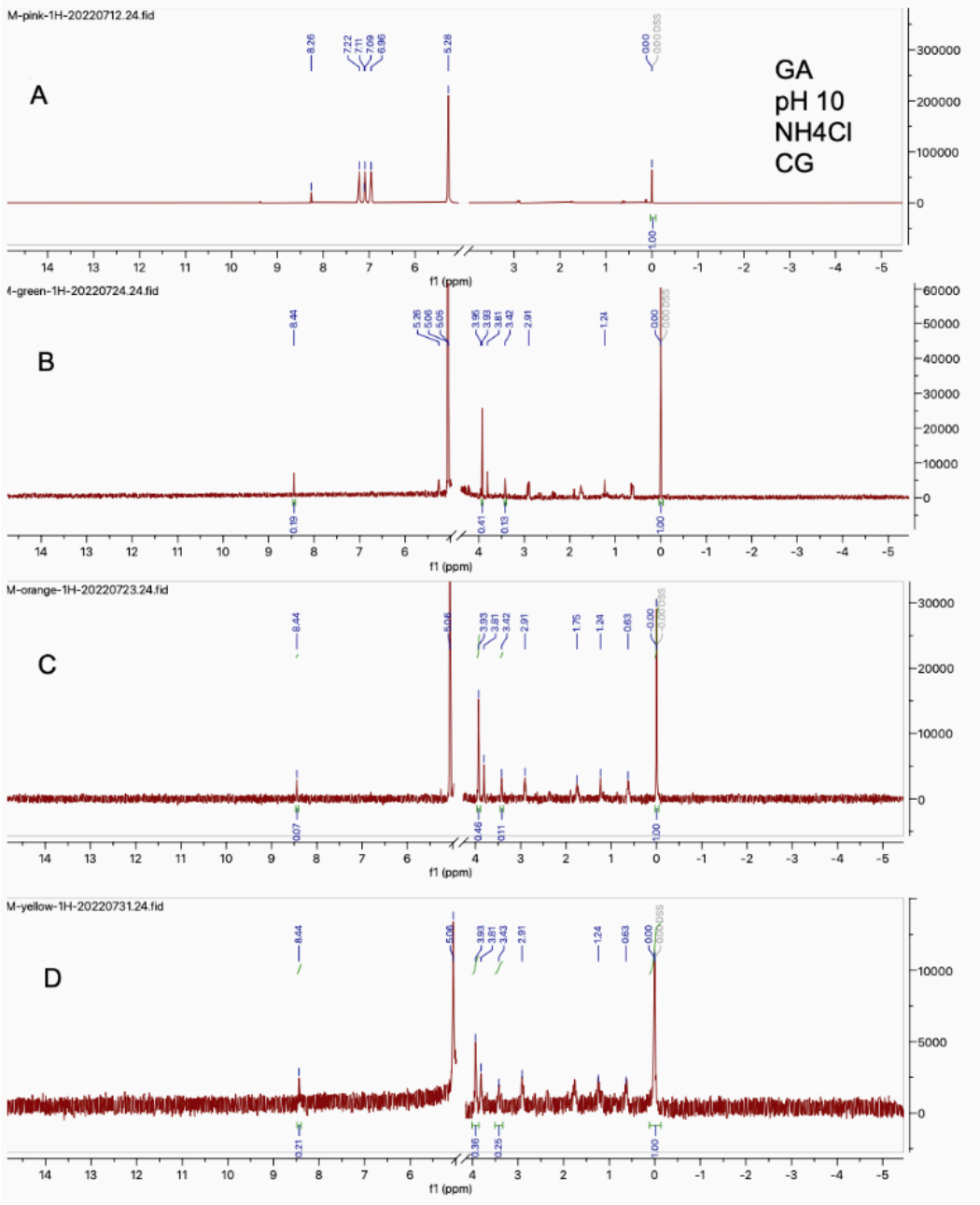


Figure A.77: NMR spectra; glyoxylate, ammonium chloride, and chemical garden reaction under anaerobic conditions, pH 10. A: t = 0 weeks, B: t = 1 week, C: t = 2 weeks, D: t = 3 weeks.

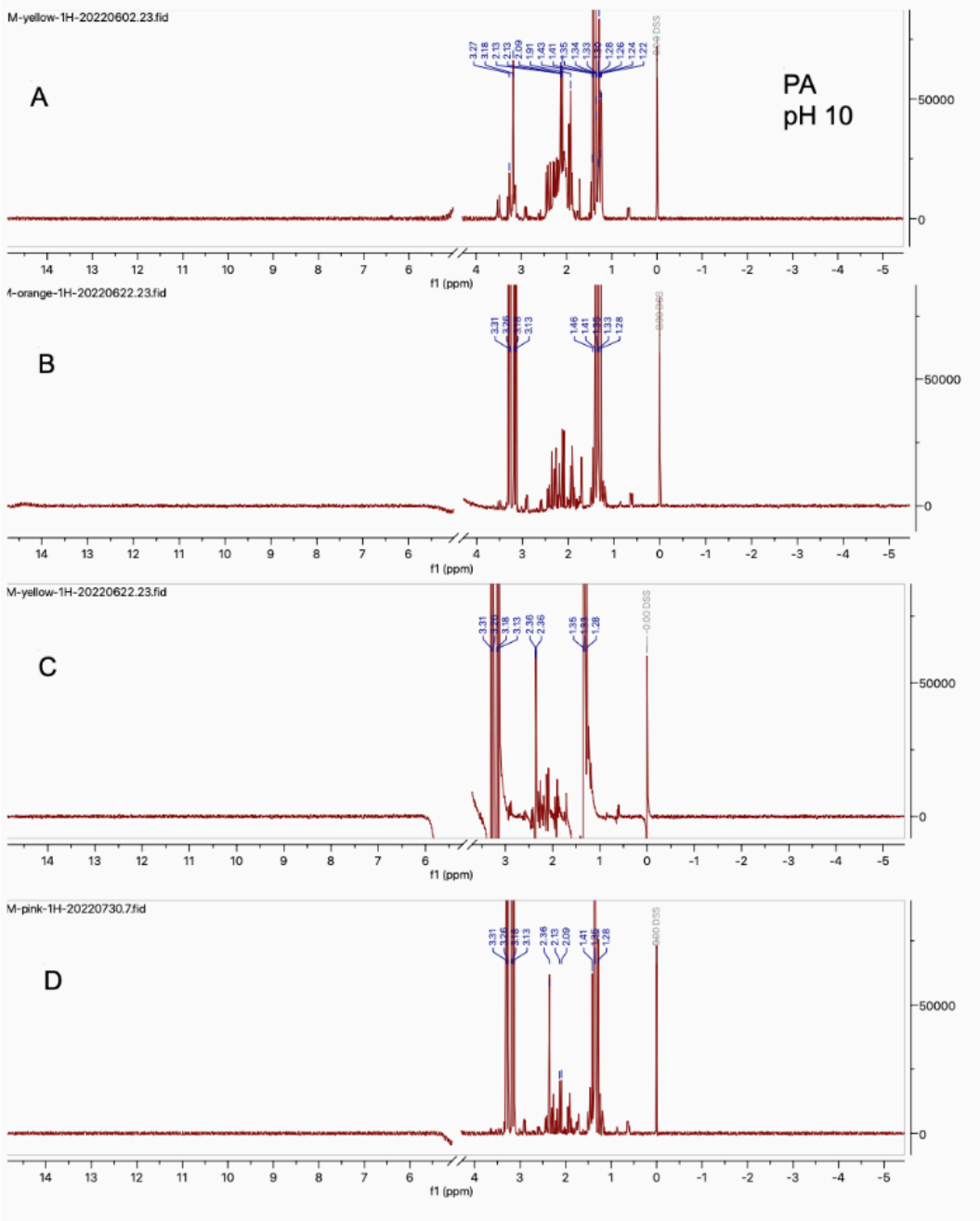


Figure A.78: Control NMR spectra; pyruvate reaction under anaerobic conditions, pH 10. A: t = 0 weeks, B: t = 1 week, C: t = 2 weeks, D: t = 3 weeks.

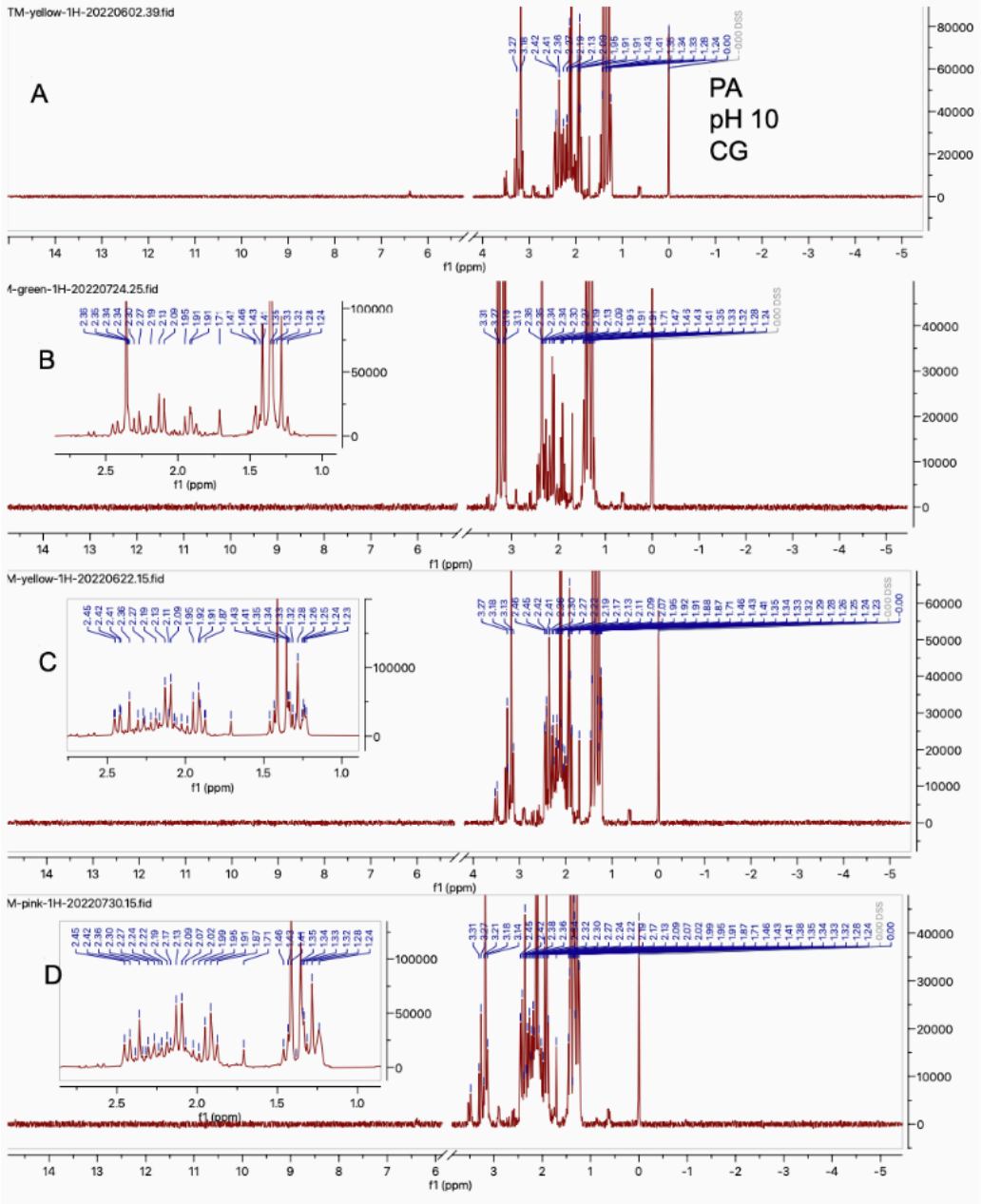


Figure A.79: NMR spectra; pyruvate and chemical garden reaction under anaerobic conditions, pH 10. A: t = 0 weeks, B: t = 1 week, C: t = 2 weeks, D: t = 3 weeks.

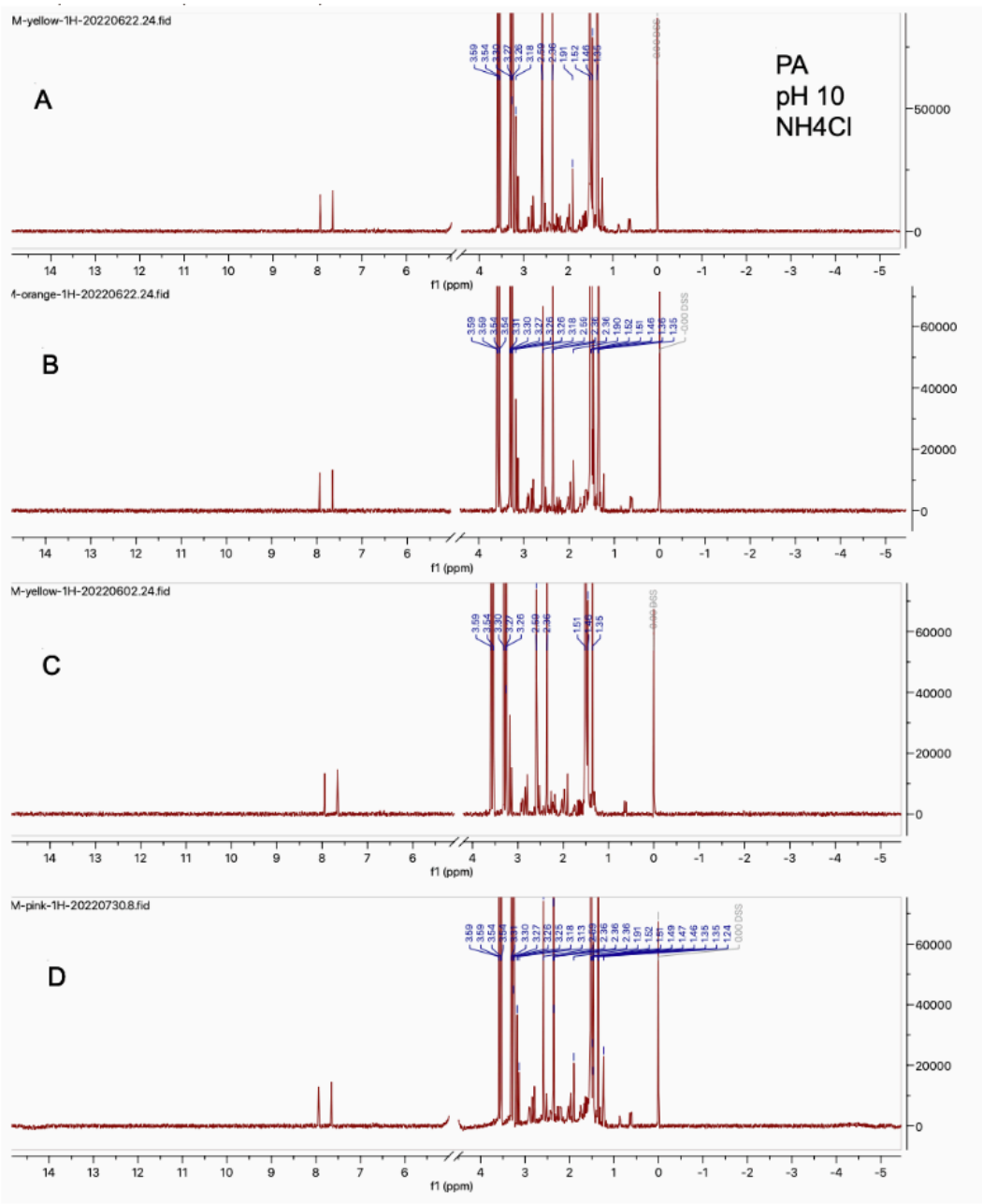


Figure A.80: Control NMR spectra; pyruvate and ammonium chloride reaction under anaerobic conditions, pH 10. A: t = 0 weeks, B: t = 1 week, C: t = 2 weeks, D: t = 3 weeks.

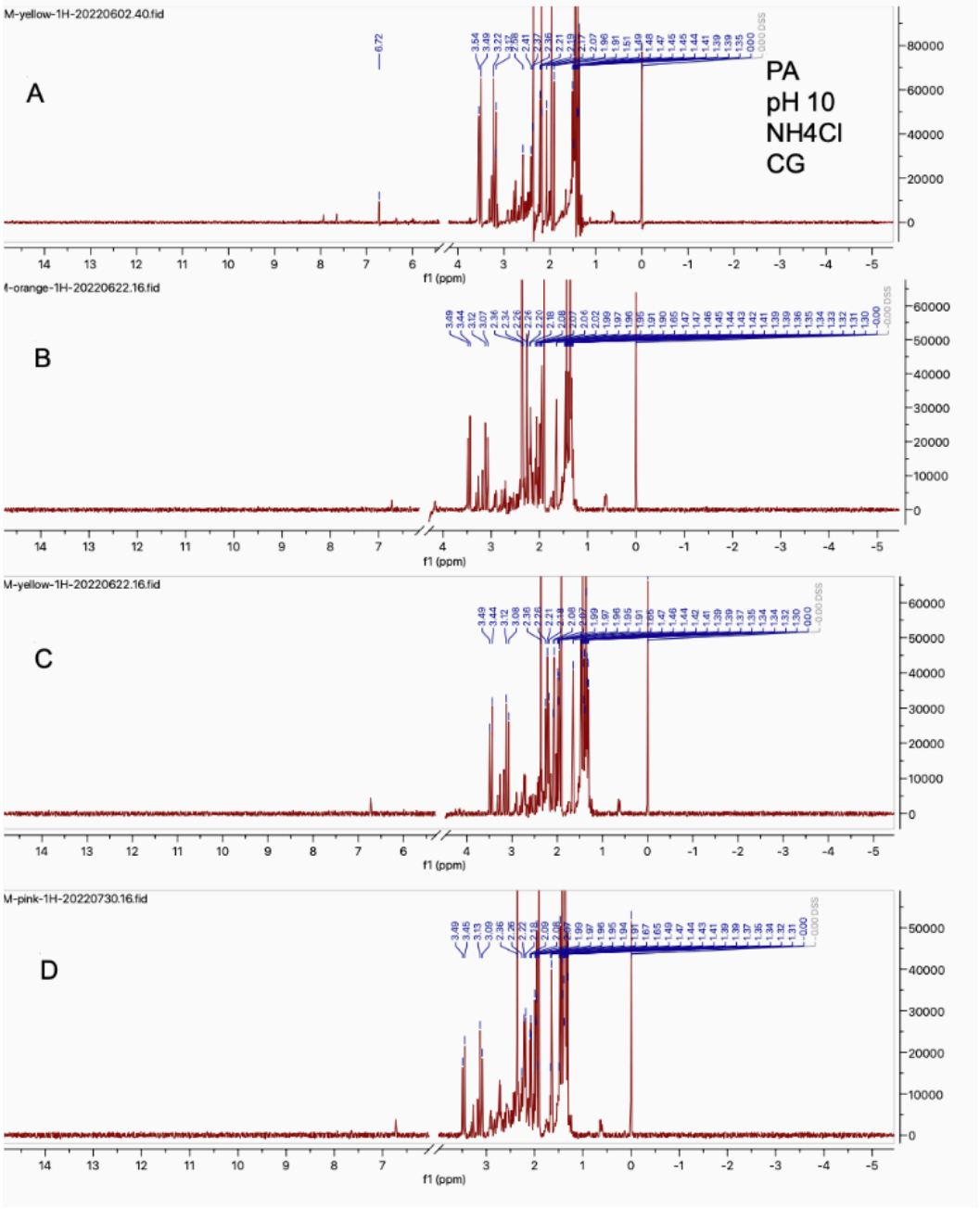


Figure A.81: NMR spectra; pyruvate, ammonium chloride, and chemical garden reaction under anaerobic conditions, pH 10. A: t = 0 weeks, B: t = 1 week, C: t = 2 weeks, D: t = 3 weeks.

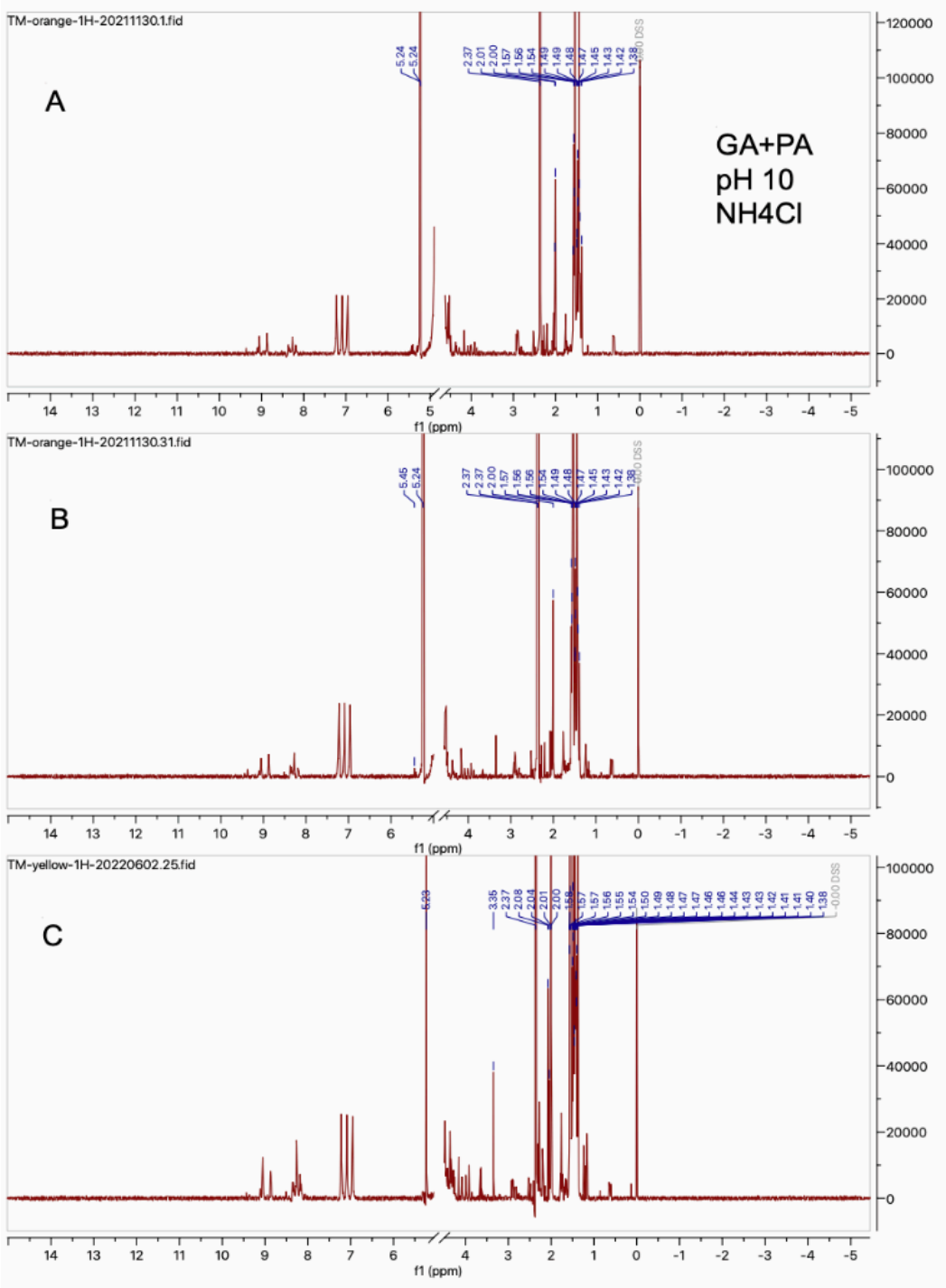


Figure A.82: Control NMR spectra; pyruvate, glyoxylate, and ammonium chloride reaction under anaerobic conditions, pH 10. A: t = 0 weeks, B: t = 1 week, C: t = 3 weeks.

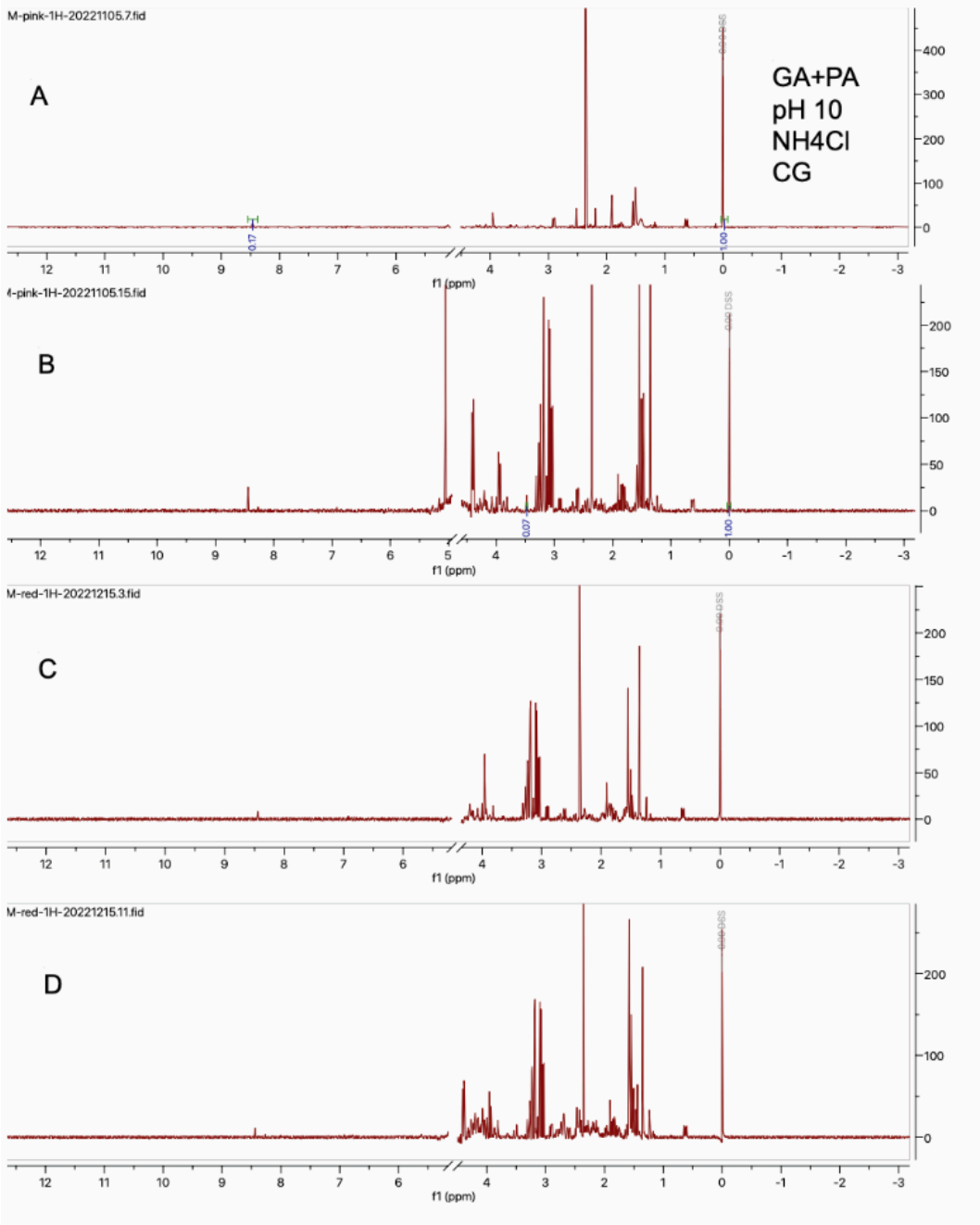


Figure A.83: NMR spectra; pyruvate, glyoxylate, ammonium chloride, and chemical garden reaction under anaerobic conditions, pH 10. A: t = 0 weeks, B: t = 1 week, C: t = 2 weeks, D: t = 3 weeks.

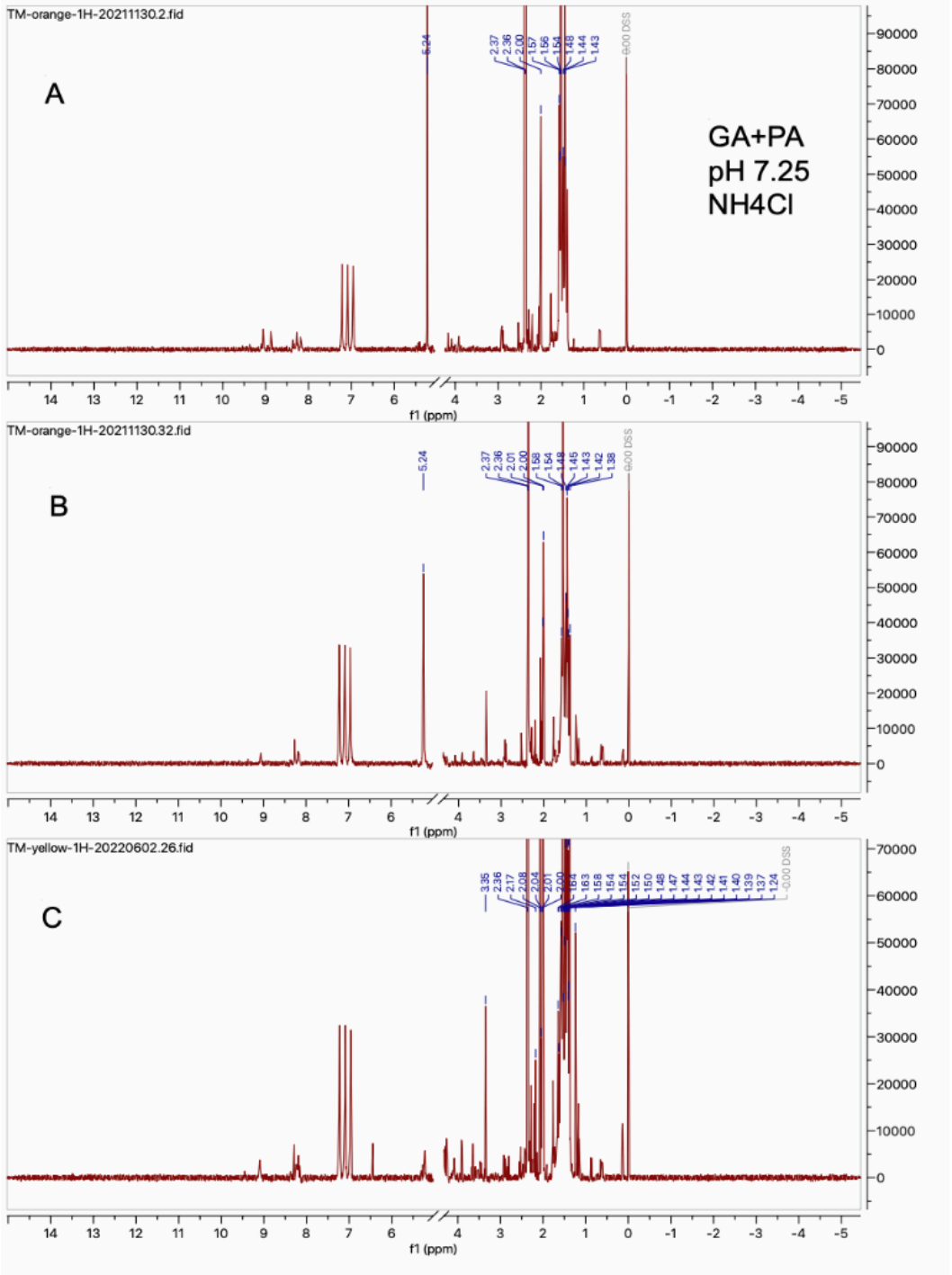


Figure A.84: Control NMR spectra; pyruvate, glyoxylate, and ammonium chloride reaction under anaerobic conditions, pH 7.25. A: t = 0 weeks, B: t = 1 week, C: t = 3 weeks.

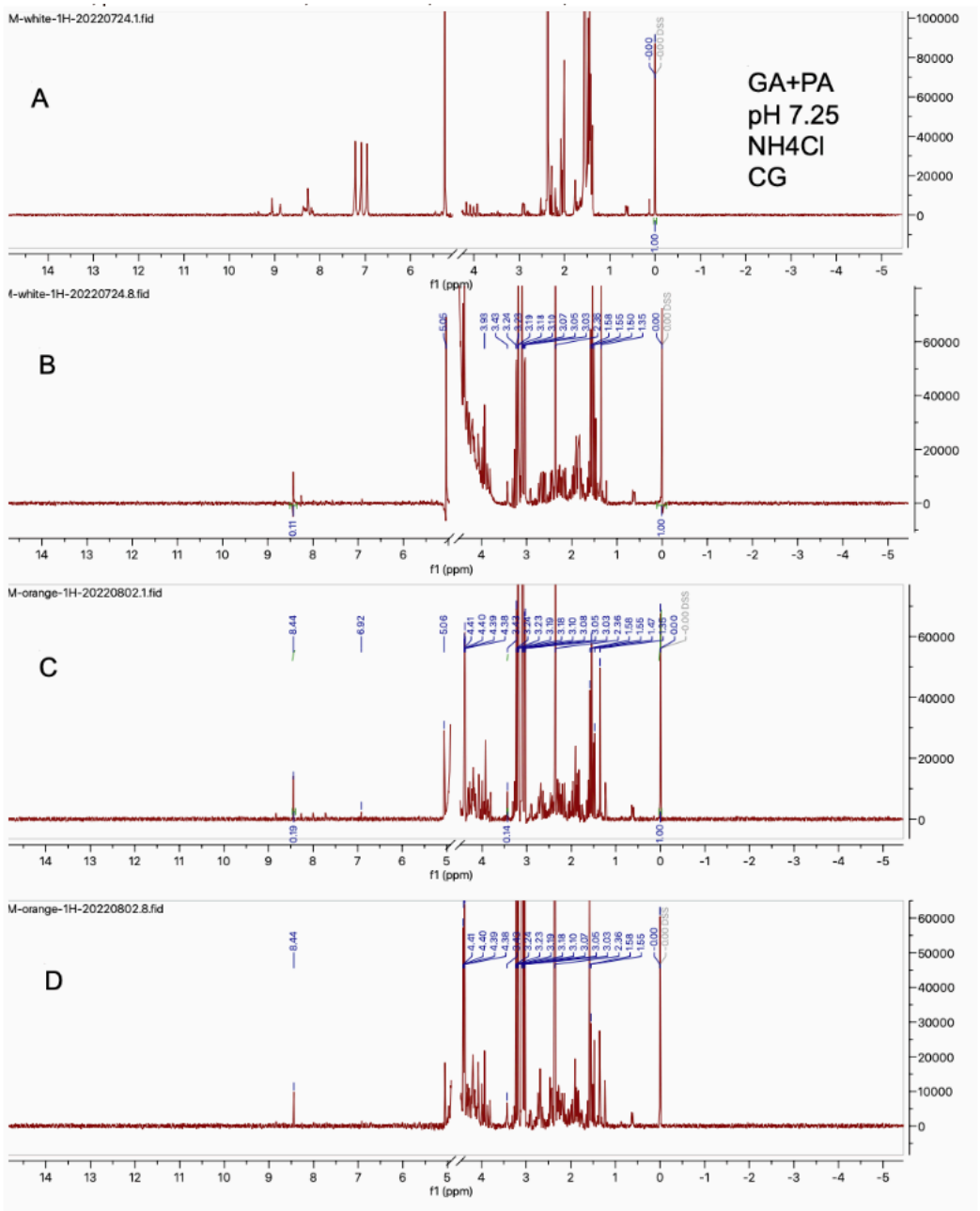


Figure A.85: NMR spectra; pyruvate, glyoxylate, ammonium chloride, and chemical garden reaction under anaerobic conditions, pH 7.25. A: t = 0 weeks, B: t = 1 week, C: t = 2 weeks, D: t = 3 weeks.

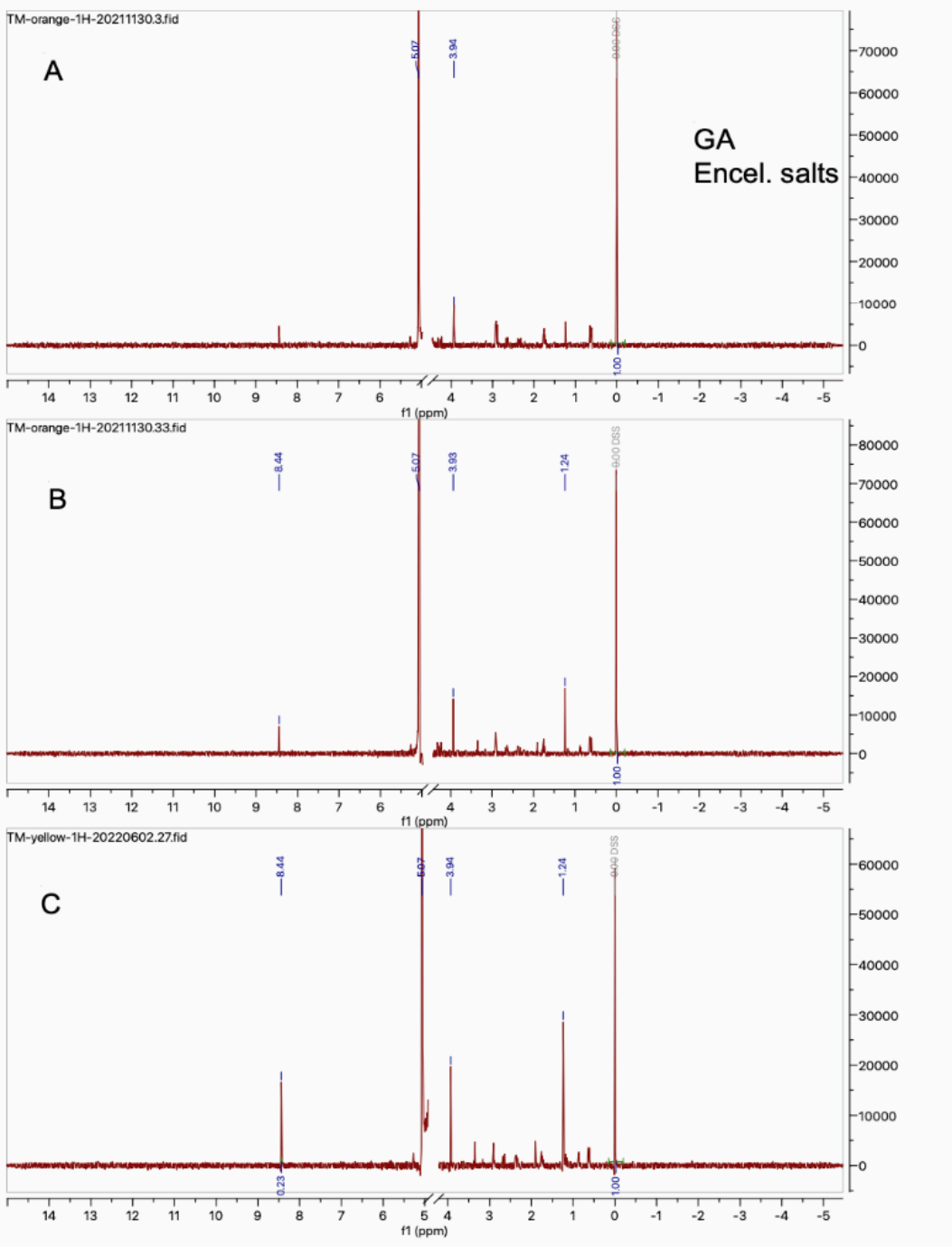


Figure A.86: Control NMR spectra; glyoxylate, sodium chloride, and sodium carbonate reaction under anaerobic conditions. A: t = 0 weeks, B: t = 1 week, C: t = 3 weeks.

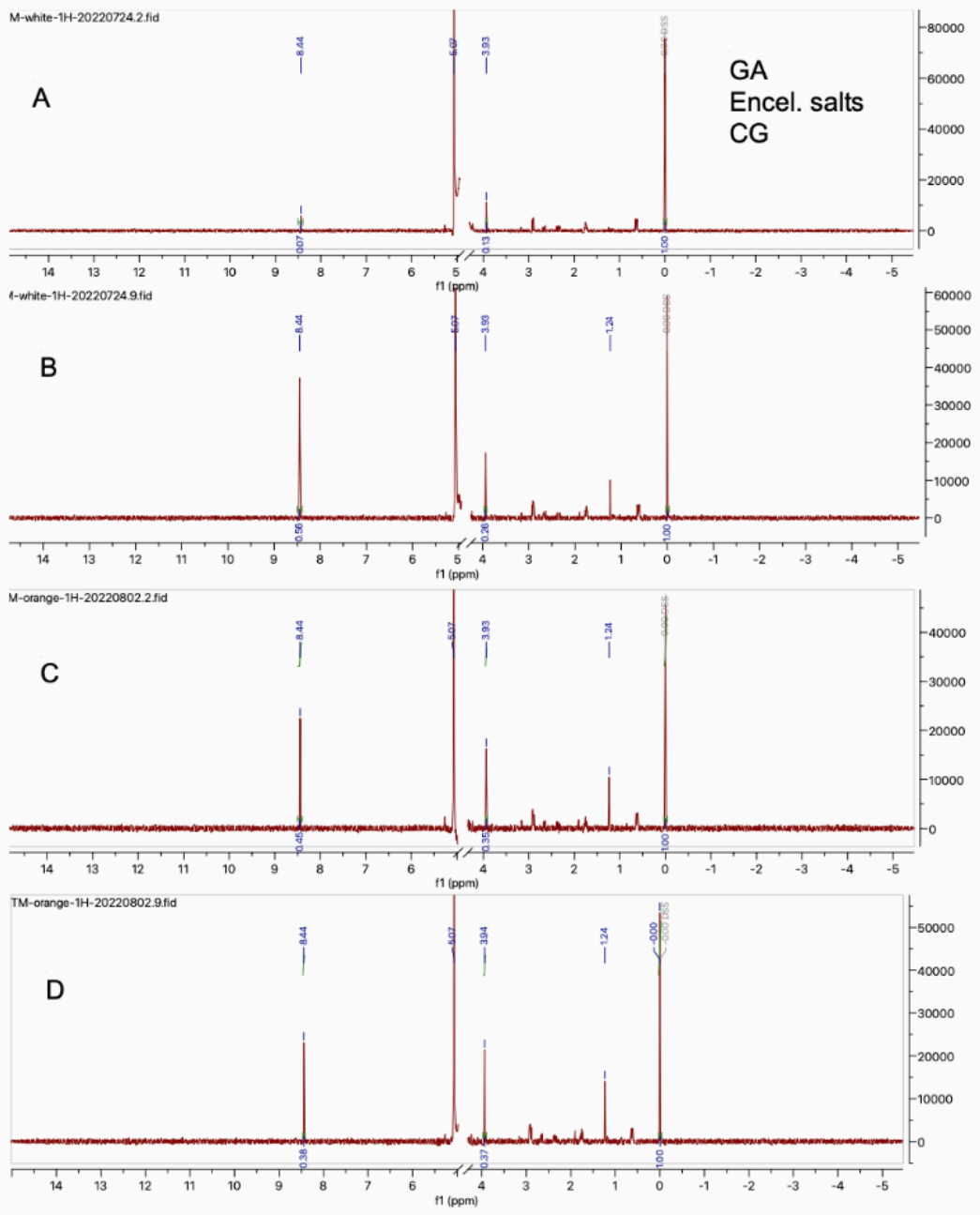


Figure A.87: NMR spectra; glyoxylate, sodium chloride, sodium carbonate, and chemical garden reaction under anaerobic conditions. A: t = 0 weeks, B: t = 1 week, C: t = 2 weeks, D: t = 3 weeks.

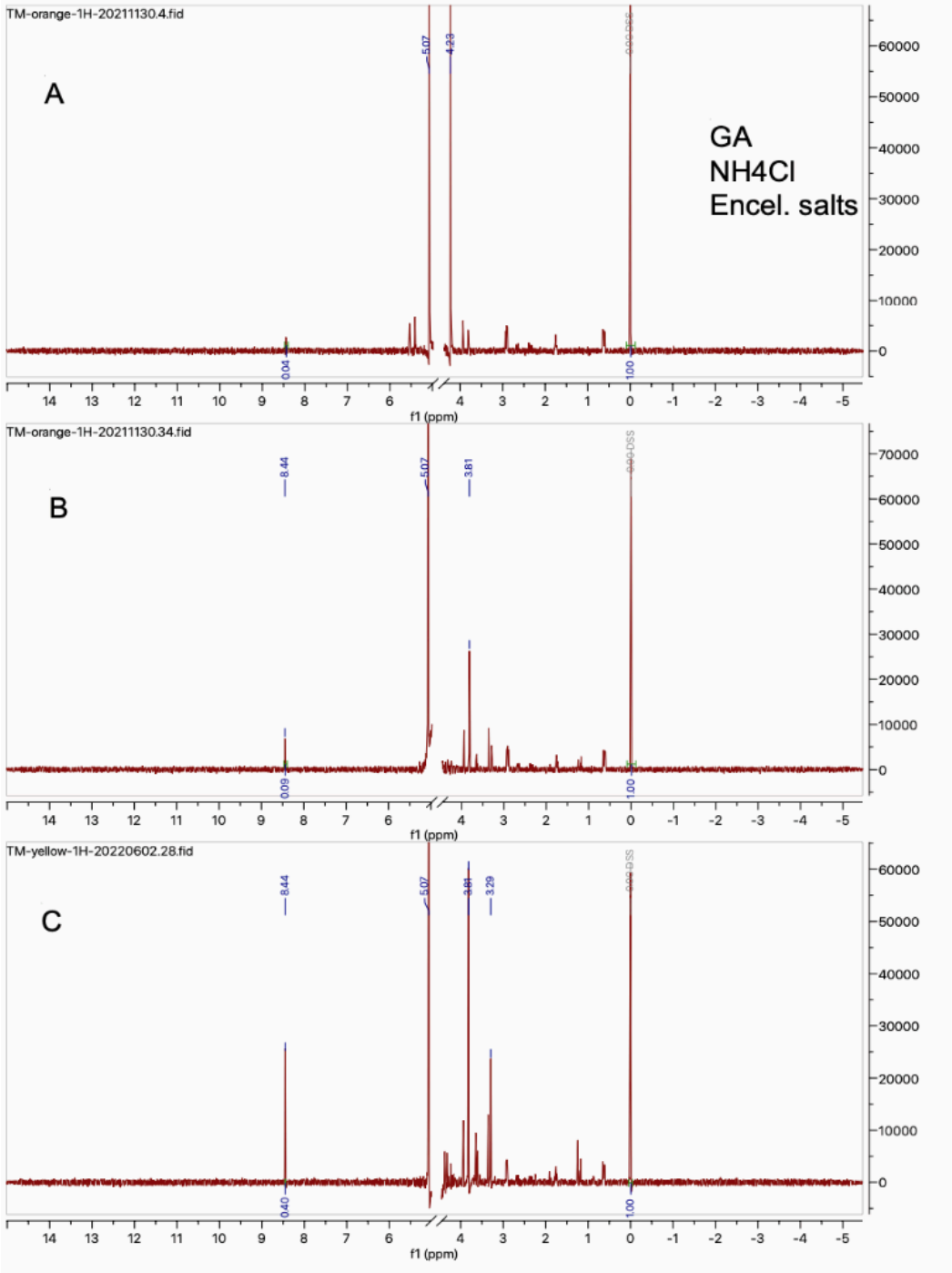


Figure A.88: Control NMR spectra; glyoxylate, sodium chloride, sodium carbonate, and ammonium chloride reaction under anaerobic conditions. A: t = 0 weeks, B: t = 1 week, C: t = 3 weeks.

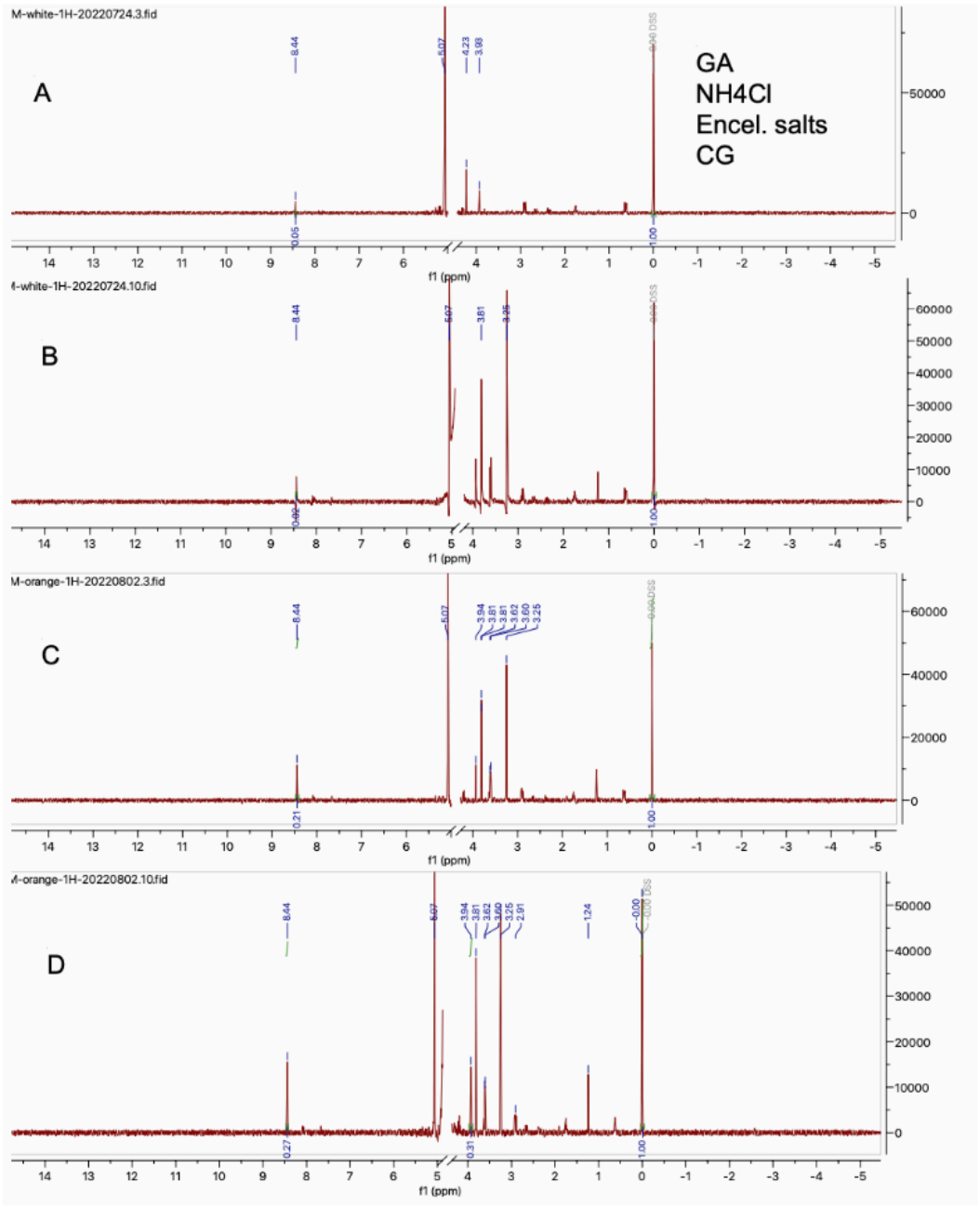


Figure A.89: NMR spectra; glyoxylate, sodium chloride, sodium carbonate, ammonium chloride, and chemical garden reaction under anaerobic conditions. A: t = 0 weeks, B: t = 1 week, C: t = 2 weeks, D: t = 3 weeks.

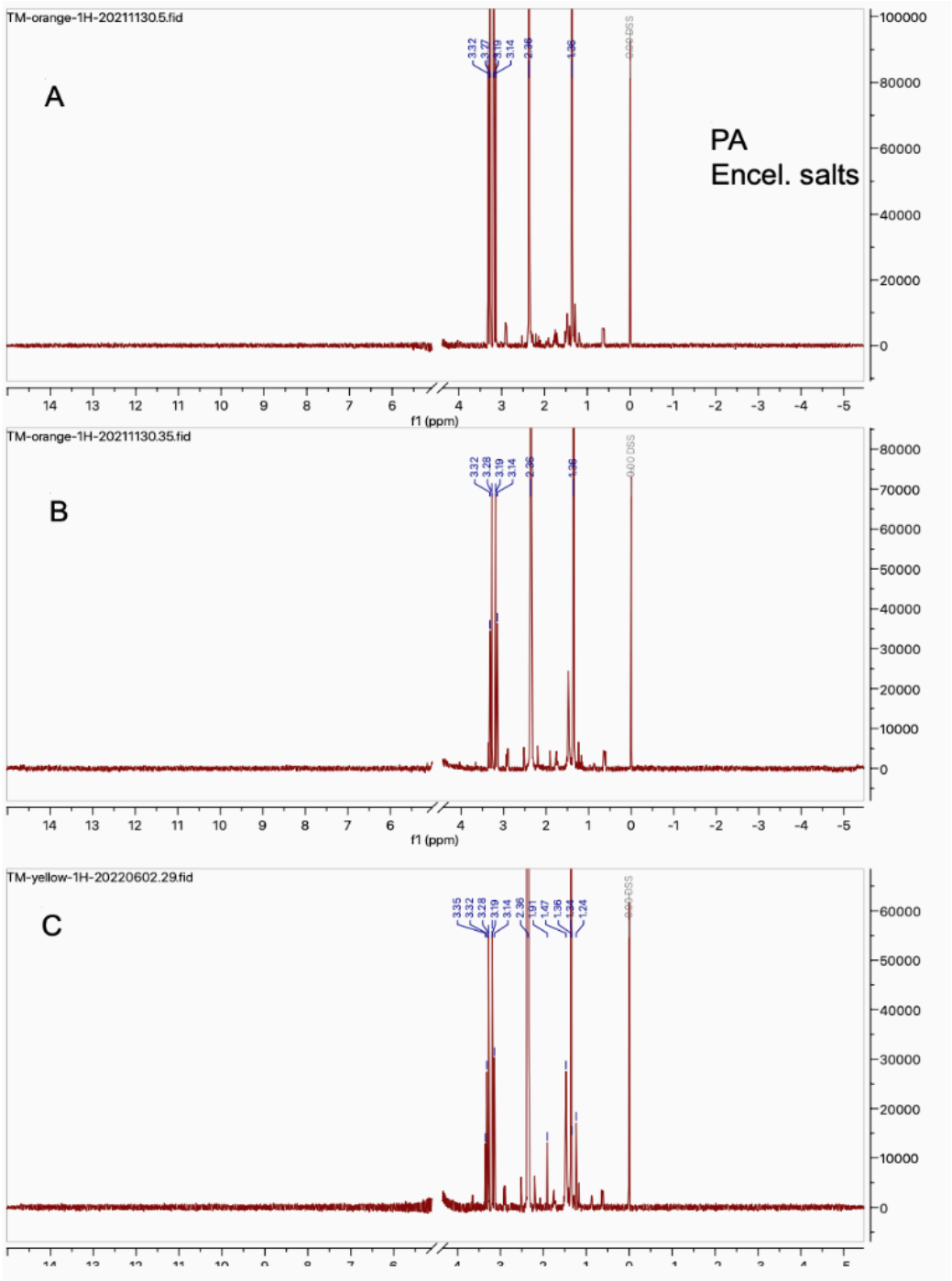


Figure A.90: Control NMR spectra; pyruvate, sodium chloride, and sodium carbonate reaction under anaerobic conditions. A: t = 0 weeks, B: t = 1 week, C: t = 3 weeks.

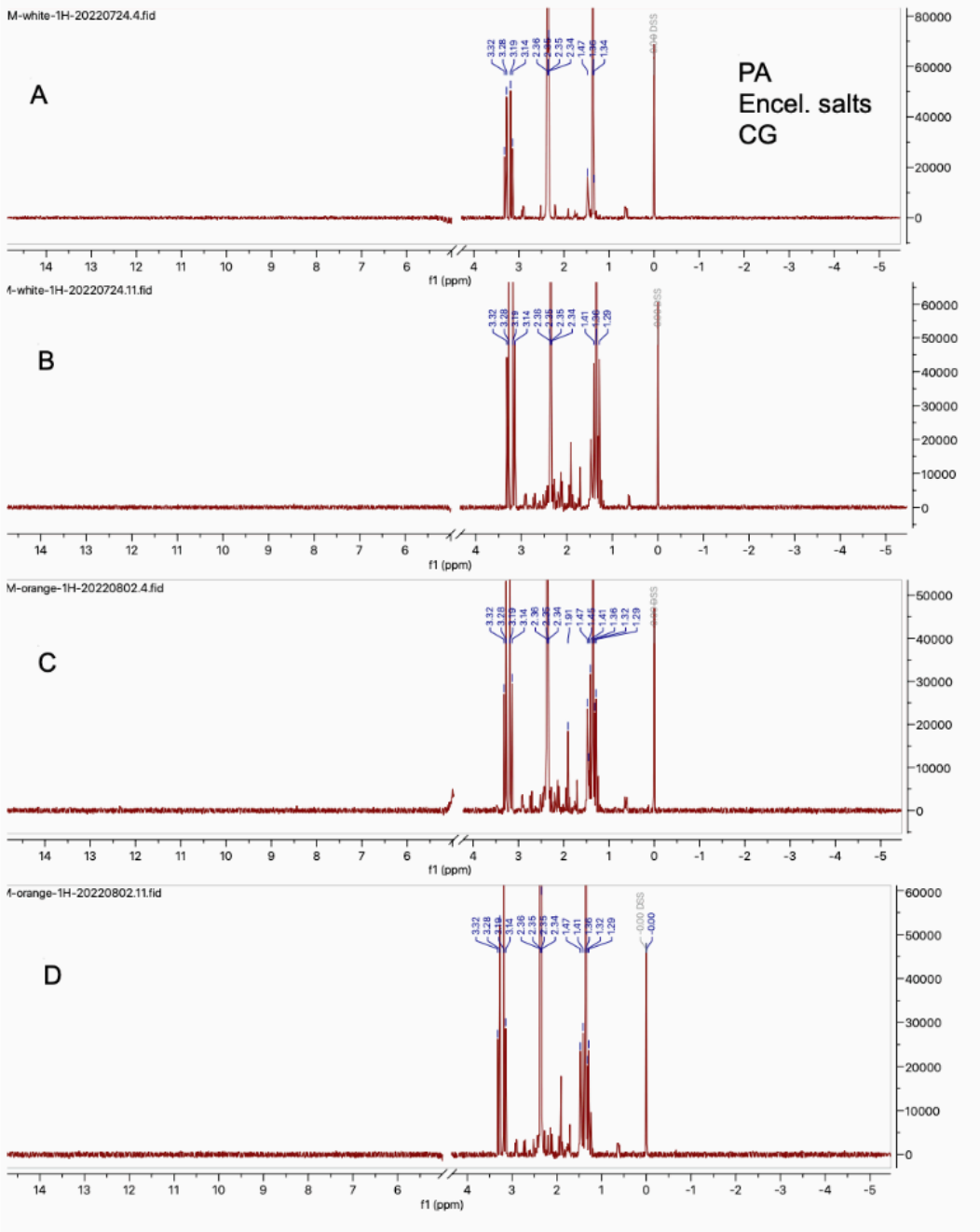


Figure A.91: NMR spectra; pyruvate, sodium chloride, sodium carbonate, and chemical garden reaction under anaerobic conditions. A: t = 0 weeks, B: t = 1 week, C: t = 2 weeks, D: t = 3 weeks.

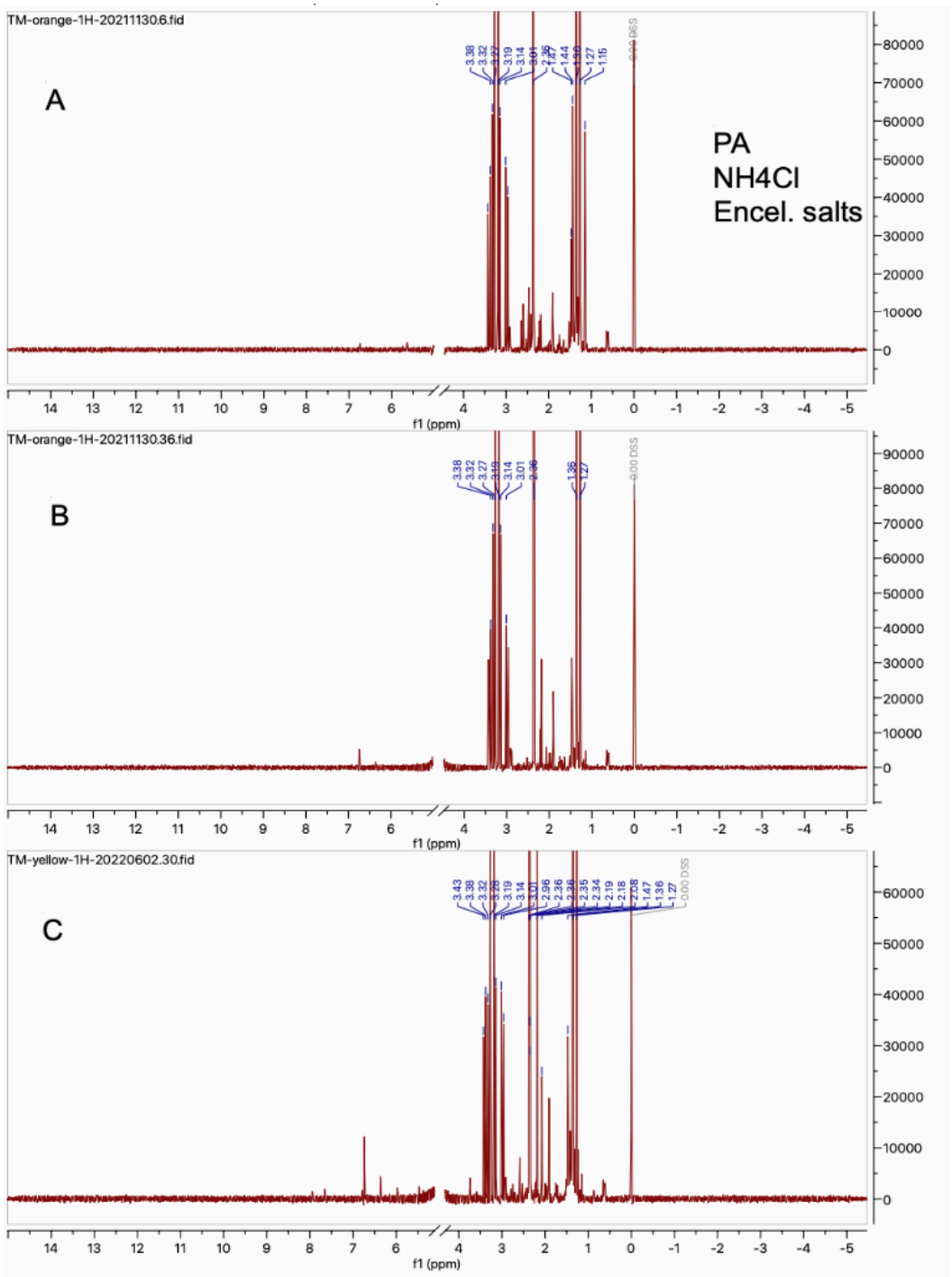


Figure A.92: Control NMR spectra; pyruvate, sodium chloride, sodium carbonate, and ammonium chloride reaction under anaerobic conditions. A: t = 0 weeks, B: t = 1 week, C: t = 3 weeks.

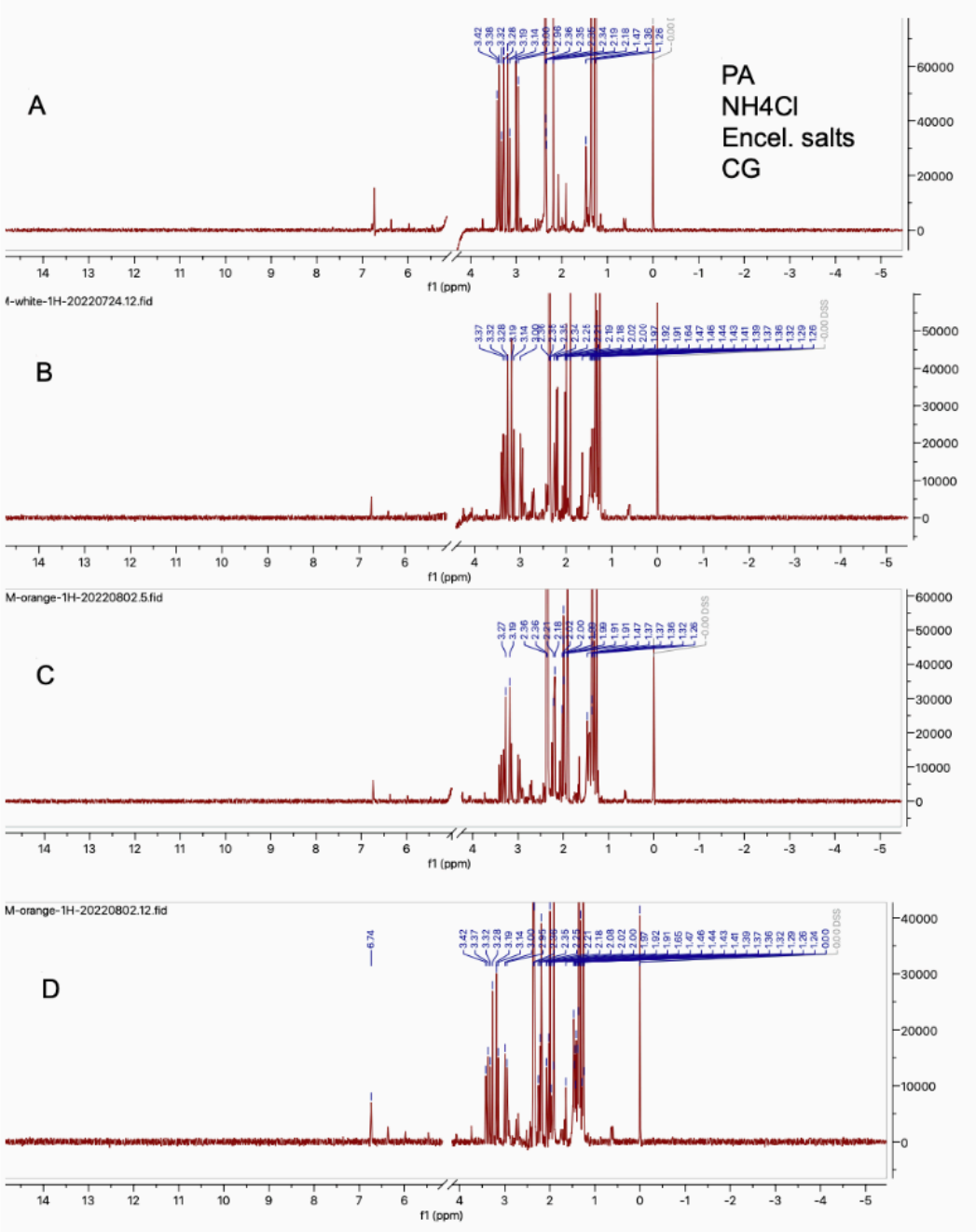


Figure A.93: NMR spectra; pyruvate, sodium chloride, sodium carbonate, ammonium chloride, and chemical garden reaction under anaerobic conditions. A: t = 0 weeks, B: t = 1 week, C: t = 2 weeks, D: t = 3 weeks.

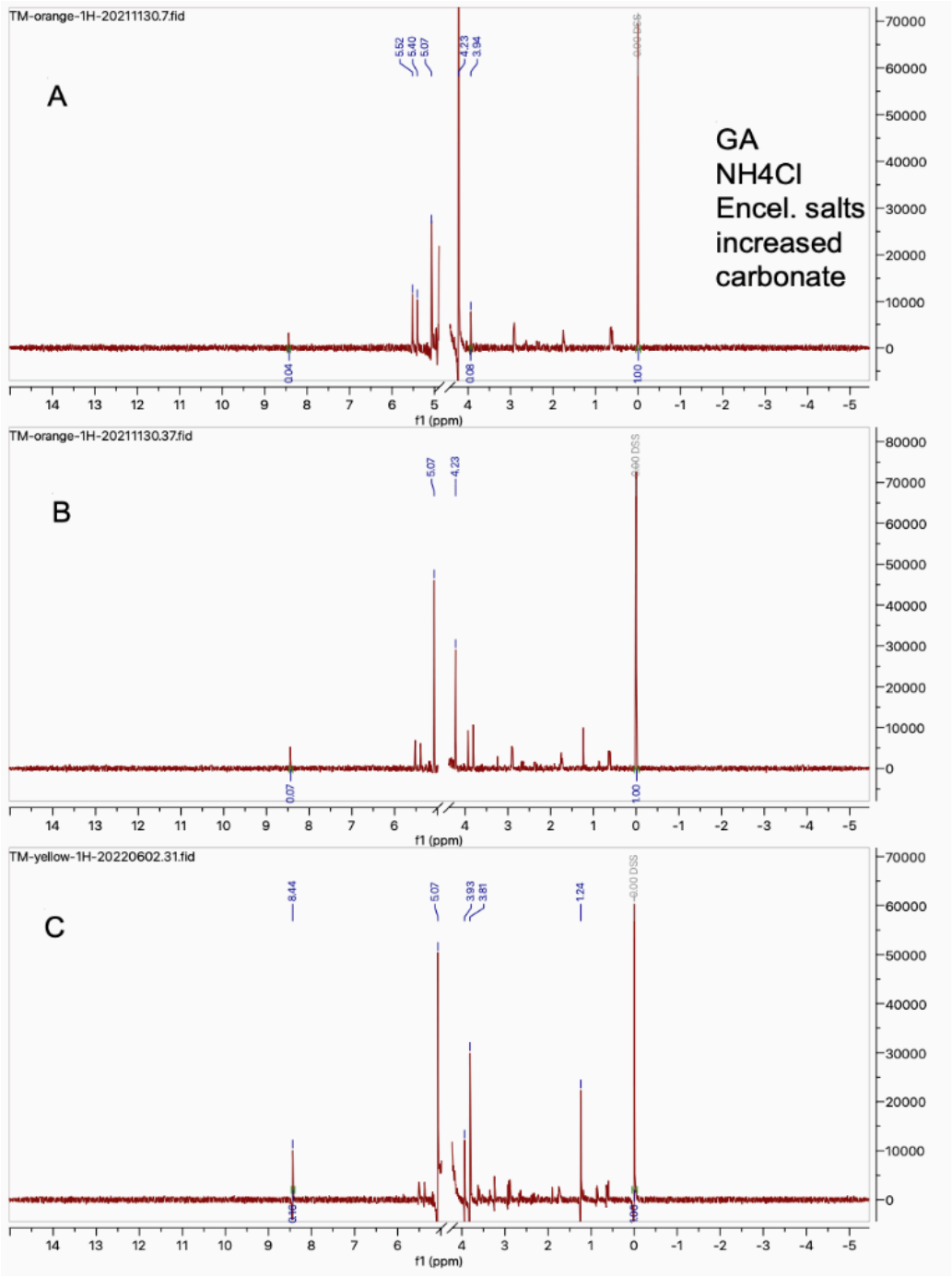


Figure A.94: Control NMR spectra; glyoxylate, sodium chloride, increased sodium carbonate, and ammonium chloride reaction under anaerobic conditions. A: t = 0 weeks, B: t = 1 week, C: t = 3 weeks.

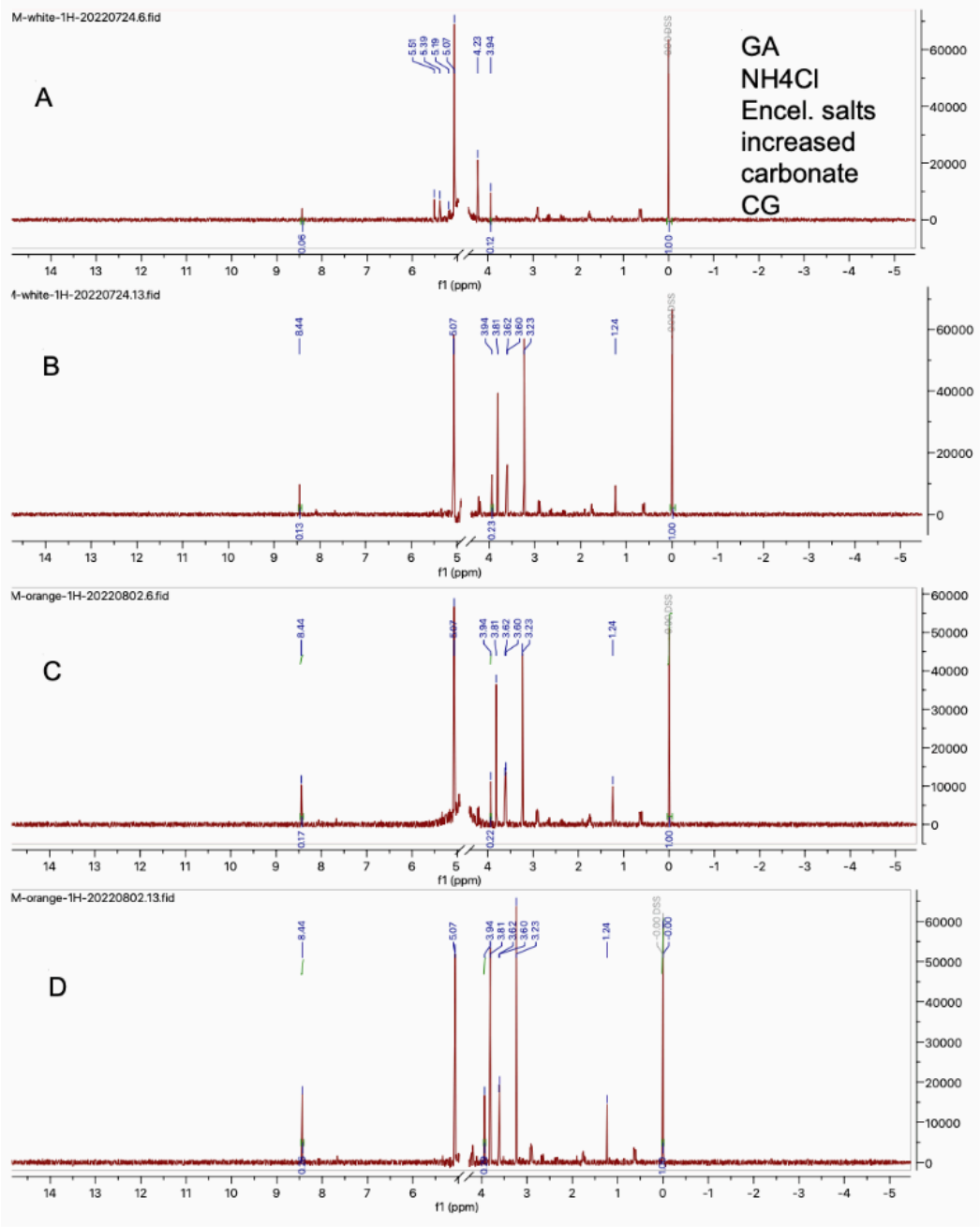


Figure A.95: NMR spectra; glyoxylate, sodium chloride, increased sodium carbonate, ammonium chloride, and chemical garden reaction under anaerobic conditions. A: t = 0 weeks, B: t = 1 week, C: t = 2 weeks, D: t = 3 weeks.

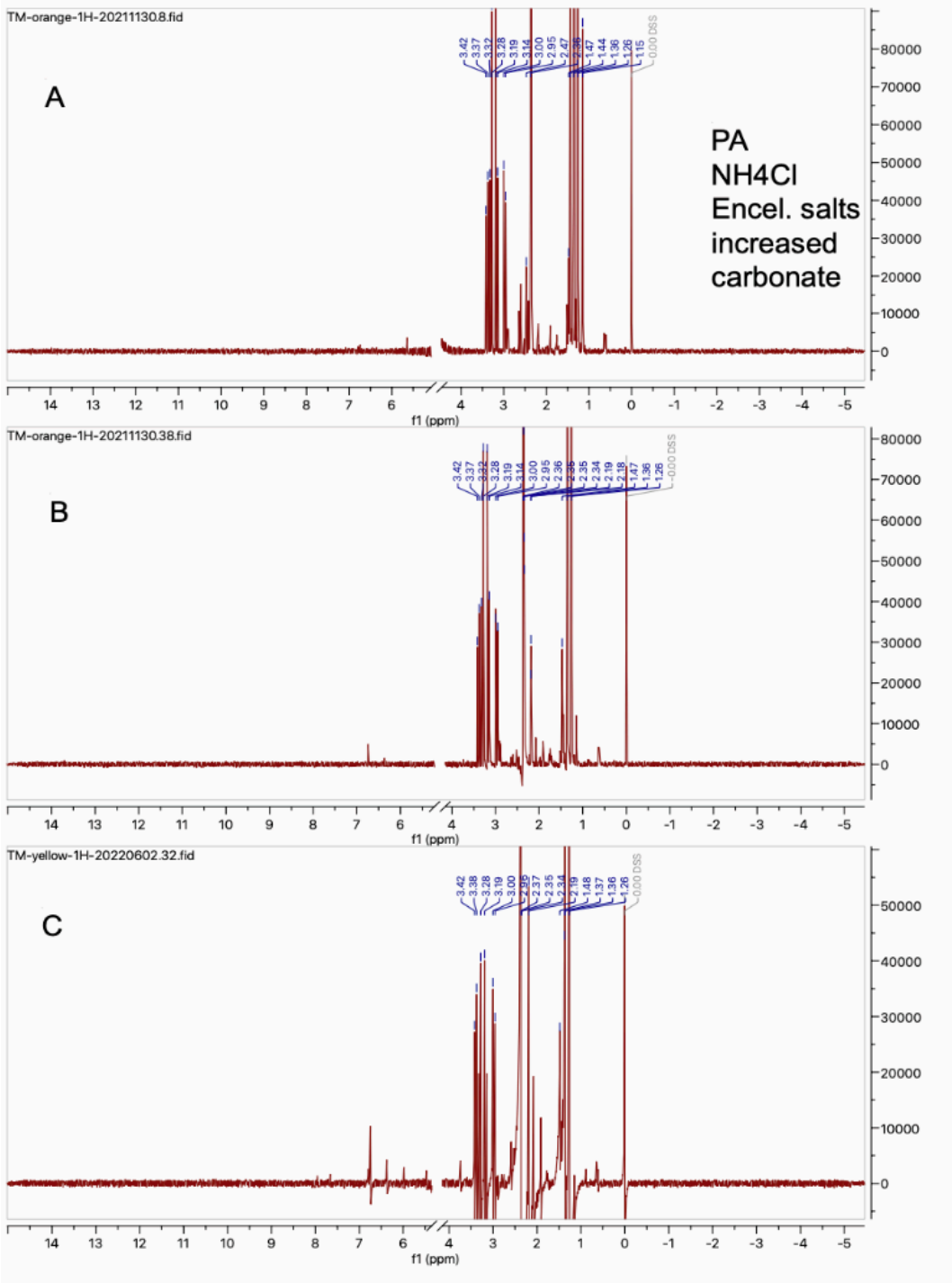


Figure A.96: Control NMR spectra; pyruvate, sodium chloride, sodium carbonate, and ammonium chloride reaction under anaerobic conditions. A: t = 0 weeks, B: t = 1 week, C: t = 3 weeks.

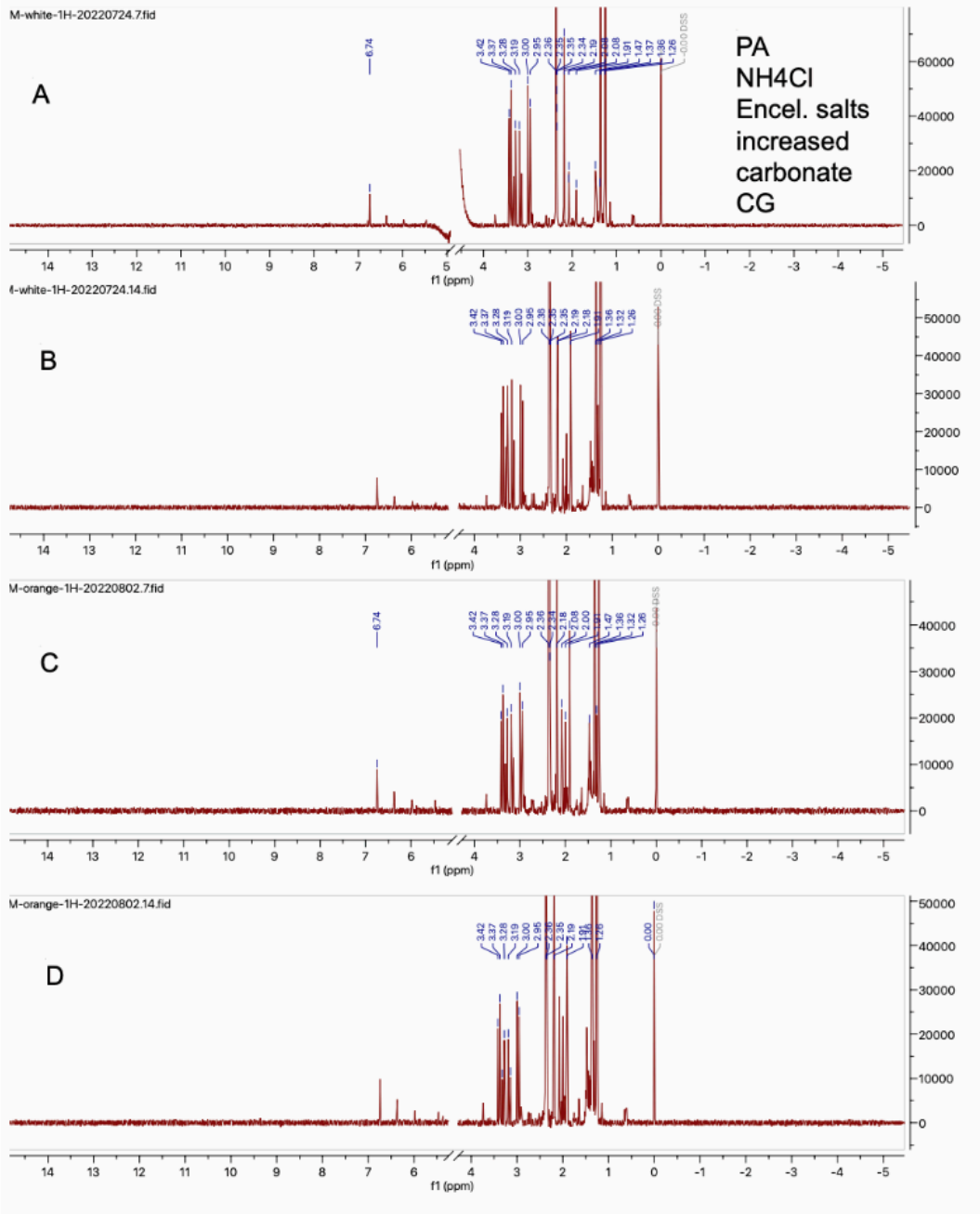


Figure A.97: NMR spectra; pyruvate, sodium chloride, sodium carbonate, ammonium chloride, and chemical garden reaction under anaerobic conditions. A: t = 0 weeks, B: t = 1 week, C: t = 2 weeks, D: t = 3 weeks.

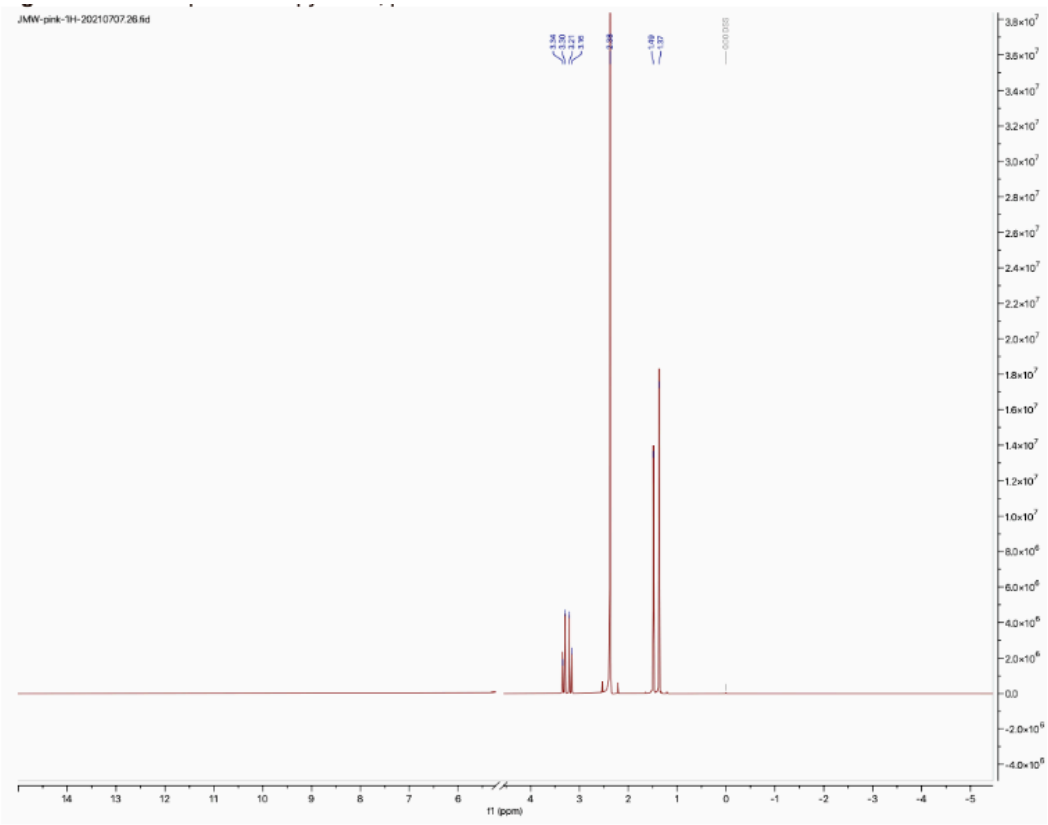


Figure A.98: NMR spectrum of pyruvate, pH 7.25.

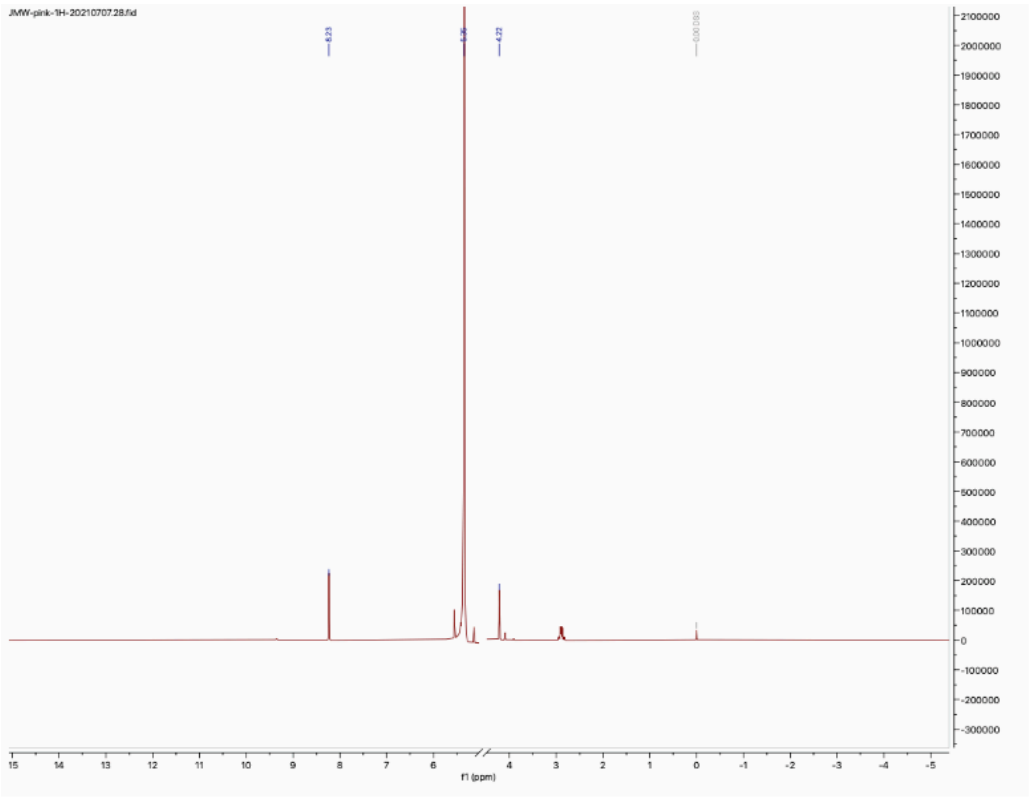


Figure A.99: NMR spectrum of glyoxylate, pH 7.25.

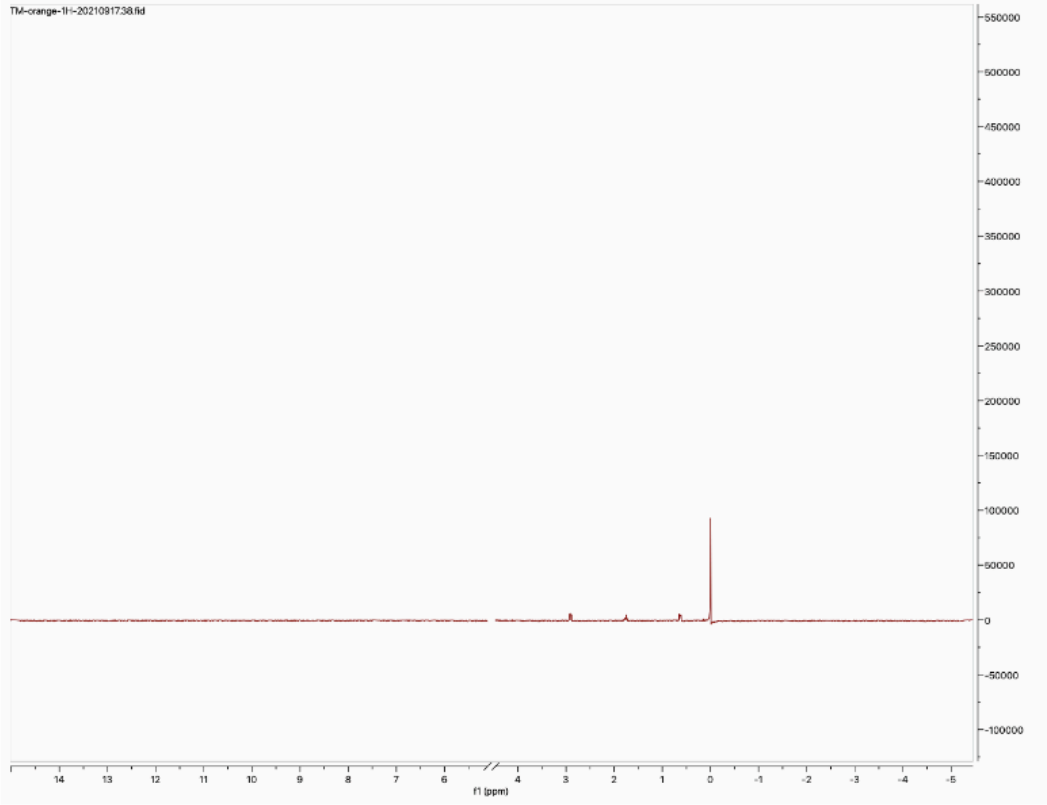


Figure A.100: NMR spectrum of D_2Or/DSS, pH 7.25.

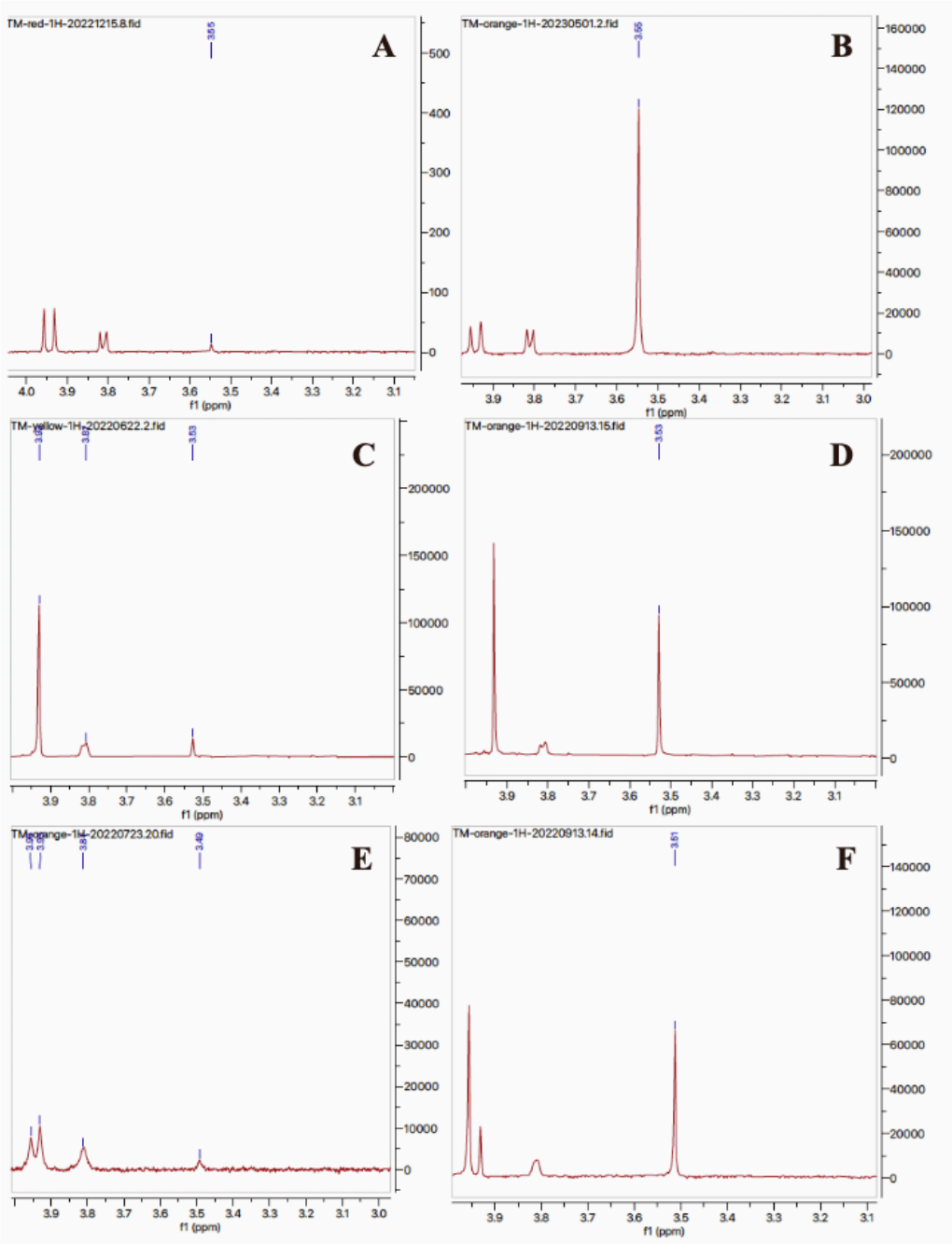


Figure A.101: NMR spectra; glycine spikes at pH 7.25. (A) – Glyoxylate, ammonia; regular/benchtop conditions. (B) – same as (A) with spike of glycine. (C) – Glyoxylate, ammonia; heated conditions. (D) – same as (C) with spike of glycine. (E) – Glyoxylate, ammonia; anaerobic conditions. (F) – same as (E) with spike of glycine.

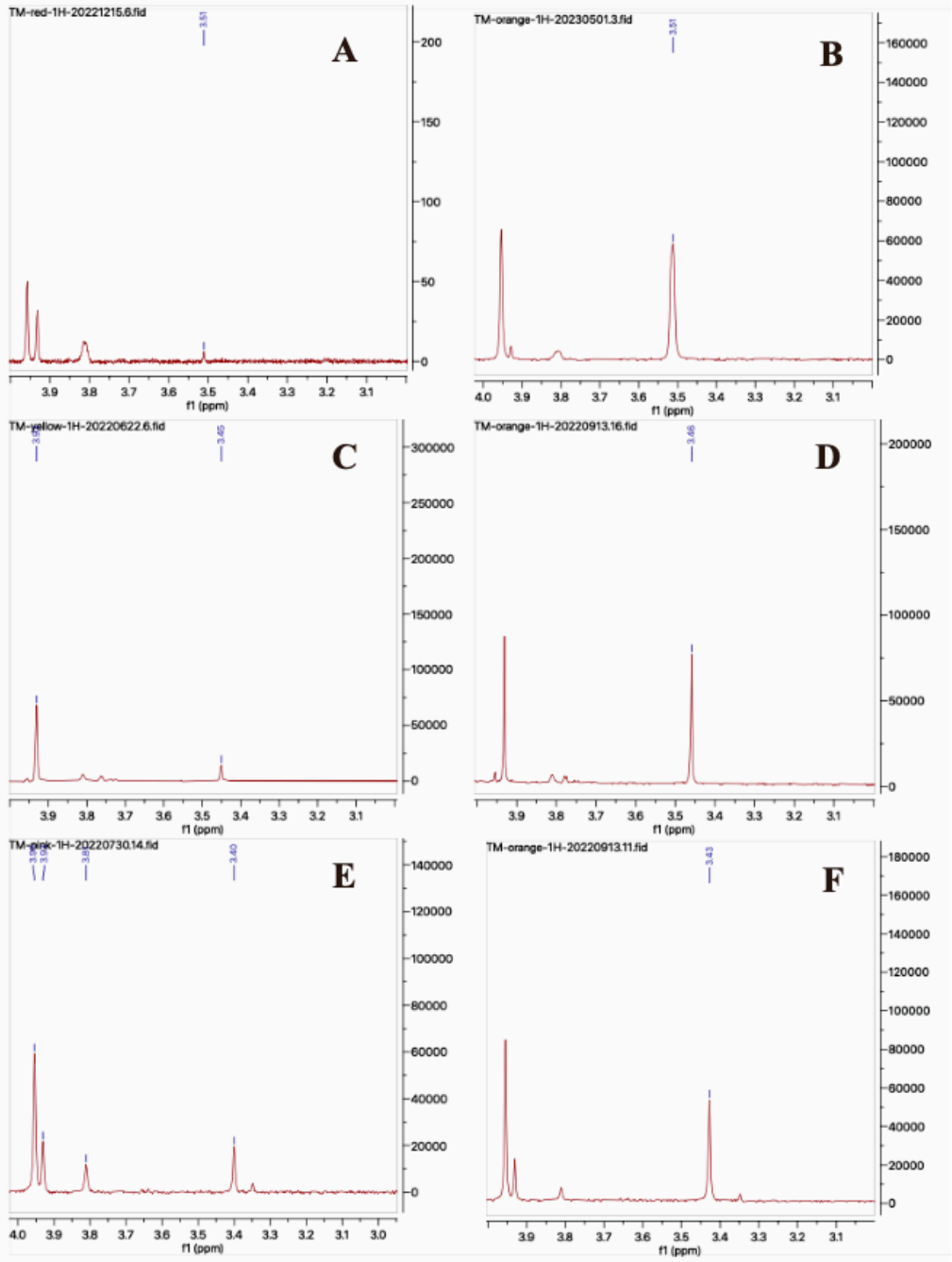


Figure A.102: NMR spectra; glycine spikes at pH 10. (A) – Glyoxylate, ammonia; regular/benchtop conditions. (B) – same as (A) with spike of glycine. (C) – Glyoxylate, ammonia; heated conditions. (D) – same as (C) with spike of glycine. (E) – Glyoxylate, ammonia; anaerobic conditions. (F) – same as (E) with spike of glycine.

Peak (ppm)	Organics	Num.	Ammonia	Condition	pH	Encel. salts	Notes	Identity
1.36	PA	90			-	Present	Widespread formation	
1.37–1.46	PA	230	Present		-	None	Widespread formation	
1.50–1.58	GA+PA	79	Present**		7.25, 10**	None**		
1.71	PA	19	None	Heat, Anaerobic	7.25, 10	None		
1.87–1.88	PA	28	None	-	7.25, 10	None		
1.91	PA	231			-			Acetate
1.96	PA	17	Present	-	7.25, 10			
2.28	GA+PA	13	Present**	Heat	7.25, 10	None**		
2.34–2.37	PA GA+PA GA+PA PA	508			-			Pyruvate
2.43–2.46	PA	33			7.25, 10	None		
2.95–2.96	PA	24	Present		-	Present		
2.99	GA+PA	9	Present**	Heat	-	None**		
3.13–3.14 3.18–3.19	PA	508			-	None (3.13, 3.18,		Decomposition

3.27–3.28 3.31–3.32 3.31–3.32 3.31–3.32						3.27, 3.31) Present (3.14, 3.19 3.28, 3.32)		
3.18, 3.19, 3.23, 3.24	GA+PA	240	Present**	Regular, Anaerobic	7.25, 10	None**		Maloyl formate
3.37–3.38	PA	25	Present		-	Present (3.38), present with increased carbonate (3.37)		
3.40–3.54	GA	98	Present		7.25, 10	None		Glycine (peak shifts)
3.60, 3.62	GA	20	Present	Anaerobic	-	Present		
3.81	GA	34	Present	Anaerobic	-			Glycolic acid oligomer
3.93	GA+PA, GA	124			-			Glycolate
4.08–4.09	GA+PA, GA (4.09)	23		Heat	7.25, 10	None		
4.31–4.33	GA	23		Heat	-	None (4.31–4.32), Present (4.32–4.33)		
4.38, 4.39,	GA+PA	65	Present	Regular,	7.25, 10	None		

4.40, 4.41				(Anaerobic)				
5.05–5.07	GA, GA+PA	128			7.25, 10 (5.05-5.06)	None (5.05–6) Present (5.07)		Glyoxylate
6.37	PA	4	Present	Regular	-	Present	Second and third weeks	
8.27	GA+PA	11	Present	Heat	7.25, 10	None		
8.44	GA, GA+PA	174			-			Formate

Table A.3: Experimental and control reactions conducted. Conditions in every row correspond to reactions conducted both without and with a chemical garden (control). Both control and experimental reactions in each row were conducted in all three experimental conditions: benchtop, heated/aerobic, and anaerobic. (*) concentrations are approximating those of Enceladus from (Glein et al., 2020) (0.2 M NaCl and 0.07 M $NaHCO_3$); (**) concentrations refer to the same set of Enceladuslike conditions but with increased (doubled) carbonate.

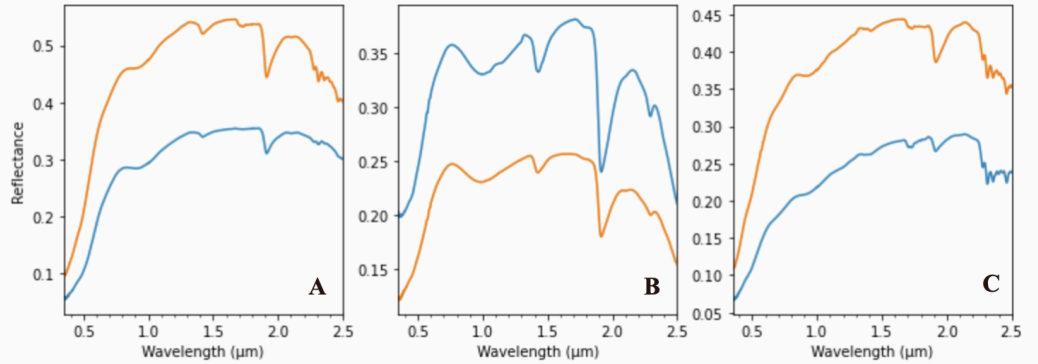


Figure A.103: VNIR spectra of glyoxylate, pyruvate, and ammonia under pH 10 (blue) and pH 7.25 (orange). (A) aerobic/benchtop conditions. (B) heated conditions. (C) anaerobic conditions.

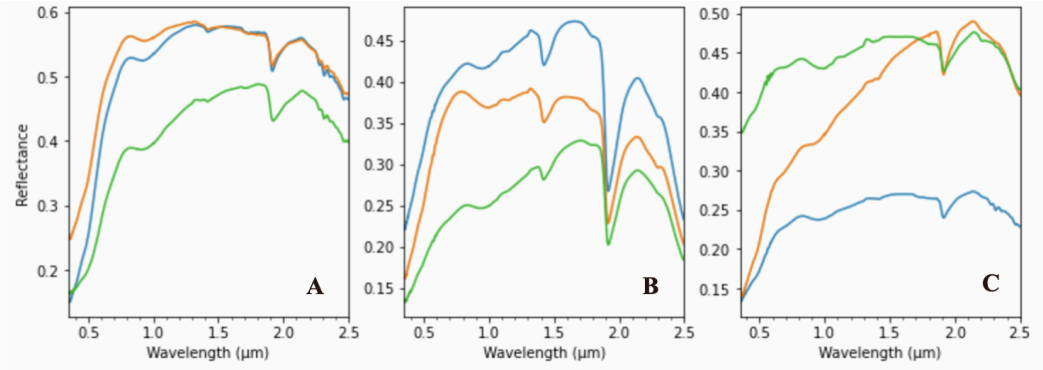


Figure A.104: VNIR spectra of glyoxylate in Enceladuslike salts (blue), glyoxylate and ammonia in Enceladuslike salts (orange) and glyoxylate and ammonia in Enceladuslike salts with increased salinity (green). (A) aerobic/benchtop conditions. (B) heated conditions. (C) anaerobic conditions.

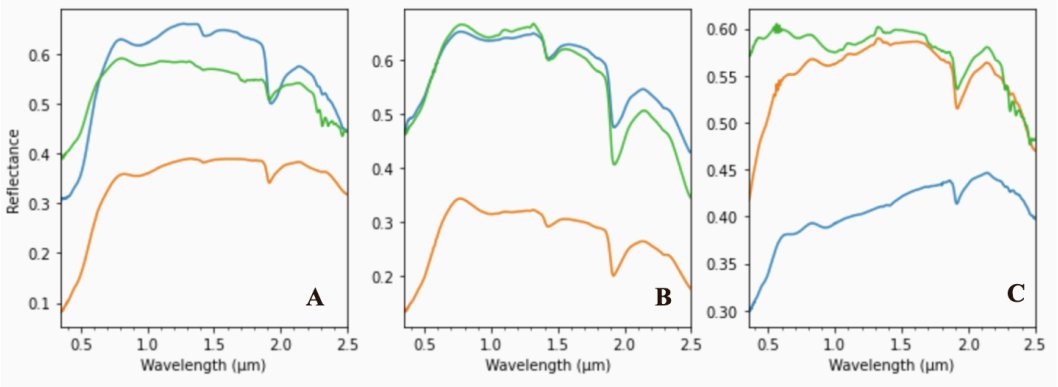


Figure A.105: VNIR spectra of pyruvate in Enceladuslike salts (blue), pyruvate and ammonia in Enceladuslike salts (orange) and pyruvate and ammonia in Enceladuslike salts with increased salinity (green). (A) aerobic/benchtop conditions. (B) heated conditions. (C) anaerobic conditions.

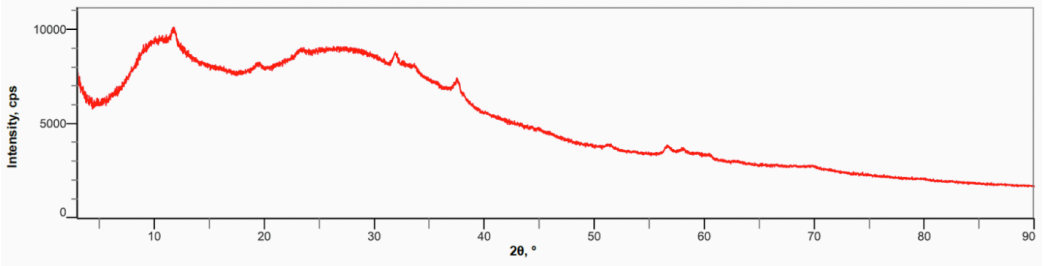


Figure A.106: XRD spectrum of a chemical garden.

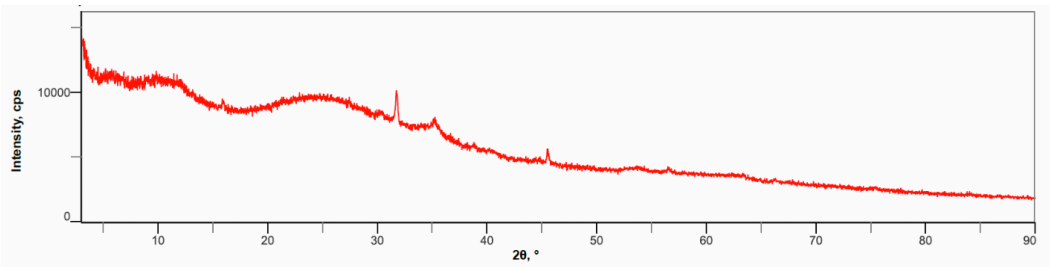


Figure A.107: XRD spectrum of a fully oxidized chemical garden.

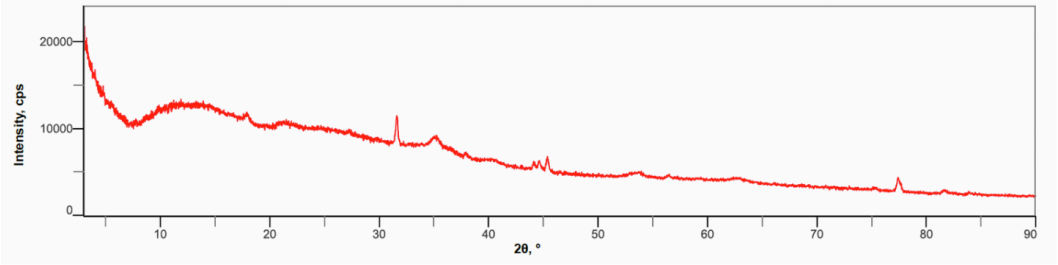


Figure A.108: XRD spectrum of solids formed from a reaction containing glyoxylate, a chemical garden, and ammonia at pH 7.25.

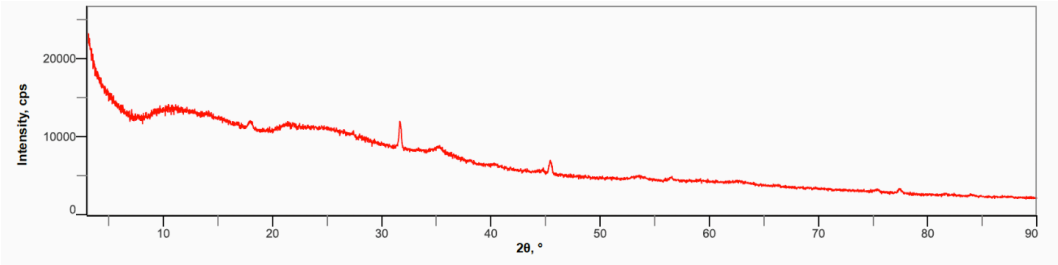


Figure A.109: XRD spectrum of solids formed from a reaction containing glyoxylate, a chemical garden, and ammonia at pH 10.

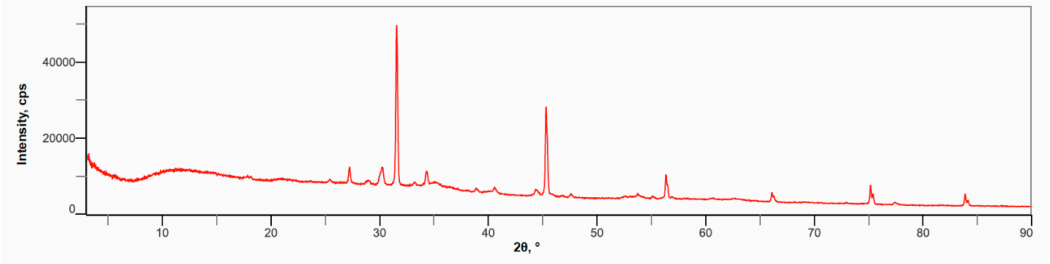


Figure A.110: XRD spectrum of solids formed from a reaction containing pyruvate, a chemical garden, ammonia, and Enceladuslike salts.

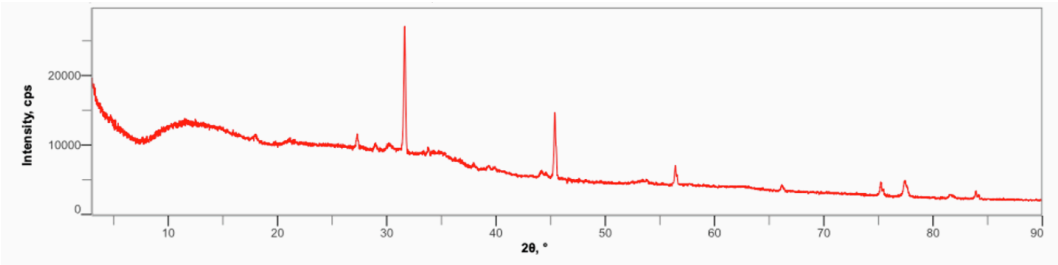


Figure A.111: XRD spectrum of solids formed from a reaction containing pyruvate, a chemical garden, ammonia, and Enceladuslike salts with increased salinity.

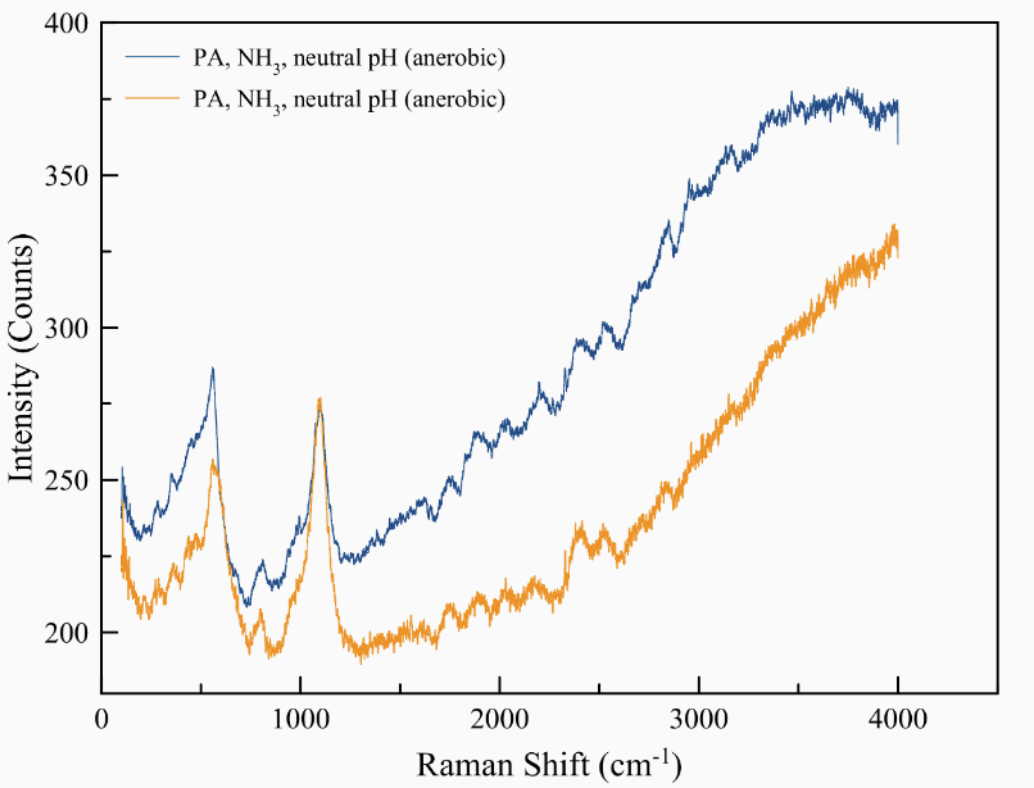


Figure A.112: Raman spectra of solids formed from a reaction containing pyruvate, a chemical garden, and ammonia at pH 7.25 in an anaerobic environment. Separate traces denote different locations of the same sample.

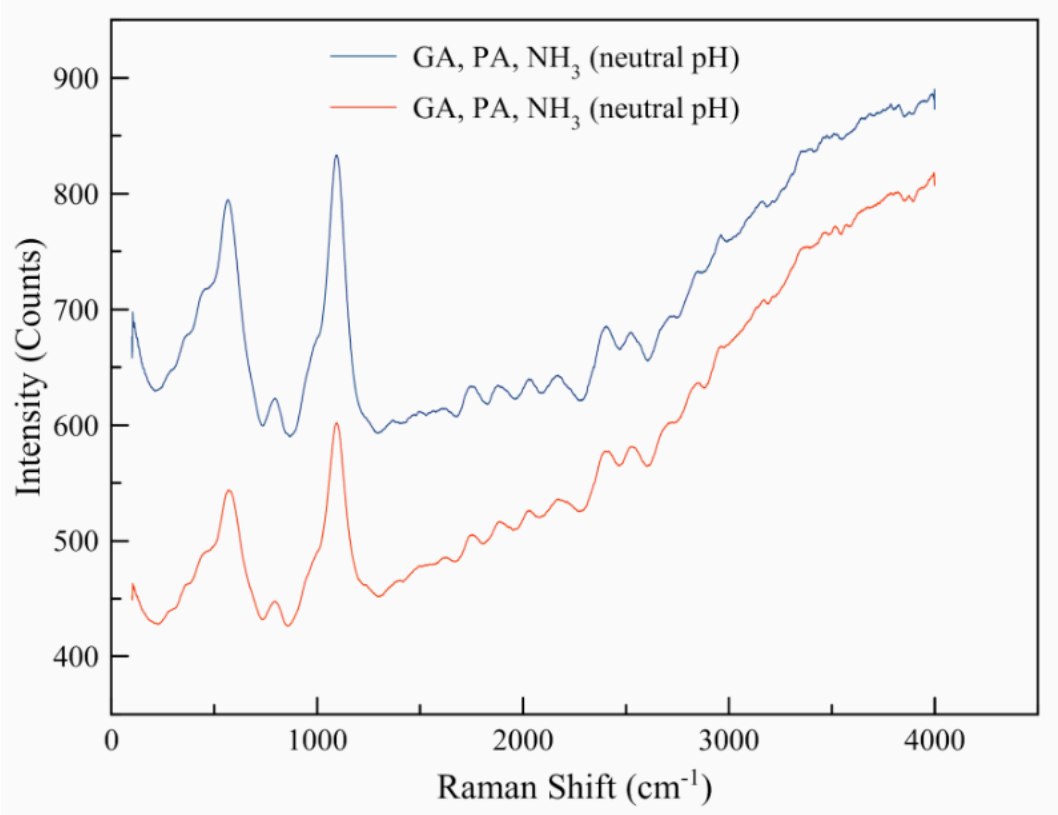


Figure A.113: Raman spectra of solids formed from a reaction containing glyoxylate, pyruvate, a chemical garden, and ammonia. Separate traces denote different locations of the same sample.

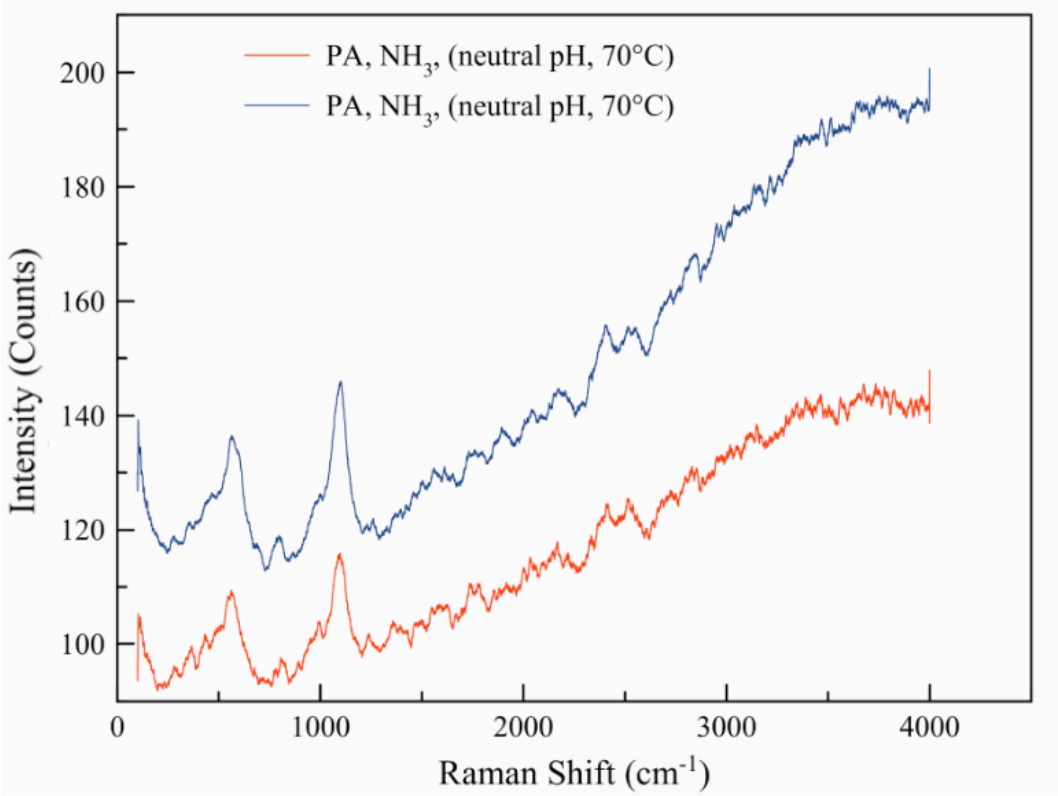


Figure A.114: Raman spectra of solids formed from a reaction containing pyruvate, a chemical garden, and ammonia at pH 7.25 conducted in a heated environment. Separate traces denote different locations of the same sample.

A.2 Experimental Procedures

Chemical garden growth:

Chemical gardens were grown in 50-milliliter polypropylene Falcon conical tubes by adding an iron salt to a silicate solution in order to produce a self-assembling precipitate (Barge et al., 2015); this procedure was adapted from Hooks et al., 2020. Dilute sodium silicate (sodium trisilicate, ~ 4 M (calculated based on weight percent), Sigma-Aldrich) was mixed in a 2:1 ratio with water (Milli-Q filtered 18.2 Mω·cm @ 25 °C) for a total of 40 mL. 0.4 grams of ferrous chloride tetrahydrate ($FeCl_2 \cdot 4H_2O$) was added to each tube containing the silicate solution, and the tube was tapped to ensure that crystals settled to the bottom. The tubes were capped and chemical gardens were allowed to grow for seven days. After seven days, the solid chemical garden precipitates were separated from the silica solution by carefully pouring through Whatman cytiva folded filter paper (diameter 240 mm, grade 598 1/2) and rinsed with 7 mL of Milli-Q water (Barge et al., 2015). Chemical gardens were stored in an anaerobic environment (COY chamber) in Falcon 50-ml conical tubes until used in the reactions below. All chemical gardens were stored for a minimum of one week in a N2 filled COY glovebox between harvesting and use in chemical reactions. The chemical gardens were not subjected to any additional drying prior to use.

Reaction procedure and conditions:

The chemical garden precipitates were added to aqueous solutions containing organic substrates and sometimes Enceladus-relevant salts to test whether the chemical gardens drive prebiotic reactions. Reactions (each with 40 ml volume of liquid) were conducted in 50 ml Falcon conical tubes (for non-heated reactions) or in 50 ml crimp top glass vials (for heated reactions). The reactions contained: the desired alpha keto acid anion (pyruvate (sodium pyruvate, J.T. Baker), glyoxylate (glyoxylic acid monohydrate, 97%; Alfa Aesar), or both; organics added at a 10 mM concentration), the presence or absence of 20 mM ammonia (added as NH_4Cl, Fisher Scientific), with basic (pH 10) or neutral (pH 6.5-7.5) Milli-Q water, and in the presence or absence of 0.2 M chloride (added as NaCl, Fisher Scientific), 0.07 M or 0.14 M carbonate (added as sodium carbonate, Na_2CO_3, Fisher Scientific) [S1]. Water was added directly from the Milli-Q without modification after measuring its pH with a pH meter. For reactions conducted with a basic pH, the pH of water from the Milli-Q was raised to pH 10 by addition of NaOH. All pH adjustments were carried out before the addition of any other reaction components. Reactions were conducted

(1) on the benchtop at room temperature while being continuously stirred, (2) on the benchtop submerged in a hot water bath heated to 70°C, and (3) in an anaerobic (nitrogen-filled) environment (COY vinyl anaerobic chamber with Type C Auto Airlock, Mod 260 Pump, and Mod 10 Gas Analyzer, O_2 < 200 ppm) at room temperature while being continuously stirred. Continuous stirring was carried out using an Ika magnetic stir plate. Anaerobic reactions were conducted with N_2-sparged water. Control reactions (identical conditions with organics but with no chemical gardens) were conducted for each set of experimental conditions.

Both glyoxlate and pyruvate are important prebiotic molecules often studied in the origins of life context. This work is focused on both early Earth conditions and Enceladus relevant conditions. While glyoxylate and pyruvate have not yet been detected on Enceladus (with *Cassini* making limited in situ measurements), we suggest a possible scenario for the presence of these molecules on Enceladus. Marín-Yaseli et al., 2016 studied HCN polymer synthesis; they observed formation of both pyruvic acid and glyoxylic acid from HCN under a variety of conditions. Their tested conditions are similar to ours, including the presence or absence of ammonia, the presence or absence of salts, and anaerobic versus aerobic environments. Although their reaction matrix also studies the presence or absence of aqueous aerosols, we do not consider these relevant to Enceladus and note that formation of both glyoxylic acid and pyruvic acid was detected in the absence of these aerosols. As HCN has recently been detected in Enceladus' plume (Peter et al., 2024), HCN polymerization is a possible pathway to formation of pyruvate and glyoxylate on Enceladus. Additionally, pyruvic acid, while not directly detected on Enceladus, has been identified in an extraterrestrial setting — it was found in carbonaceous chondritic meteorites (Cooper et al., 2011). We justify the inclusion of ammonia in our experiments since ammonia can be synthesized by hydrothermal vents (Takahagi et al., 2023). While high, the ammonia concentration is consistent with that predicted in Enceladus' ocean (Fifer et al., 2022) or what could occur in a localized early Earth environment following bombardment by an ammonia-rich meteorite (Pizzarello et al., 2011). Water-rock interactions on Enceladus are thought to occur at elevated temperatures (Hsu et al., 2015; Sekine et al., 2015), and 70°C is a reasonable temperature for a warm alkaline hydrothermal vent on the early Earth (Kelley et al., 2005).

Step	Specifics
Thermal treatment	-45°, 300 min
Secondary set point	+99
Post heat setting	40° (temp.), 100 min (time) 150 (vacuum)
Freeze, Condenser, Vacuum phases	-45 (condenser), 150 (vacuum)
Drying cycle	-10°, 1250 min, 150 (vacuum)

Table A.4: Freeze-dryer procedure used to dry the remaining solid mineral after the course of the reaction.

.

Liquid and solid sampling:

For liquid sampling, the vials were removed from the stir plates or hot bath, opened, and 1 mL aliquots were taken using a pipette at t = 0, 1, 2, and 3 weeks. After three weeks, the vials were removed from the stir plates or hot bath, and the solids were allowed to settle. The supernatant was removed by pipette and the remaining mineral was freeze-dried using an AdVantage XL Freeze Dryer (Freeze dryer recipe used can be found in Table A.4). The minerals were frozen in the original reaction vials and stored in the anaerobic COY chamber until analysis. Samples were stored in an anaerobic COY chamber unless otherwise noted.

^{1}H liquid Nuclear magnetic resonance (NMR) spectroscopy:

Organic analysis of the liquid samples was conducted with ^{1}H nuclear magnetic resonance (NMR) spectroscopy. Prior to NMR sample preparation, all 1 mL samples were centrifuged with a benchtop microfuge to separate out any iron or solid particles that were suspended in solution. No additional purification steps were taken prior to sample preparation. 540 μl of sample and 60 μl of sodium trimethylsilylpropanesulfonate (DSS)/D_2O standard were combined in an NMR tube. Water-suppressed ^{1}H spectra were acquired on a Bruker NEO 400 equipped with a hybrid broadband probe. The water signal was suppressed with presaturation in a 1D NOESY pulse sequence with a 10 millisecond mixing time. Each spectrum consisted of 64 scans preceded by 4 steady state scans. The pre-acquisition delay was 2 seconds and the acquisition time was 2 seconds. The spectra were processed in MestReNova 14 (Mestrelab Research S.L.) with 0.3 Hz of exponential multiplication followed by baseline correction. Spectra were referenced using the added sodium trimethylsilylpropanesulfonate (DSS)/D_2O standard. This standard presents a singular peak around 0 ppm and does not interact with anything else present in solution. All other peak assignments were made in reference to the DSS/D2O standard. In samples

where the presence of glycine was suspected (a challenging molecule to confirm due to its single and pH dependent peak), an additional spectrum was collected where the sample was spiked with 5 mM glycine to ascertain whether the peak in question was indeed glycine. In MestreNova, spectra were processed by removing the solvent (water) peak and conducting baseline correction as needed via the Whittaker Smoother algorithm.

X-ray diffraction (XRD):

Solid samples of the chemical garden precipitates under various reaction conditions were analyzed using XRD. Samples were transferred into an Anaerobe Systems AS-150 anaerobic chamber with a 5% CO_2, 10% H2, balance N_2 atmosphere. Although the solid precipitates analyzed by XRD were briefly exposed to a CO_2-containing atmosphere prior to XRD analysis, we do not anticipate that any contamination or side reactions occurred as previous handling of sensitive minerals has not led to contamination (Aguirre et al., 2021). Approximately 1 ml of each sample was ground in an agate mortar and pestle into a fine powder, then transferred into a Rigaku A00012148 airtight sample holder. They were then placed in a Rigaku Miniflex 600 powder X-ray diffractometer. XRD was conducted for chemical garden samples from the following experiments:

- 10 mM pyruvate, 0.2 M chloride, 0.07 M, 20 mM ammonia
- 10 mM glyoxylate, 20 mM ammonia
- 10 mM pyruvate, 0.2 M chloride, 0.14 M carbonate, 20 mM ammonia
- 10 mM glyoxylate, 20 mM ammonia, pH 10
- Fully oxidized chemical garden (unreacted, stored outside of COY as a control)
- Pre-reaction chemical garden

VNIR reflectance spectroscopy:

Solid samples (freeze-dried, and then stored in the anaerobic COY chamber) of the chemical garden precipitates were analyzed using visible-near infrared (VNIR) reflectance spectroscopy. Powdery solid samples were transferred to Cinefoil, a matte black coated aluminum foil that absorbs excess light. A spectrum of each sample from 0.35-2.5 μm (spectral resolution 0.003 μm) was then collected using a

FieldSpec 3 spectroradiometer from Analytical Spectral Devices (ASD) with a contact probe grip that was placed flush against the sample and Cinefoil. Spectra were collected against a Spectralon white reference. Powdered samples were returned to their storage vials.

Raman spectroscopy:

Select solid samples of the chemical garden precipitates were analyzed with Raman spectroscopy using a Horiba spectrometer with a green (532 nm) laser. A small portion of each mineral was removed using a scoopula. Samples were transferred to a glass microscope slide using a metal spatula. At least two sites per sample were looked at for each chemical garden. All samples were crushed prior to Raman analysis. The samples were subjected to four six-second acquisitions and worked up using Python 3.8 in JupyterLab.

References

Aguirre, Vincent P. et al. (Jan. 2021). "Synthesis and Characterization of Mixed-Valent Iron Layered Double Hydroxides ("Green Rust")". In: *ACS Earth and Space Chemistry* 5.1. Publisher: American Chemical Society, pp. 40–54. DOI: 10.1021/acsearthspacechem.0c00272. URL: https://doi.org/10.1021/acsearthspacechem.0c00272 (visited on 03/17/2024).

Barge, Laura M. et al. (Aug. 2015). "From Chemical Gardens to Chemobrionics". In: *Chemical Reviews* 115.16. Publisher: American Chemical Society, pp. 8652–8703. ISSN: 0009-2665. DOI: 10.1021/acs.chemrev.5b00014. URL: https://doi.org/10.1021/acs.chemrev.5b00014.

Cooper, George et al. (Aug. 2011). "Detection and formation scenario of citric acid, pyruvic acid, and other possible metabolism precursors in carbonaceous meteorites". In: *Proceedings of the National Academy of Sciences of the United States of America* 108.34, pp. 14015–14020. ISSN: 0027-8424. DOI: 10.1073/pnas.1105715108. URL: https://www.ncbi.nlm.nih.gov/pmc/articles/PMC3161584/ (visited on 05/25/2024).

Cui, Qiu et al. (2008). *Glyoxylic*. DOI: 10.13018/BMSE000471. URL: https://bmrb.io/metabolomics/mol_summary/show_data.php?id=bmse000471 (visited on 08/28/2023).

Fifer, Lucas M., David C. Catling, and Jonathan D. Toner (Aug. 2022). "Chemical Fractionation Modeling of Plumes Indicates a Gas-rich, Moderately Alkaline Enceladus Ocean". In: *The Planetary Science Journal* 3.8. Publisher: IOP Publishing, p. 191. ISSN: 2632-3338. DOI: 10.3847/PSJ/ac7a9f. URL: https://iopscience.iop.org/article/10.3847/PSJ/ac7a9f/meta (visited on 03/17/2024).

Glein, Christopher R. and J. Hunter Waite (Feb. 2020). "The Carbonate Geochemistry of Enceladus' Ocean". In: *Geophysical Research Letters* 47, e85885. ISSN: 0094-8276. DOI: 10.1029/2019GL085885. URL: https://ui.adsabs.harvard.edu/abs/2020GeoRL..4785885G.

Hooks, Michelle R. et al. (June 2020). "Effects of Amino Acids on Iron-Silicate Chemical Garden Precipitation". In: *Langmuir* 36.21. Publisher: American Chemical Society, pp. 5793–5801. ISSN: 0743-7463. DOI: 10.1021/acs.langmuir.0c00502. URL: https://doi.org/10.1021/acs.langmuir.0c00502.

Hsu, Hsiang-Wen et al. (Mar. 2015). "Ongoing hydrothermal activities within Enceladus". In: *Nature* 519.7542. Number: 7542 Publisher: Nature Publishing Group, pp. 207–210. ISSN: 1476-4687. DOI: 10.1038/nature14262. URL: https://www.nature.com/articles/nature14262.

Kelley, Deborah S. et al. (Mar. 2005). "A serpentinite hosted ecosystem: the Lost City hydrothermal field". In: *Science* 307.5714. Publisher: American Association for the Advancement of Science, pp. 1428–1434. DOI: 10.1126/science.1102556. URL: https://www.science.org/doi/full/10.1126/science.1102556.

Marín-Yaseli, Margarita R. et al. (2016). "The Role of Aqueous Aerosols in the "Glyoxylate Scenario": An Experimental Approach". In: *Chemistry – A European Journal* 22.36, pp. 12785–12799. ISSN: 1521-3765. DOI: 10.1002/chem.201602195. URL: https://onlinelibrary.wiley.com/doi/abs/10.1002/chem.201602195.

Peter, Jonah S., Tom A. Nordheim, and Kevin P. Hand (Feb. 2024). "Detection of HCN and diverse redox chemistry in the plume of Enceladus". In: *Nature Astronomy* 8.2. Publisher: Nature Publishing Group, pp. 164–173. ISSN: 2397-3366. DOI: 10.1038/s41550-023-02160-0. URL: https://www.nature.com/articles/s41550-023-02160-0 (visited on 05/25/2024).

Pizzarello, Sandra et al. (Mar. 2011). "Abundant ammonia in primitive asteroids and the case for a possible exobiology". In: *Proceedings of the National Academy of Sciences* 108.11. Publisher: Proceedings of the National Academy of Sciences, pp. 4303–4306. DOI: 10.1073/pnas.1014961108. URL: https://www.pnas.org/doi/10.1073/pnas.1014961108 (visited on 03/17/2024).

Sekine, Yasuhito et al. (Oct. 2015). "High-temperature water–rock interactions and hydrothermal environments in the chondrite-like core of Enceladus". In: *Nature Communications* 6.1. Number: 1 Publisher: Nature Publishing Group, p. 8604. ISSN: 2041-1723. DOI: 10.1038/ncomms9604. URL: https://www.nature.com/articles/ncomms9604 (visited on 04/05/2023).

Sodium acetate - Optional[1H NMR] - Chemical Shifts - SpectraBase (2024). URL: https://spectrabase.com/spectrum/JdihSmpJhVu (visited on 03/28/2024).

Takahagi, Wataru et al. (Oct. 2023). "Extreme accumulation of ammonia on electroreduced mackinawite: An abiotic ammonia storage mechanism in early ocean hydrothermal systems". In: *Proceedings of the National Academy of Sciences* 120.41. Publisher: Proceedings of the National Academy of Sciences, e2303302120. DOI: 10.1073/pnas.2303302120. URL: https://www.pnas.org/doi/abs/10.1073/pnas.2303302120 (visited on 03/26/2024).

Weber, Jessica M. and Laura M. Barge (2021). "Iron-Silicate Chemical Garden Morphology and Silicate Reactivity with Alpha-Keto Acids". In: *ChemSystemsChem* 3.3, e2000058. ISSN: 2570-4206. DOI: 10.1002/syst.202000058. URL: https://onlinelibrary.wiley.com/doi/abs/10.1002/syst.202000058.

Wishart, David S. et al. (Jan. 2009). "HMDB: a knowledgebase for the human metabolome". In: *Nucleic Acids Research* 37.Database, pp. D603–D610. ISSN: 0305-1048, 1362-4962. DOI: 10.1093/nar/gkn810. URL: https://academic.oup.com/nar/article-lookup/doi/10.1093/nar/gkn810 (visited on 08/28/2023).

Appendix B

PROPYNE SUPPLEMENTAL INFORMATION

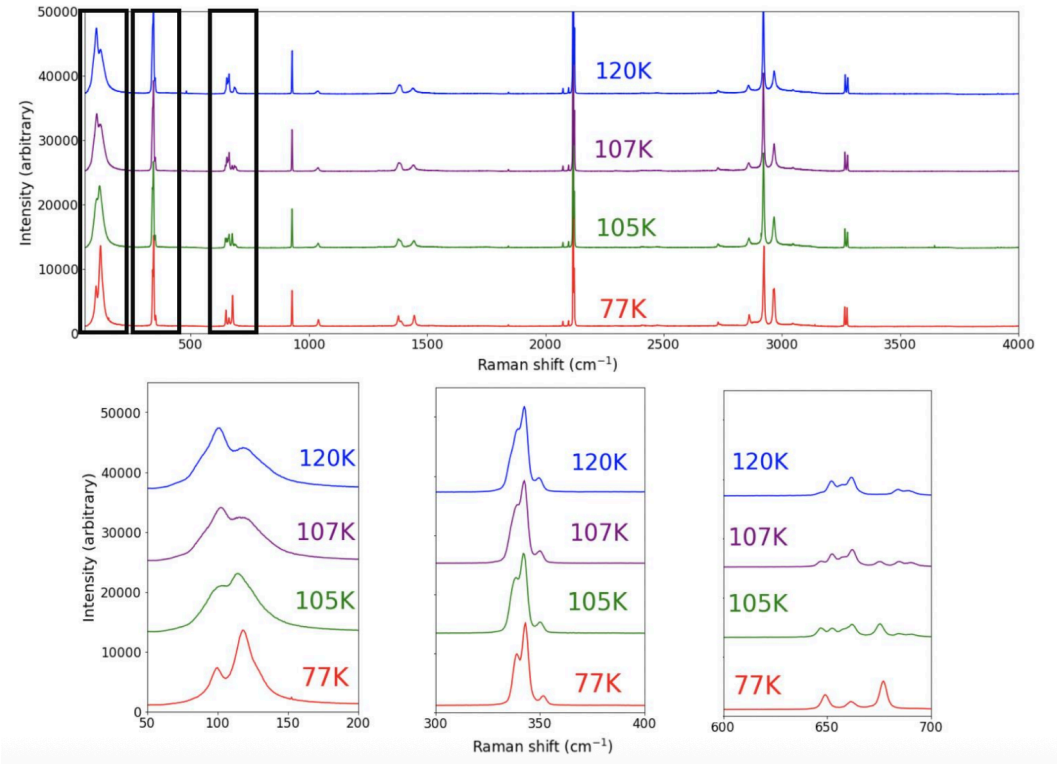
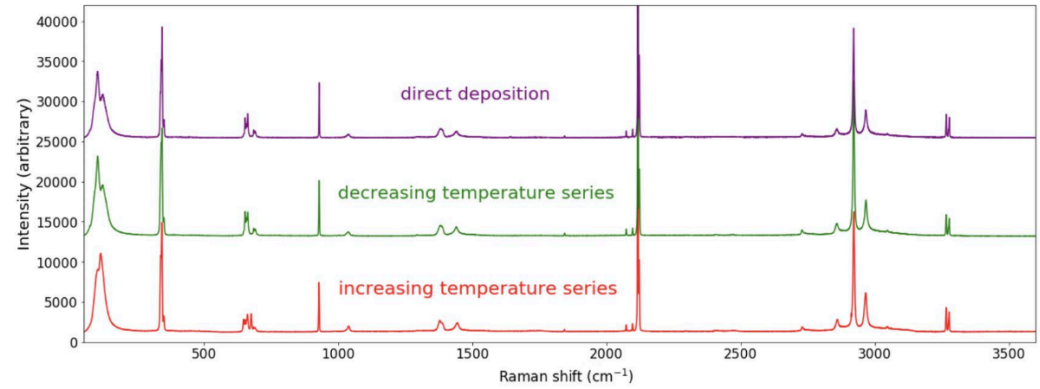


Figure B.1: Raman spectroscopy of pure propyne ice deposited at 75 K under low pressure, with increasing temperatures. A phase transition is observed around 105-107 K. Expanded views of various spectral regions are shown at the bottom panels.



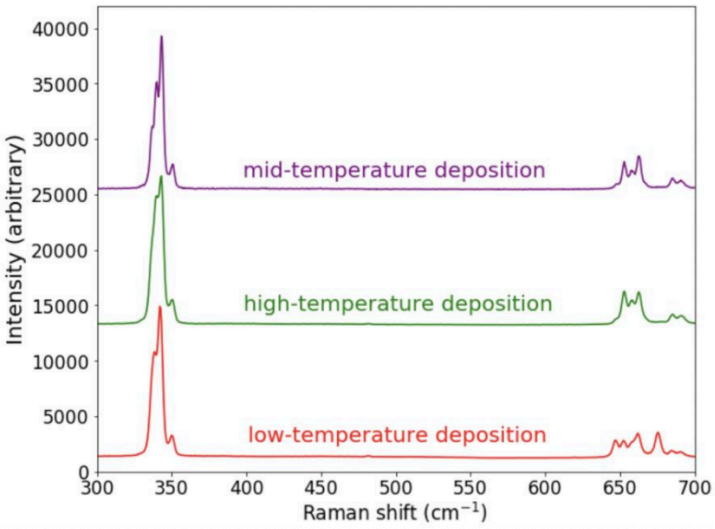


Figure B.2: Spectra at 105 K; low-temperature deposition at 75 K (increasing temperature series; warmed to 105 K), high-temperature deposition at 120 K (decreasing temperature series; cooled to 105 K), and direct deposition at 105 K comparisons. Direct deposition at 105 K has a crystalline structure.

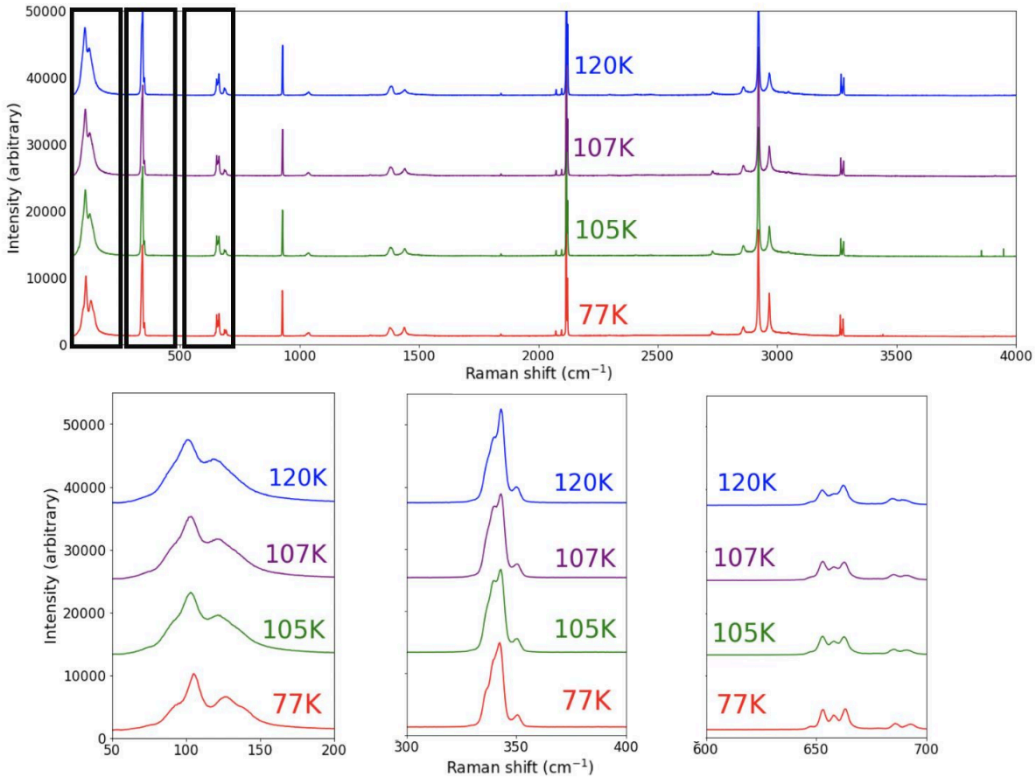


Figure B.3: Raman spectroscopy of pure propyne ice deposited at 120 K under low pressure, with decreasing temperatures. No phase transitions are observed. Expanded views of various spectral regions are shown at the bottom panels.

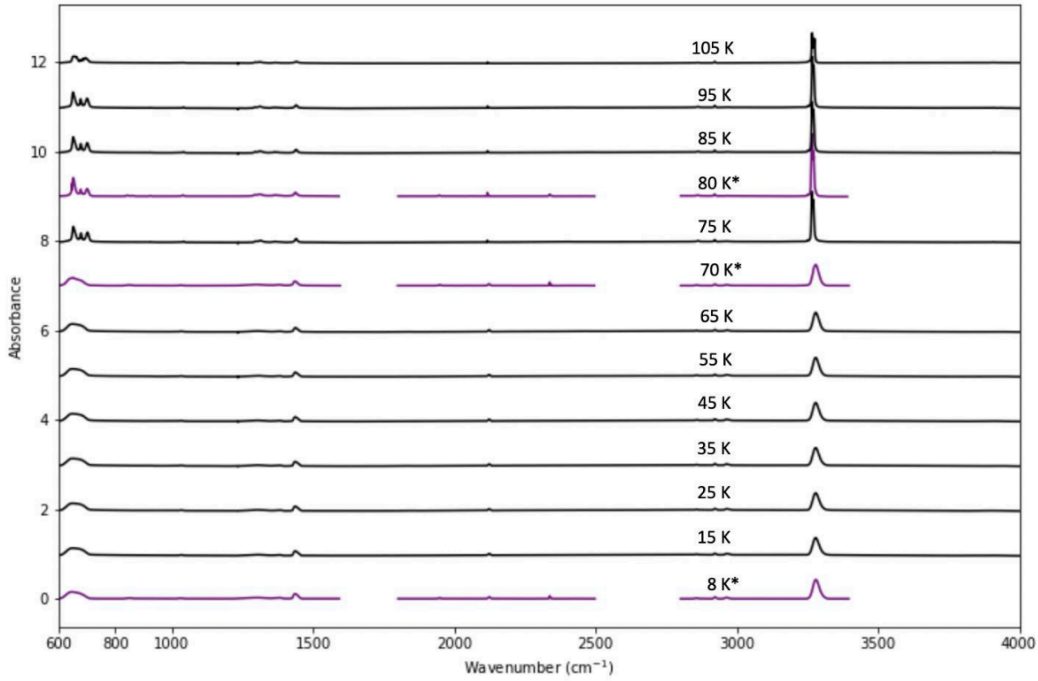


Figure B.4: Infrared spectroscopy temperature series of pure propyne deposited at 15 K and annealed to 105 K, under vacuum. Transition from amorphous to crystalline propyne is observed between 65 K and 75 K. Spectra highlighted in purple and denoted with an asterisk (8 K, 70 K, and 80 K) are from previously published work by Hudson et al., 2021 (Figure 11-13).

References

Hudson, Reggie L. et al. (Jan. 2021). “Infrared spectra and optical constants of astronomical ices: III. Propane, propylene, and propyne”. In: *Icarus* 354, p. 114033. ISSN: 0019-1035. DOI: 10.1016/j.icarus.2020.114033. URL: https://www.sciencedirect.com/science/article/pii/S0019103520303924.

Appendix C

OCCULTATION SUPPLEMENTAL INFORMATION

Input atmosphere	Combined SSE	Ingress SSE	Egress SSE
$L_s0°$	882.0	57.9	824.1
$L_s10°$	868.6	52.8	815.8
$L_s20°$	885.2	61.9	823.4
$L_s30°$	772.9	100.3	672.6
$L_s40°$	766.6	109.4	657.2
$L_s50°$	722.2	99.5	622.6
$L_s60°$	720.2	68.7	651.5
$L_s70°$	658.5	56.5	601.9
$L_s80°$	623.6	58.4	565.2
$L_s90°$	594.0	64.6	529.4
$L_s100°$	584.1	71.5	512.6
$L_s110°$	573.2	73.2	499.9
$L_s120°$	570.5	73.8	496.7
$L_s130°$	576.7	72.3	504.3
$L_s140°$	587.7	67.1	520.6
$L_s150°$	606.3	61.2	545.2
$L_s160°$	651.6	57.3	594.3
$L_s170°$	717.3	67.3	650.0
$L_s180°$	807.7	67.3	740.4
$L_s190°$	820.5	53.8	766.7
$L_s200°$	881.4	74.2	807.2
$L_s210°$	841.6	68.6	773.0
$L_s220°$	932.2	71.0	861.2
$L_s230°$	950.0	78.6	871.4
$L_s240°$	966.6	72.5	894.1
$L_s250°$	887.1	78.2	808.9
$L_s260°$	803.5	90.3	713.1
$L_s270°$	727.4	96.4	631.0
$L_s280°$	678.7	98.2	580.5
$L_s290°$	655.7	98.7	557.0
$L_s300°$	651.7	96.0	555.6
$L_s310°$	649.9	94.4	555.5
$L_s320°$	672.8	92.4	580.4
$L_s330°$	702.5	90.3	612.2
$L_s340°$	780.4	84.9	695.5
$L_s350°$	861.9	68.5	793.4
$ALMA$	664.3	42.6	621.7

Table C.1: Sum of squared errors table of all model-data matches for both ingress and egress spots combined, ingress spots alone, and egress spots alone (36 GCM snapshots and one ALMA profile).

Input atmosphere	Combined SSE	Ingress SSE	Egress SSE
$2 \times L_s 0°$	1263.6	160.1	1103.5
$2 \times L_s 10°$	1633.3	276.1	1357.2
$2 \times L_s 20°$	1625.4	585.8	1039.5
$2 \times L_s 30°$	2237.3	1349.2	888.1
$2 \times L_s 40°$	2175.5	1377.7	797.8
$2 \times L_s 50°$	2062.2	1308.8	753.4
$2 \times L_s 60°$	2023.8	1340.6	683.2
$2 \times L_s 70°$	1811.2	1126.9	684.3
$2 \times L_s 80°$	1769.7	843.1	926.6
$2 \times L_s 90°$	1513.1	719.1	794.0
$2 \times L_s 100°$	1277.4	562.0	715.5
$2 \times L_s 110°$	1063.6	370.4	693.2
$2 \times L_s 120°$	997.5	330.7	666.8
$2 \times L_s 130°$	1103.6	406.3	697.3
$2 \times L_s 140°$	1210.8	508.5	702.3
$2 \times L_s 150°$	1529.7	746.2	783.5
$2 \times L_s 160°$	1849.1	1083.5	765.6
$2 \times L_s 170°$	1977.7	1304.0	673.7
$2 \times L_s 180°$	2016.6	1246.7	770.0
$2 \times L_s 190°$	2141.3	1040.3	1101.0
$2 \times L_s 200°$	1346.2	272.9	1073.3
$2 \times L_s 210°$	1406.0	219.9	1186.0
$2 \times L_s 220°$	1383.8	92.3	1291.5
$2 \times L_s 230°$	1382.8	36.6	1346.1
$2 \times L_s 240°$	1349.7	28.9	1320.8
$2 \times L_s 250°$	1406.6	30.8	1375.8
$2 \times L_s 260°$	1740.8	38.8	1702.0
$2 \times L_s 270°$	1376.4	26.0	1350.5
$2 \times L_s 280°$	1219.1	45.3	1173.8
$2 \times L_s 290°$	1171.4	52.1	1119.3
$2 \times L_s 300°$	1228.4	46.9	1181.5
$2 \times L_s 310°$	1247.0	40.0	1207.0
$2 \times L_s 320°$	1200.5	44.1	1156.4
$2 \times L_s 330°$	1237.0	38.2	1198.8
$2 \times L_s 340°$	1434.0	30.3	1403.7
$2 \times L_s 350°$	1062.8	36.2	1026.5
$2 \times ALMA$	1955.1	907.1	1048.1

Table C.2: Sum of squared errors table of all model-data matches for both ingress and egress spots combined, ingress spots alone, and egress spots alone. The profiles correspond to input profiles with doubled magnitudes (36 GCM snapshots and one ALMA profile).

Input atmosphere	Combined SSE	Ingress SSE	Egress SSE
$0.5 \times L_s 0°$	583.4	86.4	497.0
$0.5 \times L_s 10°$	581.4	81.2	500.3
$0.5 \times L_s 20°$	569.0	75.5	493.5
$0.5 \times L_s 30°$	565.0	74.6	490.3
$0.5 \times L_s 40°$	553.2	70.9	482.3
$0.5 \times L_s 50°$	545.8	75.6	470.1
$0.5 \times L_s 60°$	540.6	74.1	466.5
$0.5 \times L_s 70°$	534.2	79.1	455.0
$0.5 \times L_s 80°$	516.4	80.0	436.3
$0.5 \times L_s 90°$	522.2	82.6	439.5
$0.5 \times L_s 100°$	524.9	83.2	441.8
$0.5 \times L_s 110°$	512.8	84.7	428.1
$0.5 \times L_s 120°$	518.0	84.4	433.6
$0.5 \times L_s 130°$	514.4	83.9	430.5
$0.5 \times L_s 140°$	519.9	80.2	439.7
$0.5 \times L_s 150°$	528.0	81.7	446.3
$0.5 \times L_s 160°$	529.2	78.7	450.5
$0.5 \times L_s 170°$	542.2	79.8	462.4
$0.5 \times L_s 180°$	556.6	75.2	481.5
$0.5 \times L_s 190°$	563.1	76.6	486.6
$0.5 \times L_s 200°$	591.0	78.6	512.4
$0.5 \times L_s 210°$	601.8	81.5	520.3
$0.5 \times L_s 220°$	612.9	84.1	528.8
$0.5 \times L_s 230°$	607.8	86.3	521.5
$0.5 \times L_s 240°$	598.8	84.4	514.4
$0.5 \times L_s 250°$	583.0	85.9	497.1
$0.5 \times L_s 260°$	557.3	87.2	470.1
$0.5 \times L_s 270°$	557.2	89.8	467.4
$0.5 \times L_s 280°$	542.9	88.3	454.6
$0.5 \times L_s 290°$	543.8	90.5	453.3
$0.5 \times L_s 300°$	529.8	90.3	439.5
$0.5 \times L_s 310°$	534.7	90.3	444.4
$0.5 \times L_s 320°$	538.0	87.5	450.4
$0.5 \times L_s 330°$	546.2	85.9	460.3
$0.5 \times L_s 340°$	557.8	87.1	470.7
$0.5 \times L_s 350°$	579.0	87.8	491.3
$0.5 \times ALMA$	524.5	72.9	451.5

Table C.3: Sum of squared errors table of all model-data matches for both ingress and egress spots combined, ingress spots alone, and egress spots alone. The profiles correspond to input profiles with halved magnitudes (36 GCM snapshots and one ALMA profile).